SCUOLA DI DOTTORATO
UNIVERSITÀ DEGLI STUDI DI MILANO-BICOCCA

Dipartimento di Fisica Giuseppe Occhialini

Dottorato di Ricerca in Fisica ed Astronomia Ciclo XXXI
Curriculum in Fisica subnucleare e tecnologie fisiche

Measurements of CP violation in B decays to charmless charged two-body final states at LHCb

Cognome: Fazzini Nome: Davide

Matricola: 727161

Tutore: Prof. Marta Calvi

Cotutore: Dr. Stefano Perazzini

Coordinatore: Prof. Marta Calvi

ANNO ACCADEMICO 2017/2018

Abstract

This thesis presents the results obtained from the measurements of both the time-integrated (TI) *CP* asymmetries of the $B^0 \to K^+\pi^-$ and $B_s^0 \to \pi^+K^-$ decays and the time-dependent (TD) *CP* asymmetries of the $B^0 \to \pi^+\pi^-$ and $B_s^0 \to K^+K^-$ decays. Such measurements have been performed using a data sample corresponding to an integrated luminosity of 3.0 fb^{-1} collected in proton-proton (pp) collisions at the centre-of-mass energy of 7-8 TeV at the LHCb experiment during the 2011 and 2012 data taking (Run 1). The final values of the *CP* parameters and asymmetries are:

$$\begin{aligned}
C_{\pi^+\pi^-} &= -0.34 \pm 0.06 \pm 0.01, \\
S_{\pi^+\pi^-} &= -0.63 \pm 0.05 \pm 0.01, \\
C_{K^+K^-} &= 0.20 \pm 0.06 \pm 0.02, \\
S_{K^+K^-} &= 0.18 \pm 0.06 \pm 0.02, \\
A_{K^+K^-}^{\Delta\Gamma} &= -0.79 \pm 0.07 \pm 0.10, \\
A_{CP}(B^0 \to K^+\pi^-) &= -0.084 \pm 0.004 \pm 0.003, \\
A_{CP}(B_s^0 \to \pi^+K^-) &= 0.213 \pm 0.015 \pm 0.007,
\end{aligned}$$

where the first uncertainty is statistical and the second is systematic. The results are in good agreement with the previous measurements.

The values of $C_{\pi^+\pi^-}$, $S_{\pi^+\pi^-}$, $A_{CP}(B^0 \to K^+\pi^-)$ and $A_{CP}(B_s^0 \to \pi^+K^-)$ are the most precise measurements achieved by a single experiment and the results obtained for $C_{K^+K^-}$, $S_{K^+K^-}$ and $A_{K^+K^-}^{\Delta\Gamma}$ represent the strongest evidence for the TD *CP* violation in the B_s^0 meson sector to date. These measurements are published in Physical Review D98 [1]. In addition, the preliminary results of the analysis update performed using the data corresponding to an integrated luminosity of 2.0 fb^{-1} collected at the LHCb experiment in pp collisions at the centre-of-mass energy of 13 TeV during the 2015 and 2016 data taking are presented. The values obtained for the *CP* parameters and asymmetries are:

$$\begin{aligned}
C_{\pi^+\pi^-} &= -0.375 \pm 0.061, \\
S_{\pi^+\pi^-} &= -0.682 \pm 0.053, \\
C_{K^+K^-} &= 0.124 \pm 0.051, \\
S_{K^+K^-} &= 0.186 \pm 0.052, \\
A_{K^+K^-}^{\Delta\Gamma} &= -0.786 \pm 0.065, \\
A_{CP}(B^0 \to K^+\pi^-) &= -0.083 \pm 0.003 \pm 0.003, \\
A_{CP}(B_s^0 \to \pi^+K^-) &= 0.244 \pm 0.014 \pm 0.003,
\end{aligned}$$

where the first uncertainty is statistical and the second is systematic. The statistical precision on the *CP* parameters measured from the TD *CP* asymmetries is expected to be reduced by a relative 30%,

when the analysis will be completed. The study of the systematic sources of uncertainties has to be finalized and the total uncertainty is expected to be slightly lower than the Run 1 analysis.

Sintesi

In questa tesi vengono mostrati i risultati ottenuti dalla misura delle asimmetrie di *CP* integrate nel tempo nei decadimenti $B^0 \to K^+\pi^-$ e $B_s^0 \to \pi^+K^-$, e delle asimmetrie di *CP* dipendenti dal tempo nei decadimenti $B^0 \to \pi^+\pi^-$ e $B_s^0 \to K^+K^-$. Queste misure sono state realizzate utilizzando un campione di dati corrispondente ad una luminosità integrata di 3.0 fb^{-1} generato da collisioni protone-protone (pp) ad un'energia nel centro di massa pari a 7-8 TeV all'esperimento LHCb. I valori finali dei parametri di *CP* e delle asimmetrie sono:

$$\begin{aligned}
C_{\pi^+\pi^-} &= -0.34 \pm 0.06 \pm 0.01, \\
S_{\pi^+\pi^-} &= -0.63 \pm 0.05 \pm 0.01, \\
C_{K^+K^-} &= 0.20 \pm 0.06 \pm 0.02, \\
S_{K^+K^-} &= 0.18 \pm 0.06 \pm 0.02, \\
A_{K^+K^-}^{\Delta\Gamma} &= -0.79 \pm 0.07 \pm 0.10, \\
A_{CP}(B^0 \to K^+\pi^-) &= -0.084 \pm 0.004 \pm 0.003, \\
A_{CP}(B_s^0 \to \pi^+K^-) &= 0.213 \pm 0.015 \pm 0.007,
\end{aligned}$$

dove la prima incertezza è statistica e la seconda è sistematica. I risultati ottenuti sono in buono accordo con le misure precedenti. I valori di $C_{\pi^+\pi^-}$, $S_{\pi^+\pi^-}$, $A_{CP}(B^0 \to K^+\pi^-)$ e $A_{CP}(B_s^0 \to \pi^+K^-)$ sono i più precisi ottenuti da un singolo esperimento. Inoltre, i risultati ottenuti per le osservabili $C_{K^+K^-}$, $S_{K^+K^-}$ e $A_{K^+K^-}^{\Delta\Gamma}$ risultano essere ad oggi la più forte evidenza di violazione di *CP* dipendente dal tempo nel settore dei mesoni B_s^0. Questi risultati sono stati pubblicati sulla rivista scientifica Physical Review D98 [1]. In questa tesi sono anche presentati i risultati preliminari relativi all' aggiornamento di questa analisi, realizzato utilizzando il campione di dati corrispondente ad una luminosità integrata di 2.0 fb^{-1} raccolto dall'esperimento LHCb in collisioni pp ad un'energia nel centro di massa pari a 13 TeV nel Run 2. I valori ottenuti per i parametri di *CP* e delle asimmetrie sono:

$$\begin{aligned}
C_{\pi^+\pi^-} &= -0.375 \pm 0.061, \\
S_{\pi^+\pi^-} &= -0.682 \pm 0.053, \\
C_{K^+K^-} &= 0.124 \pm 0.051, \\
S_{K^+K^-} &= 0.186 \pm 0.052, \\
A_{K^+K^-}^{\Delta\Gamma} &= -0.786 \pm 0.065, \\
A_{CP}(B^0 \to K^+\pi^-) &= -0.083 \pm 0.003 \pm 0.003, \\
A_{CP}(B_s^0 \to \pi^+K^-) &= 0.244 \pm 0.014 \pm 0.003,
\end{aligned}$$

dove la prima incertezza è statistica e la seconda è sistematica. Ad analisi conclusa, la precisione statistica per i parametri di *CP* misurati dalle asimmetrie dipendenti dal tempo è attesa ridursi del 30%. Lo studio delle sorgenti sistematiche deve ancora essere finalizzato e si prevede che l'incertezza complessiva sarà inferiore rispetto a quella dell'analisi nel Run 1.

Table of Contents

Introduction

The Standard Model of the particle physics describes correctly most of the physics processes known at date. However many other questions remain still opened. One of these concerns the almost completely disappearance of anti-matter from the Universe. In the first moments after the Big Bang the amount of matter and anti-matter created is believed to be exactly the same. In the successively instants particles and antiparticles started to interact with each other, producing as a result an Universe dominated by matter. Such a situation can be explained only by means of physics phenomena which distinguish between matter and anti-matter particles. The first discovery of a physics process of this kind dates back to 1964: the so-called *CP* symmetry was observed to be broken for the very first time in the K weak sector. This observation was just the first of a long row which continues even nowadays, including the B and D sectors. According to the Standard Model, *CP* violation can be interpreted as the consequence of a complex phase entering in the elements of the Cabibbo-Kobayashi-Maskawa (CKM) matrix. The family of the charged charmless two body decays $H_b \to h^+ h'^-$, where H_b can be a B^0 meson, B_s^0 meson or Λ_b^0 baryon, while h and h' stand for a pion (π), a kaon (K) or a proton (p), comprise a set of physics processes very sensitive for probing the CKM matrix and revealing the presence of New Physics effects. This kind of decays receive significant contributions form both tree-level and 1-loop transitions and the presence of loop is exactly the reason why such decays are sensitive to New Physics effects. On the other hand, because of the loop presence, it is not possible to obtain a clean measurement of the CKM phases from such decays. One interesting method to exploit the loop diagrams consists in combining the measurements of the $B^0 \to \pi^+\pi^-$ and $B_s^0 \to K^+K^-$ time-dependent *CP* asymmetries, assuming the invariance of the strong interaction dynamics under U-spin symmetry, i.e. the exchange of the $d \leftrightarrow s$ quarks in the B^0 and B_s^0 mesons. In such a way the CKM angle γ can be determined and, because of the possible New Physics contributions, its value could differ significantly from the measurement of γ obtained from other B decays

dominated by tree-level diagrams. Finally, since the U-spin symmetry is not exactly conserved, also the measurement of the direct CP asymmetries of the $B^0 \to K^+\pi^-$ and $B_s^0 \to \pi^+K^-$ decays covers an important role, in order to constrain the size of the symmetry breaking effects.

In this thesis the measurements of the time-dependent and time-integrated CP asymmetries on the $H_b \to h^+h'^-$ decays are discussed. In the first chapter the Standard Model is introduced focusing on the basic formalism of the CKM matrix and the CP violation. Then an overview of the phenomenology related to the $H_b \to h^+h'^-$ decays is presented. Different experiments performed measurements concerning the CP violation on the $H_b \to h^+h'^-$ decays and all the results are in good agreement. A brief description of the status of art is presented in the second chapter. In the third chapter an introduction to the LHC collider and the description of the LHCb detector are reported. In particular, the technologies and the performance of each sub-detector of LHCb are summarised. The fourth chapter is focused on the "flavour tagging" technique, a fundamental tool in every time-dependent analysis since it allows to determine the flavour at production of the B^0 or B_s^0 mesons. The fifth chapter is dedicated to the measurement of the time-dependent and time-integrated CP asymmetries of the $H_b \to h^+h'^-$ decays, performed using the data collected by LHCb during the 2011 and 2012 data taking at $\sqrt{s} = 7 - 8$ TeV, corresponding to an integrated luminosity of about 3 fb^{-1} (Run 1 analysis). The corresponding analysis has been published during 2018 in Physical Review D98 [1]. An update of this analysis, performed using the events collected by LHCb during the 2015 and 2016 data taking at $\sqrt{s} = 13$ TeV and corresponding to an integrated luminosity of about 2 fb^{-1} (Run 2 analysis), is presented in the sixth chapter. Finally, in the last chapter the conclusions of this thesis are discussed.

The Run 1 analysis have been carried out in collaboration with the LHCb group of the University of Bologna. My main contributions to this analysis comprise the development of the BDT used in the offline selection, discussed in Section 5.1.4, the calibrations of the flavour tagging algorithms, reported in Section 4.4, and the determination of the decay-time acceptance for signal and background components, shown Section 5.4.2. The Run 2 analysis is conducted with the LHCb group of the University of Bologna while, in parallel, the LHCb group of the University of Glasgow is performing the same analysis using an independent fitting strategy. In this case, my main contributions are related to the optimisation of the event selection, reported in Section 6.1.2, the studies of the flavour tagging algorithms, shown in Section 4.6, the calibration of the decay-time resolution, discussed in Section 6.3.1, the evaluation of the corrections to $A_{CP}(B^0 \to K^+\pi^-)$ and $A_{CP}(B_s^0 \to \pi^+K^-)$, discussed in Section 6.4.1, and to the final CP fit, whose results are presented in Section 6.4. Nevertheless, for sake of completeness and clarity, all the analysis ingredients needed to achieve the final results have been discussed in this thesis.

In Chapters 4 and 5, the plots that are not reported in any official LHCb document are labelled as "LHCb unofficial". Similarly, since the Run 2 analysis is still on-going, all the plots shown in Chapter 6 are labelled in the same way because no publication is currently available.

1

Theoretical Introduction

One of the most important topics in modern particle physics is the violation of the *CP* symmetry: the non invariance of fundamental interactions under the combined transformation of charged conjugation, *C*, and parity, *P*. Under *C* symmetry particles are turned into antiparticles, "reversing" their internal quantum numbers, for example $Q \to -Q$ for the electromagnetic charge. Under *P* instead, the spatial coordinates are reversed, inverting the handedness of the reference frame, for example $\overrightarrow{x} \to -\overrightarrow{x}$. If the combination of these two transformations was an exact symmetry of Nature, matter and antimatter would behave in the same way. The first observation of *CP* violation (*CPV*) occurred in 1964 in neutral kaon decays [2] and in the following decades it has been extensively studied, including also *B* and *D* meson decays.

In the latest years the LHCb collaboration performed many analyses related to this topic and the work described in this thesis represents one of the strongest evidences for *CP* violation in B_s meson decays. Nowadays, *CP* violation is considered a well established experimental fact in K^0, $B^{\pm}$ and $B^0_{(s)}$ decays, thanks to the combined effort provided by different experiments. In recent years the LHCb collaboration claimed also the observation of *CP* violation in the D^0 sector [3, 4].

CP violation is an important ingredient in order to describe the structure of our universe, giving an explanation to the disappearance of the antimatter. However it is well known that the size of the *CP* violation expected from the Standard Model (*SM*) is not sufficient to generate the large baryon asymmetry that we observe [5]. This is one of the reasons which pushed the physicists to postulate a new kind of physics beyond the *SM* which, including new particles and interactions, could lead to additional sources of *CP* violation. This new physics is associated to high energy scales, at the moment not directly accessible at the colliders nowadays. Anyway, it could also manifest itself as small deviations of some observables from the their *SM* predictions. Thus the *CP* violation represents a very important topic to be explored with constantly increasing precision, since any improvements, both experimental and theoretical, can play a crucial role for the understanding of the physics be-

Table 1.1: Fermions described in the Standard Model. The respective masses are also reported.

	1^{st} generation		2^{nd} generation		3^{rd} generation	
Leptons	ν_e	$< 2\ eV$	ν_μ	$< 2\ eV$	ν_τ	$< 2\ eV$
	e	511 KeV	μ	105.7 MeV	τ	1.78 GeV
Quarks	u	2 MeV	c	1.27 GeV	t	173 GeV
	d	5 MeV	s	95 MeV	b	4.18 GeV

yond the SM.

1.1 The Standard Model

The Standard Model was introduced in 1961 by Glashow, Weinberg and Salam [6, 7, 8] and it represents the best model able to describe the interactions of the fundamental particles, i.e. bosons and fermions. Among the fundamental interactions of Nature only the electromagnetic, the weak and the strong forces are included within the SM. The action of these forces is mediated by bosons: the massless, chargeless photon (γ) is linked to the electromagnetic field, the weak interaction is carried by the Z^0 and $W^\pm$ massive gauge bosons, and the strong force is mediated by eight massless, chargeless gluons. In addition to these particles, the SM predicts also the existence of the Higgs boson (H) This scalar boson is not responsible for a fundamental interaction but it is linked to the spontaneous symmetry breaking mechanism which gives mass to the other particles.

The fermions, organized in three generations, are classified in leptons and quarks. The lepton family consists of the electron (e^-), muon (μ^-) and tauon (τ^-) and their associated neutrinos (ν_e, ν_μ and ν_τ). On the other side, quarks are classified in two groups: up (u), charm (c), top (t), denoted up-type quarks, and down (d), strange (s), bottom (b) named the down-type quarks. In addition, each of these particles is linked to an antiparticle which possess equal mass and spin but opposite quantum numbers. Fermions and bosons are summarized in Tables 1.1,1.2. Differently from the leptons it is not possible observing quarks on their own in nature, they are always observed in bounded states made by two or more quarks, named hadrons. The responsible for binding quarks together is the strong force. Hadrons are classified differently according to the number of quarks they possess: mesons, made by two quarks, baryons, with three quarks, and finally tetraquarks and pentaquarks with four and five quarks, respectively; these two latest bounded states have been observed recently for the first time at the LHCb experiment[9, 10, 11, 12].

Table 1.2: Bosons described in the Standard Model with their mass and relative strength of the interaction.

Interaction	Bosons	Mass	Relative strength
Electromagnetic	γ	0	$\alpha_{em} \sim O(10^{-2})$
Weak	$W^{\pm}$	80.4 GeV	$\alpha_W \sim O(10^{-6})$
	Z^0	91.2 GeV	
Strong	g $(g_1, \ldots, g_8)$	0	$\alpha_s \sim O(1)$
-	H^0	125.9 GeV	-

1.1.1 *CP* symmetry

Our Universe shows a significant discrepancy in amount of matter and antimatter, however, according to many theories, at the beginning for each matter particle an antimatter particle existed. In 1917 a German mathematician, namely Emmy Noether, proved a theorem according to which each symmetry implies the existence of a conserved quantity [13]. Thus the dominance of the matter over the antimatter could be explained as the consequence of a certain physics quantity which is not conserved.

In modern physics any alteration or perturbation of the system state can be described as an operator $\widehat{\mathcal{O}}$ acting on some functions ψ:

$$\widehat{\mathcal{O}}|\psi\rangle = \lambda|\psi\rangle. \tag{1.1}$$

Any function ψ which satisfies the Eq.1.1 is named eigenfunction of the operator $\widehat{\mathcal{O}}$ and λ represents its eigenvalue.

The *CP* operator can be represented as the combination of two operators: the charge operator (C) which basically switches the charge quantum number of all the particles described by the state function; and the parity operator (P) which change the sign of the quantum number describing the spin onto a specific axis for all particles included in the system. In other words, the C operator convert any particle into its related antiparticle while the P operator creates a mirror image of the initial system. In conclusion, when the *CP* operator acts on a system both spin and charge quantum number of all the particles are switched transforming, for example, a left-handed particle into a right-handed antiparticle.

1.2 The *CKM* matrix

The *SM* request of a Lagrangian invariant under local gauge transformations leads to massless fermions and gauge bosons. When the symmetry group of the electroweak interaction, $SU(2)_L \times$

$U(1)_Y$, is broken through the *Spontaneous Symmetry Breaking* mechanism a vacuum expectation value is assigned to the Higgs field.The Higgs field can be represented as a doublet of complex scalar fields:

$$\Phi(x) = \begin{pmatrix} \Phi^+(x) \\ \Phi^0(x) \end{pmatrix}, \tag{1.2}$$

where the minimum of the potential is chosen as $\Phi(x) = \frac{1}{\sqrt{2}}\left(0, \sqrt{-\frac{\mu^2}{\lambda}} + h(x)\right)$ and the expectation value on the vacuum state is $\langle\phi\rangle = \left(0, \frac{\nu}{\sqrt{2}}\right)$, with $\nu = -\frac{\mu}{\sqrt{\lambda}}$ [14].

According to the *SM*, the quark masses and the *CP* asymmetry are due to complex phases in the Yukawa coupling of quarks with the Higgs scalar field:

$$\mathcal{L}_Y = -Y^d_{ij}\overline{Q^I_{Li}}\phi d^I_{Rj} - Y^u_{ij}\overline{Q^I_{Li}}\varepsilon\phi^* u^I_{Rj} + h.c., \tag{1.3}$$

where $Y^{u,d}$ are 3x3 complex Yukawa matrices, ϕ is the Higgs field, ε is the 2×2 antisymmetric tensor, Q^I_L are the left handed quark doublets, d^I_R, u^I_R are the generic right-handed down-type and up-type quark weak singlets and i, j are the generation labels[15]. The physical states can be obtained by diagonalizing the Yukawa matrix by means of four unitary matrices $V^{u,d}_{L,R}$ as:

$$M^f_{diag} = \frac{\nu}{\sqrt{2}} V^f_L Y^f V^{f\dagger}_R \tag{1.4}$$

where $f = u, d$ and $\frac{\nu}{\sqrt{2}}$ is the expectation value for the Higgs scalar. As a result, the mass eigenstates are not the same as the eigenstates related to the weak interaction but can be expressed as a their linear combination, as Cabibbo suggests in 1963 [16]. Furthermore, the interactions between quarks and weak gauge bosons $W^\pm$ are expressed in terms of charged currents:

$$\mathcal{L}_{W^\pm} = \frac{g}{\sqrt{2}}\overline{U_{Li}}\gamma^\mu (V^u_L V^{d\dagger}_L)^{ij} D_{Lj} W^+_u + h.c., \tag{1.5}$$

where g stands for the electroweak coupling constant U_{Li} and D_{Li} represent the left handed up-type and down-type quarks and the i index runs over the three generations. The expression $V^u_L V^{d\dagger}_L$ stands for a 3×3 unitary matrix, so-called Cabibbo-Kobayashi-Maskawa (*CKM*) matrix[17]:

$$V_{CKM} = V^u_L V^{d\dagger}_L = \begin{pmatrix} V_{ud} & V_{us} & V_{ub} \\ V_{cd} & V_{cs} & V_{cb} \\ V_{td} & V_{ts} & V_{tb} \end{pmatrix} \tag{1.6}$$

The weak (d', s', b') and mass (d, s, b) eigenstates are connected by the *CKM* matrix by the following relation:

$$\begin{pmatrix} d' \\ s' \\ b' \end{pmatrix} = \begin{pmatrix} V_{ud} & V_{us} & V_{ub} \\ V_{cd} & V_{cs} & V_{cb} \\ V_{td} & V_{ts} & V_{tb} \end{pmatrix} \begin{pmatrix} d \\ s \\ b \end{pmatrix} \tag{1.7}$$

The Feynman diagrams representing the charged-current weak interactions between up-type and down-type quarks are shown in Figure 1.1. The strength of the couplings depends on the value of

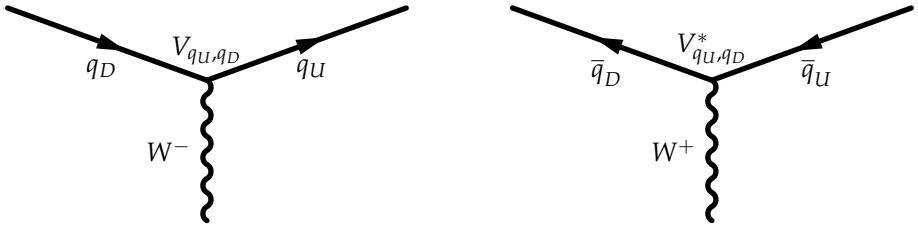

Figure 1.1: On the left, th Feynman diagram for the charged-current weak interactions between up-type (q_U) and down-type quarks (D). The plot on the right represents its CP conjugate diagram. The labels $V_{U,D}$ and $V^*_{U,D}$ indicates the V_{CKM} factor quantifying the strength of the coupling.

Table 1.3: Best determination of the magnitudes of the *CKM* matrix elements [15].

CKM element	Experimental value	Physic process
$\|V_{ud}\|$	0.97420 ± 0.00021	Nuclear beta decay ($d \to ue\overline{\nu}_e$)
$\|V_{us}\|$	0.2243 ± 0.0005	Semileptonic kaons decay ($s \to ul\overline{\nu}_l$)
$\|V_{cd}\|$	0.218 ± 0.004	Semileptonic D decay ($c \to dl\overline{\nu}_l$)
$\|V_{cs}\|$	0.997 ± 0.017	Semileptonic and leptonic D decay ($c \to sl\overline{\nu}_l$, $D_s \to l\overline{\nu}_l$)
$\|V_{cb}\|$	0.0422 ± 0.0008	Exclusive and inclusive semileptonic B decays to charm ($b \to cl\overline{\nu}$)
$\|V_{ub}\|$	0.00394 ± 0.00036	Exclusive and inclusive semileptonic B decays ($b \to ul\overline{\nu}$)
$\|V_{td}\|$	0.0081 ± 0.0005	B^0_d mixing assuming $\|V_{tb} = 1\|$
$\|V_{ts}\|$	0.0394 ± 0.0023	B^0_s mixing assuming $\|V_{tb} = 1\|$
$\|V_{tb}\|$	1.019 ± 0.025	Single top-quark-production cross-section

the related *CKM* element. The best determination of the magnitudes of the *CKM* matrix elements is reported in Table 1.3 while in Figure 1.2 a schematic representation of the matrix is shown. From the experimental measurements it is possible to conclude that the transition within the same generation are $\mathcal{O}(1)$, between the first and second are $\mathcal{O}(10^{-1})$, between the second and the third $\mathcal{O}(10^{-2})$ and between the first and the third are $\mathcal{O}(10^{-3})$.

1.2.1 *CKM* matrix properties

The main property of the *CKM* matrix is the unitarity which determines the number of free parameters of the matrix. A generic unitary matrix has $2n^2$ real parameters, however due to the unitarity condition:

$$\sum_i V_{ji} V^*_{ik} = \delta_{ij} \tag{1.8}$$

we can apply n constraints to the diagonal elements and $n^2 - n$ constraints to the off-diagonal elements. Thus the number of independent real parameters is reduce to n^2: $d(d-1)/2$ mixing angles

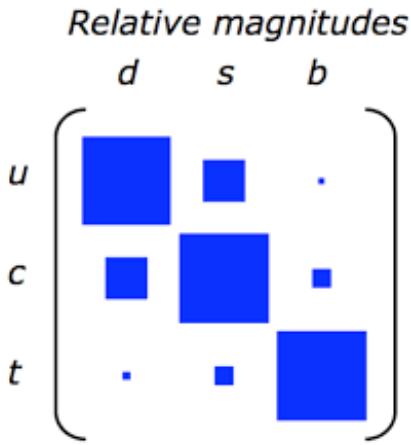

Figure 1.2: Schematic representation of the *CKM* matrix magnitude. The size of the boxes represents the order of magnitude of the related matrix element.

and $d(d+1)/2$ complex phases, where d is the matrix dimension. However, it is possible to redefine the phase of each quark field as:

$$U \to e^{-i\phi U} U, \qquad D \to e^{-i\phi D} D \tag{1.9}$$

inducing such a transformation on the *CKM* matrix:

$$V \to \begin{pmatrix} e^{-i\phi_1 U} & \cdots & 0 \\ \vdots & \ddots & \vdots \\ 0 & \cdots & e^{-i\phi_n U} \end{pmatrix} V \begin{pmatrix} e^{-i\phi_1 D} & \cdots & 0 \\ \vdots & \ddots & \vdots \\ 0 & \cdots & e^{-i\phi_n D} \end{pmatrix} \tag{1.10}$$

In this way we can remove $2n-1$ unphysical phases remaining with $(n-1)^2$ parameters of which $\frac{1}{2}(n-1)(n-2)$ are phases and $\frac{1}{2}n(n-1)$ are rotation angles. It is interesting to notice that in case where $n = 2$, i.e. there are only two quark generations, we have only one rotation angle θ_c, and no phases. Thus in this case the *CP* violation could not rise. The parameter θ_c is named Cabibbo's angle [16] and the *CKM* matrix could be written as:

$$V_c = \begin{pmatrix} \cos\theta_c & \sin\theta_c \\ -\sin\theta_c & \cos\theta_c \end{pmatrix} \tag{1.11}$$

This matrix describes the relative probability that d and s quarks decay into u and c quarks and provides an explanation of the suppression of the flavour changing neutral current (*FCNC*). In case of three quarks generations the free parameters are three mixing angles and one phase, which is responsible for the *CP* violation in the weak interactions.

1.2.2 Parametrizations of the CKM matrix

A Standard parametrization of the CKM matrix is known as "Chau-Keung parametrization" where $V_{CKM} = R_{23} \times R_{13} \times R_{12}$. The form of the R_{ij} matrices is:

$$R_{12} = \begin{pmatrix} c_{12} & s_{12} & 0 \\ -s_{12} & c_{12} & 0 \\ 0 & 0 & 1 \end{pmatrix} \quad R_{23} = \begin{pmatrix} 1 & 0 & 0 \\ 0 & c_{23} & s_{23} \\ 0 & -s_{23} & c_{23} \end{pmatrix} \quad R_{13} = \begin{pmatrix} c_{13} & 0 & s_{13}e^{-i\delta} \\ 0 & 1 & 0 \\ -s_{13}e^{i\delta} & 0 & c_{13} \end{pmatrix} \tag{1.12}$$

Defining $\cos\theta_{ij} = c_{ij}$ and $\sin\theta_{ij} = s_{ij}$, where i, j are index for the quark generations, the CKM matrix can be represented as:

$$V_{CKM} = \begin{pmatrix} c_{12}c_{13} & s_{12}c_{13} & s_{13}e^{-i\delta} \\ -s_{12}c_{23} - c_{12}s_{23}s_{13}e^{i\delta} & c_{12}c_{23} - s_{12}s_{23}s_{13}e^{i\delta} & s_{23}c_{13} \\ -s_{12}s_{23} - c_{12}c_{23}s_{13}e^{i\delta} & c_{12}s_{23} - s_{12}c_{23}s_{13}e^{i\delta} & c_{23}c_{13} \end{pmatrix} \tag{1.13}$$

where δ is the phase responsible for the CP violation[15]. As shown in Equation 1.13 if the angle $\theta_{ij} = 0$ the mixing between the quark generations i and j vanishes. In similar way, assuming $\theta_{13} = \theta_{23} = 0$ decouples the third generation and the CKM matrix would take the form of the V_c matrix in Equation 1.11

It's important to notice that the presence of a complex phase is necessary but not sufficient condition for the CP violation. Another fundamental condition is that:

$$(m_t^2 - m_c^2)(m_t^2 - m_u^2)(m_c^2 - m_u^2)(m_b^2 - m_s^2)(m_b^2 - m_d^2)(m_s^2 - m_d^2) \times \mathcal{J}_{CP} \neq 0 \tag{1.14}$$

where $\mathcal{J}_{CP}$ is the phase-convention-independent Jarlskog parameter which contains the dependence on the CKM elements:

$$(i \neq j, \alpha \neq \beta) Im(V_{i\alpha} V_{j\beta} V_{i\beta}^* V_{j\alpha}^*) = \mathcal{J}_{CP} \sum_{m,n=1}^{3} \varepsilon_{ijm} \varepsilon_{\alpha\beta n} \tag{1.15}$$

where $V_{i\alpha}$ are the CKM matrix elements and ε_{ijm} is the total antisymmetric tensor [18]. This relation shows how the origin of CP violation is closely related to the the quark mass hierarchy and the number of quark generations. Indeed if any of the quark couples was degenerated in mass it would be possible to remove the CKM phase. The Jarlskog parameter can be expressed in the "Chau-Keung parametrization' as:

$$\mathcal{J}_{CP} = c_{12}c_{23}c_{13}^2 s_{12}s_{23}s_{13} \sin\delta. \tag{1.16}$$

Empirically $\mathcal{J}_{CP} = \mathcal{O}(10^{-5})$ which is very small if compared to its mathematical maximum value of $1/6\sqrt{3} \approx 0.1$, proving that CP violation is suppressed in the SM.

Another parametrization, named "Wolfenstein parametrization", can be derived from the previous one defining:

$$\lambda = \sin\theta_c = \sin\theta_{12} \tag{1.17}$$

where θ_c is the Cabibbo angle. In this way the parameters s_{ij} can be re-written as function of λ, A, ρ and η:

$$s_{12} = \lambda = \frac{|V_{us}|}{\sqrt{|V_{ud}|^2 + |V_{us}|^2}}, \qquad s_{23} = A\lambda^2 = \lambda \left| \frac{V_{cb}}{V_{us}} \right|, \qquad s_{13} e^{i\delta} = A\lambda^3(\rho - i\eta) = V_{ub} \tag{1.18}$$

Introducing λ in Equation 1.13 the *CKM* matrix can be expanded in as power series of the parameter λ:

$$V_{CKM} = \begin{pmatrix} 1 - \frac{\lambda^2}{2} & \lambda & A\lambda^3(\rho - i\eta) \\ -\lambda & 1 - \frac{\lambda^2}{2} & A\lambda^2 \\ A\lambda^3(1 - \rho - i\eta) & -A\lambda^2 & 1 \end{pmatrix} + \mathcal{O}(\lambda^4) \tag{1.19}$$

The "Wolfenstein parametrization" highlights the experimentally well known hierarchy between the *CKM* elements, shown in Figure 1.2, expressing each of them as a power of λ. If we expand the *CKM* matrix to the next order the matrix in Equation 1.19 is turned into:

$$V_{CKM} = \begin{pmatrix} 1 - \frac{\lambda^2}{2} - \frac{\lambda^4}{8} & \lambda & A\lambda^3(\rho - i\eta) \\ -\lambda + \frac{A^2}{2}\lambda^5[1 + 2(\rho - i\eta)] & 1 - \frac{\lambda^2}{2} - \frac{\lambda^4}{8}(1 + 4A^2) & A\lambda^2 \\ A\lambda^3[1 - (\rho + i\eta)\left(1 - \frac{\lambda^2}{2}\right)] & -A\lambda^2 + \frac{A}{2}\lambda^4[1 - 2(\rho + i\eta)] & 1 + \frac{A}{2}\lambda^4 \end{pmatrix} + \mathcal{O}(\lambda^6) \tag{1.20}$$

The Jarlskog parameter expressed with the “Wolfenstein parametrization” reads

$$\mathcal{J} = A^2\lambda^6\eta\left(1 - \frac{\lambda^2}{2}\right) + \mathcal{O}(\lambda^{10}) \tag{1.21}$$

and also in this case it is directly connected to the *CP* violation parameter η.

1.2.3 Unitarity Triangles

As mentioned in Section 1.2.1 the main property of the *CKM* matrix is the unitarity:

$$V_{CKM} V_{CKM}^{\dagger} = V_{CKM}^{\dagger} V_{CKM} = 1. \tag{1.22}$$

Requiring this condition leads to a set of 12 equations, 6 for the diagonal terms and 6 for the off-diagonal terms:

$$\begin{aligned} &\sum_{i=0}^{3} |V_{ij}|^2 = 1, && \text{with } j = 1,2,3, \\ &\sum_{i=0}^{3} V_{ji} V_{ki}^* = \sum_{i=0}^{3} V_{ij} V_{ik}^* = 0, && \text{with } j,k = 1,2,3 \text{ and } j \neq k \end{aligned} \tag{1.23}$$

The equation of the second set are expanded in Equation 1.24 and can be represented as triangles in the complex plane, where each term can be identified as a side. It is important to notice that all the triangles are equivalent and the their area is equal to half of the Jarlskog invariant J_{CP}. This is a geometrical interpretation of the phase invariance of J_{CP}: a phase redefinition of the *CKM* matrix

would rotate the unitarity triangle while would leave its area invariant.

$$\begin{aligned}
&1) V_{us}V_{ub}^* + V_{cs}V_{cb}^* + V_{ts}V_{tb}^* = 0,\\
&2) V_{ud}V_{ub}^* + V_{cd}V_{cb}^* + V_{td}V_{tb}^* = 0,\\
&3) V_{ud}V_{us}^* + V_{cd}V_{cs}^* + V_{td}V_{ts}^* = 0,\\
&4) V_{ud}V_{td}^* + V_{us}V_{ts}^* + V_{ub}V_{tb}^* = 0,\\
&5) V_{cd}V_{td}^* + V_{cs}V_{ts}^* + V_{cb}V_{tb}^* = 0,\\
&6) V_{ud}V_{cd}^* + V_{us}V_{cs}^* + V_{ub}V_{cb}^* = 0.
\end{aligned} \tag{1.24}$$

Exploiting the "Wolfenstein parametrization" of the *CKM* element we can express the relations in Equation 1.24 at the leading order in λ:

$$\begin{aligned}
&1)\ O(\lambda^4) + O(\lambda^2) + O(\lambda^2) = 0,\\
&2)\ O(\lambda^3) + O(\lambda^3) + O(\lambda^3) = 0,\\
&3)\ O(\lambda) + O(\lambda) + O(\lambda^5) = 0,\\
&4)\ O(\lambda^3) + O(\lambda^3) + O(\lambda^3) = 0,\\
&5)\ O(\lambda^4) + O(\lambda^2) + O(\lambda^2) = 0,\\
&6)\ O(\lambda) + O(\lambda) + O(\lambda^5) = 0.
\end{aligned} \tag{1.25}$$

Thus it turns out that the only triangles with all the sides of the same order of magnitude are 2) and 4) while all others are degenerated. The two non-degenerate triangles, rescaled by $|V_{cd}V_{cb}^*| = A\lambda^3$, are shown in Figure 1.3. The triangle related to the 2) equation it is referred to as "The Unitary Triangle" or "B_d^0 Triangle" since all its sides and angles can be determined by means of B_d^0 decays. The angle amplitudes and side lengths depend on the *CKM* matrix elements:

$$\begin{aligned}
R_b &= \sqrt{\overline{\rho}^2 + \overline{\eta}^2} = \left(1 - \frac{\lambda^2}{2}\right)\frac{1}{\lambda}\frac{|V_{ub}|}{|V_{cb}|},\\
R_t &= \sqrt{(1-\overline{\rho})^2 + \overline{\eta}^2}\frac{1}{\lambda}\frac{|V_{ub}|}{|V_{cb}|},\\
\alpha &\equiv \arg\left(-\frac{V_{td}V_{tb}^*}{V_{ud}V_{ub}^*}\right) = \arg\left(-\frac{1-\overline{\rho}-i\overline{\eta}}{\overline{\rho}+i\overline{\eta}}\right),\\
\beta &\equiv \arg\left(-\frac{V_{cd}V_{cb}^*}{V_{td}V_{tb}^*}\right) = \arg\left(\frac{1}{1-\overline{\rho}-i\overline{\eta}}\right) = \phi_d,\\
\gamma &\equiv \arg\left(-\frac{V_{ud}V_{ub}^*}{V_{cd}V_{cb}^*}\right) = \arg\left(\overline{\rho}+i\overline{\eta}\right),
\end{aligned} \tag{1.26}$$

where R_b and R_t are the two slanting sides, α, β and γ are the three angles and $\overline{\rho}$ and $\overline{\eta}$ are defined as:

$$\overline{\rho} = \rho\left(1 - \frac{\lambda^2}{2}\right) \qquad \overline{\eta} = \eta\left(1 - \frac{\lambda^2}{2}\right) \tag{1.27}$$

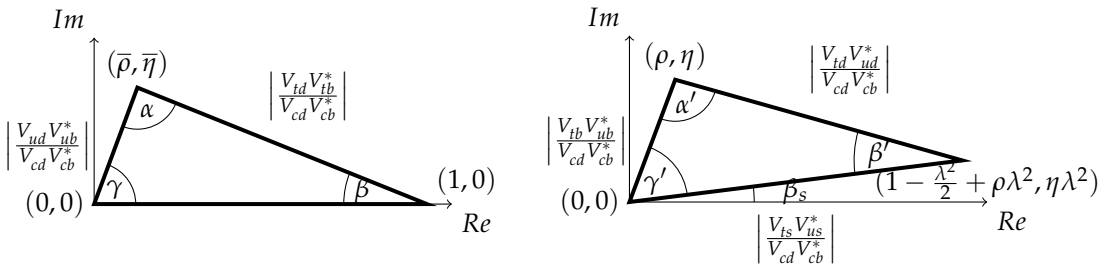

Figure 1.3: The two main important Unitary Triangles. On the left the triangle from 2) and on the right the triangle from 4). The sides are scaled of a factor $|V_{cd}V_{cb}^*| = A\lambda^3$, while the vertices are calculated using the "Wolfenstein parametrization

Table 1.4: Values of the Wolfenstein parameters extracted from the global fit performed by CKMfitter and UTfit groups [15].

Parameter	CKMfitter	UTfit
A	0.836 ± 0.015	0.832 ± 0.009
λ	0.22453 ± 0.00044	0.22465 ± 0.00039
$\overline{\eta}$	$0.355^{+0.012}_{-0.011}$	0.436 ± 0.010
$\overline{\rho}$	$0.122^{+0.18}_{-0.17}$	0.139 ± 0.016

The other non-degenerate triangle has similar properties to the "B_d^0 Triangle" but it is rotated by an angle

$$\beta_s = \arg\left(\frac{V_{ts}V_{tb}^*}{V_{cs}V_{cb}^*}\right) = \frac{\phi_s}{2} \tag{1.28}$$

The "Unitary Triangle" (UT) parameters can be determined from many different quark transitions by means of a global fit. The values extrapolated from the fit can provide a test of the SM and a difference with respect to the expected values could be a confirmation of new physics beyond the SM. A detailed description of the methods used to evaluate the parameters can be found in Ref. [19, 20].The global fit results obtained by UTFit group are shown in Figure 1.4, where the shaded areas represent the 68% probability regions [19]. The value of the Wolfenstein parameters extracted from the global fit, considering the constraints implied by the unitary of the CKM matrix, are reported in Table 1.4.

1.3 Neutral meson oscillations

In this section the neutral meson oscillations are described. Even if from the theoretical point of view the mixing is unique to the neutral K, D and B mesons, the focus will be on $B_{(s)}^0$ mesons since are the only relevant for this thesis. A more detailed and complete description can be found

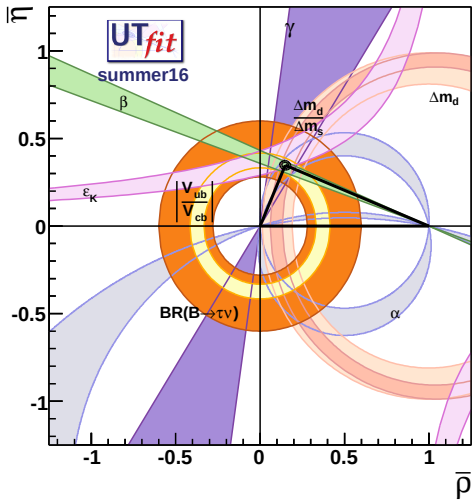

Figure 1.4: Global fit results obtained by UTFit group. 68% probability intervals for the UT parameters [19]. The contours related to 68% and 95% confidence level for the $\overline{\rho}$ and $\overline{\eta}$ parameters are also shown.

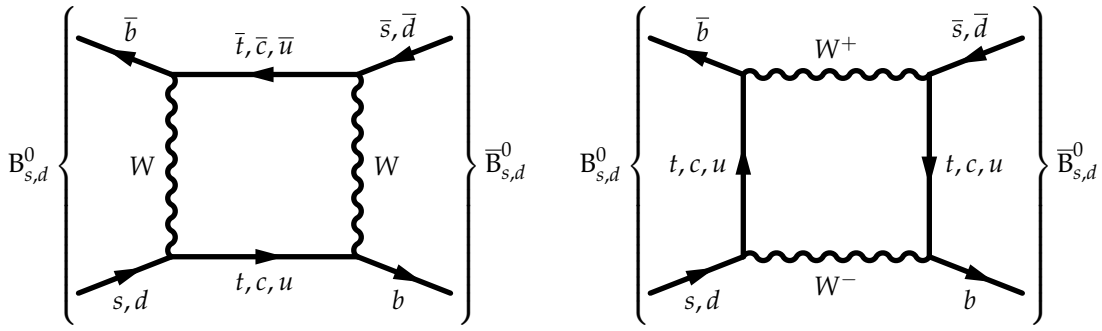

Figure 1.5: Example of leading order box diagrams involved in B^0_d- $\overline{B}^0_d$ mixing.

in Refs [21], [22], [23]. The neutral meson oscillations were observed for the very first time in B^0 sector in 1987 [24, 25]. Successively they were observed also in B^0_s mesons by the CDF collaboration in 2006 [26]. This kind of process consists in a transmutation of a neutral particle into its own anti-particle and it occurs through weak interactions. In the SM such a processes are allowed only in higher order processes, like loop diagrams, since the transitions of the form $b \to d, s$, the so-called FCNC, are forbidden at the tree-level. The diagrams responsible for the $B^0_{(s)} \to \overline{B}^0_{(s)}$ transitions, called box diagrams since they involve the exchange of two W bosons, are shown in Figure 1.5. The effect of the B^0 and B^0_s oscillation is shown in Figure 1.6.

For sake of simplicity, in the following the relations describing the neutral meson oscillations will be referred to only the B^0 meson, however the same ones hold also for the B^0_s meson. For sake of simplicity and because of the similar phenomenology, in the following of the section the B^0 and B^0_s mesons, as well as their corresponding antiparticles, will be indicated with a common notation:

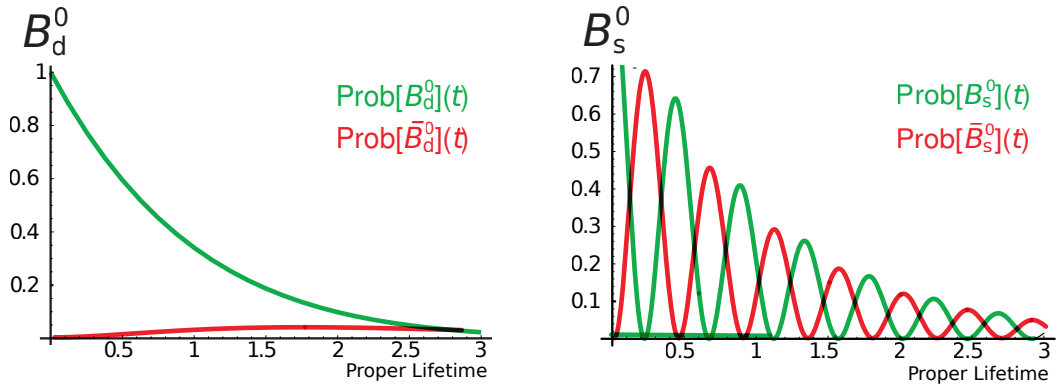

Figure 1.6: Probability function of having a $B^0_{d(s)}$ (green) or $\overline{B}^0_{d(s)}$ (red) as function of the decay-time, assuming a pure $B^0_{d(s)}$ initial state.

B_q and $\overline{B}^0_q$, with $q = d, s$. Due to the Glashow-Iliopoulos-Maiani (GIM) suppression [27], the leading contribution to these diagrams is given by the top quark. The total amplitude is proportional to:

$$m_u^2 V_{uq} V_{ub}^* + m_c^2 V_{cq} V_{cb}^* + m_t^2 V_{tq} V_{tb}^* \tag{1.29}$$

where m_u, m_c and m_t are the mass of the three up-type quarks and V_{xy} represents the x, y element of the CKM matrix.

The time evolution of the B^0_q flavour eigenstates is described by the Schrödinger equation:

$$i\frac{\delta}{\delta t}|\Psi(t)\rangle = \mathcal{H}|\Psi(t)\rangle \tag{1.30}$$

where $|\Psi(t)\rangle$ is B^0_q state function which can be described as:

$$|\Psi(t)\rangle \equiv a(t)|B^0_q\rangle + b(t)|\overline{B}^0_q\rangle + c_1(t)|f_1\rangle + c_2(t)|f_2\rangle + ... \tag{1.31}$$

where f_i represent all the possible final states in which the B^0_q can decay into and c_i are the coefficients of each final state. If the time range is much larger than the typical strong interaction scale, it is possible to describe the B^0_q time evolution by means of the "Wigner-Weisskopf" approximation [28, 29] which simplifies the formalism of Equation 1.31:

$$|\Psi(t)\rangle \equiv a(t)|B^0_q\rangle + b(t)|\overline{B}^0_q\rangle \tag{1.32}$$

where $a(t)$ and $b(t)$ are such that $|a(t)|^2 + |b(t)|^2 = 1$ This means that the approximated time evolution can be defined by a 2×2 effective Hamiltonian which can be expressed in terms of Hermitian matrices $\mathbf{M}$ and $\mathbf{\Gamma}$:

$$\mathcal{H} = \mathbf{M} - \frac{i}{2}\mathbf{\Gamma} = \begin{pmatrix} M_{11} & M_{12} \\ M_{12}^* & M_{22} \end{pmatrix} - \frac{i}{2}\begin{pmatrix} \Gamma_{11} & \Gamma_{12} \\ \Gamma_{12}^* & \Gamma_{22} \end{pmatrix}. \tag{1.33}$$

where $\mathbf{M}$ and $\mathbf{\Gamma}$ are the mass and decay matrices. These two matrices represent the dispersive and absorptive parts of the B^0_q mixing, i.e. the “off-shell” and “on-shell” transitions, respectively. The

elements of the $\mathcal{H}$ matrix can be distinguished in: diagonal elements which are related to the flavour-conserving transitions and the off-diagonal elements which are associated to the flavour changing transitions. It is important to notice that, even if it is defined as a combination of Hermitian matrices, the $\mathcal{H}$ matrix is not Hermitian, otherwise the neutral mesons would not able to oscillate and decay. The eigenstates obtained solving the Schrödinger equation are:

$$\begin{aligned} |B_L\rangle &\propto p\sqrt{1-z}|B_q^0\rangle + q\sqrt{1+z}|\overline{B}_q^0\rangle, \\ |B_H\rangle &\propto p\sqrt{1+z}|B_q^0\rangle - q\sqrt{1-z}|\overline{B}_q^0\rangle, \end{aligned} \tag{1.34}$$

where the parameter z is related to the violation of the CPT[1], symmetry in mixing. Thus, as mentioned in Section 1.2, the heavy and light mass eigenstates, $|B_L\rangle$ and $|B_H\rangle$ respectively, can be expressed as linear combination of the flavour eigenstates $|B_q^0\rangle$ and $|\overline{B}_q^0\rangle$. In the following the CPT invariance condition is assumed, i.e. $z = 0$, since the study of its violation is beyond the scope of this thesis. Because of the CPT invariance assumption, the diagonal elements of the $\mathcal{H}$ matrix are equal:

$$M_{11} = M_{22} = M, \qquad \Gamma_{11} = \Gamma_{22} = \Gamma \tag{1.35}$$

and the p and q parameters satisfy the relation

$$|p|^2 + |q|^2 = 1 \tag{1.36}$$

The time evolution of the mass eigenstates is governed by the two eigenvalues:

$$\lambda_H = m_H - \frac{i}{2}\Gamma_H \qquad \text{and} \qquad \lambda_L = m_L - \frac{i}{2}\Gamma_L \tag{1.37}$$

and it is given by:

$$\begin{aligned} |B_H(t)\rangle &= e^{-\lambda_H t}|B_H(0)\rangle = e^{-im_H t}e^{-\frac{1}{2}\Gamma_H t}|B_H(0)\rangle, \\ |B_L(t)\rangle &= e^{-\lambda_L t}|B_L(0)\rangle = e^{-im_L t}e^{-\frac{1}{2}\Gamma_L t}|B_L(0)\rangle. \end{aligned} \tag{1.38}$$

The mass and lifetime average and difference (m_q, Γ_q, Δm_q and $\Delta\Gamma_q$) between the two mass eigenstates can be expressed as:

$$\begin{aligned} m_q = m_{\overline{q}} &= \frac{m_H + m_L}{2} = M, & \Delta m_q &= m_H - m_L, \\ \Gamma_q = \frac{1}{\tau_q} &= \frac{\Gamma_H + \Gamma_L}{2} = \Gamma, & \Delta\Gamma_q &= \Gamma_L - \Gamma_H \end{aligned} \tag{1.39}$$

and their values are reported in Table 1.5. It is important to be noticed that Δm_q is positive by definition while $\Delta\Gamma_q$ can have either sign. For the B^0 system, since the mixing frequency is comparable to their lifetime, the mesons oscillate at most once before decaying ($\Delta m_d/\Gamma_d \sim 0.77$). The null value of $\Delta\Gamma_d$ means that the two mass eigenstates have the same lifetime[2]. The mixing frequency for the B_s^0 mesons is instead much higher ($\Delta m_s/\Gamma_s \sim 27$) and the measured value of $\Delta\Gamma_s$ corresponds to about

Table 1.5: Mass and lifetime parameters of B^0 and B_s^0 meson system [15].

Parameter	B^0	B_s^0
m_q	(5279.63 ± 0.15) MeV	(5366.89 ± 0.19) MeV
Δm_q	(0.506 ± 0.002) ps^{-1}	(17.757 ± 0.021) ps^{-1}
τ_q	(1.520 ± 0.004) ps	(1.509 ± 0.004) ps
$\Delta\Gamma_q$	-	(0.088 ± 0.006) ps^{-1}
$\Delta m_q/\Gamma_q$	(0.770 ± 0.004)	(26.72 ± 0.09)

the 15% of the B_s^0 lifetime itself. Inverting Equation 1.34 the flavour eigenstates can be defined as:

$$\begin{aligned} |B_q^0(t)\rangle &= \frac{1}{2p}(|B_H(t)\rangle + |\overline{B}_L(t)\rangle) \\ |\overline{B}_q^0(t)\rangle &= \frac{1}{2q}(|B_H(t)\rangle - |\overline{B}_L(t)\rangle). \end{aligned} \tag{1.40}$$

Considering a pure state of B_q^0 and $\overline{B}_q^0$ the time evolution can be expressed as:

$$\begin{aligned} |B_q^0(t)\rangle &= g_+(t)|B_q^0\rangle + \frac{q}{p}g_-(t)|\overline{B}_q^0\rangle, \\ |\overline{B}_q^0(t)\rangle &= g_+(t)|\overline{B}_q^0\rangle + \frac{p}{q}g_-(t)|B_q^0\rangle \end{aligned} \tag{1.41}$$

where

$$\begin{aligned} g_+(t) &= \left(\frac{e^{-i\lambda_H t} + e^{-i\lambda_L t}}{2}\right) = e^{-im_q t}e^{-i\Gamma_q t/2}\left[\cosh\frac{\Delta\Gamma_q t}{4}\cos\frac{\Delta m_q t}{2} - i\sinh\frac{\Delta\Gamma_q t}{4}\sin\frac{\Delta m_q t}{2}\right], \\ g_-(t) &= \left(\frac{e^{-i\lambda_H t} - e^{-i\lambda_L t}}{2}\right) = e^{-im_q t}e^{-i\Gamma_q t/2}\left[-\sinh\frac{\Delta\Gamma_q t}{4}\cos\frac{\Delta m_q t}{2} + i\cosh\frac{\Delta\Gamma_q t}{4}\sin\frac{\Delta m_q t}{2}\right]. \end{aligned} \tag{1.42}$$

It is possible to verify that $g_+(0) = 1$ and $g_-(0) = 0$ as well as that $g_\pm(t)$ has no zeros for $t > 0$ if $\Delta\Gamma \neq 0$, meaning that the initially produced B_q^0 ($\overline{B}_q^0$) state will never turn into a pure $\overline{B}_q^0$ (B_q^0) or back into a pure B_q^0 ($\overline{B}_q^0$) state. The coefficients in Equation 1.42 will enter the formulae for the decay asymmetries in the combinations:

$$\begin{aligned} |g_\pm(t)|^2 &= \frac{e^{-\Gamma_q t}}{2}\left[\cosh\frac{\Delta\Gamma_q t}{2} \pm \cos\Delta m_q t\right], \\ g_+^*(t)g_-(t) &= \frac{e^{-\Gamma_q t}}{2}\left[-\sinh\frac{\Delta\Gamma_q t}{2} + i\sin\Delta m_q t\right]. \end{aligned} \tag{1.43}$$

Finally, it is interesting to calculate the probability for a B_q^0 ($\overline{B}_q^0$) meson, produced initially in a pure state, to be oscillated after a time t:

$$\begin{aligned} |\langle\overline{B}_q^0|B_q^0(t)\rangle|^2 &= \frac{e^{-\Gamma_q t}}{2}\left[\cosh\frac{\Delta\Gamma_q t}{2} - \cos\Delta m_q t\right]|\frac{q}{p}|^2, \\ |\langle B_q^0|\overline{B}_q^0(t)\rangle|^2 &= \frac{e^{-\Gamma_q t}}{2}\left[\cosh\frac{\Delta\Gamma_q t}{2} + \cos\Delta m_q t\right]|\frac{p}{q}|^2 \end{aligned} \tag{1.44}$$

[1] T represent the time-reversal operator which invert the time flow direction ($t \to -t$)

[2] A significant discrepancy from 0 would be a sign of New Physics beyond the *SM*.

1.3.1 Mixing parameters

The formalism introduced so far is sufficient to describe the $B_q^0 \to \overline{B_q^0}$ oscillations however a further step is required in order to determine the SM predictions of the characteristic observables of the mixing process. The observables m_q, Γ_q, Δm_q, $\Delta\Gamma_q$ and $\frac{q}{p}$ can be expressed as function of the more theoretical quantities M_{12} and Γ_{12}. By solving the secular equation

$$(H_{11} - \lambda_{H(L)})^2 - H_{12}H_{21} = 0 \tag{1.45}$$

for the two eigenvalues $\lambda_{H(L)}$ of $\mathcal{H}$ the result is:

$$\begin{aligned} \lambda_H &= M - \frac{i}{2}\Gamma + \frac{q}{p}\left(M_{12} - \frac{i}{2}\Gamma_{12}\right), \\ \lambda_L &= M - \frac{i}{2}\Gamma - \frac{q}{p}\left(M_{12} - \frac{i}{2}\Gamma_{12}\right), \end{aligned} \tag{1.46}$$

In addition the following relations can be established:

$$\begin{aligned} (\Delta m_q)^2 - \frac{1}{4}(\Delta\Gamma_q)^2 &= 4|M_{12}|^2 - |\Gamma_{12}|^2, \\ \Delta m_q \Delta\Gamma_q &= -4\Re(M_{12}\Gamma_{12}^*) = 4|M_{12}||\Gamma_{12}\cos\phi, \\ \frac{q}{p} &= -\frac{\Delta m_q + \Delta\Gamma_q/2}{2M_{12} - i\Gamma_{12}} = -\frac{2M_{12}^* - i\Gamma_{12}^*}{\Delta m_q + i\Delta\Gamma/2}. \end{aligned} \tag{1.47}$$

where ϕ is the relative phase between M_{12} and Γ_{12}:

$$\phi = \arg\left(-\frac{M_{12}}{\Gamma_{12}}\right) \tag{1.48}$$

and it is responsible for CP violation in mixing discussed in Section 1.4.2. Finally, the difference between the two mass eigenstates can be written as:

$$\begin{aligned} \lambda_H - \lambda_L &= 2\sqrt{\left(M_{12} - \frac{i}{2}\Gamma_{12}\right)\left(M_{12}^* - \frac{i}{2}\Gamma_{12}^*\right)} \\ &= 2|M_{12}|\sqrt{1 - \frac{|\Gamma_{12}|^2}{4|M_{12}|^2} - i\frac{|\Gamma_{12}|}{|M_{12}|}\cos\phi}. \end{aligned} \tag{1.49}$$

As mentioned at the beginning of the section the box diagrams, shown in Figure 1.5, are dominated by the top-quark contribution, thus

$$\frac{\Gamma_{12}}{M_{12}} \propto \frac{m_b^2}{m_t^2} = O(10^{-3}) \tag{1.50}$$

and Equation 1.49 can be expanded to the first order term as:

$$\lambda_H - \lambda_L \approx 2|M_{12}| - \frac{i}{2}\frac{|\Gamma_{12}|}{|M_{12}|}\cos(\phi_M - \phi_\Gamma) \tag{1.51}$$

where the real and imaginary term represents Δm_q and $\Delta\Gamma_q$, respectively:

$$\begin{aligned} \Delta m_q &= 2|M_{12}|\left[1 + \mathcal{O}\left(|\frac{\Gamma_{12}}{M_{12}}|^2\right)\right], \\ \Delta\Gamma_q &= 2|\Gamma_{12}|\cos\phi\left[1 + \mathcal{O}\left(|\frac{\Gamma_{12}}{M_{12}}|^2\right)\right]. \end{aligned} \tag{1.52}$$

It is also possible to rewrite Equation 1.46 as function of Δm_q and $\Delta\Gamma_q$, as:

$$\begin{aligned}\lambda_H &= M + \frac{\Delta m}{2} - \frac{i}{2}\left(\Gamma + \frac{\Delta\Gamma}{2}\right),\\ \lambda_L &= M - \frac{\Delta m}{2} - \frac{i}{2}\left(\Gamma - \frac{\Delta\Gamma}{2}\right).\end{aligned} \tag{1.53}$$

.

1.3.2 Time-dependent decay-rates

The time-dependent decay-rates of an initially B_q^0 and $\overline{B}_q^0$ into a certain final state f or $\overline{f}$ are defined as:

$$\begin{aligned}\Gamma(B_q^0(t) \to f) &= \frac{1}{N_B}\frac{d\mathcal{N}(B_q^0(t) \to f)}{dt},\\ \Gamma(\overline{B}_q^0(t) \to f) &= \frac{1}{N_{\overline{B}}}\frac{d\mathcal{N}(\overline{B}_q^0(t) \to f)}{dt},\\ \Gamma(\overline{B}_q^0(t) \to \overline{f}) &= \frac{1}{N_{\overline{B}}}\frac{d\mathcal{N}(\overline{B}_q^0(t) \to \overline{f})}{dt}\\ \Gamma(B_q^0(t) \to \overline{f}) &= \frac{1}{N_B}\frac{d\mathcal{N}(B_q^0(t) \to \overline{f})}{dt},\end{aligned} \tag{1.54}$$

where $d\mathcal{N}$ represents the number of decays observed within a time interval between t and $t + dt$ and N_B ($N_{\overline{B}}$) is the total number of B_q^0 ($\overline{B}_q^0$) mesons produced at time $t = 0$. In order to calculate the time-dependent decay-rates is necessary to define the instantaneous decay amplitudes of B_q^0 and $\overline{B}_q^0$ to final states f and $\overline{f}$ as:

$$\begin{aligned}A_f &= \mathcal{A}(B_q^0 \to f) = \langle f|\mathcal{H}|B_q^0\rangle,\\ \overline{A}_f &= \mathcal{A}(\overline{B}_q^0 \to f) = \langle f|\mathcal{H}|\overline{B}_q^0\rangle,\\ \overline{A}_{\overline{f}} &= \mathcal{A}(\overline{B}_q^0 \to \overline{f}) = \langle \overline{f}|\mathcal{H}|\overline{B}_q^0\rangle,\\ A_{\overline{f}} &= \mathcal{A}(B_q^0 \to \overline{f}) = \langle \overline{f}|\mathcal{H}|B_q^0\rangle\end{aligned} \tag{1.55}$$

and the *CP* violation parameters of the processes:

$$\lambda_f = \frac{q}{p}\frac{\overline{A}_f}{A_f}, \qquad \overline{\lambda}_{\overline{f}} = \frac{p}{q}\frac{A_{\overline{f}}}{\overline{A}_{\overline{f}}}. \tag{1.56}$$

As discussed in the following sections, the λ_f ($\overline{\lambda}_{\overline{f}}$) parameter plays a fundamental role in *CP* asymmetries and other observables in B_q^0 mixing. Exploiting the notation reported in Equation 1.55, it is

possible to express the decay rate to a final state f or $\overline{f}$ as:

$$\begin{aligned}
\Gamma_{B_q^0\to f}(t) &= \mathcal{N}_f|\langle f|\mathcal{H}|B_q^0(t)\rangle|^2 = \mathcal{N}_f\frac{e^{-\Gamma_q t}}{2}|A_f|^2|g_+(t)+\lambda_f g_-(t)|^2,\\
\Gamma_{\overline{B}_q^0\to f}(t) &= \mathcal{N}_f|\langle f|\mathcal{H}|\overline{B}_q^0(t)\rangle|^2 = \mathcal{N}_f\frac{e^{-\Gamma_q t}}{2}|A_f|^2\left|\frac{p}{q}\right|^2|g_-(t)+\lambda_f g_+(t)|^2\\
\Gamma_{\overline{B}_q^0\to \overline{f}}(t) &= \mathcal{N}_{\overline{f}}|\langle \overline{f}|\mathcal{H}|\overline{B}_q^0(t)\rangle|^2 = \mathcal{N}_{\overline{f}}\frac{e^{-\Gamma_q t}}{2}|\overline{A}_{\overline{f}}|^2|g_+(t)+\overline{\lambda}_{\overline{f}} g_-(t)|^2,\\
\Gamma_{B_q^0\to \overline{f}}(t) &= \mathcal{N}_{\overline{f}}|\langle \overline{f}|\mathcal{H}B_q^0(t)\rangle|^2 = \mathcal{N}_{\overline{f}}\frac{e^{-\Gamma_q t}}{2}|\overline{A}_{\overline{f}}|^2\left|\frac{q}{p}\right|^2|g_-(t)+\overline{\lambda}_{\overline{f}} g_+(t)|^2.
\end{aligned} \tag{1.57}$$

where $\mathcal{N}_f$ and $\mathcal{N}_{\overline{f}}$ represent the normalisation factor accounting for the integration over the phase-space. Finally, using Equation 1.53 the decay rate, reported in Equation 1.57, can be expressed as:

$$\begin{aligned}
\Gamma_{B_q^0\to f}(t) &= \mathcal{N}_f\frac{e^{-\Gamma_q t}}{2}|A_f|^2|I_+(t)+I_-(t)|,\\
\Gamma_{\overline{B}_q^0\to f}(t) &= \mathcal{N}_f\frac{e^{-\Gamma_q t}}{2}|A_f|^2\left|\frac{p}{q}\right|^2|I_+(t)-I_-(t)|\\
\Gamma_{\overline{B}_q^0\to \overline{f}}(t) &= \mathcal{N}_{\overline{f}}\frac{e^{-\Gamma_q t}}{2}|\overline{A}_{\overline{f}}|^2|\overline{I}_+(t)+\overline{I}_-(t)|,\\
\Gamma_{B_q^0\to \overline{f}}(t) &= \mathcal{N}_{\overline{f}}\frac{e^{-\Gamma_q t}}{2}|\overline{A}_{\overline{f}}|^2\left|\frac{q}{p}\right|^2|\overline{I}_+(t)-\overline{I}_-(t)|
\end{aligned} \tag{1.58}$$

where

$$\begin{aligned}
I_+(t) &= \left(1+|\lambda_f|^2\right)\cosh\left(\frac{\Delta\Gamma_q}{2}t\right) - 2\Re(\lambda_f)\sinh\left(\frac{\Delta\Gamma_q}{2}t\right),\\
I_-(t) &= \left(1-|\lambda_f|^2\right)\cos(\Delta m_q t) - 2\Im(\lambda_f)\sin(\Delta m_q t),\\
\overline{I}_+(t) &= \left(1+|\overline{\lambda}_{\overline{f}}|^2\right)\cosh\left(\frac{\Delta\Gamma_q}{2}t\right) - 2\Re(\overline{\lambda}_{\overline{f}})\sinh\left(\frac{\Delta\Gamma_q}{2}t\right),\\
\overline{I}_-(t) &= \left(1-|\overline{\lambda}_{\overline{f}}|^2\right)\cos(\Delta m_q t) - 2\Im(\overline{\lambda}_{\overline{f}})\sin(\Delta m_q t).
\end{aligned} \tag{1.59}$$

The decay-rates reported in this section have been determined without making any particular assumption of the decay mode. It is important to be noticed that these expressions represent only the theoretical time-dependent decay-rates evaluated without taking into account experimental effects, such as the production and final state detection asymmetries, as well as the wrong determination of the B_q^0 flavour at production. All these effects will be taken into account in Chapters 4, 5 and the complete decay-time rates, related to the $H_b \to h^+h'^-$ decay modes, are reported in Section 5.4.

1.4 *CP* violation

Both the strong and electromagnetic interactions conserve the *CP* symmetry, however the weak force seems to slightly violate it. In 1957[30] and 1964[31] two experiments were conducted proving the

violation of the *CP* symmetry in certain types of weak decays. After this discovery many experiments were performed in the following 50 years attempting to improve the precision of the *CP* violation measurements. The most precise information related to the phase of the *CKM* matrix at present are provided by measurements of time-dependent *CP* asymmetries in *B* decays, whose formalism will be detailed described in the next sections. In general, all forms of *CP* violation are related to interference phenomena because the *CP* violation is due to irreducible phases in the Lagrangian, which are observable only in interference processes. In the *SM* there are three phase convention independent physical *CP* violating observables:

$$\left|\frac{q}{p}\right|, \qquad \left|\frac{\overline{A}_{\overline{f}}}{A_f}\right|, \qquad \lambda_f = \frac{q}{p}\frac{\overline{A}_f}{A_f}. \tag{1.60}$$

A significant discrepancy from 1 for any of these variables (from -1 for λ_f) means that *CP* symmetry is violated. According to the Standard Model the phenomenon of *CP* violation can occur in three different ways:

- *CP* violation in the Decay
- *CP* violation in *B* Mixing
- *CP* violation in the Interference of Mixing and Decay

1.4.1 *CP* violation in decay

The *CP* violation in decay is conceptually the simplest form of *CP* violation and it can occur in both charged and neutral meson as well as baryon decays (generically labelled as *B* in the following). It is also named "Direct *CP* violation" since it takes place when the rate of a process and its own conjugate are different. In particular it occurs due to interference between various terms in the decay amplitude. Supposing that at least two amplitudes with non-zero strong (δ_k) and relative weak (ϕ_k) phases, which are even and odd under *CP* symmetry respectively, contribute to the decay, the decay amplitudes (A_f and $\overline{A}_{\overline{f}}$) can be defined as:

$$A_f = \langle f|\mathcal{H}|B\rangle = \sum_k A_k e^{i\delta_k} e^{i\phi_k}, \qquad \overline{A}_{\overline{f}} = \langle \overline{f}|\mathcal{H}|\overline{B}\rangle = \sum_k A_k e^{i\delta_k} e^{-i\phi_k}. \tag{1.61}$$

where k labels the different contributions to the amplitudes and A_k are the magnitudes of each term. The individual phases δ_k and ϕ_k are convention dependent but the phase differences between different terms, i.e. $\delta_i - \delta_j$ and $\phi_i - \phi_j$, are physical. Thus the *CP* symmetry can be broken if $\left|\frac{\overline{A}_{\overline{f}}}{A_f}\right| \neq 1$ and the amount of time-independent *CP* violation can be evaluated as:

$$A_{CP} = \frac{\Gamma(B \to f) - \Gamma(\overline{B} \to \overline{f})}{\Gamma(B \to f) + \Gamma(\overline{B} \to \overline{f})} = \frac{1 - \left|\frac{\overline{A}_{\overline{f}}}{A_f}\right|^2}{1 + \left|\frac{\overline{A}_{\overline{f}}}{A_f}\right|^2} \tag{1.62}$$

Because this form of *CP* asymmetry depend on the strong phases, arising from the strong amplitude $|A|$, its interpretation is in the most of the cases model dependent.

1.4.2 *CP* violation in B mixing

The neutral meson mixing can induce a form of *CP* violation named "Indirect *CP* violation". The evolution of a physical B_q^0 meson can be described as a linear combination of both B_q^0 and $\overline{B}_q^0$ state, as reported in Equation 1.41. The p and q coefficients represent the relative proportions of B_q^0 and $\overline{B}_q^0$ states. In case of $p = q = \frac{1}{\sqrt{2}}$, i.e. $|p/q| = 1$, the physical mass eigenstates correspond to the flavour eigenstates and the probability of a B_q^0 and a $\overline{B}_q^0$ to oscillate on its own ant-particle is the same. By multiplying the two expressions for q/p reported in Equation 1.47 with each other it follows:

$$\left(\frac{q}{p}\right)^2 = \frac{2M_{12}^* - i\Gamma_{12}^*}{2M_{12} - i\Gamma_{12}} = \frac{M_{12}^*}{M_{12}} \frac{1 + i\left|\frac{\Gamma_{12}}{2M_{12}}\right| e^{i\phi}}{1 + i\left|\frac{\Gamma_{12}}{2M_{12}}\right| e^{-i\phi}}. \tag{1.63}$$

where ϕ is the relative phase between M_{12} and Γ_{12}. It is possible verify that $\phi \neq 0, \pi$ implies $|q/p| \neq 1$, which defines the *CP* violation in mixing. The indirect *CP* violation can be determined studying the time-dependent asymmetry ($A_{CP}(t)$) in mixing rates in decays to flavour specific final state (f):

$$A_{CP}(t) = \frac{\Gamma(|\overline{B}^0(t)\rangle \to \overline{f}) - \Gamma(|B^0(t)\rangle \to f)}{\Gamma(|\overline{B}^0(t)\rangle \to \overline{f}) + \Gamma(|B^0(t)\rangle \to f)}. \tag{1.64}$$

Since the time dependent terms cancel out, this kind of asymmetry turns out to be independent on the decay-time t:

$$A_{CP} = \frac{1 - |q/p|^4}{1 - |q/p|^4} \tag{1.65}$$

whose value is null in case of $|p/q| = 1$.

1.4.3 *CP* violation in interference

The *CP* violation in interference, also named "mixing-induced *CP* violation", is the third type of *CP* asymmetry predicted by the *SM*. It arises when both B_q^0 and $\overline{B}_q^0$ can decay to the same final state, i.e. the final state is an *CP* eigenstate (f_{CP}). In particular it results from the *CP* violating interference between $B^0 \to f_{CP}$ and $B_q^0 \to \overline{B}_q^0 \to f_{CP}$. In this case, even if there is no *CP* violation neither in decay nor in the mixing individually, it can occur from the interference between their phases. As described in Section 1.4.2, the $\lambda_{f_{CP}}$ term is defined as:

$$\lambda_{f_{CP}} = \frac{q}{p} \frac{\overline{A}_{f_{CP}}}{A_{f_{CP}}} \tag{1.66}$$

and it is suitable to be an observable in neutral meson decays since it is invariant under rephasing of the initial and final states. The *CP* violation in interference appears when $\lambda_{f_{CP}} \neq \pm 1$, condition

which can occur even if $|q/p| = 1$, $|A_{f_{CP}}/\overline{A}_{f_{CP}}| = 1$ assuming $Im(\lambda_{f_{CP}}) \neq 0$. The time-dependent asymmetry can be defined as:

$$A_{CP}(t) = \frac{\Gamma(|\overline{B}^0(t)\rangle \to f_{CP}) - \Gamma(|B^0(t)\rangle \to f_{CP})}{\Gamma(|\overline{B}^0(t)\rangle \to f_{CP}) + \Gamma(|B^0(t)\rangle \to f_{CP})}. \tag{1.67}$$

which, assuming $|q/p| \approx 1$ becomes equal to:

$$A_{CP}(t) = \frac{A^{\text{dir}}\cos(\Delta m_q t) + A^{\text{mix}}\sin(\Delta m_q t)}{\cosh\left(\frac{\Delta\Gamma_q}{2}t\right) - A^{\Delta\Gamma_q}\sinh\left(\frac{\Delta\Gamma_q}{2}t\right)} \tag{1.68}$$

where

$$A^{\text{dir}} = \frac{|\lambda_{f_{CP}}|^2 - 1}{|\lambda_{f_{CP}}|^2 + 1}, \qquad A^{\text{mix}} = \frac{2Im(\lambda_{f_{CP}})}{|\lambda_{f_{CP}}|^2 + 1}, \qquad A^{\Delta\Gamma} = \frac{2Re(\lambda_{f_{CP}})}{|\lambda_{f_{CP}}|^2 + 1}. \tag{1.69}$$

These three terms satisfy the relation:

$$|A^{\text{dir}}|^2 + |A^{\text{mix}}|^2 + |A^{\Delta\Gamma}|^2 = 1 \tag{1.70}$$

It is important to notice that the cosine term disappear in case of both no direct CP violation (i.e. $|A_{f_{CP}}/\overline{A}_{f_{CP}}| = 1$) and no CP violation in mixing (i.e. $|q/p| = 1$). However the difference in the weak phase between and $A_{f_{CP}}/\overline{A}_{f_{CP}}$ and q/p ($Im(\lambda_{f_{CP}}) \neq 0$) determines a non vanishing sine term.

1.5 Phenomenology of two-body B decays

The hadronic B meson decays, which occur by means of $b \to q_1\bar{q}_2 d(s)$ transitions, where $q_{1,2} \in (u, d, c, s)$, are of importance for testing the SM. They are very suitable to study the CP violation via interference between tree and penguin (or 1-loop level) contributions. Looking at the flavour content of the final state it is possible to split the two-body decays in three groups:

- transitions mediated by tree-level topologies ($q_1 \neq q_2 \in u, c$)
- transitions mediated by penguin topologies ($q_1 = q_2 \in d, s$)
- transitions mediated by both tree and penguin topologies ($q_1 = q_2 \in u, c$)

The Feynman diagrams of tree, QCD and EW penguin contributions are reported in Figures 1.7, 1.8, 1.9. Indeed taking into account the strong interactions between the quarks constituting the hadrons is fundamental for a correct weak decay description. Because of the QCD asymptotic freedom the short distance corrections can be described in perturbation theory by means of the Operator Product Expansion (OPE) [32, 33]. Through this framework the transition matrix elements can be written as:

$$\langle f|\mathcal{H}_{eff}|i\rangle = \frac{G_F}{\sqrt{2}}\lambda_{CKM}\sum_k C_k(\mu)\langle f|Q_k(\mu)|i\rangle \tag{1.71}$$

where G_F is the Fermi constant, λ_{CKM} is a factor related to the CKM matrix and μ is a suitable renormalization scale. The perturbative Wilson coefficients C_k and the non-perturbative matrix elements $\langle f|Q_k(\mu)|i\rangle$ represent the short and long distance contributions, respectively. Considering the Feynman diagrams governing the hadronic two-body transitions, shown in Figure 1.10, $\mathcal{H}_{eff}$ can be expressed as [34, 35, 36]:

$$\mathcal{H}_{eff} = \frac{G_F}{\sqrt{2}}\left[V_{ur}^* V_{ub} \sum_{k=1}^{2} C_k(\mu) Q_k^{ur} + V_{cr}^* V_{cb} \sum_{k=1}^{2} C_k(\mu) Q_k^{cr} - V_{tr}^* V_{tb} \sum_{k=3}^{10} C_k(\mu) Q_k^{r}\right] \tag{1.72}$$

where the term λ_{CKM} has been made explicit, the flavour label $r \in \{d, s\}$ distinguishes between $b \to d$ and $b \to s$ transitions. and the Q_k^{ur}, Q_k^{cr}, Q_k^{r} terms represent the tree level, QCD and EW penguin operators related to the diagrams reported in Figures 1.7, 1.8, 1.9. Specifically these operators can be written as reported in Table 1.6. The order of magnitude of the Wilson coefficients at the renormalization scale $\mu = \mathcal{O}(m_b)$ is: $C_1(\mu) = \mathcal{O}(10^{-1})$, $C_2(\mu) = \mathcal{O}(1)$ and $C_k(\mu) = \mathcal{O}(10^{-2})$ for $k \in [3, 10]$ [32, 37]. The EW penguin effect can not be neglected with respect to the QCD counterparts even if QED coupling turns out to be significantly smaller than the QCD coupling: $\alpha/\alpha_s = \mathcal{O}(10^{-2})$. The cause lies in the heaviness of the top quark which enhances the value of some Wilson coefficient (as C_9) making sizeable the EW contributions for certain B decay modes, for example the $B \to K^+\pi^-$ decay [38, 39]. It is worth to be noticed that the penguin operators with internal u and c quarks are not included in Equation 1.72, while those related to a t quark are described by the Q_k operators with $k \in [3, 10]$. The reason is that the u and c penguin diagrams have been embedded into the tree operator during the Wilson coefficient calculation, as proved in [34, 35]. The phenomenological consequences due to this kind of absorption have been detailed reported in [40, 41]. Finally, thanks to CKM unitarity assumption

$$V_{tr}^* V_{tb} = V_{ur}^* V_{ub} + V_{cr}^* V_{cb}, \tag{1.73}$$

it is possible to rewrite the Equation 1.72 as:

$$\mathcal{H}_{eff} = \frac{G_F}{\sqrt{2}}\left[\sum_{j=u,c} V_{jr}^* V_{jb}\left(\sum_{k=1}^{2} C_k(\mu) Q_k^{jr} + \sum_{k=3}^{10} C_k(\mu) Q_k^{r}\right)\right]. \tag{1.74}$$

Using this formalism, $\mathcal{H}_{eff}$ is efficient for all B decays ruled by the same $b \to q_1\bar{q}_2 d(s)$ transition, since the differences between the various decay modes are caused by the hadronic matrix elements related to the four-quark operators.

A latest useful step in describing the phenomenology of the hadronic two-body B decays consists in the evaluation of the decay amplitudes, already discussed in Section 1.3. Indeed we can rewrite the matrix element for a $\overline{B}_q^0 \to \overline{f}$ decay and for its own CP conjugate decay introducing $\mathcal{H}_{eff}$, as

Table 1.6: Hadronic operators describing tree level, *QCD* and *EW* transitions for hadronic two-body *B* decays. The term $e_{q'}$ represent the electric quark charge[32, 37].

Process	Operator	Definition
tree-level	Q_1^{jr}	$(\bar{r}_\alpha j_\beta)_{V-A}(\bar{r}_\beta j_\alpha)_{V-A}$
$(j \in [u,c])$	Q_2^{jr}	$(\bar{r}_\alpha j_\alpha)_{V-A}(\bar{r}_\beta j_\beta)_{V-A}$
	Q_3^r	$(\bar{r}_\alpha b_\alpha)_{V-A}\sum_{q'}(\bar{q}'_\beta q'_\beta)_{V-A}$
QCD penguin	Q_4^r	$(\bar{r}_\alpha b_\beta)_{V-A}\sum_{q'}(\bar{q}'_\beta q'_\alpha)_{V-A}$
$(q' \in [u,d,s,c,b])$	Q_5^r	$(\bar{r}_\alpha b_\alpha)_{V-A}\sum_{q'}(\bar{q}'_\beta q'_\beta)_{V+A}$
	Q_6^r	$(\bar{r}_\alpha b_\beta)_{V-A}\sum_{q'}(\bar{q}'_\beta q'_\alpha)_{V+A}$
	Q_7^r	$\frac{3}{2}(\bar{r}_\alpha b_\alpha)_{V-A}\sum_{q'} e_{q'}(\bar{q}'_\beta q'_\beta)_{V+A}$
EW penguin	Q_8^r	$\frac{3}{2}(\bar{r}_\alpha b_\beta)_{V-A}\sum_{q'} e_{q'}(\bar{q}'_\beta q'_\alpha)_{V+A}$
$(q' \in [u,d,s,c,b])$	Q_9^r	$\frac{3}{2}(\bar{r}_\alpha b_\alpha)_{V-A}\sum_{q'} e_{q'}(\bar{q}'_\beta q'_\beta)_{V-A}$
	Q_{10}^r	$\frac{3}{2}(\bar{r}_\alpha b_\beta)_{V-A}\sum_{q'} e_{q'}(\bar{q}'_\beta q'_\alpha)_{V-A}$

defined in Equation 1.74 [36]:

$$\begin{aligned}
\mathbf{A}(\overline{B}_q^0 \to \overline{f}) =& \langle \overline{f}|\mathcal{H}_{eff}|\overline{B}_q^0\rangle = \\
& \frac{G_F}{\sqrt{2}}\left[\sum_{j=u,c} V_{jr}^* V_{jb}\left(\sum_{k=1}^{2} C_k(\mu)\langle \overline{f}|Q_k^{jr}|\overline{B}_q^0\rangle + \sum_{k=3}^{10} C_k(\mu)\langle \overline{f}|Q_k^{r}|\overline{B}_q^0\rangle\right)\right], \\
\mathbf{A}(B_q^0 \to f) =& \langle f|\mathcal{H}_{eff}^\dagger|B_q^0\rangle = \\
& \frac{G_F}{\sqrt{2}}\left[\sum_{j=u,c} V_{jr}^* V_{jb}\left(\sum_{k=1}^{2} C_k(\mu)\langle f|Q_k^{jr\dagger}|B_q^0\rangle + \sum_{k=3}^{10} C_k(\mu)\langle f|Q_k^{r\dagger}|B_q^0\rangle\right)\right].
\end{aligned} \tag{1.75}$$

Exploiting the invariance of the strong interaction under *CP* symmetry and the unitary of the *CP* operator, i.e. $(CP)^\dagger(CP) = 1$ the following relations hold:

$$\begin{aligned}
(CP)Q_k^{jr\dagger}(CP)^\dagger &= Q_k^{jr}, \\
(CP)Q_k^{r\dagger}(CP)^\dagger &= Q_k^{r}, \\
(CP)|f\rangle &= e^{i\phi_f}|\overline{f}\rangle, \\
(CP)|B_q^0\rangle &= e^{i\phi_B}|\overline{B}_q^0\rangle.
\end{aligned} \tag{1.76}$$

Including the relations of Equation 1.76 into Equation 1.75 the decay amplitude can be expressed as:

$$\begin{aligned}
\mathbf{A}(B_q^0 \to f) =& \pm e^{i(\phi_B - \phi_f)} \times \\
& \frac{G_F}{\sqrt{2}}\left[\sum_{j=u,c} V_{jr}^* V_{jb}\left(\sum_{k=1}^{2} C_k(\mu)\langle \overline{f}|Q_k^{jr}|\overline{B}_q^0\rangle + \sum_{k=3}^{10} C_k(\mu)\langle \overline{f}|Q_k^{r}|\overline{B}_q^0\rangle\right)\right]
\end{aligned} \tag{1.77}$$

and similarly also the decay amplitude $\mathbf{A}(\overline{B} \to \overline{f})$ can be defined. Consequently:

$$\begin{aligned}
\mathbf{A}(\overline{B} \to \overline{f}) &= e^{i\phi_1}|A_1|e^{i\delta_1} + e^{i\phi_2}|A_2|e^{i\delta_2}, \\
\mathbf{A}(B \to f) &= e^{i(\phi_B - \phi_f)} \times [e^{-i\phi_1}|A_1|e^{i\delta_1} + e^{-i\phi_2}|A_2|e^{i\delta_2}],
\end{aligned} \tag{1.78}$$

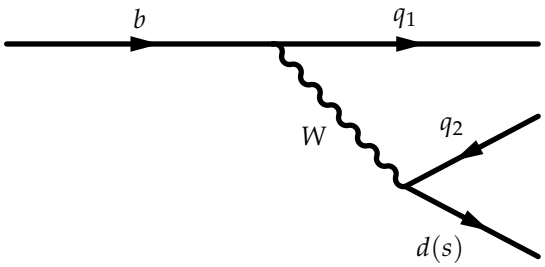

Figure 1.7: Feynman diagram dominating the tree-level transition of a hadronic B decay, with $q_1 \neq q_2 \in [u, c]$.

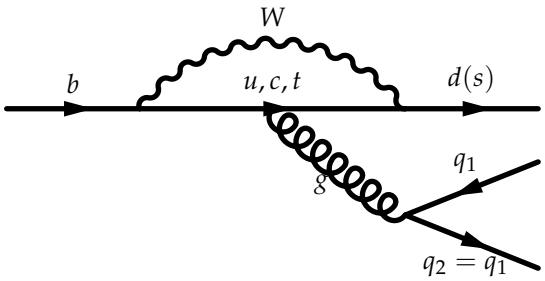

Figure 1.8: Feynman diagram dominating the QCD penguin transition of a hadronic B decay, with $q_1 = q_2 \in [u, d, c, s]$.

where $\phi_{1(2)}$ representing the CP violating phase of the CKM matrix elements ($V_{jr}V_{jb}^*$) and $|A_{1(2)}|e^{i\delta_{1(2)}}$ standing for the CP no-violating strong amplitude:

$$|A|e^{i\delta} \sim \sum_k C_k(\mu) \times \langle \overline{f}|Q_k(\mu)|\overline{B}\rangle. \tag{1.79}$$

The $|A|e^{i\delta}$ term is defined as the product of the perturbative Wilson parameter $C_k(\mu)$ and the non-perturbative hadronic matrix elements $\langle f|Q_k(\mu)|B_q^0\rangle$.

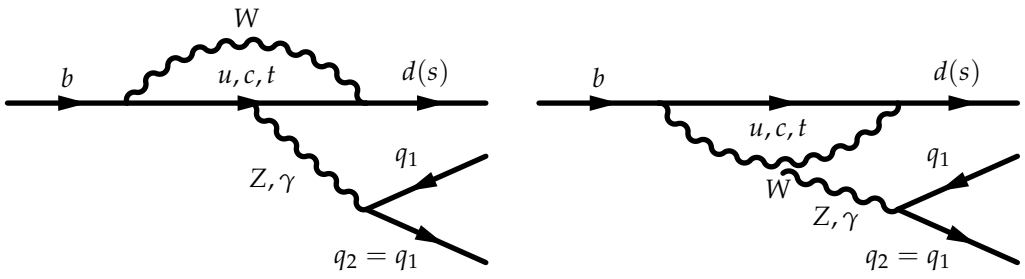

Figure 1.9: Feynman diagram dominating the EW penguin transition of a hadronic B decay, with $q_1 = q_2 \in [u, d, c, s]$.

1.5.1 *CP* violation in two-body B decays

Using the formalism discussed in the previous section it is possible redefining the *CP* asymmetries described in Section 1.4 in the two-body B decay system. The direct *CP* asymmetry reported in Equation 1.62 can be rewritten including Equation 1.78:

$$\begin{aligned} A_{CP} =& \frac{1-\left|\frac{\overline{A}_{\overline{f}}}{A_f}\right|^2}{1+\left|\frac{\overline{A}_{\overline{f}}}{A_f}\right|^2} \\ =& \frac{2|A_1||A_2|\sin(\delta_1-\delta_2)\sin(\phi_1-\phi_2)}{|A_1|^2+2|A_1||A_2|\cos(\delta_1-\delta_2)\cos(\phi_1-\phi_2)+|A_2|^2}. \end{aligned} \tag{1.80}$$

In this case, the *CP* asymmetry comes from the interference between the two weak amplitudes and in order to not be null requires a non-vanishing difference both in the two weak phases $\phi_{1(2)}$ and in the strong phases $\delta_{1(2)}$. Since $\phi_1 - \phi_2$ is in general related to one of the angles of the unitary triangle, the aim is to measured the A_{CP} value and then extrapolate this quantity. The main complication that has to be faced performing this extrapolation is related to the hadronic uncertainties coming from the strong amplitudes $|A_{1(2)}|e^{i\delta_{1(2)}}$. The hadronic matrix elements can be calculated both through the theoretical tools described in Section 1.5 and by means of specific experimental approaches aimed to deal with their uncertainties. One of these strategies consists in exploiting the flavour symmetries of the strong interactions, $SU(2)$[3] and $SU(3)$[4] to derive the amplitude relations and get rid of the uncertainties related to the factorization and the infinite mass limit. These assumptions are proved to be efficient within few percent of accuracy and are confirmed by the experimental observation of almost degenerated mass-eigenstates of u, d and s quarks. This strategy was used to extract of the UT α angle from $B \to \pi\pi, \rho\pi, K\pi$ inclusive decays. The main complication, limiting the efficacy of this technique, is the number of precise measurements available which make necessary introducing further dynamical hypothesis in order to reduce the hadronic parameters. A $SU(3)$-based strategy to extract the γ angle from the hadronic charmless two-body B decays, initially suggested in [42], is discussed in Section 2.4.

The *CP* asymmetry in mixing and interference are related to the parameter q/p: the former type of *CP* violation is related to the absolute value of q/p and the latter one to the phase of this parameter. Using the definition reported in Section 1.3 for M_{12} and Γ_{12} it is possible to write Equation 1.63 as:

$$\frac{q}{p} = \sqrt{\frac{4|M_{12}^2|e^{-2i\phi_m}+|\Gamma_{12}|^2e^{-2i\phi_\Gamma}}{4|M_{12}|^2+|\Gamma_{12}|^2-4|M_{12}||\Gamma_{12}|\sin(\phi_m-\phi_\Gamma)}}, \tag{1.81}$$

which, using the approximation $\frac{\Gamma_{12}}{M_{12}} \propto O(10^{-3})$ reported in Equation 1.50, can be further simplified

[3] The isospin relations are based on the assumption that strong interaction stay unvaried under flavour exchange $u \leftrightarrow d$.

[4] The relations based on the $SU(3)$ symmetry arise as an extension of the $SU(2)$ where the invariance of the strong interaction is assumed true under the quark-flavour exchange $d \leftrightarrow s$.

as:

$$\frac{q}{p} = \sqrt{1 + \frac{|\Gamma_{12}|}{|M_{12}|}\sin(\phi_m - \phi_\Gamma)}e^{-i\phi_m} \approx e^{-\phi_m}. \tag{1.82}$$

On the other hand the *CP* violation in the interference depends also on the ratio between A_f and $\overline{A}_f$. Using the Equation 1.77 and considering the case where f is a *CP* eigenstate, the resulting ratio can be evaluated as:

$$\frac{\overline{A}_f}{A_f} = \pm e^{i\phi}\left[\frac{\sum_{j=u,c} V_{jr}^* V_{jb}\langle f|Q^{jr}|\overline{B}\rangle}{\sum_{j=u,c} V_{jr} V_{jb}^*\langle f|Q^{jr}|B\rangle}\right] \tag{1.83}$$

where

$$Q^{jr} = \sum_{k=1}^{2} C_k(\mu)Q_k^{jr} + \sum_{k=3}^{10} C_k(\mu)Q_k^r. \tag{1.84}$$

The hadronic matrix elements introduce large hadronic uncertainties which affect significantly the measurement of the amplitude ratio of Equation 1.83. In any case, if the signal B decay is governed by a unique *CKM* amplitude, the parameters $\overline{A}_f$, A_f and their ratio can be simplified as:

$$\begin{aligned} \overline{A}_f &= e^{i\phi_{CKM}}(|A_s|e^{i\delta}), \\ A_f &= e^{i\phi}e^{-i\phi_{CKM}}(|A_s|e^{i\delta}), \\ \frac{\overline{A}_f}{A_f} &= e^{i\phi}e^{2i\phi_{CKM}} \end{aligned} \tag{1.85}$$

where $\phi_{CKM} = \arg(V_{jr}^* V_{jb})$, A_s and δ are the strong amplitude and *CP* non-violating phase, respectively.

1.5.2 Hadronic charmless two-body B decays

In this work only the family of hadronic charmless two-body B decays are taken into account and in particular the following modes: $B^0 \to \pi^+\pi^-$, $B^0 \to K^+\pi^-$, $B^0 \to K^+K^-$, $B_s^0 \to K^+K^-$, $B_s^0 \to K^+\pi^-$, $B_s^0 \to \pi^+\pi^-$, $\Lambda_b \to p\pi^-$ and $\Lambda_b \to pK^-$ (and the relative *CP* conjugate modes). These channels, named in the following as $B \to h^+h^-$ for simplicity, were deeply studied at the Tevatron [43, 44, 45, 46], the B factories [47, 48, 49, 50, 51, 52] and at the LHCb experiment [53, 54].

The $B \to h^+h^-$ decays are induced by the tree level diagrams, classified as leading order, and penguin level weak interactions. A rich set of physics contributions participate to these processes and their Feynman diagrams are shown in Figure 1.10. All diagrams contributing in each decay mode are listed in Table 1.7. The considerable size of the QCD ($b \to d(s) + g$) and EW ($b \to d(s) + \gamma(Z^0)$) penguin transitions don't allow a very clean measurement of the *CKM* phases and, consequently, of the *CP* violating observables. However, if on one hand the presence of loop diagrams introduce further complication to the *CP* violation measurement using these decays, on the other hand it has very interesting implications, being sensitive to New Physics beyond the *SM* that would inflate the small effect of the penguin diagrams.

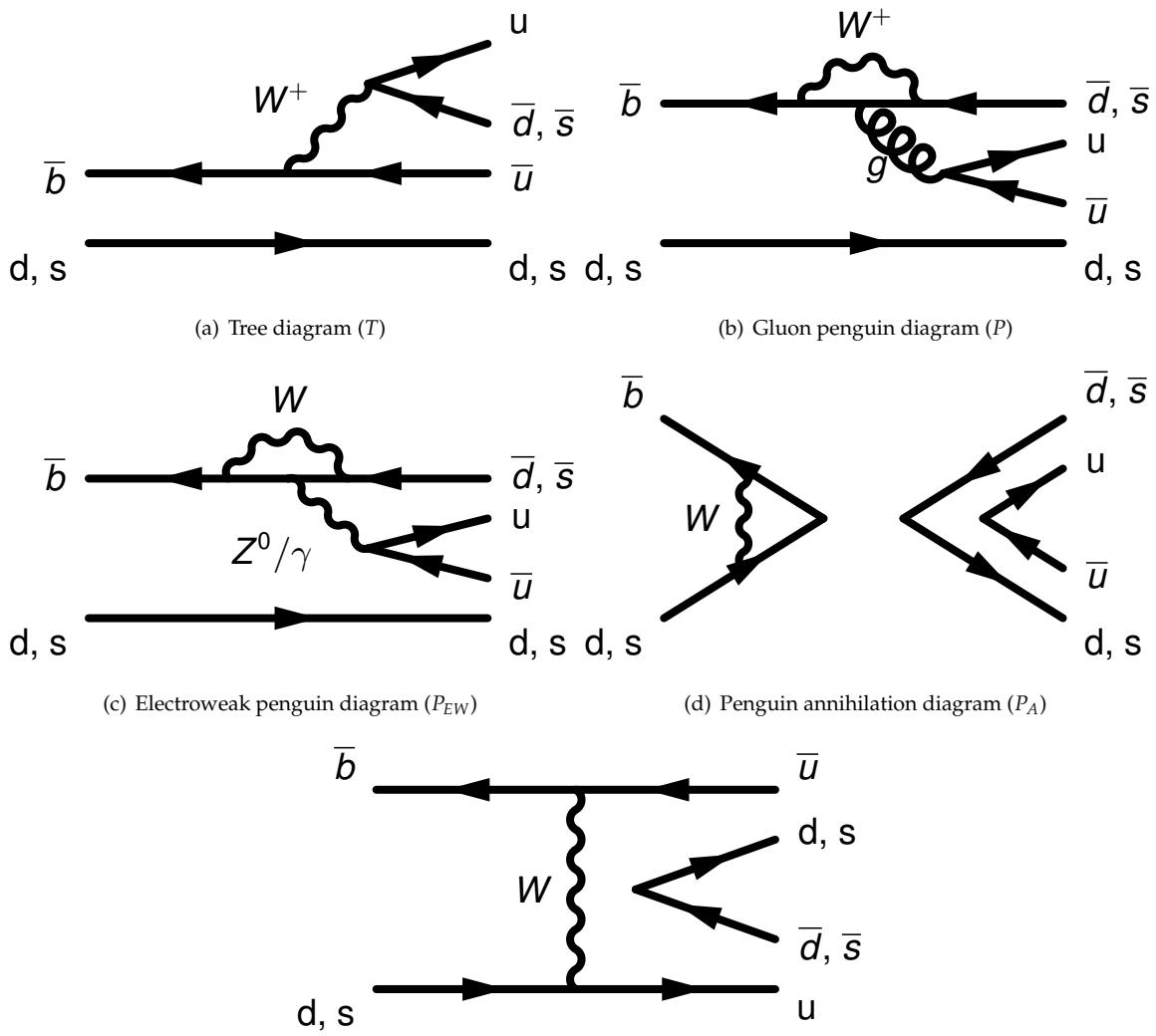

Figure 1.10: Feynman diagrams contribution to the amplitudes of charmless $B \to h^+h^-$ decays.

Table 1.7: Feynman diagrams contributing to the amplitudes of each charmless $B \to h^+h^-$ decays.

Decay	Diagram contributions
$B^0 \to \pi^+\pi^-$	T, P, P_{EW}, P_A, E
$B^0 \to K^+\pi^-$	T, P, P_{EW}
$B^0 \to K^+K^-$	P_A, E
$B_s^0 \to K^+K^-$	T, P, P_{EW}, P_A, E
$B_s^0 \to \pi^+K^-$	T, P, P_{EW}
$B_s^0 \to \pi^+\pi^-$	P_A, E
$\Lambda_b \to p\pi^-$	T, P, P_{EW}
$\Lambda_b \to pK^-$	T, P, P_{EW}

An optimal strategy for studying the *CP* violation in this kind of decays, initially suggested in 1999 [42] and revisited in 2007 [55], consists in combining the measurements of time-dependent *CP* asymmetry for the $B^0 \to \pi^+\pi^-$ and $B_s^0 \to K^+K^-$ decays modes. This idea turn out to be very promising when the *U*-spin symmetry[5] is assumed, which allows to overcome the loop limitations. In this way, it will be possible to obtain a clean measurement of the angle $\gamma = \arg(V_{ub}^*)$ which, being the channels sensitive to New Physics, could differ significantly from the measurement performed on the *B* decays completely dominated by the leading order [56].

The *U*-spin symmetry connect the strong interaction dynamics between two decay modes which differ by the interchange of a quark d or s: $B^0 \to \pi^+\pi^-$ and $B_s^0 \to \pi^+K^-$ as well as $B_s^0 \to K^+K^-$ and $B^0 \to K^+\pi^-$. In this case the *U*-spin symmetry is not completely satisfied since the P_A, P_E diagrams contribute only to the former decay channel. However the contribution coming from these topologies is expected to be very small and can be measured by means of the $B^0 \to K^+K^-$ and $B_s^0 \to \pi^+\pi^-$ modes which occur only through these two diagrams.

The couples of modes liked by a fully *U*-spin symmetry are $B^0 \to K^+\pi^-$ and $B_s^0 \to \pi^+K^-$, and similarly $B^0 \to \pi^+\pi^-$ and $B_s^0 \to K^+K^-$.

1.5.3 $B^0 \to K^+\pi^-$ and $B_s^0 \to \pi^+K^-$ decay modes

The $B_q^0 \to K^+\pi^-$ ($q = d, s$) decays originates from the $\bar{b} \to \bar{u}u\bar{d}(\bar{s})$ at the leading order but receive contributions also from penguin topologies, dominated by 1-loop diagrams with a top quark, as reported in Table 1.7. The tree and 1-loop level topologies contribute to the decay amplitude with a *CKM* factor equal to $V_{ub}^*V_{us}$ and $V_{tb}^*V_{ts}$, respectively. Since the ratio between the two *CKM* factors is equal to 0.02 and *EW* penguin topology can contribute only through a color-suppress mode, the $B_q^0 \to K^+\pi^-$ decays turn out to be dominated by the *QCD* penguin amplitude. Using the "Wolfenstein parametrization" and introducing the *CKM* unitarity the decay amplitudes can be written as:

$$\begin{aligned} A(B_d^0 \to K^+\pi^-) &= -P(1 - re^{i\gamma}e^{i\delta}), \\ A(B_s^0 \to \pi^+K^-) &= -P_s\sqrt{\varepsilon}\left(1 + \frac{1}{\varepsilon}r_s e^{i\delta_s}e^{i\gamma}\right) \end{aligned} \tag{1.86}$$

where $P_{(s)}$ represents the penguin amplitude, $r_{(s)}$ describes the ratio between tree and penguin amplitudes, $\delta_{(s)}$ is the *CP* conserving hadronic phase and γ is the *UT* angle.

Since $B_q^0 \to K^+\pi^-$ is a flavour specific decay, the probability for a $B^0 \to \pi^+K^-$, $B_s^0 \to K^+\pi^-$ and their *CP* conjugate transitions are null. Thus the *CP* violating parameter λ_f and $\overline{\lambda}_f$, described in

[5] Invariance of the strong interaction dynamics under the exchange of the $d \leftrightarrow s$ quarks.

Section 1.3, are both equal to 0 and the decay rates for the $B^0 \to K^+\pi^-$ can be evaluated as:

$$\begin{aligned}
\Gamma_{B_q^0 \to K^+\pi^-}(t) &= |A_f|^2 \left[\cosh\left(\frac{\Delta\Gamma_q}{2}t\right) + \cos\left(\Delta m_q t\right) \right], \\
\Gamma_{B_q^0 \to \pi^+K^-}(t) &= |\overline{A}_{\overline{f}}|^2 \left[\cosh\left(\frac{\Delta\Gamma_q}{2}t\right) - \cos\left(\Delta m_q t\right) \right], \\
\Gamma_{\overline{B}_q^0 \to K^+\pi^-}(t) &= |A_f|^2 \left[\cosh\left(\frac{\Delta\Gamma_q}{2}t\right) - \cos\left(\Delta m_q t\right) \right], \\
\Gamma_{\overline{B}_q^0 \to \pi^+K^-}(t) &= |\overline{A}_{\overline{f}}|^2 \left[\cosh\left(\frac{\Delta\Gamma_q}{2}t\right) + \cos\left(\Delta m_q t\right) \right].
\end{aligned} \tag{1.87}$$

From the combination of the Equation 1.87 and Equation 1.80 it is possible to define the following time-independent quantity:

$$A_{B_q^0}^{CP} = \frac{|\overline{A}_{\overline{f}}|^2 - |A_f|^2}{|\overline{A}_{\overline{f}}|^2 + |A_f|^2} = \frac{2r_q \sin(\delta_q)\sin(\gamma)}{1 + 2\cos(\gamma)(\delta_q) + r_q^2}. \tag{1.88}$$

As the direct *CP* asymmetry depends explicitly on γ, the amplitude of the *UT* angle can be obtained from the measurement of $A_{B_q^0}^{CP}$.

1.5.4 $B^0 \to \pi^+\pi^-$ and $B_s^0 \to K^+K^-$ decay modes

The $B^0 \to \pi^+\pi^-$ and $B_s^0 \to K^+K^-$ decays arise from $\overline{b} \to \overline{u}u\overline{d}$ and $\overline{b} \to \overline{u}u\overline{d}$ tree-level transition, respectively. The $B^0 \to \pi^+\pi^-$ decay amplitude can be evaluated as:

$$A(B^0 \to \pi^+\pi^-) = \lambda_u^{(d)}(A_T^u + A_P^u) + \lambda_c^{(d)}A_P^c + \lambda_t^{(d)}A_P^t \tag{1.89}$$

where A_T represents the leading order contribution, A_P^i are the QCD and EW penguin contributions related to the i up-type quark ($i =, u, c, t$) and the coefficients $\lambda_i^{(d)}$ stand for the *CKM* factors $\lambda_i^{(d)} = V_{jd}V_{jb}^*$. Assuming the *CKM* unitarity and using the "Wolfenstein parametrization", the Equation 1.89 can be written as:

$$A(B^0 \to \pi^+\pi^-) = \left(1 - \frac{\lambda^2}{2}\right) C[e^{-i\gamma} - de^{-i\theta}] \tag{1.90}$$

with

$$\begin{aligned}
C &= \lambda^3 A R_b (A_T^u + A_P^u - A_P^t), \\
de^{-i\theta} &= \frac{1}{R_b(1 - \frac{\lambda^2}{2})} \left(\frac{A_P^c - A_P^t}{A_T^u + A_P^u - A_P^t} \right).
\end{aligned} \tag{1.91}$$

where the parameters A, R_b, λ and γ have been already defined in Section 1.2.3. The quantity $A(B_s^0 \to K^+K^-)$ can be evaluated in similar way and it turns out to be:

$$A(B_s^0 \to K^+K^-) = \lambda C' \left[e^{i\gamma} + \frac{1}{\varepsilon} d' e^{i\theta'} \right] \tag{1.92}$$

where C', d' and θ' are the counterpart of C, d and θ for the $B^0 \to \pi^+\pi^-$ decay and $\varepsilon = \lambda^2/(1 - \lambda^2/2)$. The branching ratio of the $B^0 \to \pi^+\pi^-$ and $B_s^0 \to K^+K^-$ decays were measured by several experiments whose results are reported in Table 2.9. The significant *CP* observables measurable in these decay modes are the one reported in Section 1.4.3, which can be re-written in terms of the parameters $d^{(\prime)}$, $\theta^{(\prime)}$, γ and $\beta_{(s)}$. For the $B^0 \to \pi^+\pi^-$ the observables are:

$$\begin{aligned} A^{dir}_{\pi^+\pi^-} &= C_{\pi^+\pi^-} = -\frac{2d\sin\theta\sin\gamma}{1 - 2d\cos\theta\cos\gamma + d^2}, \\ A^{mix}_{\pi^+\pi^-} &= S_{\pi^+\pi^-} = \frac{\sin(2\beta + 2\gamma) - 2d\cos\theta\sin(2\beta + \gamma) + d^2\sin 2\beta}{1 - 2d\cos\theta\cos\gamma + d^2} \end{aligned} \tag{1.93}$$

where β stands for the B mixing phase and the *CP* violating parameter λ_f has been replace by;

$$\lambda_f = -e^{-2i\beta}\left[\frac{e^{i\gamma} - de^{i\theta}}{e^{-i\gamma} - de^{i\theta}}\right]. \tag{1.94}$$

Since the value of $\Delta\Gamma_d$ results to be very small the *CP* parameter $A^{\Delta\Gamma}$ turns out to be too small to be measured [57]. Regarding the $B_s^0 \to K^+K^-$ decay the *CP* observables can be defined as:

$$\begin{aligned} A^{dir}_{K^+K^-} &= C_{K^+K^-} = -\frac{2d'\sin\theta'\sin\gamma}{1 - 2d'\cos\theta'\cos\gamma + d'^2}, \\ A^{mix}_{K^*K^-} &= S_{K^+K^-} = \frac{\sin(2\beta_s + 2\gamma) - 2d'\cos\theta'\sin(2\beta_s + \gamma) + d'^2\sin 2\beta_s}{1 - 2d'\cos\theta'\cos\gamma + d'^2} \\ A^{\Delta\Gamma}_{K^+K^-} &= D_{K^+K^-} = \frac{d'^2\sin 2\beta_s + 2\varepsilon d'\cos\theta'\cos(2\beta_s + \gamma) + \varepsilon^2\cos(2\beta_s + 2\gamma)}{1 - 2d'\cos\theta'\cos\gamma + d'^2} \end{aligned} \tag{1.95}$$

1.5.5 $B^0 \to K^+K^-$ and $B_s^0 \to \pi^+\pi^-$ decay modes

The *SM* predicts that only the P_A and E penguin topologies contribute to the amplitude of $B^0 \to K^+K^-$ and $B_s^0 \to \pi^+\pi^-$ decays. The first evidence of $B_s^0 \to \pi^+\pi^-$ was obtained by CDF experiment [43]. Then also LHCb measured the branching ratios of both the decays, with a significance of more than 5σ [58]. The measurements of the branching fractions are reported in Table 2.9.

1.5.6 $\Lambda_b^0 \to pK^-$ and $\Lambda_b^0 \to p\pi^-$ decay modes

As claimed in Reference [59], the measurement of the *CP* asymmetry in $\Lambda_b^0 \to pK^-$ and $\Lambda_b^0 \to p\pi^-$ is sensitive to possible New Physics effects within the Minimal Supersymmetric Standard Model assuming the R-parity. Indeed these New Physics contributions affect significantly the *CP* asymmetry value, *SM* predictions is that $A^{CP} \approx 8\%$ but it can become negligible in the R-parity violating model. In similar way also the branching ratio is modified by New Physics effects, enhancing its value from $\sim 10^{-6}$, predicted by the *SM*, to $\sim 10^{-4}$. For this reason both CDF and LHCb experiment performed measurements in order to determine both the branching ratio and the *CP* asymmetry with high precision. Recently the LHCb collaboration published the latest results related to the *CP* violation in the Λ_b charmless decays, obtained using the full Run 1 data, observing no *CP* violation [60].

2

Status of the art

Due to the great importance covered by the charmless two-body B decays for studying the CP violation in and beyond the SM, as described in the previous chapter, many experiments performed different analyses over the last decade. In particular time-dependent as well as time-independent analyses were performed by the B factories BaBar and Belle, at SLAC and KEK respectively, by CDF experiment at Tevatron and by LHCb experiment at CERN. In this chapter the latest results obtained by these experiments are reported.

2.1 B factories

The term "B factory" indicates a facility that can produce B mesons at sufficiently high rate to allow the observation and the study of CP violation phenomena and other rare processes. The two main B factories were designed and built in the 1990s, namely the BaBar experiment at the PEP-II collider at SLAC laboratory in California (United States) and the Belle experiment at the KEKB collider at KEK in Tsukuba (Japan). Both of them are based on electron-positron collider with a centre of mass energy tuned to the Y(4S) threshold ($\sim 10\,\text{GeV}$), allowing the production of B^+B^- and $B^0\bar{B}^0$ pairs. In order to separate the signal decay vertices, allowing a better observation of the time-evolution of the $B^0\bar{B}^0$ decay and improving the tagging of the B meson, both the experiment boosted the Y(4S) center of mass by means of unequal collisions energies. The main advantages of such a design are [61]:

- "*Cleanliness*": the $B\bar{B}$ pairs are produced without extra particles, it means that the backgrounds are extremely suppressed and are even more readily reduced by the specification of both beam polarizations;
- "*Democracy*": the e^+e^- initial state is electrically neutral and has no overall quantum numbers, meaning that both leptonic and hadronic sectors may be explored with comparable statistics;
- copious production of b-mesons with a $b\bar{b}$ cross section $\sigma_{b\bar{b}} \sim 1$ nb;

- the B meson energy (E_B) is known precisely, a very powerful feature which reveals its important role in the reconstruction of B decays;
- good detector energy resolution which, along with the precise knowledge of E_B, allows one to rule out a missing π^0 meson;
- the $B^0\overline{B}^0$ pair is produced as *coherent state* and remains so until one of the two particles decays, thus tagging the flavour of one of the two mesons through its decay establishes the flavour of the partner (phenomenon known as *quantum entanglement*);
- the use of a tight energy constraint around E_B allows use of partial reconstruction methods for tagging, increasing the tagging efficiency.

2.1.1 Charmless two-body B decays at BaBar experiment

The BaBar experiment exploits an asymmetric accelerator to make collide electrons and positrons together at high energies: in particular the collision energy is fixed at the $\Upsilon(4S)$ mass resonance. This is the reason why their analysis includes only the $B \to hh$ decays coming from B^0_d, since a couple of B^0_s mesons is too heavy to be produced. On the other hand, thanks to their detector characteristics, BaBar was able to identify with high precision also the neutral pions and kaons produced in the B^0_d decays allowing to reconstruct, in addition to the B^0_d modes described in the previous chapter, also the $B^0_d \to \pi^0\pi^0$ and $B^0_d \to K^0\pi^0$ decays. Thanks to the measurements obtained on the neutral and charged $B^0_d \to hh$ modes and to the isospin relations between their rates and asymmetries, BaBar was capable of determining constraints on the Unitary Triangle angle $\alpha \equiv \arg[-V_{td}V^*_{tb}/V_{ud}V^*_{ub}]$. The α angle is measured through the interference between two decay amplitudes, where one of them involves the $B^0_d - \overline{B}^0_d$ oscillations. In this case the time-dependent *CP* asymmetry can be determined as:

$$A_{CP}(\Delta t) = \frac{|\overline{A}(\Delta t)|^2 - |A(\Delta t)|^2}{|\overline{A}(\Delta t)|^2 + |A(\Delta t)|^2} = S_{\pi^+\pi^-}\sin(\Delta m_d \Delta t) - C_{\pi^+\pi^-}\cos(\Delta m_d \Delta t) \tag{2.1}$$

where Δt represents the difference between the decay time of the B meson which decays in the $\pi\pi$ final state and the other B meson generated in the event, Δm_d is the $B^0 - \overline{B}^0$ mixing frequency, A and $\overline{A}$ are the decay amplitudes. The direct and the mixing-induced *CP* asymmetry, represented by $C_{\pi\pi}$ and $C_{\pi\pi}$ respectively, are defined as:

$$\begin{aligned} C_{\pi^+\pi^-} =& \frac{|A|^2 - |\overline{A}|^2}{|A|^2 - |\overline{A}|^2} \\ S_{\pi^+\pi^-} =& \sqrt{1 - C^2_{\pi^+\pi^-}}\sin(2\alpha - 2\Delta\alpha_{\pi\pi}) \end{aligned} \tag{2.2}$$

Both the asymmetry $C_{\pi^+\pi^-}$ and the phase $\Delta\alpha_{\pi\pi} = \alpha - \alpha_{eff}$ may deviate from 0 due to the 1-loop contributions to the decay amplitudes. The magnitude and the phase of the 1-loop contribution

Table 2.1: Final results for the *CP* parameters in $B^0_d \to \pi^+\pi^-$, $B^0_d \to K^+\pi^-$ and $B^0_d \to \pi^0\pi^0$ decays. The measurement of the branching fraction of the $B^0_d \to \pi^0\pi^0$ and $B^0_d \to K^0\pi^0$ decays is also shown. [62].

Parameter	Value
$S_{\pi^+\pi^-}$	$-0.68 \pm 0.10 \pm 0.03$
$C_{\pi^+\pi^-}$	$-0.25 \pm 0.08 \pm 0.02$
$A_{K^+\pi^-}$	$-0.107 \pm 0.016^{0.006}_{0.004}$
$C_{\pi^0\pi^0}$	$-0.43 \pm 0.26 \pm 0.05$
$B(B^0_d \to \pi^0\pi^0)$	$(1.83 \pm 0.21 \pm 0.13) \cdot 10^{-6}$
$B(B^0_d \to K^0\pi^0)$	$(10.1 \pm 0.6 \pm 0.4) \cdot 10^{-6}$

to the mixing-induced asymmetry is determined by means of an analysis of the isospin relations between the $B^0_d \to \pi\pi$ decay amplitudes. The amplitudes A^{ik}, related to the decay $B^0_d \to \pi^i\pi^k$, and its *CP* conjugate amplitude, $\overline{A}^{ik}$, can be defined as:

$$\begin{aligned} A^{+0} &= \frac{1}{\sqrt{2}} A^{+-} + A^{00} \\ \overline{A}^{-0} &= \frac{1}{\sqrt{2}} \overline{A}^{+-} + \overline{A}^{00} \end{aligned} \tag{2.3}$$

The direct *CP* asymmetry for the $B^0_d \to \pi^0\pi^0$ can be described using a notation similar to the $\pi^+\pi^-$ system:

$$C_{\pi^0\pi^0} = \frac{|A^{00}|^2 - |\overline{A^{00}}|^2}{|A^{00}|^2 - |\overline{A^{00}}|^2} \tag{2.4}$$

Finally the BaBar collaboration provided a measurement of the direct *CP* violation in $B^0_d \to K^+\pi^-$ and in $B^0_d \to \pi^+\pi^-$ with a significance of 6.1σ and 6.1σ respectively, and provide a measurements of the branching fraction for the $B^0_d \to \pi^0\pi^0$ and $B^0_d \to K^0\pi^0$. The final results are reported in Table 2.1. The plots related to the $B^0_d \to \pi^+\pi^-$ decay are shown in Figure 2.1. They find also a 68% confidence level (C.L.) region for α of[71°,109°], excluding the region between [23°, 67°] at 90% C.L. In addition they determined an upper bound on $\Delta\alpha_{\pi\pi}$ of 43° at 90% C.L. as shown in Figure 2.2. The relevant results obtained by the BaBar collaboration regarding the *CP* violation in the $B \to hh$ family were published in 2013 [62].

2.1.2 Charmless two-body B decays at Belle experiment

The Belle experiment at the KEKB asymmetric-energy e^+e^- collider published two different analysis measuring the *CP* asymmetries and the branching fraction of the charmless two-body B decays [63, 64]. Also in this case both the neutral and the charged $B_{u,d}$ decays to $K\pi$, $\pi\pi$ and KK final states are taken into account. The data used in the analyses have been collected at the $\Upsilon(4S)$ mass resonance ($\sqrt{s} = 10.58$ GeV). Thanks to the U-spin symmetry between the charged and neutral $B_{u,d} \to \pi\pi$

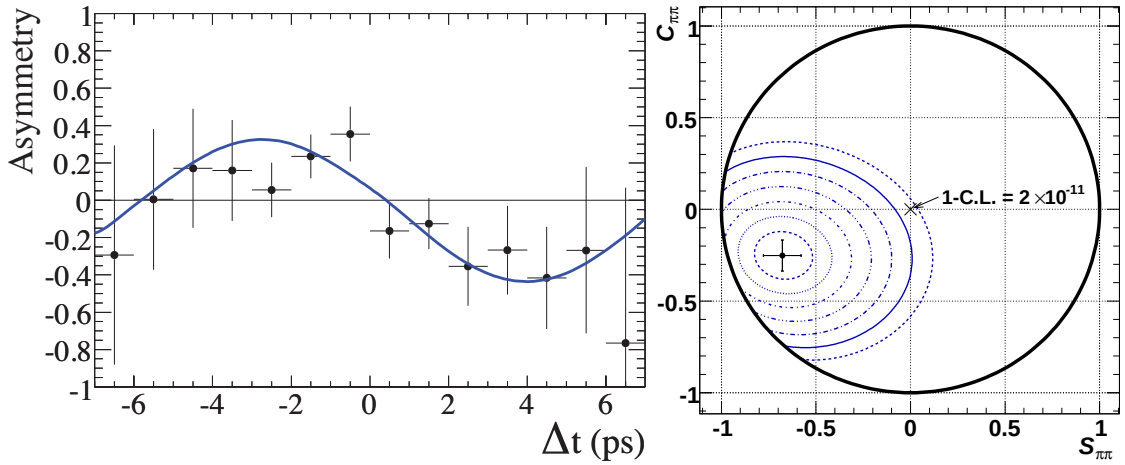

Figure 2.1: On the left the asymmetry $A(\Delta t)$ for the $\pi^+\pi^-$ system is shown, while on the right a plot with the constraints for the $C_{\pi^+\pi^-}$ and $S_{\pi^+\pi^-}$ is shown, where the point with error bars represents the measured value and the blue circle indicates the C.L from 1σ to 7σ. [62]

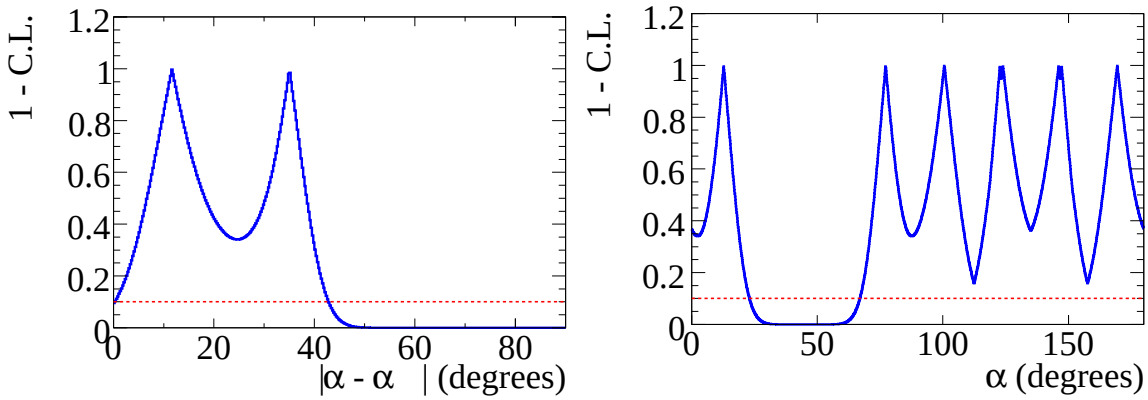

Figure 2.2: On the left a plot showing the constraints on $\Delta\alpha_{\pi\pi} = \alpha - \alpha_{eff}$ expressed as one minus the C.L. as function of $\Delta\alpha$ is reported. On the right instead the plot of the constraints for the Unitary Triangle angle α is shown [62]. The dashed red line represents the 90% C.L..

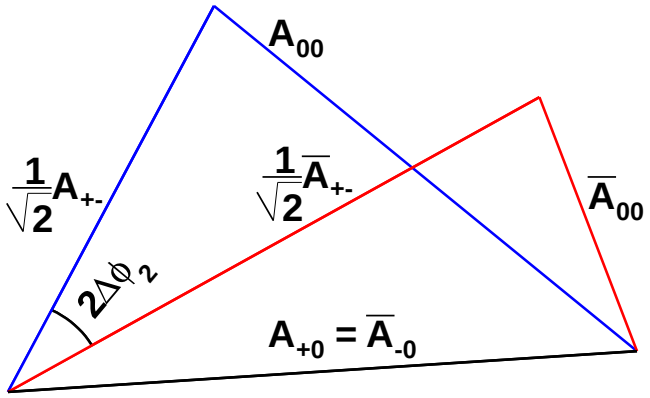

Figure 2.3: Representation in the complex plane of the amplitude relations reported in Equation 2.3 [63]. From the difference of the two triangle is possible to determine $\Delta\alpha$ parameter (indicated as $\Delta\phi_2$ in the figure.)

modes the UT angle α (named ϕ_2 in Belle's convention) can be determined, in similar way to the BaBar experiment. Thus the complex decay amplitudes of these decays obey to the relations reported in Equation 2.3 which can be represented as triangles in a complex plane, as shown in Figure 2.3.

Because the $B_u^+ \to \pi^+\pi^0$ is a pure tree decay the two triangles have the same base, $A^{+0} = \overline{A}^{-0}$, and the $\Delta\alpha$ parameter can be evaluated from the difference between the two triangles. The sides and angles of the triangles along with the α parameter can be fully determined from the branching fractions and both the direct and mixing-induced CP asymmetry of the $B_d^0 \to \pi^+\pi^-$, $B_d^0 \to \pi^0\pi^0$ and $B_u^+ \to \pi^+\pi^0$ decays. Unfortunately this method has a eightfold discrete ambiguity in the α determination that arises from the four possible triangle orientations of A^{+0} and the two solutions of α^{eff} in the measurement of S_{CP}.

In one the two analysis, whose results are reported in the paper [63], Belle confirms the CP violation in the $B_d^0 \to \pi^+\pi^-$ channel. The time-dependent results are reported in Table 2.2 while the Δt distributions and the asymmetry plot are shown in Figure 2.4. In addition they provide a measurement of α excluding the range $23.8^\circ < \alpha < 66.8^\circ$ at the 1σ C.L. and a constraint on the $\Delta\alpha$ shift, caused by the penguin contributions, to be lower than 44.8° at the 1σ level. The constraints on these two variables are shown in Figure 2.5.

In the other analysis Belle measured the branching fractions and the direct CP asymmetries of the various $B_{u,d}$ charmless modes. The results are reported in Table 2.3 and were published in the paper [64].

Table 2.2: Final results for the *CP* parameters in $B^0_d \to \pi^+\pi^-$, $B^0_d \to K^+\pi^-$ [63].

Parameter	Value
$S_{\pi^+\pi^-}$	$-0.64 \pm 0.08(stat) \pm 0.03(syst)$
$C_{\pi^+\pi^-}$	$-0.33 \pm 0.06(stat) \pm 0.03(syst)$
$A_{K^+\pi^-}$	-0.061 ± 0.014

Table 2.3: Direct *CP* asymmetries (A_{CP}) for all the $B_{d,u}$ modes. The first and the second quoted uncertainties are statistical and systematic, respectively [64].

Mode	A_{CP}
$K^*\pi^-$	$-0.068 \pm 0.014 \pm 0.007$
$K^+\pi^0$	$0.043 \pm 0.024 \pm 0.002$
$\pi^+\pi^0$	$0.025 \pm 0.043 \pm 0.007$
$\overline{K}^0 K^+$	$0.014 \pm 0.168 \pm 0.002$
$K^0\pi^+$	$-0.011 \pm 0.021 \pm 0.006$

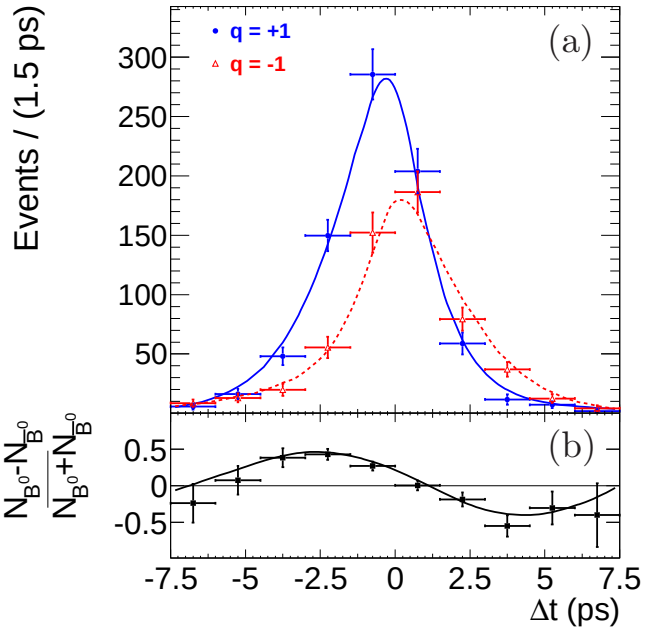

Figure 2.4: Time-dependent fit results for the $B^0 \to \pi^+\pi^-$ decay [63]. The upper part of the plot shows the Δt distribution for each B^0 flavour (q) used to tag the event, where $q = 1$ indicates the B^0 meson (solid blue line) and $q = -1$ represents the $\overline{B}^0$ meson (dashed red line). In the lower part of the plot the asymmetry between the plots shown above is reported. The plot is determined evaluating for each bin of Δt the quantity $(N_{B^0} - N_{\overline{B}^0})/(N_{B^0} + N_{\overline{B}^0})$ where N is the measured signal yield of B^0 and $\overline{B}^0$ events.

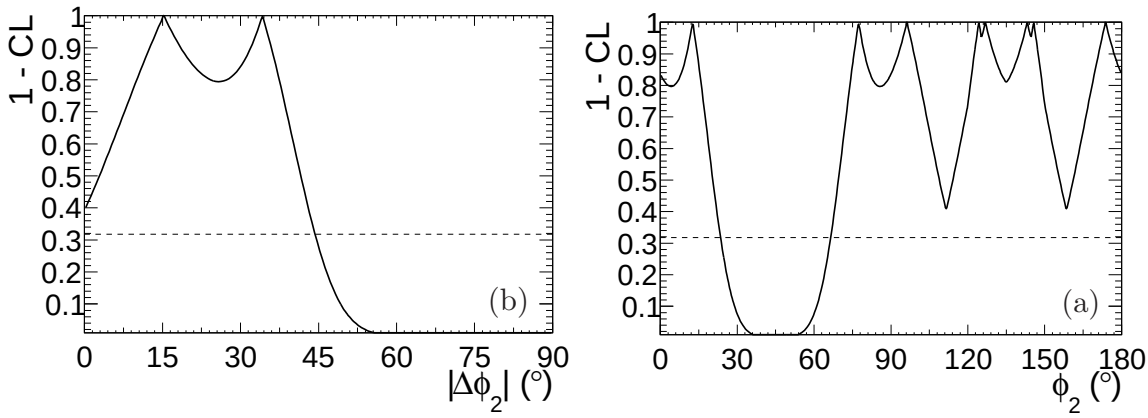

Figure 2.5: On the left a plot showing the constraints on $\Delta\alpha_{\pi\pi}$ ($\Delta\phi_2$) expressed as one minus the C.L. as function of $\Delta\alpha$ is reported. On the right instead the plot of the constraints for the Unitary Triangle angle α (ϕ_2) is shown [63]. The dashed line represents the 1σ exclusion level.

2.2 Hadronic colliders

While initially the B physics was dominated by the e^+e^- machines operating on the $\Upsilon(4S)$ resonance, successively the UA1 collaboration has shown that this kind of physics was feasible also at a hadron collider environment [65]. The first signal of fully reconstructed B mesons at a hadron collider has been published by the CDF collaboration in 1992 [66]. Nowadays, B physics results from a hadron collider are fully competitive with the e^+e^- B factories and in many cases the two kind of measurements result to be complementary with each other: for example, no B_s^0 and B_c^+ mesons or b-baryons are produced on the $\Upsilon(4S)$ resonance. The main features of the B physics at a hadron collider are [67, 68]:

- enormous production of b-hadrons resulting in a $b\bar{b}$ cross section $\sigma_{b\bar{b}} \sim 50$ μb for CDF and $\sigma_{b\bar{b}} \sim 500$ μb for LHCb;
- capability to study the physics of all the particles in the b-hadron zoo;
- B meson pairs produced in an "incoherent state", which lead to more difficulties in tagging the B flavour at production;
- no well-defined jet structure is visible with respect to the B factories where the $B^0\bar{B}^0$ or B^+B^- pairs are produced nearly at rest, resulting in spherical event shape;
- b-hadron produced with a large boost in order to separate the various decay vertices;
- very high average multiplicity, including tracks from the "underlying events" particles; a comparison between the track multiplicity in LHCb and Belle experiment is shown in Figure 2.6;

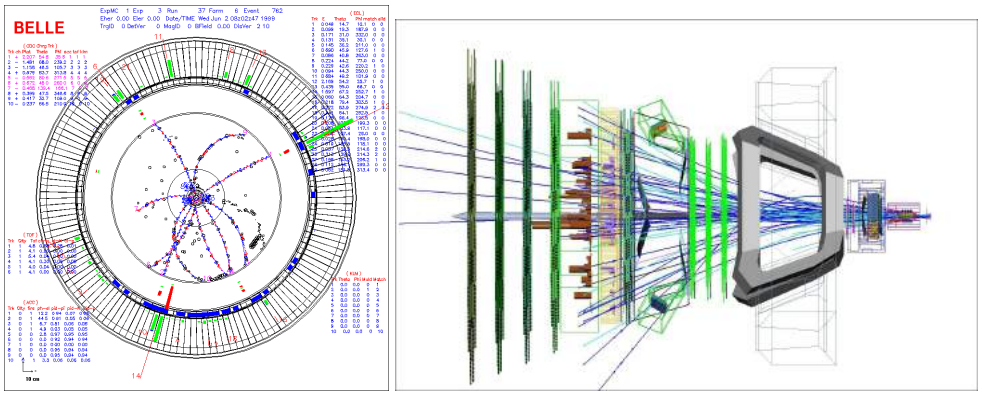

Figure 2.6: Comparison between a typical B event in a B factory (left, $r\phi$ view), as the Belle experiment, and in an hadron collider (right, zx plane), as the LHCb experiment.

- good tracking capability and excellent track momentum resolution along with a superb vertexing, required by the large amount of tracks produced in each event;

2.2.1 Charmless two-body B decays at CDF experiment

The Collider Detector at Fermilab (CDF) is one of the experiments located at the Tevatron particle collider. At the end of the 2014 CDF published a paper reporting the measurement of the direct CP-violating asymmetries in charmless decays of neutral b-hadrons to pairs of charged hadrons. The measurement was performed using the complete collisions data set collected at $\sqrt{s} = 1.96\,\text{TeV}$, corresponding to $9.3\,\text{fb}^{-1}$ of integrated luminosity. It was the first experiment to perform such a measurement in the B_s^0 decay modes: $B_s^0 \to \pi^+K^-$ and $B_s^0 \to K^+K^-$, which was observed for the very first time. The invariant mass distribution of the different $H_b \to h^+h'^-$ decays under the $\pi^+\pi^-$ hypothesis is shown in Figure 2.7. In this case both the b-mesons (B^0 and B_s^0) and the b-baryons (Λ_b^0) are taken into account allowing to obtain important results also in the b-baryons sector, whose CP properties are not yet well established. Their final results are reported in Table 2.4 [69]. The observation of CP violation in the $B_d^0 \to K^+\pi^-$ is confirmed with a significance larger than 5σ, while the $B_s^0 \to \pi^+K^-$ mode deviates from the no-CP violation hypothesis by a significance of 3σ. The measurements on the Λ_b^0 mode are compatible with no CP asymmetry.

2.2.2 Charmless two-body B decays at LHCb experiment

The LHCb experiment is one of the main experiments situated at one of the four points around CERN's Large Hadron Collider (LHC). The characteristics of both the LHC and LHCb experiment are extensively discussed in the next Chapter 3. The LHCb collaboration performed two measurements in the $B^0_{(d,s)} \to h^+h^-$ decays determining the time-integrated CP asymmetries in $B_d^0 \to K^+\pi^-$ and $B_s^0 \to \pi^+K^-$ modes [54], and the CP violation parameters in $B_d^0 \to \pi^+\pi^-$ and $B_s^0 \to K^+K^-$

Table 2.4: Final results for the direct *CP* asymmetry in $B_d^0 \to K^+\pi^-$, $B_s^0 \to \pi^+K^-$, $\Lambda_b^0 \to p\pi^-$, $\Lambda_b^0 \to pK^-$ [69].

Decay	A_{CP}
$B_d^0 \to K^+\pi^-$	$-0.083 \pm 0.013 \pm 0.004$
$B_s^0 \to \pi^+K^-$	$0.22 \pm 0.07 \pm 0.02$
$\Lambda_b^0 \to p\pi^-$	$0.06 \pm 0.07 \pm 0.03$
$\Lambda_b^0 \to pK^-$	$-0.10 \pm 0.08 \pm 0.04$

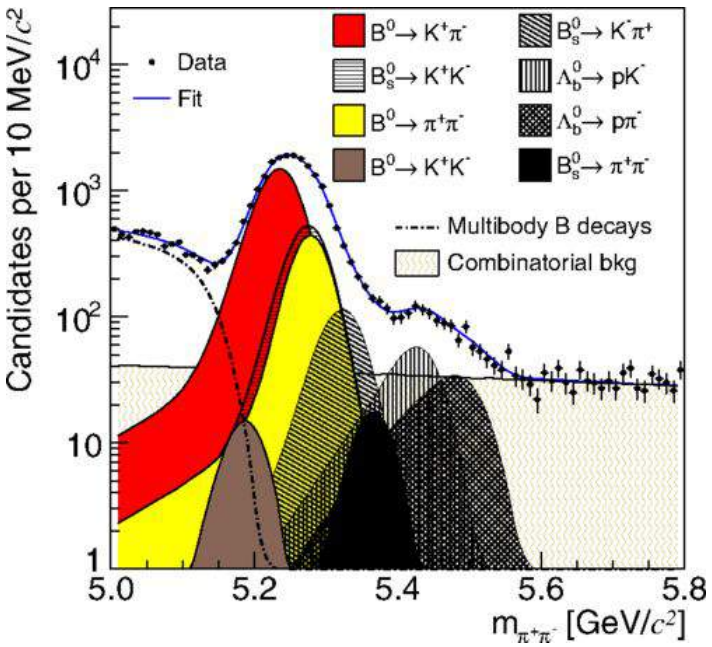

Figure 2.7: Invariant mass distribution of reconstructed candidates in CDF, where the charged pion mass is assigned to both tracks [69].

Table 2.5: Final results for the *CP* parameters in $B^0_d \to K^+\pi^-$, $B^0_s \to \pi^+K^-$, $B^0_d \to \pi^+\pi^-$ and $B^0_s \to K^+K^-$ decays [53, 54] obtained using a data sample collected by LHCb during 2011, corresponding to an integrated luminosity of 1 fb $^{-1}$. The first and the second quoted uncertainties are statistical and systematic, respectively.

Parameter	Value
$C_{\pi^+\pi^-}$	$-0.38 \pm 0.15 \pm 0.02$
$S_{\pi^+\pi^-}$	$-0.71 \pm 0.13 \pm 0.02$
$C_{K^+K^-}$	$0.14 \pm 0.11 \pm 0.03$
$S_{K^+K^-}$	$0.30 \pm 0.12 \pm 0.04$
$A_{CP}(B^0_d \to K^+\pi^-)$	$-0.080 \pm 0.007 \pm 0.003$
$A_{CP}(B^0_s \to \pi^+K^-)$	$0.27 \pm 0.04 \pm 0.01$

modes [53]. The latter measurement represented the first observation of *CP*-violating asymmetries in the $B^0_s \to K^+K^-$ decay. These two analyses were based on the data sample of pp collisions at a centre of mass energy of 7 TeV collected during the first part of the Run 1 data taking (2010-2011), corresponding to an integrated luminosity of 1.0 fb^{-1} The time-integrated asymmetry of the $B^0_d \to K^+\pi^-$ and $B^0_s \to \pi^+K^-$ decays determined from the fit (A_{raw}) does not correspond to the effective *CP* asymmetry (A_{CP}), but needs to be corrected for other nuisance asymmetries arising from experimental effects. These are the production asymmetry (A_P) and the detection asymmetry (A_D):

$$A_{raw}(t) \approx A_{CP} + A_D + A_P \cos(\Delta m_{d(s)} t) \tag{2.5}$$

On one hand the production asymmetry can be extracted directly from the fit along with the *CP* asymmetry. On the other hand the detection asymmetry is determined using high-statistics samples of Cabibbo-favoured decays of charmed mesons and taking into account the kinematic difference with respect to the B signals. The results are reported in Table 2.5 while the asymmetry plots are reported in Figures 2.8,2.9.

The measurement of A_{CP} for the $B^0_d \to K^+\pi^-$ and $B^0_s \to \pi^+K^-$ decay represented the most precise provided by single experiment with a significance exceeding the 10 standard deviation, and the first observation of *CP* violation in B^0_s system with a significance greater than 5 standard deviations, respectively. On the other hand, the measurement of the *CP* parameters for the $B^0_d \to \pi^+\pi^-$ and $B^0_s \to K^+K^-$ decays differed from the no *CP* violation hypothesis, i.e. $C = 0$ and $S = 0$, by 5.6 and 2.7 standard deviations, respectively. Also in this case the *CP* parameters related to the B^0_s meson were measured for the very first time.

The work presented in this thesis represents an update of these two analyses using the full Run 1 data taking and successively the data sample collected during the first part of the Run 2 data taking.

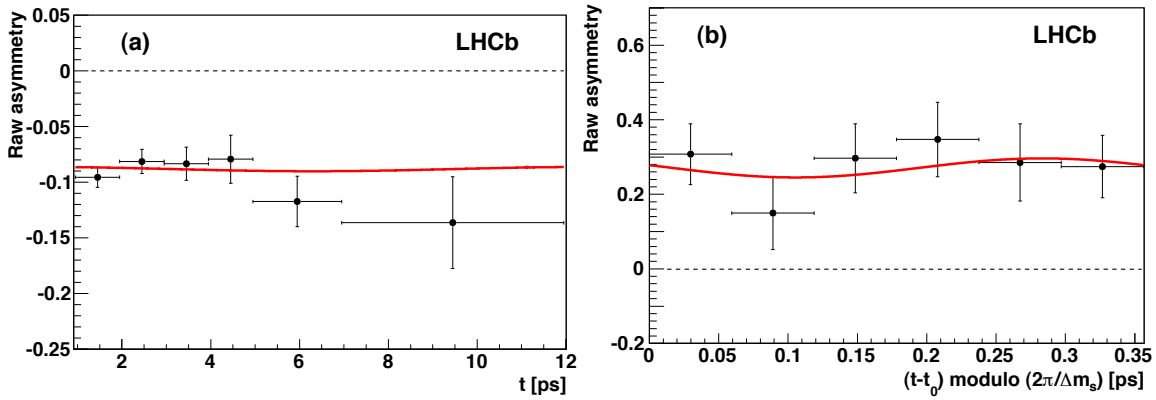

Figure 2.8: Raw asymmetries as a function of the decay-time for $B^0_d \to K^+\pi^-$ (left) and $B^0_s \to \pi^+K^-$ (right) decays [54], using data sample collected by LHCb in 2011, corresponding to an integrated luminosity of 1 fb^{-1}.

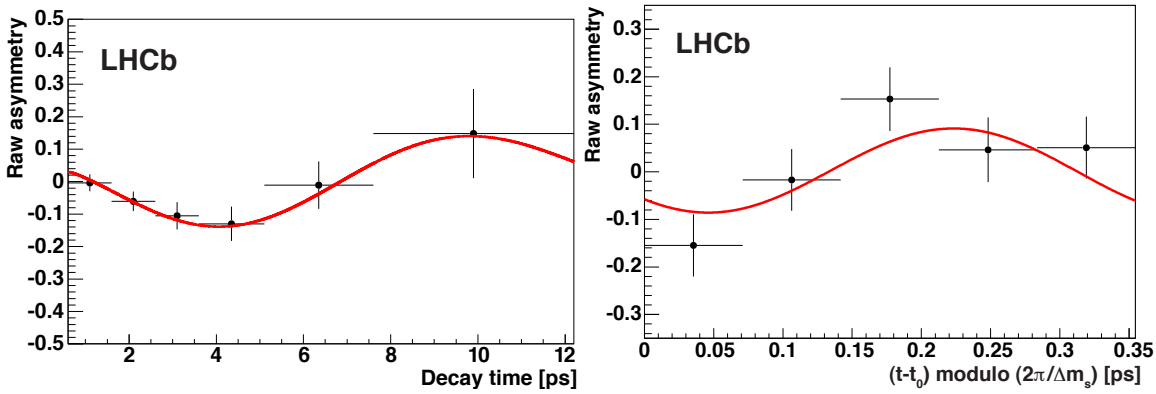

Figure 2.9: Time-dependent raw asymmetry of $B^0_d \to \pi^+\pi^-$ (left) and $B^0_s \to K^+K^-$ (right) decays [53] using data sample collected by LHCb in 2011, corresponding to an integrated luminosity of 1 fb^{-1}. In order to enhance the visibility of the oscillations only the tagging candidate with a mistag probability lower than 0.3 are used.

Table 2.6: Results for the *CP* parameters in $B^0_d \to \pi^+\pi^-$ and $B^0_s \to K^+K^-$ decays [70] obtained using the full Run 1 data sample, corresponding to an integrated luminosity of 3 fb $^{-1}$. The first and the second quoted uncertainties are statistical and systematic, respectively.

Parameter	Value
$C_{\pi^+\pi^-}$	$-0.24 \pm 0.07 \pm 0.01$
$S_{\pi^+\pi^-}$	$-0.68 \pm 0.06 \pm 0.01$
$C_{K^+K^-}$	$0.24 \pm 0.06 \pm 0.02$
$S_{K^+K^-}$	$0.22 \pm 0.06 \pm 0.02$
$A^{\Delta\Gamma}_{K^+K^-}$	$-0.75 \pm 0.07 \pm 0.11$

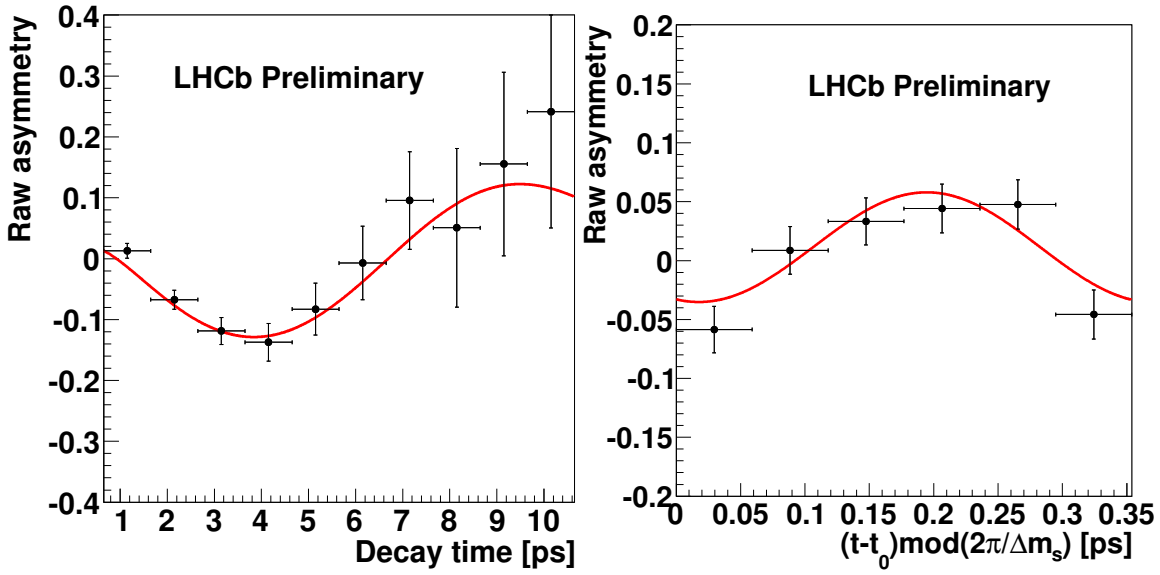

Figure 2.10: Time-dependent raw asymmetry of $B^0_d \to \pi^+\pi^-$ (left) and $B^0_s \to K^+K^-$ (right) decays [53] using data sample collected by LHCb during the Run 1, corresponding to an integrated luminosity of 3 fb^{-1}.

A preliminary update of the results obtained using the full Run 1 data sample was published as a conference note [70]. The detail related to this analysis will be discussed in the next chapters of this thesis. The results are shown in Table 2.6 while the raw asymmetries of $B^0_d \to \pi^+\pi^-$ and $B^0_s \to K^+K^-$ decays are shown in Figure 2.10.

Recently the LHCb collaboration published the results related to a measurement of *CP* violation in $\Lambda_b \to pK^-$ and $\Lambda_b \to p\pi^-$ decays. The analysis used the data sample collected by LHCb during the full Run 1 data taking, corresponding to an integrated luminosity of 3 fb^{-1}. The results, which represent the most precise measurement of such asymmetries to date, are reported in Table 2.7.

Table 2.7: Time integrated *CP* asymmetries in $\Lambda_b \to pK^-$ and $\Lambda_b \to p\pi^-$ decays [60] obtained using the full Run 1 data sample, corresponding to an integrated luminosity of 3 fb^{-1}. The first and the second quoted uncertainties are statistical and systematic, respectively.

Parameter	Value
$A_{CP}(\Lambda_b \to pK^-)$	$-0.020 \pm 0.013 \pm 0.019$
$A_{CP}(\Lambda_b \to p\pi^-)$	$-0.035 \pm 0.017 \pm 0.020$

Table 2.8: Status of art of the *CP* asymmetries of $B \to h^+h'^-$ decays.

Observable	BaBar [62]	Belle [63, 64]	CDF [69]	LHCb [53, 54]	HFLAV average [71]
$C_{\pi^+\pi^-}$	-0.25 ± 0.08	-0.33 ± 0.07	-	-0.24 ± 0.07	-0.27 ± 0.04
$S_{\pi^+\pi^-}$	-0.68 ± 0.10	-0.64 ± 0.09	-	-0.68 ± 0.06	-0.68 ± 0.04
$C_{K^+K^-}$	-	-	-	0.24 ± 0.06	-
$S_{K^+K^-}$	-	-	-	0.22 ± 0.06	-
$A^{\Delta\Gamma}_{K^+K^-}$	-	-	-	-0.75 ± 0.13	-
$A^{CP}_{B^0 \to K^+\pi^-}$	-0.107 ± 0.017	-0.069 ± 0.016	-0.083 ± 0.014	-0.080 ± 0.008	-0.082 ± 0.006
$A^{CP}_{B^0_s \to \pi^+K^-}$	-	-	0.22 ± 0.07	0.27 ± 0.04	0.26 ± 0.04

2.3 World Average Results

The World Average Results, performed by the Heavy Flavour Averaging Group (HFLAV), regarding the *CP* violation asymmetries in charmless charged *B*-meson decays are presented in this section. The value are obtained combining the results of the measurements discussed in the previous section provided by BaBar, Belle, CDF and LHCb experiment [71]. A summary of the *CP*-violating asymmetries and the average value obtained by HFLAV are reported in Table 2.8.

A representation of the time-dependent *CP* asymmetries for the $B^0 \to \pi^+\pi^-$ decay is shown in Figure 2.11 while in Figure 2.12 the HFLAV average of $C_{\pi^+\pi^-}$ and $S_{\pi^+\pi^-}$ is shown.

For sake of completeness, the branching fraction measurements, obtained by the BaBar, Belle, CLEO, CDF and LHCb experiments, of the different $H_b \to h^+h'^-$ modes are reported, along with the HFLAV average, in Table 2.9.

2.4 Extraction of the *CKM* phases

As introduced in Section 1.5.2, the *U*-spin creates pairs in $H_b \to h^+h'^-$ decays related to the exchange of $d \leftrightarrow s$ quark. Exploiting the *U*-spin symmetry it is possible to extract the *UT* angle β and γ from

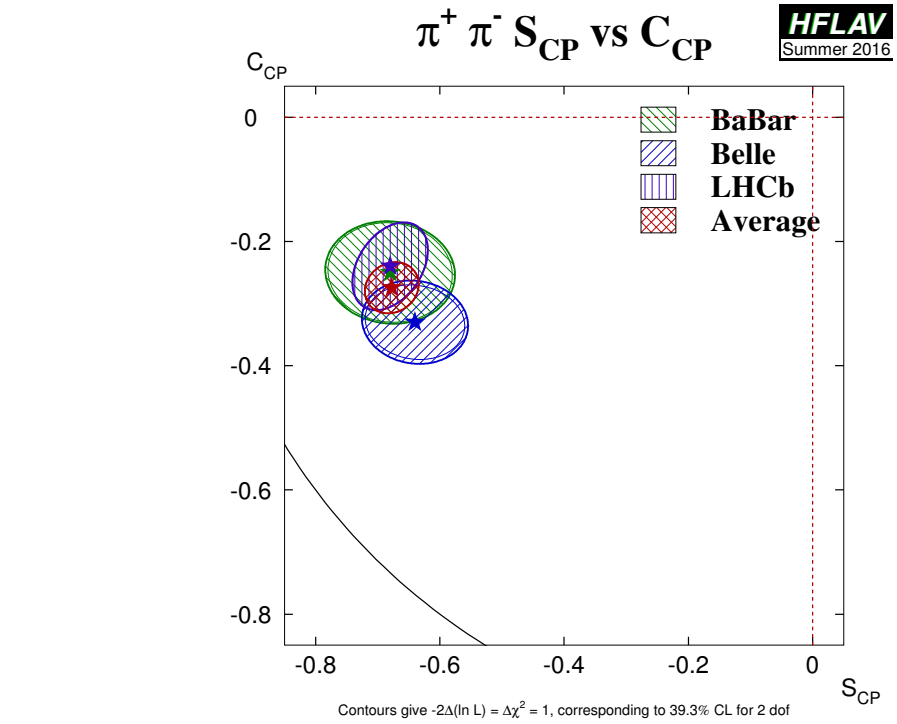

Figure 2.11: Representation of the direct and mixed-induced *CP* parameters for the $B^0 \to \pi^+\pi^-$ decay [71].

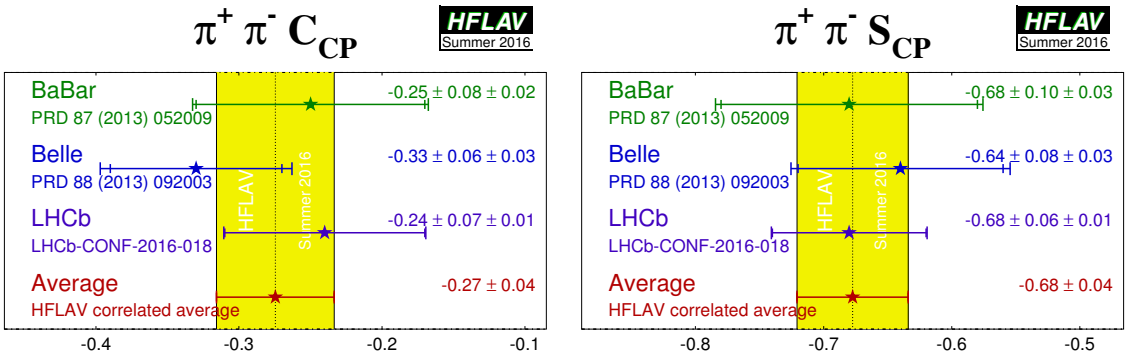

Figure 2.12: HFLAV average of the *CP* violation parameters in $B^0 \to \pi^+\pi^-$ decay [71].

Table 2.9: Branching fractions measurements for all $H_b \to h^+h'^-$ decays in unit of 10^{-6} [71].

Decay	BaBar	Belle	CLEO	CDF	LHCb	HFLAV average
$B^0 \to \pi^+\pi^-$	$5.5 \pm 0.4 \pm 0.3$	$5.04 \pm 0.21 \pm 0.18$	$4.5^{+1.4+0.5}_{-1.2-0.4}$	$5.02 \pm 0.33 \pm 0.35$	$5.08 \pm 0.17 \pm 0.37$	5.10 ± 0.19
$B^0 \to K^+\pi^-$	$19.1 \pm 0.6 \pm 0.6$	$20.0 \pm 0.34 \pm 0.60$	$18^{+2.3+1.2}_{-2.1-0.9}$	-	-	$19.57^{0.53}_{0.52}$
$B^0 \to K^+K^-$	< 0.5	$0.10 \pm 0.08 \pm 0.04$	-	$0.23 \pm 0.10 \pm 0.10$	$0.0780 \pm 0.0127 \pm 0.0084$	0.0803 ± 0.0147
$B_s^0 \to K^+K^-$	-	$38^{+10}_{-9} \pm 7$	-	$25.9 \pm 2.2 \pm 1.7$	$23.7 \pm 1.6 \pm 1.5$	24.8 ± 1.7
$B_s^0 \to \pi^+K^-$	-	< 26	-	$5.3 \pm 0.9 \pm 0.3$	$5.6 \pm 0.6 \pm 0.3$	5.5 ± 0.5
$B_s^0 \to \pi^+\pi^-$	-	< 12	-	$0.60 \pm 0.17 \pm 0.04$	$0.691 \pm 0.083 \pm 0.44$	0.671 ± 0.083
$\Lambda_b^0 \to p\pi^-$	-	-	-	$3.5 \pm 0.6 \pm 0.9$	-	3.5 ± 1.1
$\Lambda_b^0 \to pK^-$	-	-	-	$5.6 \pm 0.8 \pm 1.5$	-	5.6 ± 1.7

the time-evolution of the $B^0 \to \pi^+\pi^-$ and $B_s^0 \to K^+K^-$ [42, 55]. The strength of this method lies in being completely independent from any model or dynamical assumptions and in using the penguin topologies which makes the result accuracy affected only on the U-spin breaking corrections and by the presence of the penguin topologies them self. Taking into account the CP asymmetries A^{dir} and A^{mix} in Equations 1.93, 1.95 it is possible to create a system of four equations with seven unknowns: $d, \theta, \gamma, \phi_d, d', \theta'$ and ϕ_s. The assumption of the U-spin symmetry can be expressed with the following relations:

$$\theta = \theta' \qquad\qquad d = d' \tag{2.6}$$

which reduce the number of system unknowns to five. A further simplification of the system can be achieved excluding ϕ_d and ϕ_s from the list of the unknowns. This exclusion is reasonable because ϕ_d has been measured with high precision by both B factories and LHCb [19, 72] and because the SM foresees a very small value for ϕ_s. Thus the system, being constituted by three unknowns in four equations, become completely solvable. Still, it is also possible to provide a measurement of ϕ_s thanks to the additional equation. An important reason for measuring ϕ_s is that combining this measurement with the one obtained on the $B_s^0 \to J/\psi\phi$ decay allows an unambiguous determination of the ϕ_s value between $\phi_s = 0°$ and $\phi_s = 180°$. This determination is of great importance for the search of New Physics as stated in [55]. Finally the three remaining parameters d, θ and γ can be extracted simultaneously from a joint p.d.f making use of a Bayesian approach, as performed by the UTFit and CKMFitter collaborations.

However, fully rely on the U-spin symmetry is not possible since large non-factorizable U-spin breaking effects could play an important role. The first insight of U-spin breaking effects were obtained through the charge asymmetries and branching ratio of the U-spin pair formed by $B^0 \to K^+\pi^-$ and $B_s^0 \to \pi^+K^-$. Applying the U-spin symmetry to this decay pair leads to:

$$r = r_s \qquad\qquad \delta = \delta_s \tag{2.7}$$

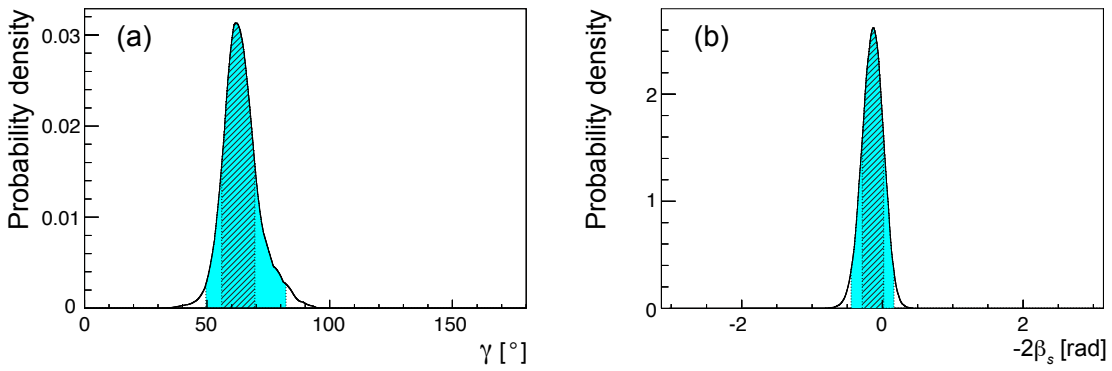

Figure 2.13: Distribution of γ (a) and $-2\beta_s$ (b) corresponding to an amount of non-factorizable U-spin breaking up to 50% [73]. The dashed and filled areas correspond to the 68% and 95% of probability intervals.

Table 2.10: Results of γ and $-2\beta_s$ obtained by the LHCb collaboration considering an amount of non-factorizable U-spin breaking up to 50% [73].

Quantity	68% prob.	95% prob.
γ	$[56°, 70°]$	$[49°, 82°]$
$-2\beta_s$	$[-0.28, 0.02]$	$[-0.44, 0.17]$

and

$$\frac{A^{CP}_{\pi^+K^-}}{A^{CP}_{K^+\pi^-}} = \left|\frac{P_s}{P}\right|^2 \frac{BR(B^0_d \to K^+\pi^-)}{BR(B^0_s \to \pi^+K^-)}. \tag{2.8}$$

Experimental insight of U-spin breaking effects can be obtain writing:

$$\left|\frac{P_s}{P}\right|_{\text{exp}} = \left|\frac{P_s}{P}\right| \sqrt{\frac{r_s}{r}\frac{\sin\delta_s}{\sin\delta}} = 1.06 \pm 0.28 \tag{2.9}$$

which is in good agreement with the theoretical results obtained with the QCD sum-rules:

$$\left|\frac{P_s}{P}\right|_{\text{QCDSR}} = 1.02^{+0.11}_{-0.10}. \tag{2.10}$$

The experimental error is still quite large, however the LHCb measurements should be able to improve it providing a more stringent result.

The LHCb collaboration provided a measurement of γ and $\phi_s = -2\beta_s$ using the $B^0 \to \pi^+\pi^-$ and $B^0_s \to K^+K^-$ decays. The results, assuming an amount of non-factorizable U-spin breaking up to 50%, are reported in Table 2.10. This measurement uses as starting point the results shown in Table 2.8. The relative distributions are shown in Figure 2.13 [73] while in Figure 2.14 is shown the dependence of the phases γ and $2\beta_s$ on the amount of non-factorizable U-spin breaking.

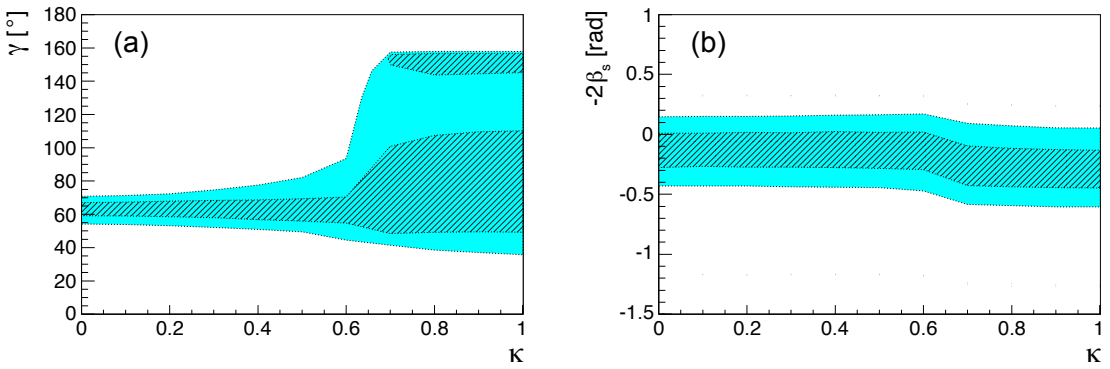

Figure 2.14: Dependence of the 68% (dashed area) and of 95% (filled area) probability intervals on the amount of non-factorizable U-spin breaking for γ (a) and $-2\beta_s$ (b) [73].

3

LHC collider and LHCb experiment

LHCb is one of the four large experiments located at the Large Hadron Collider (LHC) at CERN, the European Organization fro Nuclear Research, and it is designed to performance precision measurement of b- and c- hadron decays. This chapter is meant to give a brief description of the LHCb experiment, focusing on the information needed to understand the main experimental challenges of the CP violation measurement at LHCb. The first section provides a short description of the LHC accelerator, then the b quark and B meson production mechanisms are described. Finally the LHCb detector and all the facilities needed to achieve its physics program are discussed.

3.1 The Large Hadron Collider

The LHC [74] is a ring-hadron accelerator and collider consisting of two parallel beam pipes where protons and ions travel close to the speed of light. The two beams, travelling in opposite directions, collide in four different points where the detectors of the various experiments are located. The ring is located at 100 m underground inside the 27 km long Large Electron-Positron collider (LEP) tunnel, near the Geneva area. A graphical view of the LHC ring position is presented in Figure 3.1. The machine has been built to collide protons up to a center-of-mass energy of 14 TeV with an instantaneous luminosity of $10^{34}\,\mathrm{cm}^{-2}\,\mathrm{s}^{-1}$ and heavy ions ($Pb - Pb$) with an energy of 2.8 TeV per nucleon at a luminosity of $10^{27}\,\mathrm{cm}^{-2}\,\mathrm{s}^{-1}$. Protons are collected ionizing hydrogen atoms and removing their electrons. At the nominal regime the LHC will store 2808 proton bunches per ring, each of them containing $1.1 \cdot 10^{11}$ protons and colliding with a frequency of 40 MHz. Since accelerating a particle from the quasi-rest condition up to 7 TeV is not possible, the acceleration process of protons and ions occurs in various steps. The acceleration chain makes use of four pre-accelerators: the linear accelerator Linac2, the Proton Synchrotron Booster (PBS), the Proton Synchrotron (PS) and the Super Proton Synchrotron (SPS). In this way the protons are collected in bunches of 50 MeV energy by Linac2 before to be passed to the PBS. The PBS raises their energy up to 1 GeV and injects the

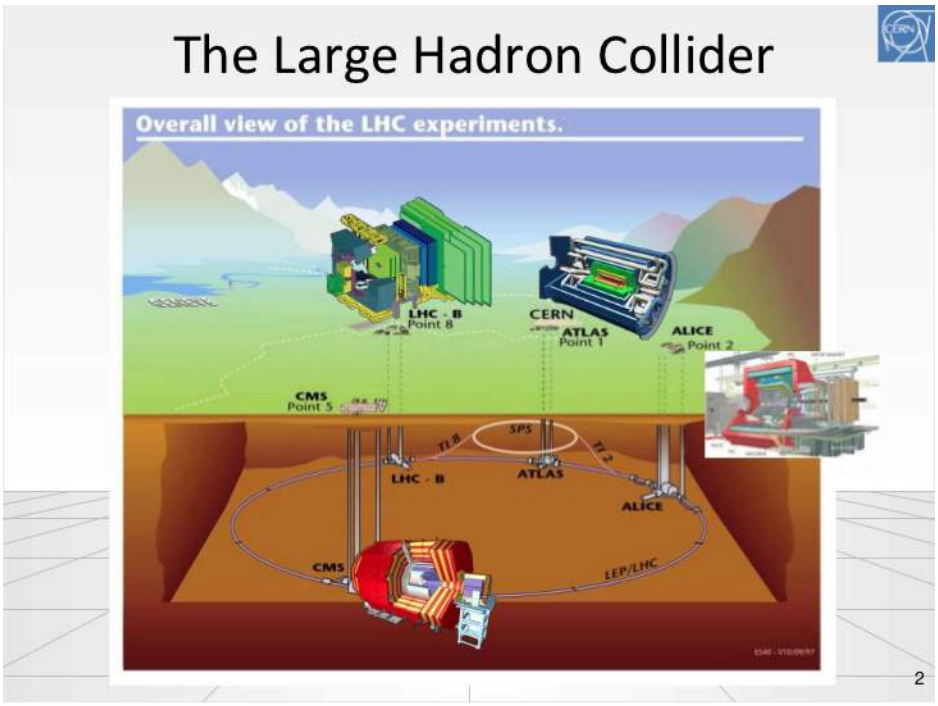

Figure 3.1: Graphical view of the LHC ring position.

protons into the PS. Successively the protons are accelerated up to 26 GeV and 450 GeV by the ps and SPS, respectively. Finally the protons are injected into the main LHC ring by means of two tunnels located near the ALICE and LHCb experiments. Once the protons have reached the main ring they are further accelerated up to the nominal energy of 7 TeV. A schematic view of the complex of CERN's accelerators are shown in Figure 3.2. In order to maintain a circular path inside the ring the protons are bended by a magnetic field of single dipole with a magnitude which can vary from 0.53 T up to 8.34 T. Such magnitude can be reached only using super-conducting dipole magnets working at a temperature of 1.9K (-271.25°C). This temperature is kept by means of approximately 96 tons of liquid helium, which makes LHC the largest cryogenic facility in the world at the liquid helium temperature.

The LHC collider represents one of the most important technological challenges ever made and the status-of-art of particle accelerators to date.

3.1.1 LHC experiments

The LHC hosts many different experiments which differ in geometry, composition and physics program. They are listed in the following and for each one of them a brief description is provided.

- **ALICE**: A Large Ion Collider Experiment [75], is a detector designed to study the properties of the matter in particular phase called Quark Gluon Plasma. This state is characterized by incredibly high temperature and density, compatible with the ones in the very early stages

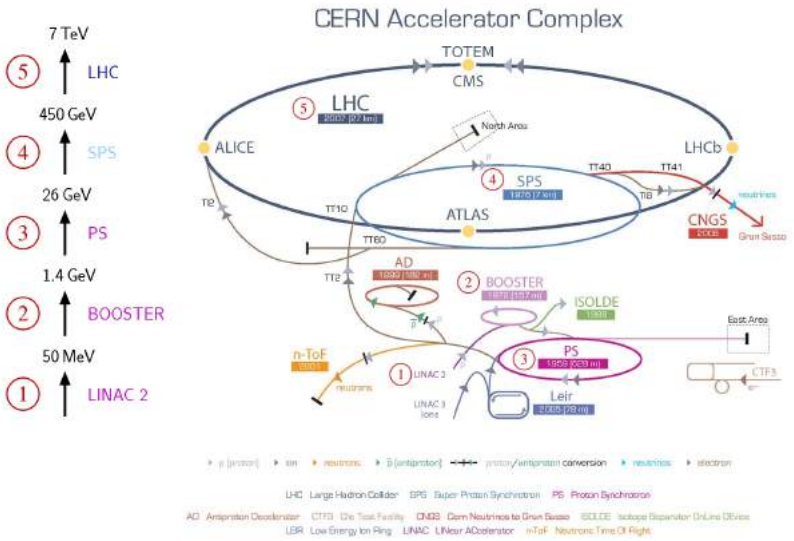

Figure 3.2: Schematic view of the complex of CERN's accelerators. The linear accelerator Linac2, the Proton Synchrotron Booster (PBS), the Proton Synchrotron (ps), the Super Proton Synchrotron (SPS) and LHC accelerators are shown. The two tunnels for the beam injection into the LHC are also shown, namely TI2 (near the ALICE experiment) and TI8 (near the LHCb experiment).

of our Universe. It is the only experiment at LHC nominally designed to deal with lead-lead collisions.

- **ATLAS**: A Toroidal LHC Apparatus [76], is a general purpose detector characterized by a cylindrical geometry around the beam-line. The aim of this experiment is the detection of new particles, beyond the Standard Model, at the TeV scale. Thus the whole detector has been designed to reconstruct high energy objects with a high accuracy. The word "Toroidal" in the ATLAS name refers to the magnetic field used in the experiment which is generated by three sets of air-core toroids complemented by a solenoid in the inner region.

- **CMS**: Compact Muon Solenoid [77], is a general purpose detector similar to ATLAS. The goal of the experiment is the discovery of new particles at the TeV scale and also in this case the designed geometry is cylindrical around the beam-pipe. One of the main difference with respect to ATLAS is the magnetic field, which is generated by a superconducting solenoid placed in an outer region.

- **LHCb**: is the experiment dedicated to the study of the heavy flavour quark physics, in particular the hadrons containing b quark [78]. It will extensively discussed in the Section 3.2.

- **LHCf**: Large Hadron Collider forward [79], is a detector located near to ATLAS. Its goal consists in the study of diffractive physics occurring in the forward region of the pp collisions, i.e.

the region described by a very small angle from the beam-line. For this reason the detector is placed around 140 m away with respect to the interaction point allowing to the decay products of the forward elastic collisions to exit from the beam-pipe.

- **MoEDAL**: Monopole and Exotics Detector at the Large Hadron Collider [80], is a passive detector specialized in the search of magnetic monopoles or dyons and highly ionizing stable and pseudo-stable massive particles. It is located in the same cavern of the LHCb experiment and consists of plastical nuclear track detectors attached to the walls of the LHCb vertex locator.
- **TOTEM**: Total Elastic and diffractive cross-section Measurement [81], is a detector located near to CMS. Its aim is the same as the LHCf experiment as well as its design and geometry.

3.1.2 LHC performance

The LHC performance can be evaluated by means of two figures of merit: beam energy and luminosity. The energy available for the production of new physics effects is the most important parameter to be taken into account. The only way to provide the large required centre-of-mass energy consists in colliding two beams where little or no energy is lost in the motion of the centre of mass system. On the other hand, the number of useful interactions (i.e. the events) is also very important, especially when rare events with a small cross-section (σ) are studied. The luminosity information quantify the ability of a particle accelerator to produce the required number of interactions and can be evaluated as:

$$\frac{dN}{dt} = L \cdot \sigma \tag{3.1}$$

where dN/dt represents the number of collisions per time unit, L indicates the instantaneous luminosity and σ is the cross-section of the process considered. The luminosity depends on the beam parameters and, assuming a Gaussian beam distribution, can be expressed as:

$$L = \frac{N_b^2 n_b f_{rev} \gamma_r}{4\pi\epsilon_n \beta^*} F \tag{3.2}$$

where N_b is the number of proton per bunch, n_b represents the number of bunches per beam, f_{rev} is the revolution frequency, γ_r indicates the relativistic gamma factor, ϵ_n is the normalized transverse beam emittance, β^* is the beta function at the collision point and F is the geometrical luminosity reduction factor due to the crossing angle at the interaction point. The β function is a related to the transverse size of the beam along the trajectory. The parameter β^* indicates the value of the β function at the collision point and it is used to quantify how much the beam is squeezed at the interaction point. The beam emittance represents the average spread of the particles in momentum and position phase-space, for example in a low emittance beam the protons have nearly the same momentum and are confined into a very small area. The evolution of the instantaneous luminosity

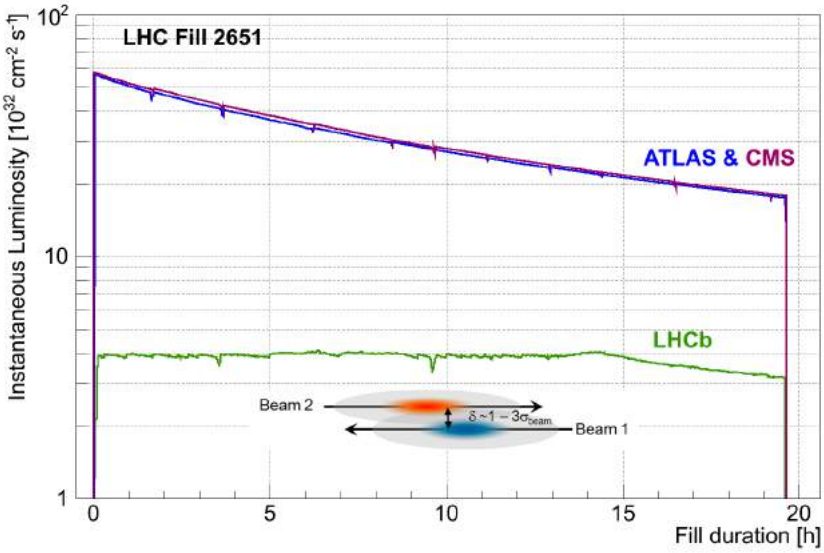

Figure 3.3: Comparison of the evolution of the instantaneous luminosity for ATLAS, CMS and LHCb during a LHC fill. Once the the desired value is reached, the instantaneous luminosity is kept constant at LHCb in a range of 5% thanks to an adjustment of the transversal beam overlap. The different behaviour between the three experiment at the end of the fill is due to differences in focusing procedure at the interaction point, named β^* [82].

during a LHC fill is shown in Figure 3.3, where the luminosity for ATLAS, CMS and LHCb are compared [82]. Integrating the instantaneous luminosity the total amount of useful events can be obtained:

$$L = \int L dt. \tag{3.3}$$

3.1.3 LHC data-taking

At the LHC collider, periods of data taking and long shut-downs are alternated. During the former ones the event information are actually stored while in the latter ones the detector and accelerator maintenance and upgrade are performed. The first phase of data-taking, namely Run 1, started in 2010 and was concluded in 2012. The nominal centre-of-mass energy was $\sqrt{s} = 7$ TeV and $\sqrt{s} = 8$ TeV during the 2011 and 2012, respectively. During the Run 1 period the LHCb collaboration collected a data-sample of pp collisions equivalent to an integrated luminosity of 3 fb^{-1}. In the period between the 2013 and 2015 the first long shut-down took place, where many improvements were performed to allow the detectors to be ready for the next LHC collisions at 14 TeV. The second data-taking period, named Run 2, started in 2015 and will be concluded at the end of 2018. In this period the nominal centre-of-mass energy is set to $\sqrt{s} = 13$ TeV and the LHCb collaboration expects to collect a data-sample of pp collisions corresponding to an integrated luminosity of 6 fb^{-1}.

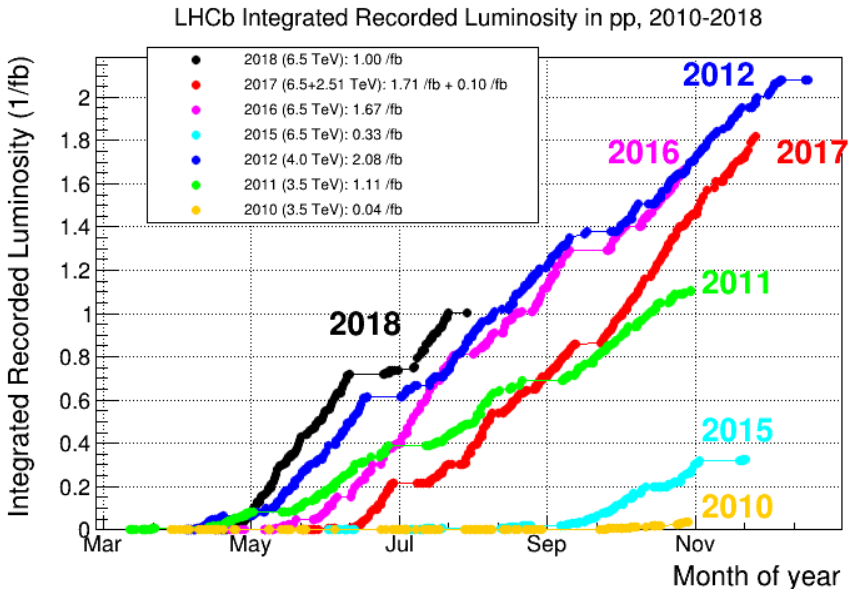

Figure 3.4: Integrated luminosity at LHCb during Run 1 and Run 2. The plot shows the curves for the recorded integrated luminosity for the different data-taking years [83].

The luminosity collected by the LHCb experiment during both Run 1 and Run 2 period is shown in Figure 3.4.

3.2 LHCb experiment

The LHC design is such as the two proton beams are bent to collide with each other with a crossing-angle at the four interaction points. In order to maximize the number of collisions, a dedicated string of three quadrupole magnets is used to achieve a low value of the β function. The main difference between the LHCb machine and the other experiments is the shifted collision point. The interaction point and the focusing quadrupoles are displaced by $3\lambda_{RF}/2$ ($\sim 11.22\,\mathrm{m}$) in order to accommodate the single arm spectrometer, described in Section 3.3, in the existing hall. This shift has some implications on the beam-beam effects [84]. In addition the LHCb experiment has a dipole magnet (discussed in Section 3.3.1) whose polarity can be reversed. This further magnetic field causes a difference in the beam crossing angles for the two magnet polarities, complicating the optics of the collider at the interaction point. As shown in Figure 3.3, the instantaneous luminosity is kept approximately constant during a unique LHC fill despite of the decaying intensity of the two beams. This effect is obtained through a *luminosity levelling* technique which, adjusting dynamically the LHCb optics, shifts the beams with respect to each other to fulfil the luminosity requirements. Nominally, the LHCb detector has been designed to deal with an average instantaneous luminosity of $2 \cdot 10^{32}\,\mathrm{cm}^{-2}\,\mathrm{s}^{-1}$ and a peak luminosity of $5 \cdot 10^{32}\,\mathrm{cm}^{-2}\,\mathrm{s}^{-1}$, assuming a centre-of-mass energy of

$\sqrt{s} = 14\,\text{TeV}$. The reason why the LHCb luminosity is lower than the nominal one, delivered by the LHC and exploited by CMS and ATLAS experiments, lies in three points. Firstly, the forward region, on which the LHCb is focused, is characterized by high occupancies in the detectors due to the high flux of particles. In the second place, the LHCb experiment is specialized in the study of b and c hadron decays, thus the ability to correctly identify the primary vertex among all the other vertices in the event is fundamental for many analysis. Having a high luminosity means increasing the number of collisions and consequently having to deal with a large number of pile-up vertices that would make this distinction much more difficult. Finally, the high occupancy in the tracking detectors (discussed in Section 3.3.1) results in a degradation of their track reconstruction efficiency. Thus the luminosity required by LHCb represents a balance between these three effects and the need to have large statistics samples to perform high precision measurements.

3.2.1 b quark production in pp collisions

When the pp collisions occur the interaction between the two partons produces $b\bar{b}$ pairs, since the strong interactions are flavour conserving. The leading order (LO) of the $b\bar{b}$ creation processes are the quark-antiquark annihilation, $q\bar{q} \rightarrow b\bar{b}$, and gluon-gluon fusion, $gg \rightarrow b\bar{b}$. At the next-to leading order (NLO) also the gluon-splitting and flavour-excitation processes become significant. The contributions from pair gluon-fusion, flavour-excitation and gluon-splitting to the total b cross-section as function of the center-of-mass energy E_{CM} are shown in Figure 3.5. Since the $b\bar{b}$ creation threshold is small with respect to the center-of-mass energy of LHC, the favourite production mechanisms turns out to be the gluon-gluon fusion, as shown in the right plot in Figure 3.5.

Since the $b\bar{b}$ production threshold is very small, if compared to the center-of-mass energy of LHC, the partons contained into the two colliding protons can have very different momenta. This implies that the $b\bar{b}$ pairs originated as products are often produced with a large boost and tend to fly along the beam axis. In addition, there is a strong correlation between the b and the $\bar{b}$ quark which makes the pair production oriented along forward and backward direction. This effect is clearly visible looking at the polar angle distribution of the $b\bar{b}$ production, shown in Figure 3.6, and it explains the forward design chosen for the LHCb experiment. In particular the LHCb geometrical acceptance lies between 10 and 300 mrad in the horizontal plane and between 10 and 250 mrad in the vertical plane. The range of pseudo-rapidity[1] (η) for the particles within the LHCb geometrical acceptance

[1]The rapidity is defined as $y = \frac{1}{2}\ln\left(\frac{E+p_z c}{E-p_z c}\right)$, where the z-axis lies along the beam line. The pseudo-rapidity, η, is a more widely-used parameter defined as

$$\eta = -\ln\left(\tan\frac{\theta}{2}\right) = \frac{1}{2}\ln\left(\frac{|\vec{p}| + p_L}{|\vec{p}| - p_L}\right). \tag{3.4}$$

Can be demonstrated that in the limit where the particle is travelling close to the speed of light, or in the approximation that the mass of the particle is negligible, the pseudorapidity converges to the rapidity definition.

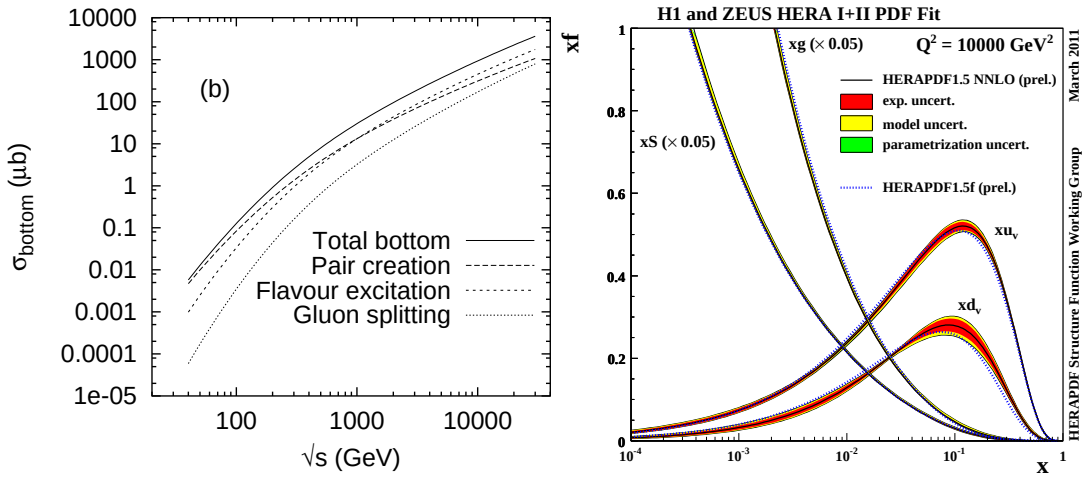

Figure 3.5: On the left, the total b cross-section as function of $E_{CM} = \sqrt{s}$ is shown. The contributions from pair gluon-fusion, flavour-excitation and gluon-splitting are shown separately [85]. On the right, the parton distribution functions from HERAPDF1.5 NNLO and HERAPDF1.0 NNLO at a relevant region for the hadron colliders, Tevatron and LHC ($Q^2 = 10000\,\text{GeV}^2$), are shown. The sea and gluon distributions are scaled down by a factor 20. The experimental, model and parametrization uncertainties are shown separately [86].

is restricted between 1.8 and 4.9.

The b and $\overline{b}$ quarks generated through the processes discussed in the previous section, create bound-state with lighter quark and antiquark constituting hadrons. This process, due to the color confinement, is known as *hadronization*. The lighter quarks/antiquarks can come from the proton remnants or from the fragmentation process in the initial interaction. Since the LHC is a pp collider and the generated hadrons depend on the quarks of the proton remnants of the fragmentation process, a hadron production asymmetry with the respect to the antihadrons is expected. A generated b quark can more likely combine with lighter quarks forming heavy baryons than a $\overline{b}$ antiquark with other lighter antiquarks. On the other hand it will be more easily for a $\overline{b}$ antiquark hadronizing into a meson, creating a bounding-state with a lighter quark, with respect to a b quark hadronizing into a antimeson.

In addition to this effect, another source of production asymmetry can arise from the soft-QCD process involved into the hadronization. A phenomenological model, describing the hadronization process, is the "Lund string model" which describes the color flow in the process through strings formed by self-interacting gluons [85]. In particular two different sources of meson-antimeson production asymmetry can be distinguished: a collapse to a B^0 meson at high p_T [88], which occurs when a $\overline{b}$ antiquark produced in a $b\overline{b}$ pair and a scattered valence quark from a proton interact together, and the beam drag effect[89]. The currently used event generators, as PYTHIA [90], are based on this model. In LHCb the hadron production asymmetry effect is expected to be at the per-

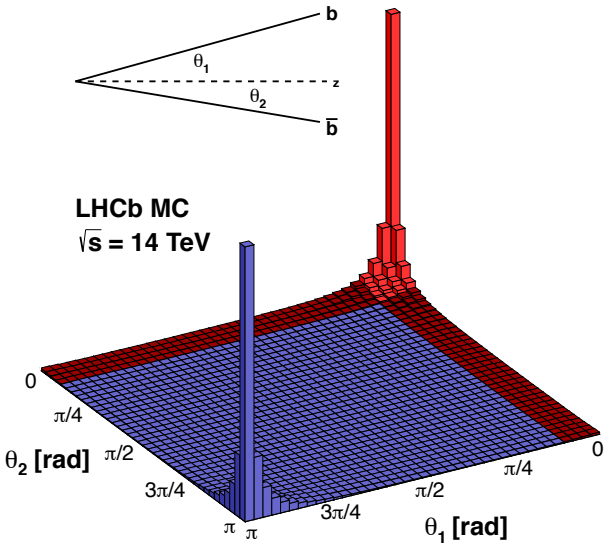

Figure 3.6: Polar angle distribution of $b\bar{b}$ production. The beam line lies on the z-axis and the red area represents the LHCb acceptance [87].

cent level, turning to be a crucial effect competitive with the *CP* violating asymmetries. Therefore, it is very important to measure with high precision this kind of asymmetries at LHCb, providing also the results as input for the theoretical models in order to obtain more accurate predictions.

3.3 LHCb detector

The LHCb experiment [78, 82] is housed in the same cavern where DELPHI [91] experiment at LEP is located. It is designed as a single arm spectrometer with a forward angular coverage in order to reconstruct a large fraction of produced particles coming from b and $\bar{b}$ quark hadronization while covering a small solid angle, as shown in Figure 3.6. The geometrical acceptance covers approximately the range from 10 mrad to 300 and 250 mrad in the horizontal and vertical plane, respectively. The difference in acceptance between the horizontal and vertical plane is due to the fact that the horizontal plane represents also the bending plane for charged particles, deflected by the LHCb dipole magnetic field. LHCb exploits a coordinate system in which the z-axis lies along the beam line, where the positive direction points from the collision point to muon system, the y-axis is perpendicular to LHC tunnel and oriented from the interaction point to the surface while the x-coordinate complete the right-handed coordinate system. The LHCb detector is organized in three parts: *the track reconstruction system*, *the particle identification system* and the *trigger system*. Each of these parts consists of multiple sub-detectors. A complete overview of the LHCb detector is shown in Figure 3.7 where the

various sub-detectors are visible:

- **VELO**: the Vertex Locator is located in the inner part of the detector close to the interaction region and provides the information necessary to reconstruct primary and secondary vertices and impact parameters of the particles;
- **RICH1**: the first Ring Imaging Cherenkov detector is located just after the VELO, providing useful information for the charged particle identification;
- **TT**: the Tracker Turicensis is the first tracking system;
- **Magnet**: the dipole magnetic field used to bend the particle, evaluating their charge and momentum;
- **T1-T3**: the three tracking stations located beyond the magnetic field;
- **RICH2**: the second Ring Imaging Cherenkov detector, with the same aim as RICH1 but in a different momentum range;
- **ECAL**: the Electromagnetic Calorimeter system, used for an efficient trigger and identification of electrons and photons;
- **HCAL**: the Hadronic Calorimeter, providing information useful for the hadronic trigger;
- **SPD and PS**: the Scintillating Pad Detector and the Pre-Shower detector, which assist the two calorimeters;
- **M1-M5**: the five Muon Stations placed in the outer part of the detector which can be reached only by muons, since all other particles will be stopped by the calorimeters or other absorbers. It is used for muon identification and for an efficient trigger of decays with muons in the final state.

The complex set of sub-detectors, which will be briefly described in the next sections, composing the LHCb detector is fundamental to let the LHCb experiment to fulfil its physics program. Indeed the broad program needs to some important requirements in order to be efficiently completed.

- The analyses based on leptonic B decay require an excellent identification of electrons and muons, as well as the analyses based on hadronic B decay require an optimal discrimination between charged hadrons (pions, kaons and protons).
- The momentum of the charged particles have to be measured with high precision ($\sim 10^{-3}$) in order to obtain a resolution on the invariant mass sufficiently small to identify the signals among the combinatorial background sources and to distinguish between B and B_s^0 decays.

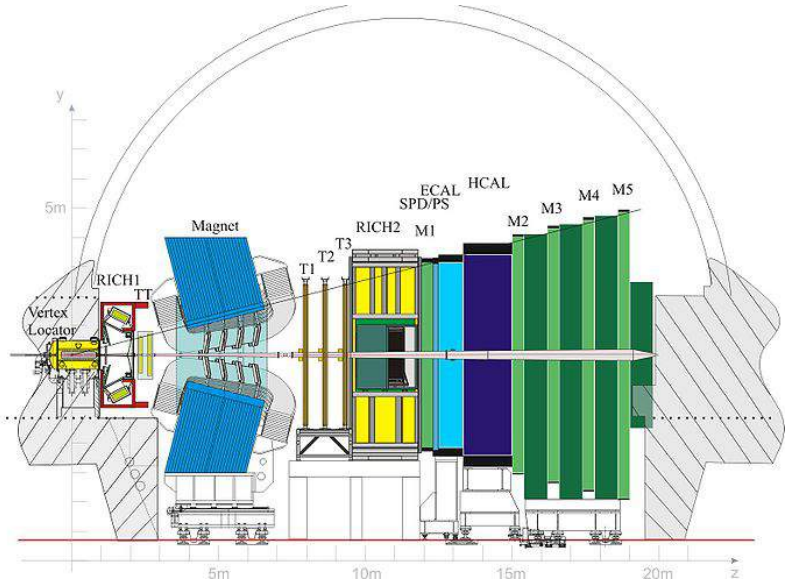

Figure 3.6: The LHCb detector

Figure 3.7: View of the LHCb detector. The various sub-detectors are visible: the Vertex Locator (VELO), the first Rich Imaging Cherenkov (RICH1), the Tracker Turicensis (TT), the dipole Magnet, the three tracking stations (T1-T3), the second Ring Imaging Cherenkov (RICH2), the Electromagnetic Calorimeter (ECAL), the Hadron Calorimeter (HCAL), the Scintillating Pad Detector (SPD) and the Pre-Shower detector (PS), and the Muon Stations (M1-M5).

- Since the major part of the LHCb analysis requires time-dependent measurements of B-hadron decays, a high precision in determining the decay-time resolution, used to describe correctly the neutral B meson oscillations, is needed. This requires a very high precision in the reconstruction of the pp interaction and B hadron decay vertices.

- As mentioned in Section 3.2, the LHCb acceptance region is characterized by a high occupancy level in the detectors due to the high flux of particles. In addition the cross-section of $b\bar{b}$ pair production is two or three orders of magnitude smaller than the minimum bias cross-section. Thus the LHCb trigger system must have a very high background rejection in order to reduce the data-sample to a size suitable to be managed and stored. Multiple trigger levels are required to achieve such high signal efficiency, as discussed in Section 3.3.3.

3.3.1 The track reconstruction system at LHCb

The track reconstruction system is designed to determine charged particle, so-called tracks, trajectories and momenta and consists of the Vertex Locator (VELO), the Trigger Tracker (TT) and the three Tracking stations (T1-T3) and the dipole magnet. The particle reconstruction is fundamental in order to achieve a high momentum resolution and a precise vertex reconstruction: the key ingredient for the LHCb performance. All the sub-detectors need to have high spacial resolution and low material

budget; in addition they are built in two halves, placed to the left and to the right of the beam pipe, which are closed during the data-taking to ensure a complete coverage, but can be opened when an intervention is necessary.

The Vertex Locator

The average distance of flight of the B hadrons, coming from the pp collisions provided by LHC, is around 1 cm. Thus a good signature for identifying their decays is the presence of a secondary vertex significantly displaced from the interaction point. The Vertex Locator (VELO) [92] is a sub-detector placed as close as possible to the collision point, designed to determine the particle trajectories in this region and to separate the primary vertices from the secondary ones with a micro metric precision. The VELO consists of a sequence of 21 circular "stations" of silicon strip sensors placed perpendicularly along the beam line, as shown in Figure 3.8. Each station has a detector module on both sides of the beam line and each module has two sensors: the r-sensor, with semi-circular strips subdivided into four sectors per halves of 45° each, measuring the radial coordinate and the ϕ-sensor, consisting of strips in radial direction subdivided into inner and outer regions, determining the azimuthal angle ϕ defined as the angle between the x-axis and a direction vector in the x-y plane. The strip pitch ranges between 40 µm and 100 µm with a finer granularity close to the beam. Both r- and ϕ-sensors are 300 µm thick. A sketch of the r- and ϕ- sensors is shown in Figure 3.9. The VELO strips are not perfectly radial but are inclined by 10° in the inner region and by 20° in the outer region in order to improve the pattern recognition. The VELO modules have a diameter of 90 mm and covers a bit more 180° in azimuthal angle, allowing them to overlap during the data-taking, when the VELO is closed. They are placed in an aluminium-walled box under vacuum. A RF foil separates the vacuum inside the VELO box from beam vacuum region from the The VELO has two further stations, located upstream of the nominal collision point, to veto the pile-up events. They consist of the r-sensor only.

During the LHC transition between injection-state and stable-beams-state the VELO halves are moved away from the beam in order to avoid any possible radiation damage. In this phase the two VELO halves are distant about 6 cm from each other, while the VELO sensors are at a radial distance of 7 mm from the beam during the data-taking. The VELO reaches a best spatial resolution of about 4 µm, which represents the best vertex detector resolution achieved at the LHC.

The Tracker Turicensis

The Tracker Turicensis (TT), also known as Trigger Tracker, is a silicon microstrip detector placed right before the dipole magnet. It comprises two stations with two layers each, called TTa and TTb. The TT is distant approximately 2.4 m from the interaction point and each layer covers a rectangular area 150 cm wide and 120 cm height. The two central layers are tilted by +5° and -5° and are named

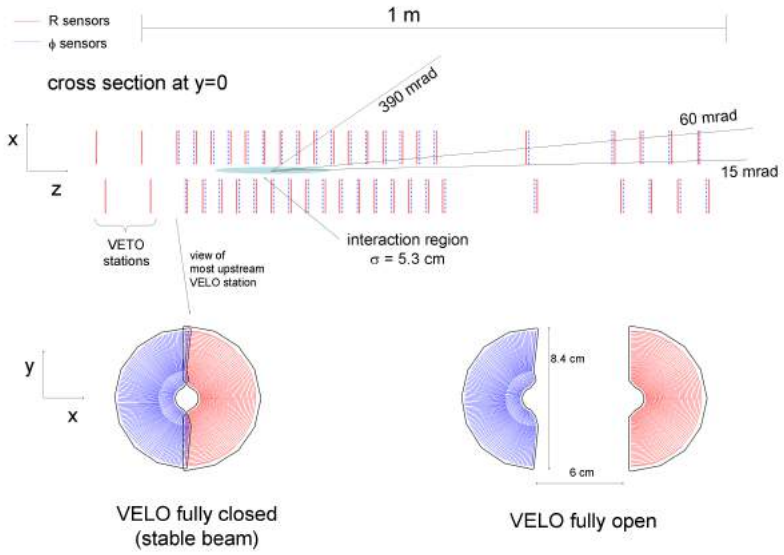

Figure 3.8: An overview of the VELO silicon sensors in the fully closed configuration is shown. The front face of the first module, both in opened and in closed configuration, is depicted. The *r*-sensors (red) and the ϕ-sensors (blue) are displayed [78].

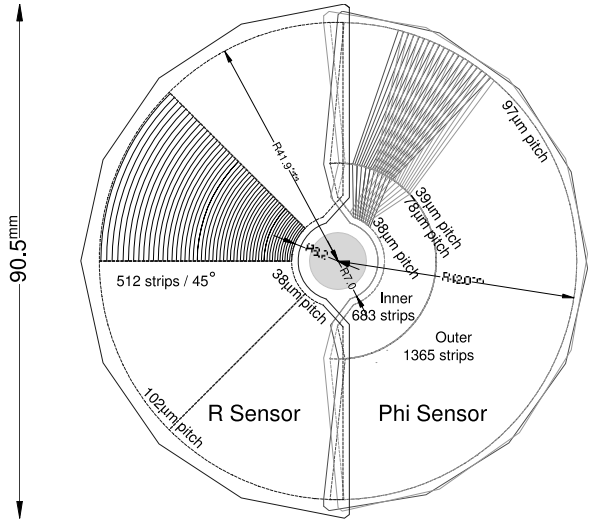

Figure 3.9: Illustration of the $r\phi$ geometry of the VELO sensors. For the ϕ sensor, the strips of two adjacent modules are depicted in order to highlight their different orientation [78].

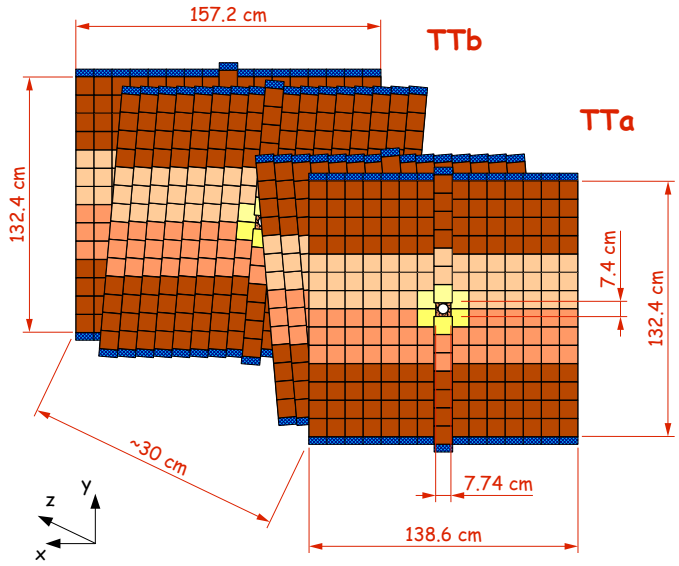

Figure 3.10: Layout of the four TT layers. The two central layers, u-layer and v-layer, are tilted by +5° and -5°, respectively. Different colours represent different readout sectors while the blue edge indicates the readout electronics [93].

u-layer and v-layer, respectively while the other two, the x-layers, are perfectly vertically aligned. This particular configuration, named $x-u-v-x$ geometry, allows to reconstruct the tracks in three dimensions through a stereo view. The strips are vertically oriented in order to perform a more accurate momentum evaluation, resulting in a best spatial resolution in the horizontal plane, the bending plane for the dipole magnet. The TT layers have two half modules where each one consists of seven silicon sensors. Each sensor is 9.46 cm wide and 9.44 cm long and has a pitch of 183 µm. The single hit resolution achieved by the TT sub-detector is ∼50 µm. The sensors are grouped in readout sectors containing one or two sensors, if the sector is located close to the beam line, and three or four sensors otherwise. This difference is due to the higher occupancy which affects the region closest to beam with respect to the other regions. The complete TT geometry is shown in Figure 3.10.

The tracking stations

The tracking stations, T1-T3, are placed among the dipole magnet and the second RICH. A view of the tracking station is reported in Figure 3.11. The T stations are characterized by two different technologies according to the distance from the beam line: the inner part of the station, namely the Inner Tracker (IT), consists of silicon microstrip sensors, while the outer part, named Outer Tracker (OT), consists of drift straw tubes. Also in this case, the difference between the IT and the OT is led by the higher track occupancy in the region close to beam pipe.

The Inner Tracker [94] consists of three stations, each one including four detection planes ar-

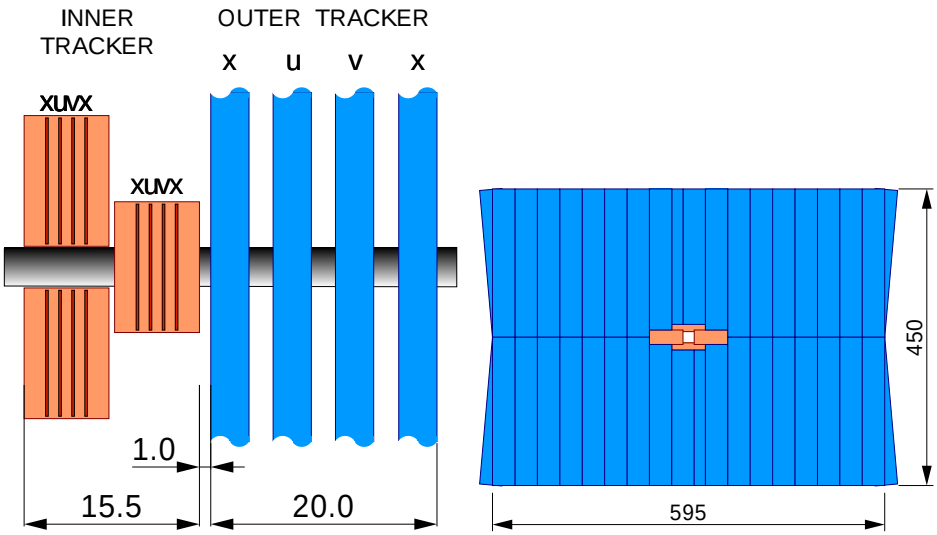

Figure 3.11: On the left, the layout of the T stations from the side view is shown. On the right, the layout of the T stations from the front view is depicted. In both pictures the Inner Tracker IT is represented in orange, while the Outer Tracker (OT) is coloured in blue.

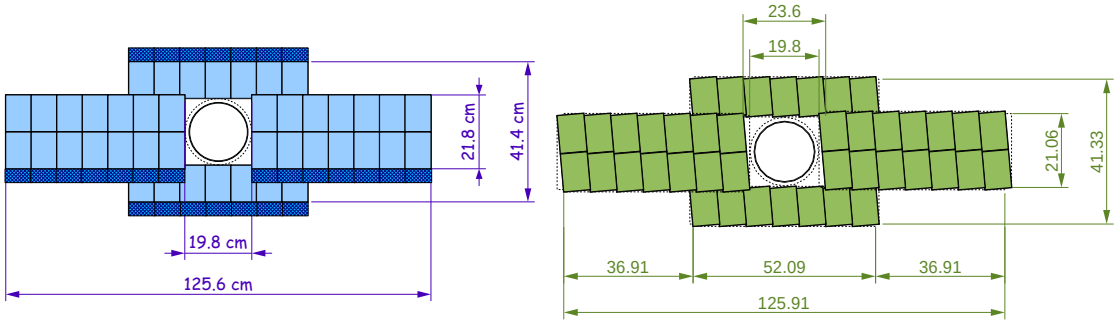

Figure 3.12: Layout of the IT sub-detector. On the left, the silicon sensors are represented in light blue, while the dark blue edges represent the readout electronics. On the right, the layout of the u-layer is shown, where the sensors are tilted by +5° with respect to the vertical direction [93, 94].

ranged around the beam pipe and divided in seven modules each. Similarly to the TT, the two inner layers are tilted by $\pm 5°$ with respect to the vertical direction, namely the u-layer and v-layer, respectively. The modules include two sensors if placed on the horizontal plane and only one sensor if located on the vertical plane. The silicon microstrip sensors are single-side p^+-on-n sensors, 7.6 cm wide and 11 cm height, with a thickness of 320 µm and 410 µm in the vertical and horizontal modules, respectively. The strip pitch is about of 198 µm which allows to achieve a resolution similar to the one obtained by the TT. The total sizes of the IT are approximately 1.2 m and 40 cm on the horizontal and vertical plane, respectively. The IT layout is shown in Figure 3.12.

The Outer Tracker [95, 96] consists of 12 double-layers of straw tubes, covering an area of about $5 \times 6\,\mathrm{m}^2$. The layers are organized in modules and the straw tubes are follow the same $x-u-v-x$ geometry used for the TT and IT microstrips. In addition, each layer includes two rows of tubes,

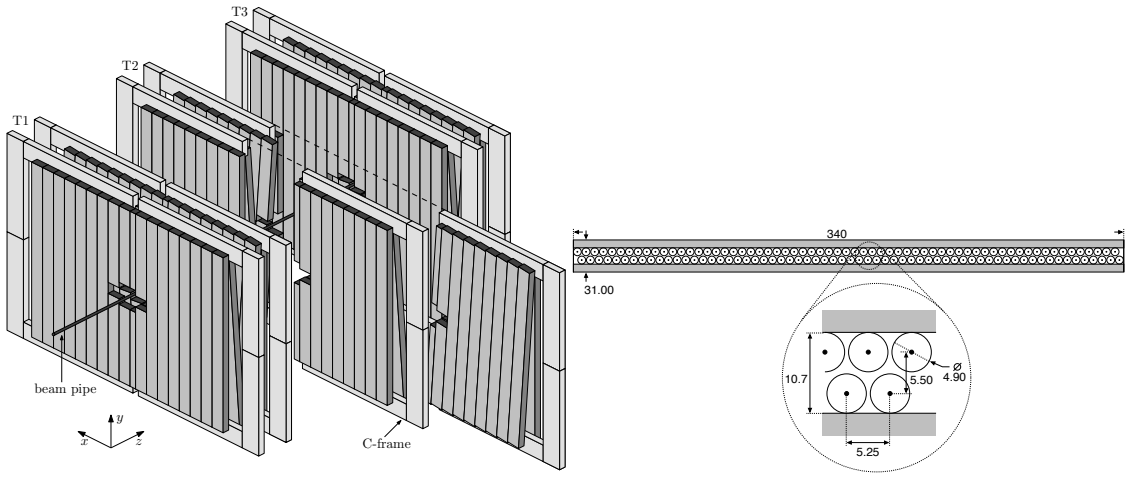

Figure 3.13: Layout of the OT sub-detector. On the left, the configuration of T stations and layers is shown. On the right, The cross-section of the OT module is depicted, showing the straw tube structure [95].

characterized by a honeycomb geometry which allows to maximize the sensible area. This particular configuration allows to measure both the spacial coordinates of the track hits, maintaining the track occupancy low. The straw tubes are 2.4 m long have a inner diameter of about 5 mm and are filled with a mixture of Ar (70%), CO_2 (28.5%) and O_2 (1.5%), which guarantees a drift-time below 50 ns. The OT layer configuration and the straw tubes structure are shown in Figure 3.13.

The dipole magnet

At the LHCb experiment the magnetic field is provided by a dipole magnet located after the TT sub-detector, just before the first tracking station (T1), and it is placed about 5 m from the interacting region [97]. Due to the LHCb acceptance, the magnet geometry consists of two coils inclined of a small angle with respect to the beam line, thus to become wider increasing the z-coordinate. A view of the dipole magnet is shown in Figure 3.14. The main component of the dipole magnetic field is oriented along the y-axis, consequently the particles are mostly bent in the horizontal plane. The strength of the y component of the magnetic field depending on the z-coordinate along the beam pipe is shown in Figure 3.15. The integrated magnetic field is $\int \vec{B}\, d\vec{l} = 4\,\mathrm{Tm}$. The momentum resolution for particles travelling the whole tracking system is $\Delta p/p = 0.4\%$ at 2 GeV and 0.6% at 100 GeV. Charged particles are bent to one side of the detector according to their charge, because of the the dipole magnetic field and the detector geometry. An unique characteristic of the LHCb magnet is the possibility to reverse periodically its polarity. In this way it is possible to better evaluate the systematics related to any left-right asymmetry introduced by the detector, which could affect CP asymmetry measurements.

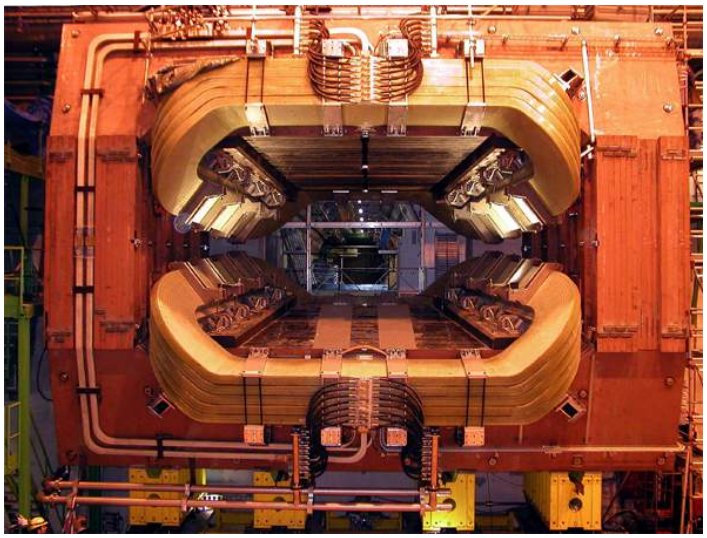

Figure 3.14: Front view of the LHCb dipole magnet. The profile of the two coils is designed to follow the detector acceptance.

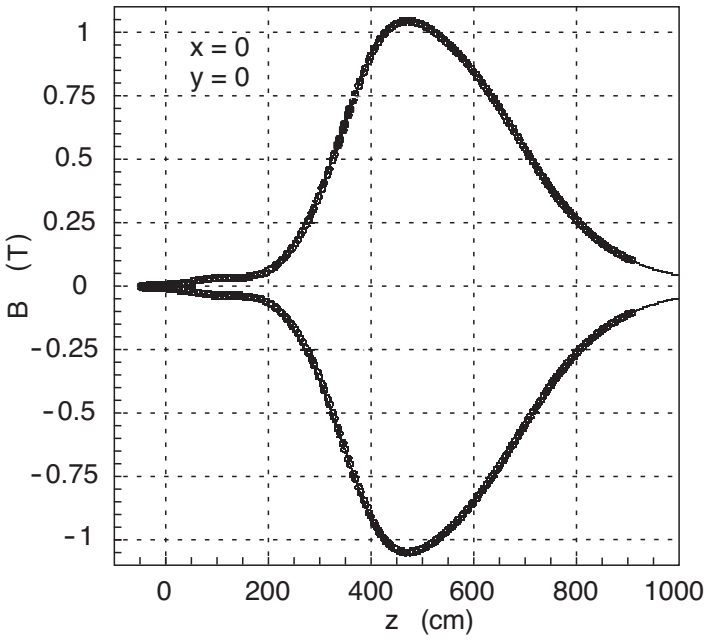

Figure 3.15: The strength of the y component of the magnetic field depending on the z-coordinate along the beam pipe. The measured values of the magnetic field are indicated by empty circles, while the lines represents the model expectation [97].

3.3.2 The particle identification system at LHCb

The particle identification system exploits several physics principles in order to identify the type of the particles created in LHCb. The system consists of the two Ring Imaging Cherenkov (RICH1 and RICH2), the two calorimeters (ECAL and HCAL), the Scintillating Pad Detector (SPD) and the Pre-Shower detector (PS), and the muon system. An efficient identification of charged leptons and hadrons is crucial for many *CP* violation measurements performed at LHCb.

The Ring Imaging Cherenkov detectors

The Ring Imaging Cherenkov (RICH) detectors exploit the Cherenkov effect in order to discriminate charged hadrons (pions, protons and kaons) in a broad momentum range. Such discrimination is fundamental in the event selection of B decays into final state containing these types of particles, such as the $B \to h^+h'^-$ decays, due to the intense hadron production at the LHC. This discrimination between the various hadron species is exploit also in the flavour tagging technique. which allows to determine the neutral B flavour at production looking at the its charge correlation with other particles generated in the event. The flavour tagging method is described in detail in Chapter 4.

The Cherenkov effect occurs when a charged particle travels in a medium with a velocity v larger than the speed of light $c' = c/n$, where n represents the refraction index of the medium. In this case photons are emitted within a cone along the particle direction of flight, whose opening angle, named Cherenkov angle θ_{Ch}, depends on v and n by the following relation:

$$\cos\theta_{Ch} = \frac{1}{n\beta} = \frac{1}{n \cdot v/c} \tag{3.5}$$

Combining the measurement of the Cherenkov angle with the particle momentum p, it is possible to estimate also the mass of the charged particle:

$$\cos\theta_{Ch} = \frac{1}{n}\sqrt{\left(\frac{m}{p}\right)^2 + 1} \tag{3.6}$$

The LHCb detector includes two RICH sub-detectors [98], named RICH1 and RICH2, covering different range of momentum in order to efficiently discriminate charged hadrons. The RICH1, located before the dipole magnet, is designed to efficiently identify low momentum tracks, approximately between 1 GeV/c and 60 GeV/c. During the Run1, the RICH1 was filled by two radiators: aerogel ($n = 1.03$) and C_4F_{10} ($n = 10014$) while the Run2 the aerogel is removed from the gas mixture. The RICH1 covers an angular acceptance of 25-300 mrad and 25-250 mrad in the x- and y-direction, respectively. The RICH2 is placed after the tracking stations and uses CF_4 ($n = 1.0005$) as radiator, covering a momentum range between 15 GeV/c and 100 GeV/c. RICH2 covers an angular acceptance of about 120 mrad in the vertical plane and about 100 mrad in the horizontal plane.

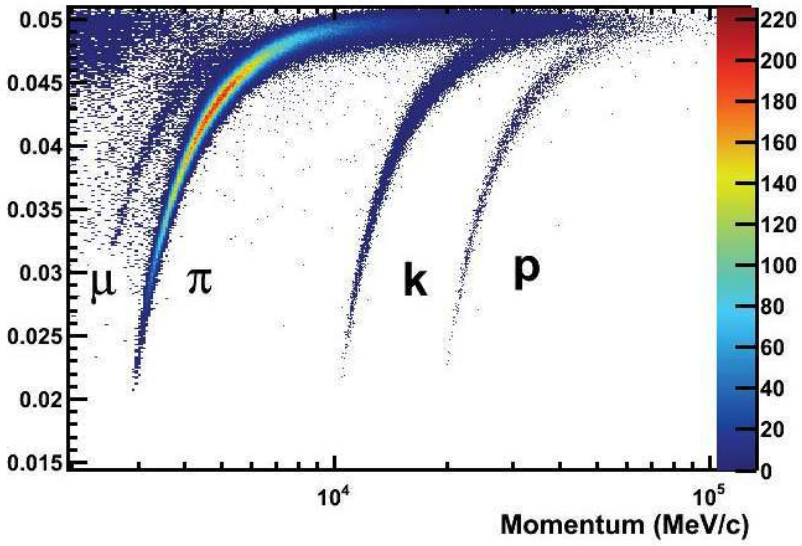

Figure 3.16: Cherenkov angle as function of the track momentum measured for isolated tracks in RICH2. The measurements for different mass-hypothesis are shown [82].

The choice of using different radiators in the two RICH is directly related to the need of covering different momentum range. Indeed, the Cherenkov light is emitted only by particles whose parameter $\beta = v/c$ satisfy the following relation: $c/n < \beta < c$. In case of $\beta = 1/n$ the Cherenkov angle results to be null, while if the particle travels close at the speed of light the angle will saturate at $\theta_{Ch} = \arccos(1/n)$. In Figure 3.16, the Cherenkov angle depending on the momentum of isolated tracks is shown.

Both the RICH detectors have an optical system consisting of two sets of spherical and plane mirrors, conveying the Cherenkov light on a lattice of Hybrid Photon Detectors (HPD), placed out of the LHCb acceptance and shielded against the remnant magnetic field. A schematic view of the RICH optical system used at LHCb is shown in Figure 3.17.

The performance achieve by the RICH detectors are studied by means of pure high statics samples of pions, kaons and protons coming from decays like $K^0_s \rightarrow \pi^+\pi^-$. The efficiency and the misidentification fraction, as function of the particle momentum, is shown in Figure 3.18 for pion, kaon and proton mass hypothesis.

The calorimeter system

The calorimeter system includes four sub-detectors: the Scintillating Pad Detector (SPD), the Pre-Shower (PS), the Electromagnetic Calorimeter (ECAL) and the Hadronic Calorimeter (HCAL) [99]. A schematic view of the LHCb calorimeter system is shown in Figure 3.19. The aim of this system is the identification of electrons, photons, and hadrons measuring the energy deposited in the various sub-detectors. In addition, the information provided by the calorimeter system are used in

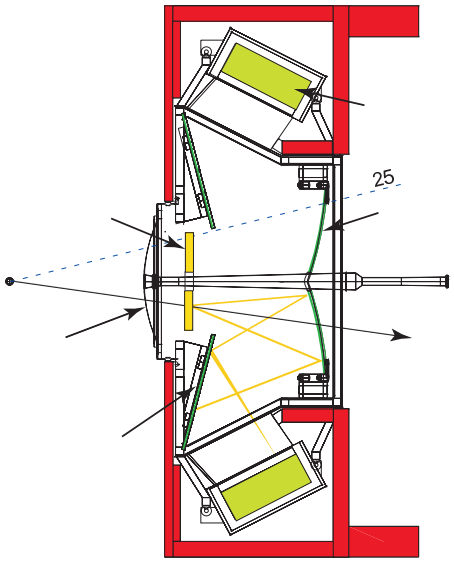

Figure 3.17: On the left, a schematic view of the RICH1 detector is shown; on the right, a top schematic view of the RICH2 detector is depicted. Both the figures shown the optical system used by RICH detectors [78].

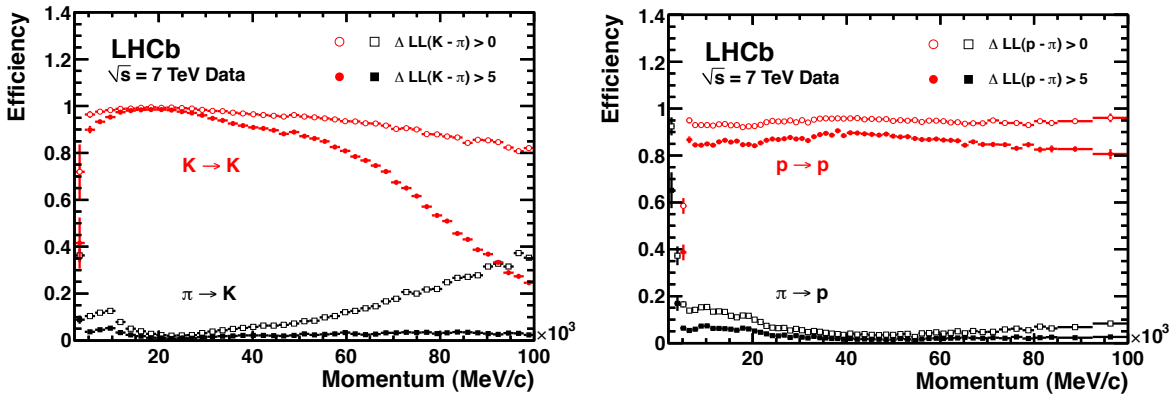

Figure 3.18: On the left, the kaon efficiency (red) and pion misidentification (black) as function of the track momentum is shown. On the right, the efficiency of protons and the probability of pion misidentification as function of the track momentum is shown [82]. The different marker indicates a different DLL requirements (this quantity is discussed in Section 3.4.

the first level trigger (L0), as discussed in Section 3.3.3. On one hand, charge particles and photons produce electromagnetic showers, through bremsstrahlung and pair production processes, when interacting with the calorimeter material. On the other hand, hadrons produce hadronic showers. The calorimeter system is designed alternating layers of absorbing material and layers of active scintillating material. The showers are created in the absorbing layers while the particles produce photons in the scintillating material. Finally the photons are read out by photomultiplier tubes.

All sub-detectors are divided in regions consisting of different sensors. ECAL, PS and SPD are divided in three regions (inner, middle and outer) while HCAL is divide only in two regions (inner and outer). The whole calorimeter system is segmented in the x-y plane and, in order to guarantee a good energy resolution and cluster position, the sizes of the segments increases moving away from the high occupancy regions close to the beam pipe. In Figure 3.20 the segmentation of the various sub-detectors is depicted.

The SPD and the PS are placed after the first muon station (M1) and they are separated by a a lead absorber 15 mm thick. Their segmentation decreases from pads of about 4 cm $\times$4 cm in the inner region to pads of 12 cm $\times$12 cm in the outer region. Working as an auxiliary sub-detectors of ECAL, their aim is to separate electrons from photons. Such separation is possible exploiting the fact that electrons, being electrically charged particles, produce light in the SPD while the photons, being electrically neutral, don't. The mis-identification rate of photons as electrons is below the 3%. Similarly the PS detector has been designed to separate electrons from pions both at the trigger level and in the offline reconstruction. The total material of the two sub-detectors has a thickness if about 2.5-3 radiations lengths.

The sampling structure of ECAL is designed alternating lead absorber layers of 2 mm thick and plastic scintillating material layers of 4 mm thick. The photons generated in the scintillating layers is collected by wavelength shifting fibres. ECAL is able to provide information about the energy and the position of the electromagnetic showers produced by photons and electrons. The best resolution in energy can be achieved only fully absorbing the electromagnetic showers within the thickness of ECAL, which has been designed to be about of 25 radiation lengths and 1.1 nuclear interaction lengths. The final energy resolution achieved by ECAL is given by $\sigma(E)/E = (8.5 - 9.5)\%/\sqrt{E} \oplus$ 0.8%. The calibration of ECAL is performed through the reconstruction of resonances decaying into two photons, such as $\pi^0 \to \gamma\gamma$ and $\eta \to \gamma\gamma$.

The HCAL is located after ECAL and has been designed to measure the energy of hadronic showers, which is the most important information required by the L0 hadronic trigger. The sampling structure consists of steal absorber layers with a thick of 16 mm alternated to scintillating layers 4 mm thick. The HCAL segmentation is similar to ECAL, but the modules have a size of 13 cm

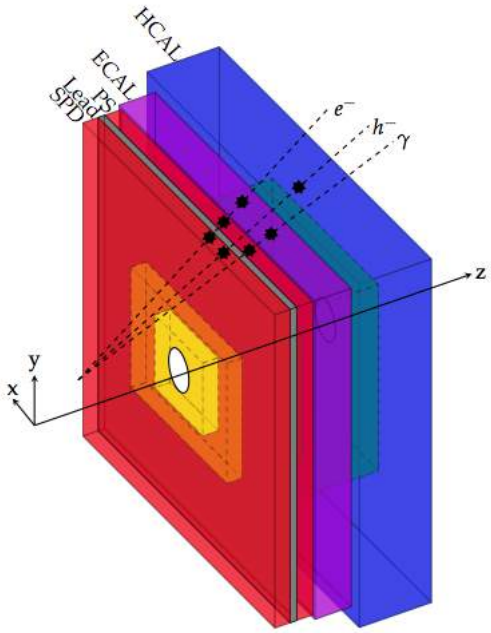

Figure 3.19: Layout of the LHCb calorimeter system. The four sub-detectors are visible as well as their interaction with different particle species. The relative dimensions of ECAL and HCAL are correct, however the z-dimension of SPD/PS is amplified [100].

$\times 13$ cm and 26 cm $\times 26$ cm in the inner and outer region, respectively. The total thickness of HCAL corresponds to 5.6 nuclear interaction lengths. The resolution in energy achieved by HCAL is given by $\sigma(E)/E = (69 \pm 5)\%/\sqrt{E} \oplus (9 \pm 2)\%$. The HCAL calibrations performed measuring the ratio E/p between the energy measured in the calorimeter, E, and the momentum measured by means of the tracking system, p.

The muon system

The muon system [101, 102] consists of five muon station, M1-M5, and is fundamental for the identification and trigger of B meson decays into final state containing muons; in particular muons with

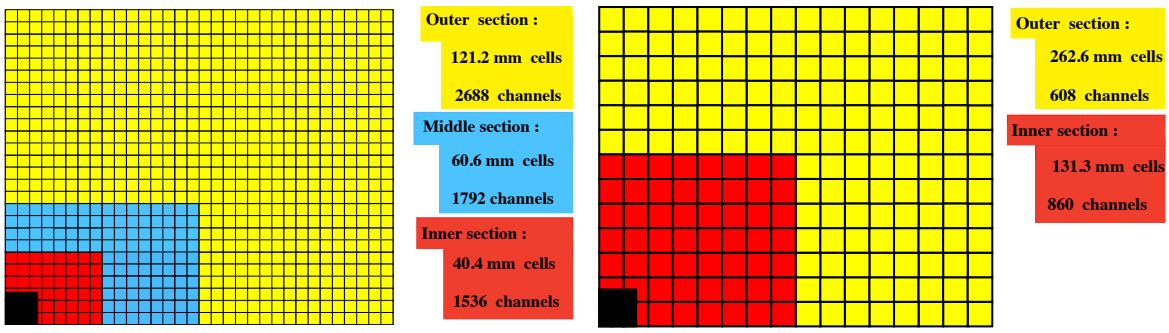

Figure 3.20: Lateral segmentation of the sub-detectors of the calorimeter system: SPD, PS and ECAL on the left, HCAL on the right. A quarter of the detector front face is shown.

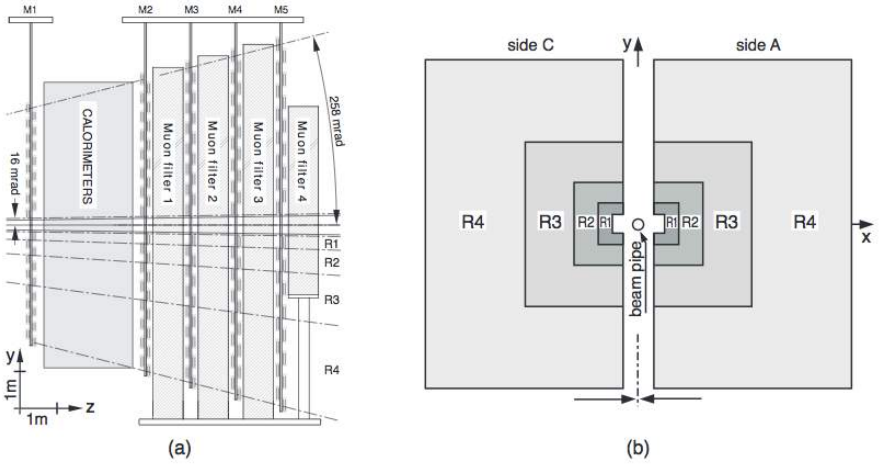

Figure 3.21: On the left, the side view of the LHCb muon system is depicted. On the right, the layout of the four regions included in a single station is shown.

high p_{T} and high impact parameter represent a clean signature for such decays. The first station is placed just before the calorimeters in order to minimize the uncertainties coming from multiple scattering in the calorimeter materials, improving the p_{T} resolution in the muon trigger. The latest four stations are separated by iron absorbers of 80 cm thick in order to get rid off the non-muon particles. Each station is divided in four regions where the ones closer to the beam pipe, which suffer of a higher track multiplicity, have a finer segmentation. The muon system covers an angular acceptance of 300 mrad and 200 mrad in the horizontal and vertical plane, respectively. The geometry of the muon system is shown in Figure 3.21. All the regions include Multi-Wire Proportional Chambers (MWPC) except for the R1 region of the M1 station, where triple-GEM detectors are used instead. The reason lies in the fact that in this region the expected particle flux exceeds the limits of radiation tolerance of the MWPC. Both the types of detector used for the muon system reach an efficiency larger than 95%, collecting the signal in less than 20 ns. The minimum momentum required for a muon to cross all the stations is about 6 GeV/c.

3.3.3 The trigger system at LHCb

The trigger system [103] is the decisive part of the LHCb experiment, since the physics processes, which will be studied, are determined at this stage. Nominally, the bunch crossing rate at LHC corresponds to 40 MHz, definitely too high to allow the data to be efficiently stored. The LHCb trigger system has the goal to reduce this rate from the nominal value to about 5 kHz, during the Run 1, and to 12.5 kHz, during Run 2, while recording the pp collisions interesting for the physics analyses. The LHCb trigger system is organized in three levels: the first is an hardware trigger while the the other two act at the software level. A sketch of the trigger system is shown in Figure 3.22.

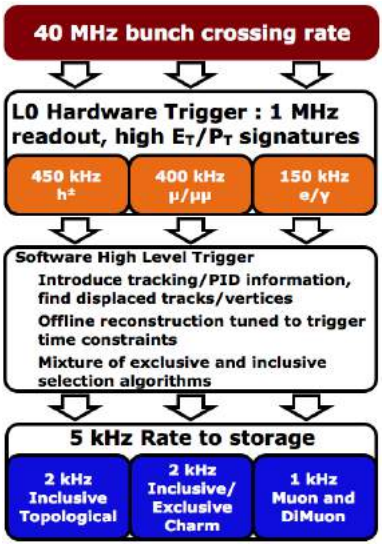

Figure 3.16: The three levels of the LHCb trigger system in 2012.

Figure 3.22: The three trigger levels of the LHCb trigger system in 2012

Level 0 Trigger

The first stage of the LHCb trigger, named Level 0 (L0), acts at the hardware level. It is designed to reduce the event rate from 40 MHz to 1 MHz, which is the maximum rate for a detector to be read out. The L0 trigger exploits fast detectors able to provide useful information without using complicated algorithms for the reconstruction. In particular, the L0 trigger uses two different system running in parallel to measure the transverse momentum of electrons, hadrons and muons. The first system is the calorimeter trigger, which uses the information provided by ECAL, HCAL, SPD and PS detectors. The events with a transverse energy of a cluster 2×2 cells greater than a certain threshold are accepted. The transverse energy is evaluated as:

$$E_T = \sum_{i=1}^{4} E_i \sin\theta_i \tag{3.7}$$

where E_i is the energy deposited in the i-th cell and θ_i is the angle between the z-axis of LHCb and the vector from the collision point and the i-th cell. Thus the calorimeter system is able to discriminate between electrons. photons and hadrons depending on the energy deposits. The second is the muon system, which exploits the information provided by the muon stations. The muon trajectories are reconstructed using the positions where the muons interacted with the five stations. Thus it is possible to determine the transverse momentum of the tracks, under the hypothesis that the muons coming from the primary vertex and get a single kink from the magnet. Since B mesons have a large The events are accepted if a muon or a muon pair have the transverse energy above a certain threshold.

If at least one of the two L0 system provide a positive decision, the full detector is read out by

the data acquisition system (DAQ).

High Level Trigger

The High Level Trigger (HLT) is a software trigger, based on C++ applications, which process only the events passing the L0 trigger. The HLT consists of two stage: the HLT1 exploits some features of the *b*- and *c*- decays, such as the high track momentum, and the displacement of tracks and vertices. It is able to reduce the event rate from 1 MHz to 40-80 kHz. The second level (HLT2) takes advantage of an event reconstruction of about the same quality as the off-line reconstruction. The main difference between the two reconstructions is related to the timing requirements which are restricted for the HLT, while are relaxed in the off-line reconstruction. After the HLT2 stage the event rate is reduce to 3-5 kHz in Run 1 and to 12.5 kHz in Run 2.

The event selection can be performed at the HLT level using different strategies, each one suitable for the specific topology of the decay of interest. The sequence of algorithms for the reconstruction and selection of an event is named "trigger line". Decays with different topology will be selected by different trigger lines. Due to the fully software nature of the HLT, the physics program of the LHCb experiment can be broad in different directions by adding new trigger algorithms.

3.4 Event reconstruction

A good event for physics analyses can contain useful information related to one or more interesting decays. The reconstruction of the particles trajectories, the vertex and particle identification are the fundamental information involved in the decay reconstruction. The trajectories of the charged particles, also named tracks, are reconstructed from the combination of electronic signals provided by the tracking sub-detectors (VELO, TT, IT, OT). The track reconstruction consists of two steps: the *pattern recognition* and the *clone removal*. The pattern recognition identifies a sequence of hits observed in different sub-detectors, which can be produced by a single charged particle. Different types of tracks are classified according to the detectors crossed by the track, as shown in Figure 3.23 where the track types are depicted:

- **VELO tracks**: defined by hits only in the VELO. They are utilized as input for the long and upstream track reconstruction. If they can not be extrapolated beyond the VELO, they are used in the reconstruction of primary vertex.
- **T tracks**: reconstructed using hits in the tracking stations. They are exploited as input for the long and downstream tracks.
- **Long tracks**: tracks defined by hits in the VELO and in the whole tracking system. Thus they

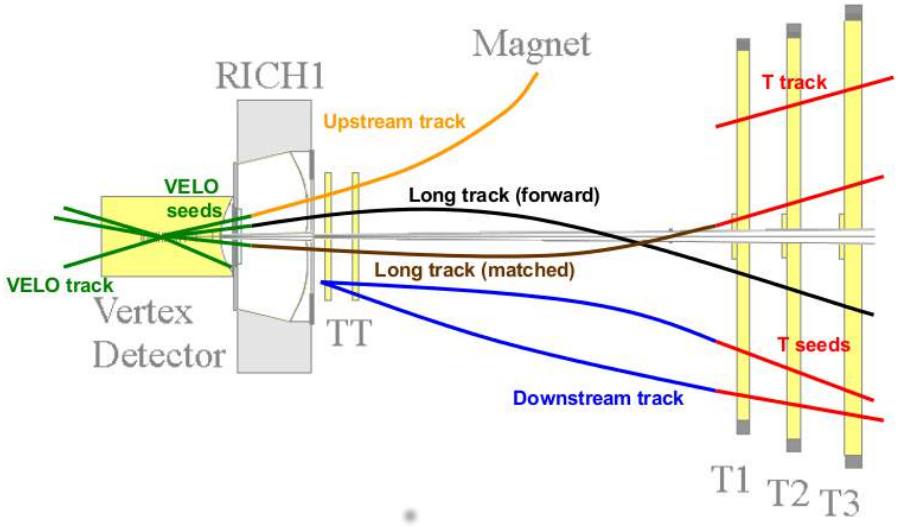

Figure 3.23: Illustration of the different track types reconstructed in LHCb.

are characterized by the most precise momentum resolution and are the tracks mostly used in LHCb. When it is possible, the reconstruction of tracks not associated to real particle is improved by using hits from the TT stations.

- **Upstream tracks**: defined by hits only in the VELO and TT stations. Due to their low momentum they are bent by the dipole magnetic field outside the LHCb acceptance.

- **Downstream tracks**: reconstructed from hits only in the TT and T stations. They are used for the decay reconstruction of the long lived resonances decaying after the VELO, such as the neutral kaons.

The long tracks reconstruction is performed using two different algorithms. The first method, named "forward tracking", consists in the extrapolation of the track, after the VELO pattern recognition, into the T stations using a "thin lens" approximation of the magnetic dipole. The second method is performed in two steps: "seeding" and "matching". Firstly the tracks are reconstructed in the T stations, then they are matched with the segments observed in VELO and T stations in order to produce long tracks. Finally a Kalman filter [104] is used for the trajectory reconstruction, taking into account effects energy loss due to ionization and multiple scattering. Exploiting the $\chi^2/ndof$ the quality of the track can be quantified and the fake tracks not associated to any real particle, named ghost, can be removed. The "clone removal" represents the last steps of the track reconstruction and consists in get rid off the tracks which shares the most of the hits, named clones. Indeed the segments, belonging to the same long track, can be reconstructed by the different algorithms as further tracks.

Another fundamental ingredient of the event reconstruction is the particle identification (PID). It is performed using the information provided by the RICH detectors, calorimeters and muon system. Indeed, as mentioned in Section 3.3.2 the mass of a travelling particle can be determined combining the measured Cherenkov angle in the RICH and the measured track momentum. The electron and photons identification is performed comparing the energy deposited in ECAL with the extrapolation of the tracks in the same region. Thus, combining all these information, it is possible to obtain an excellent separation between the charged particles: kaons, pions, protons, muons and electrons. For each track, the probability of a specific particle hypothesis x is defined by a likelihood L_x. However, as the value of the likelihood can be quite large, its logarithm $\log L_x$ is used instead. Since the pions are the most common particles generated and detected at LHCb, the likelihood for a specific hypothesis x is evaluated against the pion hypothesis: $DLL_{x\pi} = \Delta \log L_{x\pi} = \log L_x - \log L_\pi$. Larger values of $DLL_{x\pi}$ correspond to a greater probability that the track belongs to the x species and viceversa lower $DLL_{x\pi}$ values mean that the track is more likely a pion.

3.5 Monte Carlo simulation

The modelling of the data distributions, the optimisation of the selection strategies, the estimation of the fraction of the events escaping the detector acceptance or the studies regarding the response of the detector to the passage of different type of particles represent a fundamental part of several data analyses. However the analytical determination of all these requirements is often impractical or impossible. Thus an alternative method to perform such studies, named Monte Carlo (MC) simulation, consists in using numerical simulated samples. The simulation process involves various steps in order to obtain a MC samples as similar as possible to the real data. These steps describe the generation of the pp collisions, the decay processes, the detector response and finally the the processing and selection of the data [105]. The MC production consists of various steps, starting with the simulation of the pp interaction until the reconstruction of the particles in the detector. The first phase is aimed to the modelling of the pp collision and the fragmentation and hadronization processes, which lead to the generation of the different particles in the event. This steps is performed by PYTHIA tool [90, 106]. Then the time evolution and decay of the generated particles are described by means of the customized version of the EVTGEN tool [107], specialized in the heavy flavour processes of the B mesons. In addition the final state radiation is simulated by PHOTOS [108]. The final phase of the generation steps is delegated to GEANT4 tool [109, 110] which simulates the interaction of the generated decay products with the detector material, taking into account the LHCb detector geometry and data taking conditions. After having described correctly the generation and time evolution of all the particles in the event, the MC algorithms move to simulate the detector

response by means of the digitalization programme Boole [111]. At this point the MC sample looks like the real data sample consisting of the events collected by the LHCb experiment. However, the simulated samples allow to access to the MC true information regarding all the particles in the event, such as the true ID particle and the hierarchy chain, which are not available with the real data. The next steps are the same as the ones performed on the real collision data: the trigger selection applied by the Moore tool [112], the reconstruction implemented in Brunel [113] and finally the stripping executed by the DaVinci tool [114].

4

Flavour tagging technique

All the measurements of *CP* violation require the knowledge of the B candidate flavour at production. This information can be easily obtained for what concerns the charged B mesons, since the flavour at production is the same at the decay, which can be determined looking at the charge of the decay products. On the other hand, when the neutral B meson are involved, using the flavour at decay is not an optimal solution because of the neutral flavour oscillations. The Flavour Tagging (FT) technique represents a method which allows to determine the neutral B meson flavour at production by looking at the charge correlation between the signal B and the other particles generated in the event.

4.1 Flavour tagging algorithms

In LHCb, the B mesons are produced as $b\bar{b}$ pairs, charge correlated. Due to the color confinement, one of the two b quark hadronizes in the signal B meson, while the other generates another B hadron, called *opposite B*. The Flavour Tagging (FT) tool at LHCb consists of different algorithms which look for a specific type of particle, generated in the event, which could be correlated in charge with the signal B meson. These algorithms, also named *taggers*, are classified as "Opposite Side" (OS) if their target particle comes from the decay of the opposite B, and "Same Side" (SS) if the particle arises from the remnants of the signal b fragmentation. A schematic representation of the taggers available within the LHCb collaboration is shown in Figure 4.1.

The OS algorithms [115, 116] are able to tag both the B^0 and B_s^0 mesons indifferently while the SS taggers depend on the quark content of the signal B meson. In case of a B^0 meson, the remnant d hadronizes in a pion or a proton, hence these two particle species are the SS tagger target [117]. The implementation of the SSπ and SSp algorithms was the subject of the work reported in the master thesis [118] and the finalisation of their development has been the very first step of this work, because of their significant contribution to the $B \to h^+h'^-$ analysis. The two tagging algorithms have

been implemented within the LHCb framework and the results have been published in The European Physical Journal C [117]. Similarly for the B_s^0, the SS algorithms will look for a kaon [119] or a Λ. However no SSΛ tagger is available at the moment, mostly because of the scant number of Λ candidates detected in LHCb to develop such a algorithm. A dedicated study regarding the implementation of a SSΛ algorithm has been performed during the development of the $B \to h^+h'^-$ Run 2 analysis. The aim was to further increase the total tagging performance however, due to the too low tagging performance, its contribution has not been included in the $B \to h^+h'^-$ analysis. The detail about this study are reported in an internal LHCb note [120] (unpublished) and are summarised in Appendix A. Each taggers is based on the output of one or more multivariate classifiers, trained using flavour specific decays, where the flavour at decay is uniquely defined by the flavour of the decay products, and taking as input geometrical and kinematic information. The full list of all the taggers available at LHCb is reported in Table 4.1.

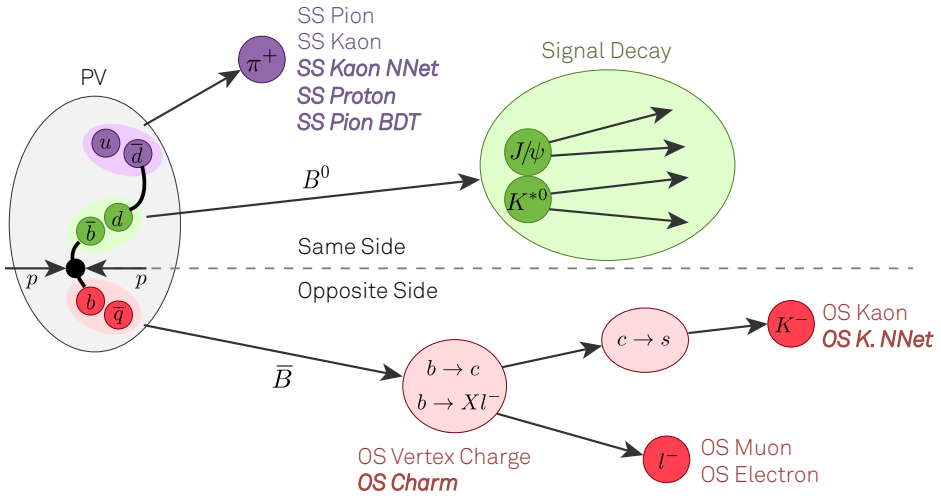

Figure 4.1: Schematic representation of the FT algorithms available at LHCb.

Table 4.1: FT algorithms available at LHCb. The OS tagger can tag both the B^0 and B_s^0 mesons. The SSK can efficiently tag only the B_s^0 mesons, while SSπ and SSp can tag efficiently only the B^0 mesons.

SS algorithms	**OS algorithms**	
Kaon (SSK) [119]	Muon (OSμ) [115]	Electron (OSe) [115]
Pion (SSπ) [117]	Kaon (OSK) [115]	Charm (OSc) [116]
Proton (SSp) [117]	Vertex Charge (OSVtx) [115]	

For each reconstructed signal candidate, the flavour tagging algorithms provide a *tag decision*, d, equal to 1 if the signal candidate is a B meson, equal to -1 if the candidate is an antimeson and null if the algorithm is not able to assign a decision on the initial flavour. The tagging decisions are based

on the charge of the tagging particle, correlated to the signal B meson charge. The performance of the various flavour tagging algorithms can be estimated by means of three different quantities: the mistag rate, the tagging efficiency and the tagging power.

Each tagger provides an estimation of the mistag rate, ω, for the tag decision to be wrong. The *mistag rate* is a continuous variable in the range [0, 0.5] and can be defined as:

$$\omega = \frac{N_W}{N_R + N_W} \tag{4.1}$$

where N_W and N_R represent the number of events wrongly and rightly tagged by the algorithm. The mistag rate can be measured only on flavour specific decays. In particular the formula in Equation 4.1 is relevant only for the charged B mesons where it is possible to compare directly the flavour of the reconstructed meson with the flavour tagging decision. The mistag estimation turns to be more complicated in case of neutral B mesons, since they are affected by neutral flavour oscillations. Thus a mistag fraction has to be extracted from a time-dependent fit on the B flavour oscillations as function of the decay-time. Finally, in case of no flavour specific decay channels the mistag can not be measured but an its reliable estimation can be obtained using a correctly calibrated response of the tagging algorithm (the calibration procedure is described in detail in Section 4.2).

The tagging efficiency represents the fraction of B candidate for which the tagging algorithm is able to provide a tagging decision and a mistag probability. It is defined as:

$$\varepsilon_{tag} = \frac{N_R + N_W}{N_R + N_W + N_U} \tag{4.2}$$

where N_U is the number of events for which the taggers in not able to give a response.

The mistag probability and the tagging efficiency determine the sensitivity to the *CP* asymmetry. Assuming they are not depending on the initial flavour of the B candidate, the measured decay rates, reported in Equation 1.58, can be defined as:

$$\begin{aligned}
\Gamma^{meas}_{tag}(B(t) \to f) &= \varepsilon_{tag}[(1-\omega)\Gamma(B(t) \to f) + \omega\Gamma(\overline{B}(t) \to f)] \\
\overline{\Gamma}^{meas}_{tag}(\overline{B}(t) \to f) &= \varepsilon_{tag}[(1-\omega)\Gamma(\overline{B}(t) \to f) + \omega\Gamma(B(t) \to f)]. \\
\Gamma^{meas}_{tag}(B(t) \to \overline{f}) &= \varepsilon_{tag}[(1-\omega)\Gamma(B(t) \to \overline{f}) + \omega\Gamma(\overline{B}(t) \to \overline{f})] \\
\overline{\Gamma}^{meas}_{tag}(\overline{B}(t) \to \overline{f}) &= \varepsilon_{tag}[(1-\omega)\Gamma(\overline{B}(t) \to \overline{f}) + \omega\Gamma(B(t) \to \overline{f})]. \\
\Gamma^{meas}_{untag}(t) &= (1-\varepsilon_{tag})[\Gamma(B(t) \to f) + \Gamma(\overline{B}(t) \to f)] \\
\overline{\Gamma}^{meas}_{untag}(t) &= (1-\varepsilon_{tag})[\Gamma(\overline{B}(t) \to \overline{f}) + \Gamma(B(t) \to \overline{f})].
\end{aligned} \tag{4.3}$$

where the first four expressions represent the decay rates for tagged events while the last two are the untagged decay rates. The measured time-dependent *CP* asymmetry, A^{meas}_{CP}, related to the tagged events is reduced by a dilution factor depending on the mistag with respect to the true asymmetry,

A_{CP}:

$$A_{CP}^{meas}(t) = \frac{\overline{\Gamma}_{tag}^{meas}(t) - \Gamma_{tag}^{meas}(t)}{\overline{\Gamma}_{tag}^{meas}(t) + \Gamma_{tag}^{meas}(t)} = (1-2\omega)A_{CP}(t). \tag{4.4}$$

where term $(1-2\omega)$ represents the tagging dilution factor D, which is equal to 1 in case of perfect tagging and to 0 in case of random tagging (i.e. $\omega = 0.5$). Thus the true *CP* asymmetry and its statistical error can be evaluated as:

$$A_{CP} = \frac{A_{CP}^{meas}}{D}, \qquad \sigma_{A_{CP}} = \frac{\sigma_{A_{CP}}}{D} \tag{4.5}$$

assuming negligible the error on ω. Using the quadratic error propagation and the following relation

$$1 - A_{CP}^{meas^2} = \frac{4\Gamma_{tag}^{meas}\overline{\Gamma}_{tag}^{meas}}{(\Gamma_{tag}^{meas} + \overline{\Gamma}_{tag}^{meas})^2} \tag{4.6}$$

the error in the measured asymmetry can be evaluated as:

$$\sigma^2_{A_{CP}^{meas}} = \frac{4\Gamma_{tag}^{meas}\overline{\Gamma}_{tag}^{meas}}{(\Gamma_{tag}^{meas} + \overline{\Gamma}_{tag}^{meas})^3} = \frac{1 - A_{CP}^{meas^2}}{\overline{\Gamma}_{tag}^{meas} + \Gamma_{tag}^{meas}} = \frac{1 - A_{CP}^{meas^2}}{N_{tag}} = \frac{1 - A_{CP}^{meas^2}}{\varepsilon_{tag} N} \tag{4.7}$$

where N is the total number of signal candidates and $N_{tag} = N_R + N_W$ represent the number of tagged events. Finally, the error on the true *CP* asymmetry can be evaluated as:

$$\sigma_{A_{CP}} = \frac{\sqrt{1 - A_{CP}^{meas^2}}}{\sqrt{\varepsilon_{tag} N} D} \tag{4.8}$$

which is inversely proportional to the quantity, named *tagging power*, defined as:

$$\varepsilon_{eff} = \varepsilon_{tag} D^2 = \varepsilon_{tag}(1-2\omega)^2. \tag{4.9}$$

Because of this relation between the tagging power and the uncertainty of the *CP* asymmetry, ε_{eff} is used as figure of merit to be maximized during the training and development of the flavour tagging algorithms. Further information about the FT performance are discussed in [121].

4.2 Flavour tagging calibration

As mentioned in Section 4.1, the tagging algorithms are based on multivariate classifiers taking as input both kinematic and geometrical information related to signal B candidate and the global event. Through a regression the output value is converted into a probability for the tagging decision to be wrong. However the samples used for the training and validation of the tagging algorithm could be different in terms of kinematic properties, trigger requirements or criteria selection, with respect to the sample used for the measurement of the *CP* asymmetry. For this reason a more reliable estimate of the mistag rate, ω, can be obtained from the calibration of the raw mistag probability predicted by the tagging algorithms, denoted as η hereafter. Since the mistag probability depends

on the kinematic properties of both the B meson and the full event, the calibration procedure is performed using control samples of flavour specific decays with similar properties of the signal decay of interest.The simplest choice of calibration function is a linear polynomial:

$$\omega(\eta) = p_0 + p_1(\eta - \langle\eta\rangle). \tag{4.10}$$

where the arithmetic mean $\langle\eta\rangle$ allows to reduce the correlation among the calibration parameters p_0 and p_1. In case of a tagger perfectly calibrated (i.e. $\omega(\eta) = \eta\ \forall\eta$) the p_0 and p_1 parameters should be equal to $\langle\eta\rangle$ and 1, respectively.

The flavour tagging performance are not necessarily independent on the initial flavour of the signal B candidate. For example, since the LHCb detector consists of matter, the tagging candidates could be detected differently accordingly to their nature of particle or antiparticle. Another possible difference in the performance could be related to the multivariate classifier itself, which could be affected by a bias, identifying more easily a particle with respect to an antiparticle or viceversa. All these effects can result in different tagging efficiencies and mistag probabilities for initial B and $\overline{B}$ mesons. For these reason a more efficient calibration function takes into account these possible tagging asymmetries defining two sets of tagging parameters: ($\omega(\eta)$, p_0, p_1 and ε_{tag}) for the signal B meson and ($\overline{\omega}(\eta)$, $\overline{p}_0$, $\overline{p}_1$ and $\overline{\varepsilon}_{tag}$) for the signal $\overline{B}$ antimeson. Thus, defining an average mistag rate $\hat{\omega}$ and a difference between the mistag probabilities of B and $\overline{B}$ mesons as:

$$\begin{aligned} \hat{\omega}(\eta) &= \frac{1}{2}(\omega(\eta) + \overline{\omega}(\eta)), \\ \Delta\omega(\eta) &= \omega(\eta) - \overline{\omega}(\eta). \end{aligned} \tag{4.11}$$

the relation reported in Equation 4.10 can be modified as:

$$\begin{aligned} \hat{\omega}(\eta) &= \hat{p}_0 + \hat{p}_1(\eta - \langle\eta\rangle), \\ \Delta\omega(\eta) &= \Delta p_0 + \Delta p_1(\eta - \langle\eta\rangle) \end{aligned} \tag{4.12}$$

Similarly the single mistag probabilities $\omega(\eta)$ and $\overline{\omega}(\eta)$ can be parametrized as:

$$\begin{aligned} \omega(\eta) &= p_0 + p_1(\eta - \langle\eta\rangle), \\ \overline{\omega}(\eta) &= \overline{p}_0 + \overline{p}_1(\eta - \langle\eta\rangle) \end{aligned} \tag{4.13}$$

where the calibration parameters can be written as:

$$\begin{aligned} p_i &= \hat{p}_i(1 + \Delta p_i), \\ \overline{p}_i &= \hat{p}_i(1 - \Delta p_i), \end{aligned} \tag{4.14}$$

with $i = 0, 1$. Also the tagging efficiencies are measured separately for B and $\overline{B}$ mesons

$$\begin{aligned} \varepsilon_{tag} &= \hat{\varepsilon}_{tag}(1 + \Delta\varepsilon_{tag}) \\ \overline{\varepsilon}_{tag} &= \hat{\varepsilon}_{tag}(1 - \Delta\varepsilon_{tag}) \end{aligned} \tag{4.15}$$

where $\hat{\varepsilon}_{tag}$ is the average tagging efficiency and $\Delta\varepsilon_{tag}$ represents the tagging asymmetry, which can be defined as:

$$A_{tag} = \Delta\varepsilon_{tag} = \frac{\bar{\varepsilon}_{tag} - \varepsilon_{tag}}{\bar{\varepsilon}_{tag} + \varepsilon_{tag}}. \tag{4.16}$$

4.3 Flavour tagging combination

Sometimes it can occur that more than one tagging algorithm provide both a tagging decision and a mistag probability to the same B candidate. In this case it is possible to combine their information into a unique response, decreasing the possibility of wrong mistag. Assuming that the responses of the various algorithms are completely independent by each other (i.e. there is no correlation between the taggers), the combination can be performed by means of the following expressions:

$$p(b) = \prod_i \left(\frac{1+d_i}{2} - d_i(1-\omega_i)\right), \qquad p(\bar{b}) = \prod_i \left(\frac{1-d_i}{2} + d_i(1-\omega_i)\right) \tag{4.17}$$

where $p(b)$ and $p(\bar{b})$ are the probabilities for the B signal candidate to contain a b and $\bar{b}$ respectively while d_i and ω_i represent the tagging decision and the calibrated mistag probability of the i-th tagger. Finally, these probabilities are normalized as:

$$P(\bar{b}) = \frac{p(\bar{b})}{p(\bar{b}) + p(b)}, \qquad P(b) = \frac{p(b)}{p(\bar{b}) + p(b)} = 1 - P(\bar{b}). \tag{4.18}$$

In case of $P(\bar{b}) > P(b)$ the combined tagging decision is positive (+1) and the predicted mistag probability is $\eta = 1 - P(\bar{b})$. Viceversa, if $P(b) > P(\bar{b})$ the final tagging decision is negative (-1) and the expected mistag fraction is $\eta = P(\bar{b})$ [115].

However the responses of the tagging algorithms available at LHCb are not completely uncorrelated with each other. In particular, the largest correlation happens between the OS Vertex Charge and the other OS algorithms, since one of these particles can be included in the secondary vertex. The correlation matrix between the OS and SS tagging algorithms, evaluated on a background subtracted sample of $B \to h^+h'^-$ decays collected with Run 1 data taking condition, is shown in Table 4.8. Because of the correlation among the taggers is completely neglected in the Equation 4.17, the resulting combined mistag probability turns out to be slightly overestimated. For this reason, in order to have a reliable mistag probability, the new combined tagger is re-calibrated on data.

4.4 Flavour tagging in CPV measurement on two-body B decays in Run 1

In the measurement of the CP violation in the charged two-body B decays both the Opposite Side and the Same Side taggers, reported in Table 4.1, are used. Each of them is calibrated using an

appropriate control sample as described in Section 4.4.3. In addition the OS taggers are combined into a unique OS tagger as well as the SSπ and the SSp tagging algorithms, which are both aimed to tag the B^0 meson. As discussed in more detail in Chapter 5, various components are taken into account in the measurement and for each of them the distribution of η has to be described.

4.4.1 Flavour tagging for $B \to h^+h'^-$ decays

For both the tagging algorithms (OS and SS) the probability functions for the tagging decision d and the predicted mistag probability η associated to the $B \to h^+h'^-$ decays are defined as:

$$\begin{aligned}\Omega^{sig}(d,\eta) &= \delta_{d,1}\varepsilon^{sig}_{tag}(1-\omega^{sig}(\eta))h^{sig}(\eta) + \delta_{d,-1}\varepsilon^{sig}_{tag}\omega^{sig}(\eta)h^{sig}(\eta) + \delta_{d,0}(1-\varepsilon^{sig}_{tag})U(\eta),\\ \overline{\Omega}^{sig}(d,\eta) &= \delta_{d,1}\overline{\varepsilon}^{sig}_{tag}(1-\overline{\omega}^{sig}(\eta))h^{sig}(\eta) + \delta_{d,-1}\overline{\varepsilon}^{sig}_{tag}\overline{\omega}^{sig}(\eta)h^{sig}(\eta) + \delta_{d,0}(1-\overline{\varepsilon}^{sig}_{tag})U(\eta),\end{aligned} \tag{4.19}$$

where $\delta_{d,i}$ is the Kronecker delta function, ε^{sig}_{tag} and $\overline{\varepsilon}^{sig}_{tag}$ represent the tagging efficiencies for the B and $\overline{B}$ meson respectively, $\omega^{sig}(\eta)$ and $\overline{\omega}^{sig}(\eta)$ are the mistag probabilities for the B and $\overline{B}$ meson as function of the predicted mistag η, $h^{sig}(\eta)$ is the p.d.f. describing the η distribution and $U(\eta)$ is an η uniform distribution associated to the untagged events. The function dependence between ω^{sig} and η is the the same reported in Equation 4.13, where $\langle\eta\rangle$ is evaluated over the $h^{sig}(\eta)$ p.d.f.. In order to reduce the correlation among the tagging parameters (p_0, $\overline{p}_0$, p_1, $\overline{p}_1$, ε^{sig}_{tag} and $\overline{\varepsilon}^{sig}_{tag}$), these variables are parametrised as reported in Equations 4.14, 4.15. Finally the two distinct probability functions for the OS and SS taggers are combined together into a unique p.d.f.:

$$\begin{aligned}\Omega^{sig}(d_{OS},\eta_{OS},d_{SS},\eta_{SS}) &= \Omega^{sig}_{OS}(d_{OS},\eta_{OS})\cdot\Omega^{sig}_{SS}(d_{SS},\eta_{SS}),\\ \overline{\Omega}^{sig}(d_{OS},\eta_{OS},d_{SS},\eta_{SS}) &= \overline{\Omega}^{sig}_{OS}(d_{OS},\eta_{OS})\cdot\overline{\Omega}^{sig}_{SS}(d_{SS},\eta_{SS}),\end{aligned} \tag{4.20}$$

which represents an accurate description of the multidimensional distribution, assuming $h^{sig}_{OS}(\eta_{OS})$ and $h^{sig}_{OS}(\eta_{SS})$ completely uncorrelated.

4.4.2 Flavour tagging for the background components

Two source of background have to be taken into account: the combinatorial and the partially reconstructed 3-body backgrounds. For both the background contributions, the probability as function of d and η, for the OS and SS taggers, can be parametrised as:

$$\Omega^{bkg}(d,\eta) = \delta_{d,1}\varepsilon^{bkg}_{tag}h^{bkg}(\eta) + \delta_{d,-1}\overline{\varepsilon}^{bkg}_{tag}h^{bkg}(\eta) + \delta_{d,0}(1-\varepsilon^{bkg}_{tag}-\overline{\varepsilon}^{bkg}_{tag})U(\eta), \tag{4.21}$$

where ε^{bkg}_{tag} and $\overline{\varepsilon}^{bkg}_{tag}$ represents the efficiency to tag a background candidate as a B or a $\overline{B}$ respectively, and $h^{bkg}(\eta)$ is the normalized η distribution for the background events. Similarly to what done for

the signal model in the previous section, the tagging efficiencies can be parametrised as:

$$\begin{aligned} \varepsilon_{tag}^{bkg} &= \frac{\hat{\varepsilon}_{tag}^{bkg}}{2}(1 + \Delta\varepsilon_{tag}^{bkg}), \\ \bar{\varepsilon}_{tag}^{bkg} &= \frac{\hat{\varepsilon}_{tag}^{bkg}}{2}(1 - \Delta\varepsilon_{tag}^{bkg}), \end{aligned} \tag{4.22}$$

where $\hat{\varepsilon}_{tag}^{bkg}$ and $\Delta\varepsilon_{tag}^{bkg}$ are the average and asymmetry of the two tagging efficiencies. Assuming that η_{OS} and η_{SS} are uncorrelated, the combined probability function including both the taggers can be expressed as:

$$\Omega^{bkg}(d_{OS}, \eta_{OS}, d_{SS}, \eta_{SS}) = \Omega_{OS}^{sig}(d_{OS}, \eta_{OS}) \cdot \Omega_{SS}^{sig}(d_{SS}, \eta_{SS}). \tag{4.23}$$

4.4.3 Calibration of the FT algorithms in Run 1

In the final unbinned maximum likelihood fit to data the OS, SS*comb* (for the $\pi^+\pi^-$ final state) and the SS*kNN* algorithm (for the K^+K^- spectrum) are combined together in order to extract the values of the *CP* asymmetries. While the OS and the SS*comb* taggers are calibrated directly during the final fit using the $B^0 \to K^+\pi^-$ flavour specific decay, the signal yield of the $B_s^0 \to \pi^+K^-$, the other natural control channel for the $H_b \to h^+h'^-$ decays, is not sufficiently large ($\sim 8\%$ of the $B^0 \to K^+\pi^-$ yield) to perform a reliable SS*kNN* tagger calibration. For this reason the SS*kNN* algorithm, as well as the SSπ*BDT* and the SSp used for the SS*comb* combination, have to be calibrated before to perform the final fit to data.

SSπ*BDT* and SSp calibration

The SSπ*BDT* and the SSp are calibrated using a background subtracted sample of $B^0 \to K^+\pi^-$ decay. The signal is extracted using the *sPlot* technique [122] by means of a unbinned maximum likelihood fit to the invariant mass distribution of the $K^\pm\pi^\mp$ final state. The various contributions are described with the p.d.f.s used in the final fit to data, reported in Section 5.3. The only difference concerns the $B^0 \to \pi^+\pi^-$ and $B_s^0 \to K^+K^-$ cross-feed backgrounds, which are neglected in this fit since their yields correspond to less than 1% of the signal. The invariant mass distribution in the $K^\pm\pi^\mp$ hypothesis is shown in Figure 4.2 with the results of the fit superimposed.

The parameters governing the relation between the predicted (η) and observed (ω) mistag, given in Equation 4.13, of the SSπ*BDT* and SSp taggers are determined by means of an unbinned maximum likelihood fit to the tagged decay-time distribution using the mistag probability on a per-event basis. The p.d.f.s used in the fit are the ones reported in Section 4.4.1. At this level, the differences between the flavour tagging calibration of B^0 and $\bar{B}^0$ are neglected, fixing the corresponding parameters to 0. Also the value of the average predicted mistag probability $\langle\eta\rangle$ has been fixed to 0.44. The results of the calibrations are reported in Table 4.2 while the relation between $\eta_{(\pi,p)}$ and $\omega_{(\pi,p)}$

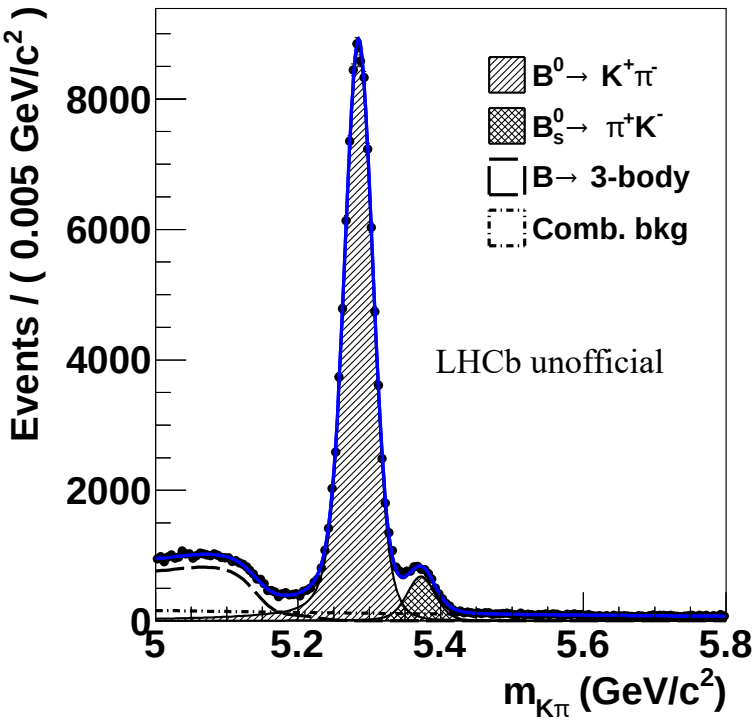

Figure 4.2: Invariant mass distribution in the $K^{\pm}\pi^{\mp}$ final-state hypothesis. The result of the fit is superimposed. The $B^0 \to \pi^+\pi^-$ and $B_s^0 \to K^+K^-$ cross-feed backgrounds have been neglected since their yields correspond to less than 1% of the signal.

are shown in Figure 4.3 with the result of the fit and the η distribution superimposed. As an additional check, the calibration is repeated splitting the sample category of the predicted mistag (η) in such a way to have approximately the same tagging power in each category. The data points depicted in Figure 4.3 represent the average observed mistag probability obtained in the different categories. The observed mistag values are determined by means of a time-dependent fit to the various sub-samples. Performing the calibration of the tagging algorithms using both a per-event and a per-category mistag probability allows to ensure the linear dependence between η and ω, which is assumed in the unbinned fit. The calibration parameters obtained using the two fit methods result to be in very good agreement, as reported in Table 4.2. Finally the S$S\pi BDT$ and SSp tagging performance are reported in Table 4.3, where the tagging power has been evaluated using a per-event mistag probability.

Table 4.2: Calibration parameters for the S$S\pi BDT$ and SSp taggers with their statistical uncertainties.

Tagger	mode	p_0	p_1	$\langle\eta\rangle$	$\rho_{p0,p1}$
S$S\pi BDT$	per-event	0.4374 ± 0.0034	0.942 ± 0.085	0.44	-0.377
	category	0.4367 ± 0.0034	0.978 ± 0.091	0.44	-0.405
SSp	per-event	0.4472 ± 0.0046	0.724 ± 0.105	0.44	-0.581
	category	0.4464 ± 0.0048	0.754 ± 0.114	0.44	-0.617

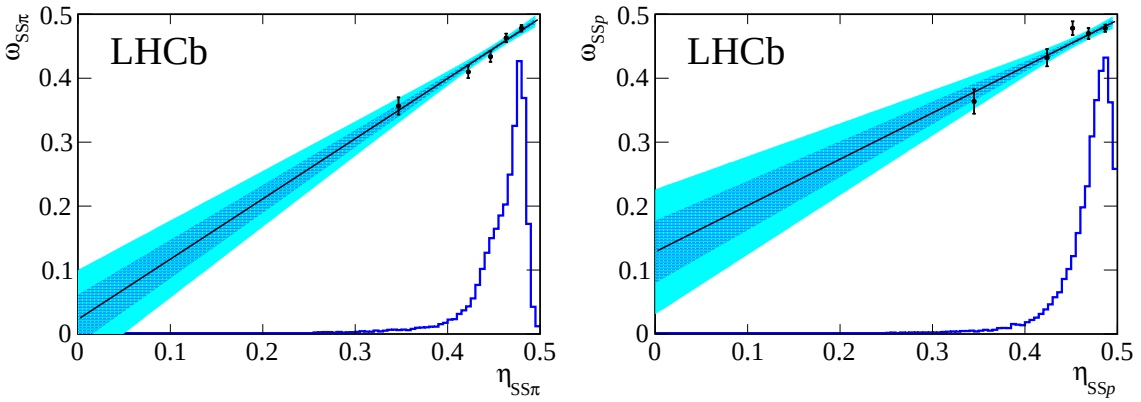

Figure 4.3: Calibration plots for S$S\pi BDT$ tagger(left), SSp tagger (right). The data points represent the average observed mistag probability obtained in different bins of the predicted mistag (η). The η distribution is also shown.

S$SkNN$ calibration

The S$SkNN$ algorithm is calibrated using a background subtracted sample of $B_s^0 \to D_s^- \pi^+$ decay. The signal is extracted through of the *sPlot* technique by means of an invariant mass fit. The signal

Table 4.3: Tagging efficiency and tagging power of the $SS\pi BDT$ and SSp algorithms.

Tagger	ε_{tag} [%]	ε_{eff} [%]
$SS\pi BDT$	65.48 ± 0.19	0.81 ± 0.13
SSp	44.73 ± 0.24	0.42 ± 0.17

decay has been parametrised using a double Gaussian function, while the background has been described using a simple exponential function. The invariant mass distribution with the fit result superimposed is shown in Figure 4.4.

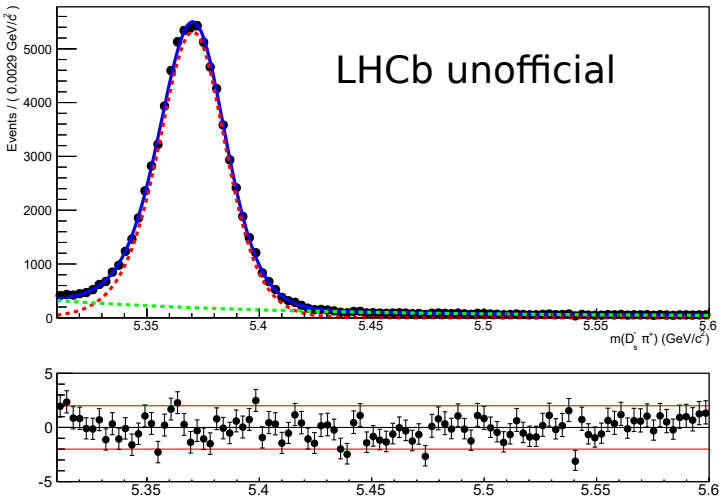

Figure 4.4: Invariant mass fit to the $B_s^0 \to D_s^- \pi^+$ mass distribution. The results of the best fit is superimposed (blue). The signal contribution has been parametrised using a double Gaussian function (red), while the combinatorial background has been described using a simple exponential function (green).

Also in this case, the calibration parameters are determined by means of an unbinned maximum likelihood fit to the tagged decay rates. The p.d.f.s used in the fit are the same used for the $SS\pi BDT$ and SSp calibration and the value of $\langle\eta\rangle$ has been fixed to 0.44. The results of the per-event fit are reported in Table 4.4. The linearity of the relation between η and ω is verified splitting the sample in predicted mistag categories and determining the average mistag fraction ($\langle\eta\rangle$) for each bin as done for the $SS\pi BDT$ and SSp taggers. In order to take into account the different kinematic and occupancy between the $B_s^0 \to D_s^- \pi^+$ and the $H_b \to h^+ h'^-$ decays, the *sWeights*, determined by means of the *sPlot* technique, are multiplied by an additional per-event weight. This reweighting is performed equalising the distributions of the transverse momentum (p_T), the pseudorapidity (η) and the azimuthal angle (ϕ) of the B_s^0 meson, the number of primary vertices ($nPVs$) and the number of tracks ($nTracks$). The distributions related to the $H_b \to h^+ h'^-$ decay modes have been obtained from

a background subtracted sample of $H_b \to h^+h'^-$ applying a per-event weight corresponding to the PID efficiency of the B candidate as function of the momentum and pseudorapidity of the final state particles. During the reweighting procedure the relevant correlations among the variables, i.e. those greater than 10%, are taken into account. According to the correlation factors reported in Table 4.5 there are two couple of variables that are not independent one from each other: the transverse momentum and the pseudorapidity of the B_s^0 meson, and the number of tracks and primary vertices. Thus, the three different reweighting are performed: a kinematic reweighting involving the p_T and η of the B_s^0 meson, an occupancy reweighting including $nPVs$ and $nTracks$, and a reweighting of the azimuthal angle. At the end, the sweights obtained through the *sPlot* technique will be multiplied by a per-event weight defined as the product of the three weights obtained from the reweightings. The distributions of all the variables, before and after the full reweighting, are shown in Figure 4.5. The SkNN calibration has been determined for each type of reweighting in order to observe any possible deviation from the calibration obtained on the $B_s^0 \to D_s^-\pi^+$ un-reweighted sample. Fixing the value of $\langle\eta\rangle$ to 0.44 has allowed an easier comparison of the various calibrations. The results of the different calibrations are reported in Table 4.4, where the "full" calibration is obtained applying all the three reweightings. The kinematic reweighting is the only one affecting significantly the SkNN calibration parameters. As consequence of further studies, performed in order to check the dependence of SkNN calibration on the average p_T of the B_s^0 meson, which are described in Appendix B, the SkNN algorithm is calibrated according to the kinematic reweighting. The final parameters, including the ones governing a possible difference between the calibrations of B_s^0 and $\bar{B}_s^0$ mesons, are reported in Table 4.6 and will be fixed in the final fit to data. Their errors and correlations, reported in Table 4.7, will be taken into account in order to determine the systematic uncertainties. After the full reweighting, the tagging power provided by the SkNN taggers is equal to $\varepsilon_{eff} = 1.26\%$, a value significantly lower with respect to the tagging power computed without any reweighting. This loss in the tagging power is expected since it is well known that the SS tagging performance depends on the transverse momentum of the B meson: B_s^0 mesons with low p_T are associated to fragmentation particles with a lower transverse momentum, and consequently more background-like, reducing the ability of the SS tagging algorithms to identify the right charge correlated tracks. The functional relation between the predicted and the real mistag evaluated using the SkNN tagger is shown in Figure 4.6.

4.4.4 Distributions of the predicted mistag

As mentioned in Section 4.3, the combined p.d.f, represents an accurate description of the multidimensional distribution only if the predicted mistag distributions for the OS and SS (SkNN) taggers

Table 4.4: Calibration parameters in the $B_s^0 \to D_s^- \pi^+$ sample after the kinematic, occupancy and the final reweighting.

Reweighting	p_0	p_1
–	0.4402 ± 0.0047	1.028 ± 0.069
kinematic	0.4552 ± 0.0054	0.752 ± 0.090
occupancy	0.4443 ± 0.0052	0.982 ± 0.052
full	0.4577 ± 0.0054	0.725 ± 0.092

Table 4.5: Correlation factors of the variables taken in account for the $B_s^0 \to D_s^- \pi^+$ reweighting.

	p_T^B	η	ϕ	N_{tracks}	N_{PVs}
p_T^B	1				
η	-0.514913	1			
ϕ	-0.00358053	0.012118	1		
N_{tracks}	-0.0656754	0.0354494	-0.0014845	1	
N_{PVs}	-0.0474417	0.0193796	-0.00507446	0.609092	1

Table 4.6: Calibration parameters for the S$SkNN$ tagger, determined using kinematic reweighted $B_s^0 \to D_s^- \pi^+$ sample. The value of $\hat{\eta}$ is fixed in the fit to 0.44. The value of $\varepsilon_{SSkNN}^{sig}$ is not reported since it will be free to vary in the final fit to data.

Parameter	Value
$\Delta\varepsilon_{SSkNN}^{sig}$	-0.00434 ± 0.00659
$\hat{p}_0^{SSkNN}$	0.45558 ± 0.00502
Δp_0^{SSkNN}	-0.01082 ± 0.00479
$\hat{p}_1^{SSkNN}$	0.7588 ± 0.0922
Δp_1^{SSkNN}	0.0341 ± 0.0514

Table 4.7: Correlation factors among the S$SkNN$ calibration parameters determined from the kinematic reweighted $B_s^0 \to D_s^- \pi^+$ sample.

Parameter	$\Delta\varepsilon_{SSkNN}^{sig}$	$\hat{p}_0^{SSkNN}$	Δp_0^{SSkNN}	$\hat{p}_1^{SSkNN}$	Δp_1^{SSkNN}
$\Delta\varepsilon_{SSkNN}^{sig}$	1.000	0.004	0.105	0.009	−0.100
$\hat{p}_0^{SSkNN}$	–	1.000	0.001	−0.114	0.021
Δp_0^{SSkNN}	–	–	1.000	0.014	−0.171
$\hat{p}_1^{SSkNN}$	–	–	–	1.000	−0.141
Δp_1^{SSkNN}	–	–	–	–	1.000

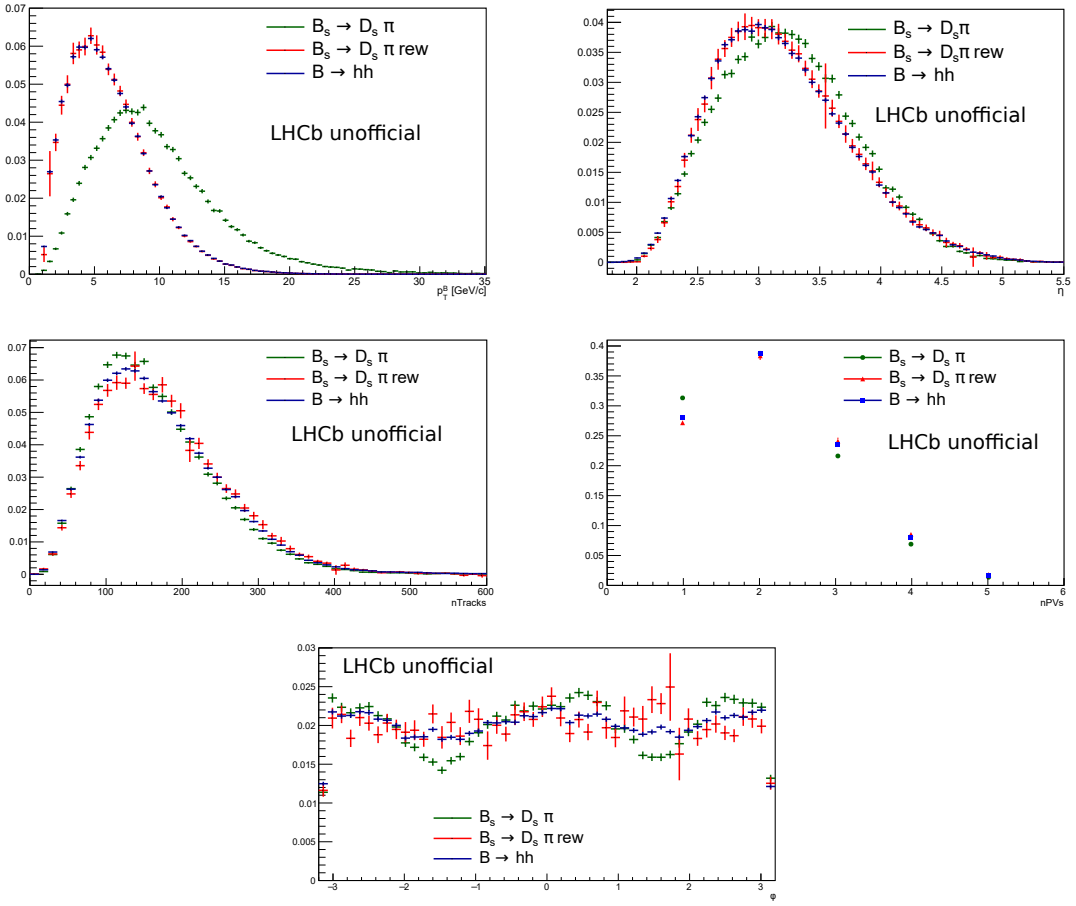

Figure 4.5: Distribution of the variables before and after the complete reweighting procedure. In the first row the plot of B transverse momentum (left) and pseudorapidity (right), in the second row nTracks (left) and nPVs (right) and in the third row the azimuthal angle distribution. For each plot the distribution of the variable in the $B_s^0 \to D_s^- \pi^+$ un-reweighted sample, the distribution on the $B_s^0 \to D_s^- \pi^+$ reweighted sample and the distribution on the $B \to h^+ h'^-$ sample are shown in green, red and blue, respectively.

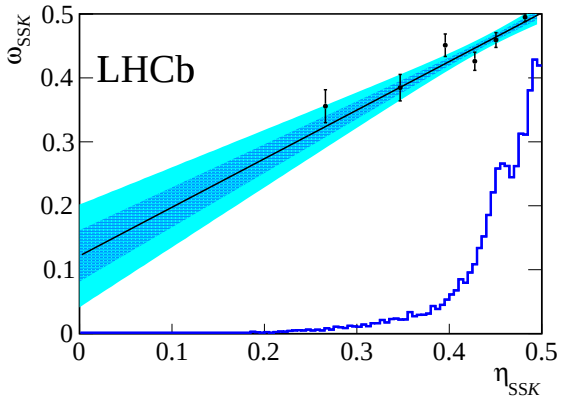

Figure 4.6: Calibration plot for S$SkNN$ tagger. The data points represent the average observed mistag probability obtained in different bins of the predicted mistag (η). The η distribution is also shown.

are uncorrelated. In order to check this assumption a background subtracted sample of $H_b \to h^+h'^-$ decays, obtained as described in Section 5.1.6, is exploited. The correlations of the predicted mistag between SS and OS taggers for the signal decays are reported in Table 4.8, proving that the different algorithms have uncorrelated η distributions. The bi-dimensional distributions of the predicted mistag used to extract the correlation factor are shown in Figure 4.7. In Table 4.8 the correlation factors for the combinatorial background, determined using the data in the upper invariant mass sideband ($m > 5.6\,\text{GeV}/c^2$), are also reported.

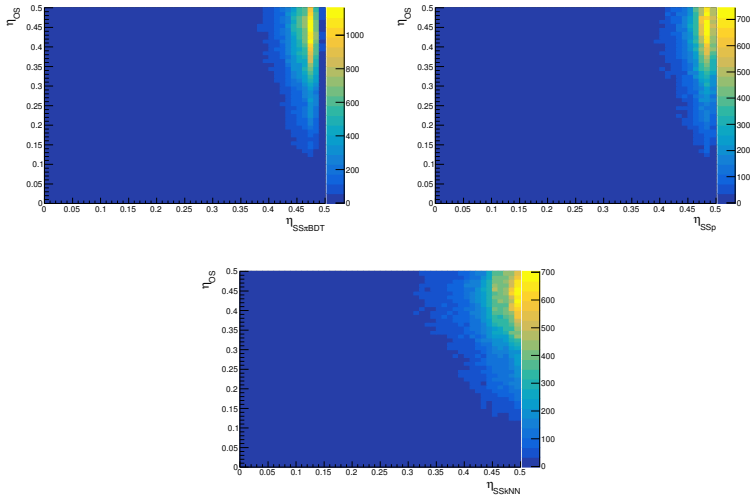

Figure 4.7: Two-dimensional distribution of the mistag fractions predicted by the OS, SSπBDT, SSp and SSkNN algorithms, obtained by means of a background subtracted sample of $H_b \to h^+h'^-$.

Table 4.8: Correlation between the predicted mistag probability of OS, SSπBDT, SSp and SSkNN algorithms determined using a background subtracted sample of $H_b \to h^+h'^-$ decays. Also the correlations factors for combinatorial background candidates, selected from the higher invariant mass region ($m > 5.6\,\text{GeV}/c^2$), are reported.

Variables	Correlation for signals	Correlation for background
η_{OS}, $\eta_{SS\pi BDT}$	-0.027	0.000
η_{OS}, η_{SSp}	0.009	0.053
η_{OS}, η_{SSkNN}	0.007	0.058

In order to obtain the final histograms describing the predicted mistag probability for the signal decay modes and cross-feed backgrounds the predicted mistag distributions, obtained from the background subtracted sample, are reweighted according the PID efficiency of the B candidate as function of the momentum and pseudorapidity of the final state particles. Indeed the PID requirements can affect the transverse momentum distribution of the B candidate and consequently

modify the η distributions. As an example, the distributions of the OS predicted mistag probability reweighted according to the PID requirements used to determine the three final states are shown in Figure 4.8. The discrepancy induced by the PID requirements is not significantly large but nonetheless is taken into account in the final fit to data.

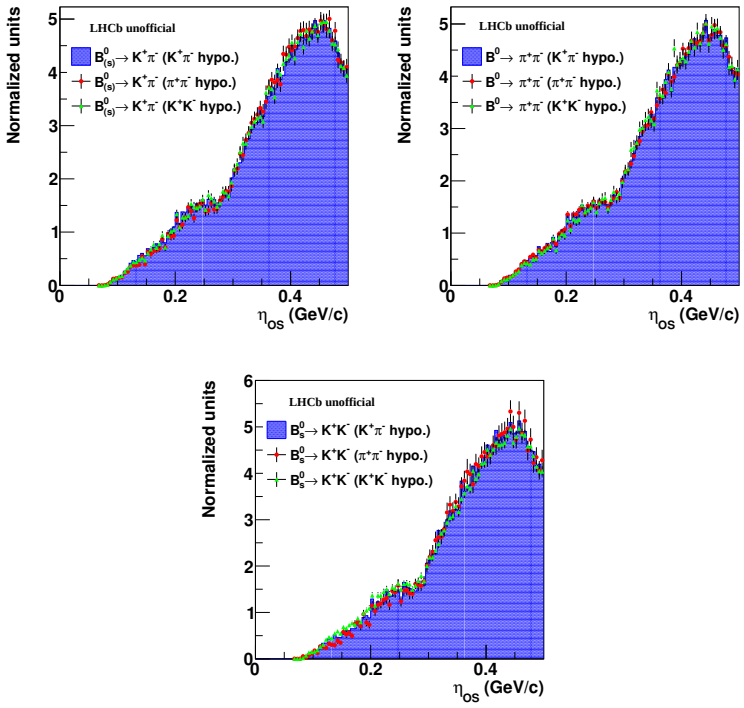

Figure 4.8: Distributions of the mistag fraction predicted by the OS algorithm, obtained using a background subtraction of the $H_b \to h^+h'^-$ sample. The effect of different PID requirement, indicted in the legends as "$h^+h'^-$ hypo" (with $h = K, \pi$), is reproduced applying a weight on a per-event basis to the B candidates.

For what concern the η distributions related to the combinatorial and partially reconstructed backgrounds, for all the three final states they are described by means of histograms filled with B candidates in the upper ($m > 5.6\,\text{GeV}/c^2$) and lower ($m < 5.2\,\text{GeV}/c^2$) invariant mass sideband, respectively. In the case of the partially reconstructed background, the residual contamination due to the combinatorial background in the lower invariant mass region is subtracted from the histogram. The amount of combinatorial background events to be removed is computed fitting the high invariant mass region with an exponential function and then extrapolating the number of expected events in the low invariant mass sideband.

The final histograms of the η distributions in all three final states are reported in Section 5.5.

4.4.5 Flavour Tagging performance

A summary of the tagging powers of the OS and SS algorithms on the $B^0 \to \pi^+\pi^-$ and $B_s^0 \to K^+K^-$ decays are reported in Table 4.9. The total tagging power available is also shown.

Table 4.9: Summary of the tagging powers for the $B^0 \to \pi^+\pi^-$ and $B_s^0 \to K^+K^-$ Run 1 data samples, with a breakdown of the OS and SS contributions.

Tagging algorithm	Tagging power [%]
OS	2.94 ± 0.17
$SS\pi$	0.81 ± 0.13
SSp	0.42 ± 0.17
$SScomb$	1.17 ± 0.11
SSK	0.71 ± 0.12
Total $B^0 \to \pi^+\pi^-$	4.08 ± 0.20
Total $B_s^0 \to K^+K^-$	3.65 ± 0.21

4.5 Flavour Tagging in Run 2

As mentioned in the previous sections, the flavour tagging performance depends on the kinematic of the decay of interest. In addition, the flavour tagging performance is also sensitive to the data taking conditions, such as the center of mass energy, the trigger efficiency, the tracks multiplicity and the number of primary vertices reconstructed in the event. Because of this dependence a difference in the flavour tagging performance is expected between the Run 1 and Run 2 data samples. However the trend of the variations is not expected to be the same for all the tagging algorithms available in LHCb, in particular due to the different characteristics between the OS and SS taggers. Indeed a raw application of the available tagging algorithms, optimised on Run 1 data, on a data sample collected with Run 2 data taking conditions leads to show a small natural improvement of about $\sim 10\%$ with respect the Run 1 data for the SS taggers. On the other hand the OS algorithms turn out to have a loss in the flavour tagging performance of about $\sim 30\%$ with respect to those in Run 1. The increase of the SS tagger performance is mainly due to a higher transverse momentum of the B mesons which allows a better discrimination of the correct tagging candidate from all the other background particles produced in the event. The loss in tagging performance affecting the OS taggers can be related to the higher track multiplicity which reduces the reconstruction efficiency of the opposite B hadron.

In order to regain the OS tagging power loss and to further increase the overall flavour tagging

performance in Run 2 data samples, a wide re-optimisation campaign has been performed. This campaign has consisted in a retuning or redesigning of the flavour tagging algorithms using the new Run 2 data. In particular the OS algorithms exploiting electrons (OS e), muons (OS μ) and kaons (OS K) have been completely revisited and optimized, while the other OS taggers (OSc and OSVtx) are remained untouched, since their performance were compatible with respect to those obtained with Run 1 data. The reoptimisation of the OS e, OS μ and OS K algorithms consists of two steps. Each of these steps is performed on an independent subsample of events taken from the $B^+ \to J/\psi K^+$ Run 2 data sample. Firstly a tagging candidate selection is performed using various kinematic, geometrical and PID information. A numerical optimisation of the candidate selection has been performed by means of gradiant boosted regression trees as a function of the applied requirements, maximising the average tagging power defined as:

$$\langle \varepsilon_{eff} \rangle = f(\hat{\theta} > \hat{x}) \tag{4.24}$$

where $\hat{\theta}$ is the set of information used in the candidate selection and $\hat{x}$ is the best set of values determined by the optimisation. At each step, the tagging track candidate with the highest transverse momentum is taken in order to evaluate the average tagging power. The second step consists in the training of the multivariate classifier. The aim of the training lies in the discrimination between the signal, represented by the tracks correctly correlated to the B meson flavour, and the background, comprising the tracks wrongly correlated to the B meson flavour. Since the B^+ meson is not affected by the flavour oscillations, the rightly and wrongly tagged B candidates are easily identified, since the true flavour is determined by the B charge. Also, in this case, both kinematic and geometrical information are used as input to the algorithm. Finally the multivariate output is converted into a predicted mistag rate. The OS tagging performance has been evaluated on an independent sample of $B^0 \to D^-\pi^+$ Run 2 data, after having properly calibrated the predicted mistag rate. The tagging performance is reported in Tab. 4.10 and is compatible with those obtained in Run 1. Thus the initial loss in the tagging power has been recovered thanks to the tagging re-optimisation.

Regarding the SS tagging algorithms the SSπ and SSp are remained untouched while the SSK has been deeply revisited replacing the two multivariate classifiers based on Neural Networks, used for determining its tagging decisions and for evaluating the predicted mistag probability [119], with two classifiers based on Boosted Decision Trees. The redesign of the SSK tagging algorithm is performed on fully simulated events of $B_s^0 \to D_s^-\pi^+$ decay mode, since the fast oscillations of the B_s^0 meson makes impossible the classifier training on data. After a loose pre-selection applied to the tagging tracks in order to reduce the background contamination, the optimisation strategy consists of two classifiers. The first multivariate algorithm is trained to discriminate between the true tagging tracks, coming from the fragmentation of the signal B_s^0 meson, and underlying tracks, originating from

soft QCD processes and uncorrelated to the signal B_s^0 meson flavour. For each B_s^0 candidate, the three tagging tracks' candidates with highest multivariate score are used for the training of the second classifier. This algorithm is trained with the aim to distinguish the B_s^0 from the $\overline{B}_s^0$ mesons and providing a tagging decision and a predicted mistag rate. The SSK tagging performance, reported in Tab. 4.10, have been obtained on a Run 2 data sample of $B_s^0 \to D_s^- \pi^+$ decays. The tagging power results to be about 45% higher with respect to those available in Run 1. For sake of completeness also the tagging performance of the algorithms that did not go through a reoptimisation process are reported in Tab. 4.10.

Table 4.10: Summary of the performance of the tagging algorithms after the re-optimisation campaign on the $B^0 \to D^- \pi^+$ decay channel ($B_s^0 \to D_s^- \pi^+$ for the SSK). The SScomb algorithm comprises only the S$S\pi$ and SSp taggers.

Tagger	ε [%]	ω [%]	$\varepsilon\langle D^2\rangle = \varepsilon(1-2\omega)^2$ [%]
OSμ	8.915 ± 0.053	30.713 ± 0.434	1.361 ± 0.062
OSe	4.451 ± 0.038	34.038 ± 0.604	0.454 ± 0.035
OSK	19.600 ± 0.073	37.557 ± 0.315	1.214 ± 0.061
OSVtx	20.834 ± 0.075	36.994 ± 0.308	1.410 ± 0.067
OSc	5.025 ± 0.040	34.062 ± 0.620	0.511 ± 0.040
OScomb	40.154 ± 0.090	35.123 ± 0.211	3.555 ± 0.101
SSK	68.190 ± 0.177	39.667 ± 0.507	2.912 ± 0.286
SSπ	83.486 ± 0.068	42.561 ± 0.145	1.848 ± 0.072
SSp	37.767 ± 0.089	43.645 ± 0.221	0.610 ± 0.042
SScomb	87.590 ± 0.061	41.787 ± 0.142	2.364 ± 0.081

4.6 Flavour tagging in CPV measurement on two-body B decays in Run 2

Also the update of the measurement concerning the CP violation in the charged two-body B decays using events collected with Run 2 conditions exploits both the Opposite Side and the Same Side taggers. The probability functions for the tagging decision d and the predicted mistag probability η associated to the $B \to h^+h'^-$ decays and various background contributions are determined exploiting the same strategy used in Run 1 analysis 4.4. However in order to take into account the different data taking conditions between Run 1 and Run 2 and the different kinematic of the signal $B_{(s)}^0$ candidates, the calibration of the flavour tagging algorithms and the templates used to describe the predicted mistag probability distributions have been determined from the top using the Run 2

data samples.

4.6.1 Calibration of the FT algorithms in Run 2

As done for the Run 1 data, the OS and the SS*comb* taggers are calibrated on the fly in the final fit using the $B^0 \to K^+\pi^-$ decay while the SSkNN, SSπBDT and SSp taggers are previously calibrated using a sample of $B_s^0 \to D_s^-\pi^+$ and $B^0 \to K^+\pi^-$ decays, respectively. However, while in Run 1 the OS algorithm was combined using non-calibrated taggers, in the Run 2 analysis a new step is introduced, with the aim to calibrate every single OS algorithm before to perform the final combination. Indeed it has been observed that performing a combination of calibrated taggers leads to higher tagging performance.

OS tagger calibration

The single OS tagging algorithms are calibrated using a background subtracted sample of $B^+ \to D^0\pi^+$ decay. In order to take into account the different kinematic and occupancy between the $B^+ \to D^0\pi^+$ and the $H_b \to h^+h'^-$ decays, a reweighting is performed equalising simultaneously the distributions of the transverse momentum (p_T) and the SPD multiplicity ($nSPD$). As done for the Run 1 analysis, the distributions related to the $H_b \to h^+h'^-$ decay modes have been obtained from a background subtracted sample of $H_b \to h^+h'^-$ applying a per-event weight corresponding to the PID efficiency of the B candidate as function of the momentum and pseudorapidity of the final state particles. The signal is then extracted using the *sPlot* technique [122] by means of a unbinned maximum likelihood fit to the invariant mass distribution and the sweights are multiplied by the per-event PID weight. The invariant mass distribution is shown in Figure 4.9 with the results of the fit superimposed.

The parameters governing the relation between the predicted (η) and observed (ω) mistag are determined by means of a binomial regression performed by the Espresso Performance Monitor tool [123], where the mistag information is used on a per-event basis. The results of the calibrations are reported in Table 4.11 while the calibration plots are shown in Figure 4.10. with the η distributions. The data points depicted in Figure 4.10 represent the average observed mistag probability obtained in different bins of the predicted mistag (η). Finally the OS tagging performance are reported in Table 4.12, where the tagging power has been evaluated using a per-event mistag probability.

SS tagger calibration

The SSπBDT, SSp tagging algorithms are calibrated using a background subtracted sample of $B^0 \to D^-\pi^+$ decays while the $B_s^0 \to D_s^-\pi^+$ decay has been exploited in order to calibrate the SSkNN tag-

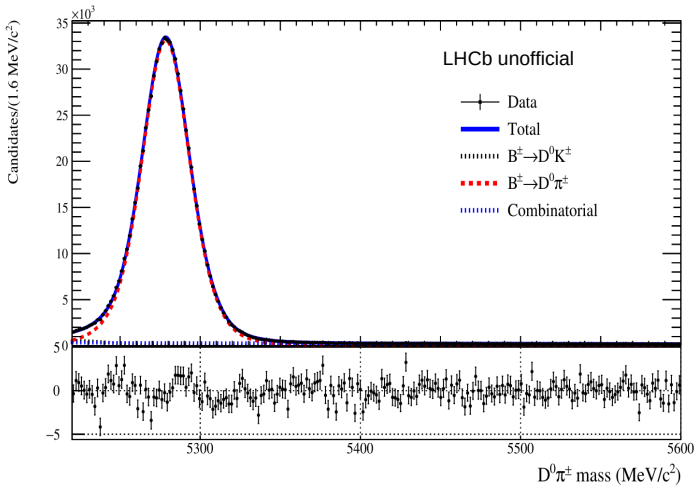

Figure 4.9: Invariant mass distribution of the $B^+ \to D^0\pi^+$ Run 2 sample. The result of the fit is superimposed.

Table 4.11: Calibration parameters for the various OS taggers with their statistical uncertainties.

Tagger	p_0	p_1	$\langle\eta\rangle$	$\rho_{p0,p1}$
OSe	0.3123 ± 0.00740	0.549 ± 0.10949	0.3247	0.11031
OS mu	0.2506 ± 0.0047	0.346 ± 0.070322	0.2747	0.20187
OS K	0.3717 ± 0.0036	0.537 ± 0.082322	0.3764	0.12223
OS Vtx	0.3696 ± 0.0032	0.794 ± 0.050699	0.3795	0.10988
OS c	0.3471 ± 0.0064	1.126 ± 0.1267	0.3566	0.13088

Table 4.12: Tagging efficiency and tagging power of the various OS tagging algorithms.

Tagger	ε_{tag} [%]	ε_{eff} [%]
OS e	3.313 ± 0.054	$0.528 \pm 0.010(stat) \pm 0.038(cal)$
OS mu	8.395 ± 0.083	$1.89 \pm 0.02(stat) \pm 0.07(cal)$
OS K	14.64 ± 0.106	$1.15 \pm 0.01(stat) \pm 0.06(cal)$
OS Vtx	19.79 ± 0.119	$1.53 \pm 0.01(stat) \pm 0.07(cal)$
OS c	4.576 ± 0.062	$0.434 \pm 0.007(stat) \pm 0.035(cal)$

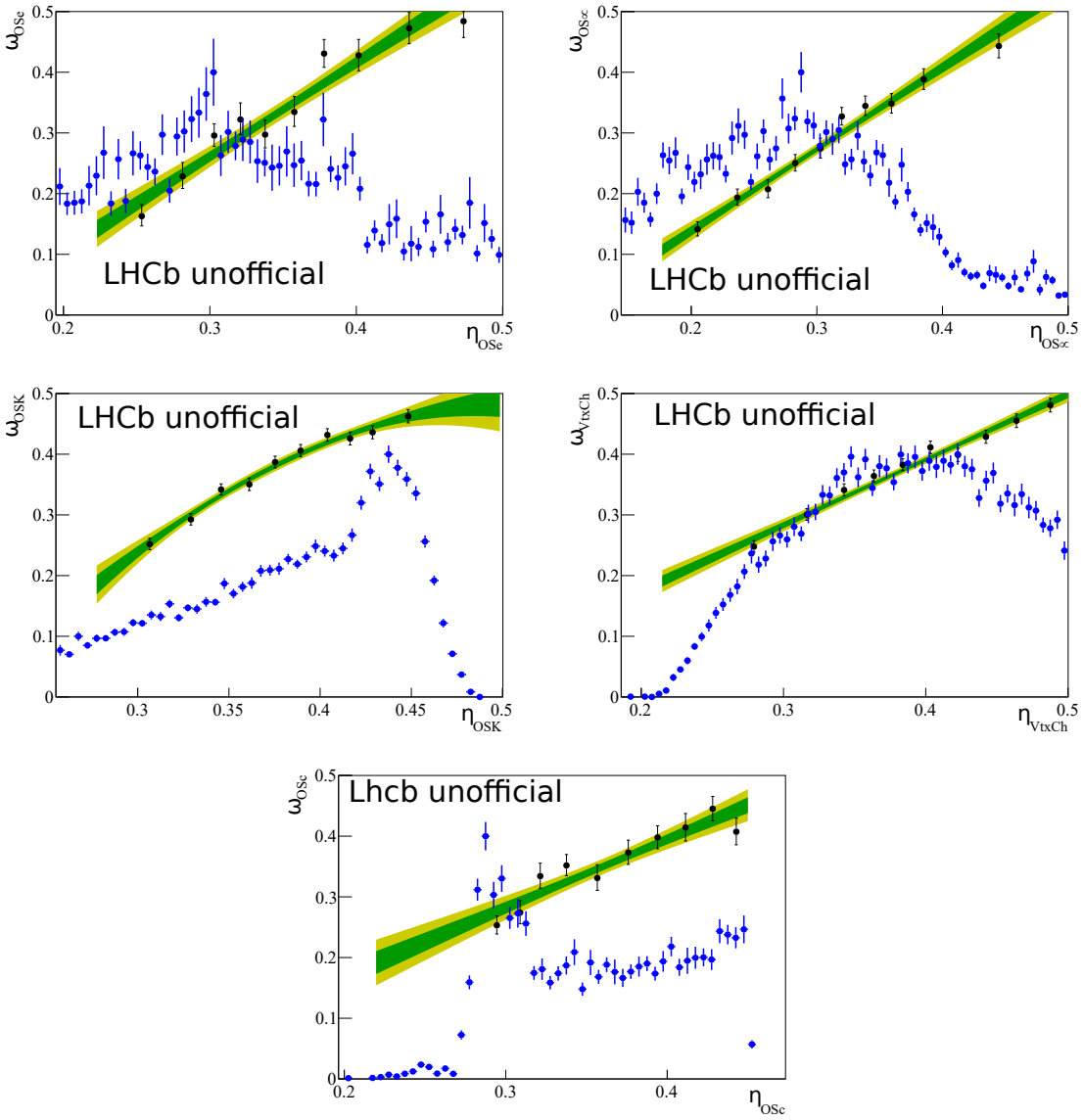

Figure 4.10: Calibration plots for the various OS taggers: from left to right OS e, OS μ, OS K, OS Vtx and OS c. The data points represent the average observed mistag probability obtained in different bins of the predicted mistag (η). The η distribution is also shown.

ger. In order to take into account the different kinematic and occupancy between the $B^0 \to D^- \pi^+$ ($B_s^0 \to D_s^- \pi^+$) and the $H_b \to h^+ h'^-$ decays, a reweighting is performed equalising simultaneously the distributions of the transverse momentum (p_T) and the SPD multiplicity ($nSPD$). Also in this case, the distributions related to the $H_b \to h^+ h'^-$ decay modes have been obtained from a background subtracted sample of $H_b \to h^+ h'^-$ applying a per-event weight corresponding to the PID efficiency of the B candidate as function of the momentum and pseudorapidity of the final state particles. Finally he signal is determined using the *sPlot* technique [122] using an unbinned maximum likelihood fit to the invariant mass distribution. The so-evaluated sweights are then multiplied by the per-event PID weight. The two invariant mass distributions are shown in Figure 4.11 with the results of the fit superimposed.

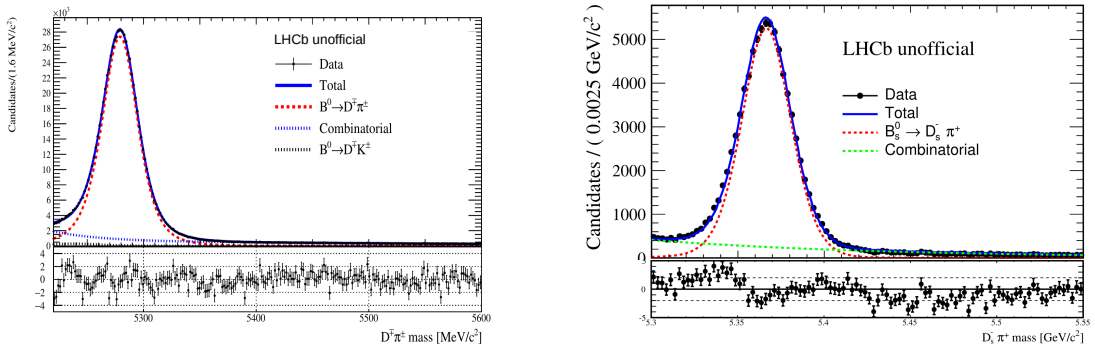

Figure 4.11: Invariant mass distribution of the $B^0 \to D^- \pi^+$ and $B_s^0 \to D_s^- \pi^+$ Run 2 samples. The result of the fit is superimposed.

The EPM tool is used to determine the calibration parameters of the different algorithm, using the mistag on a per-event basis. The results of the calibrations are reported in Table 4.13 while the calibration plots are shown in Figure 4.12 among with the η distribution. The data points depicted in Figure 4.10 represent the average observed mistag probability obtained in different bins of the predicted mistag (η). Finally the SS tagging performance are reported in Table 4.12, where the tagging power has been evaluated using a per-event mistag probability.

Table 4.13: Calibration parameters for the various SS taggers with their statistical uncertainties.

Tagger	p_0	p_1	$\langle\eta\rangle$	$\rho_{p0,p1}$
$SS\pi BDT$	0.4743 ± 0.0021	0.9762 ± 0.0433	0.4727	0.33513
SSp	0.4741 ± 0.0033	0.9528 ± 0.0675	0.4780	0.14578
$SSkNN$	0.4897 ± 0.0110	1.0230 ± 0.1322	0.4731	0.47674

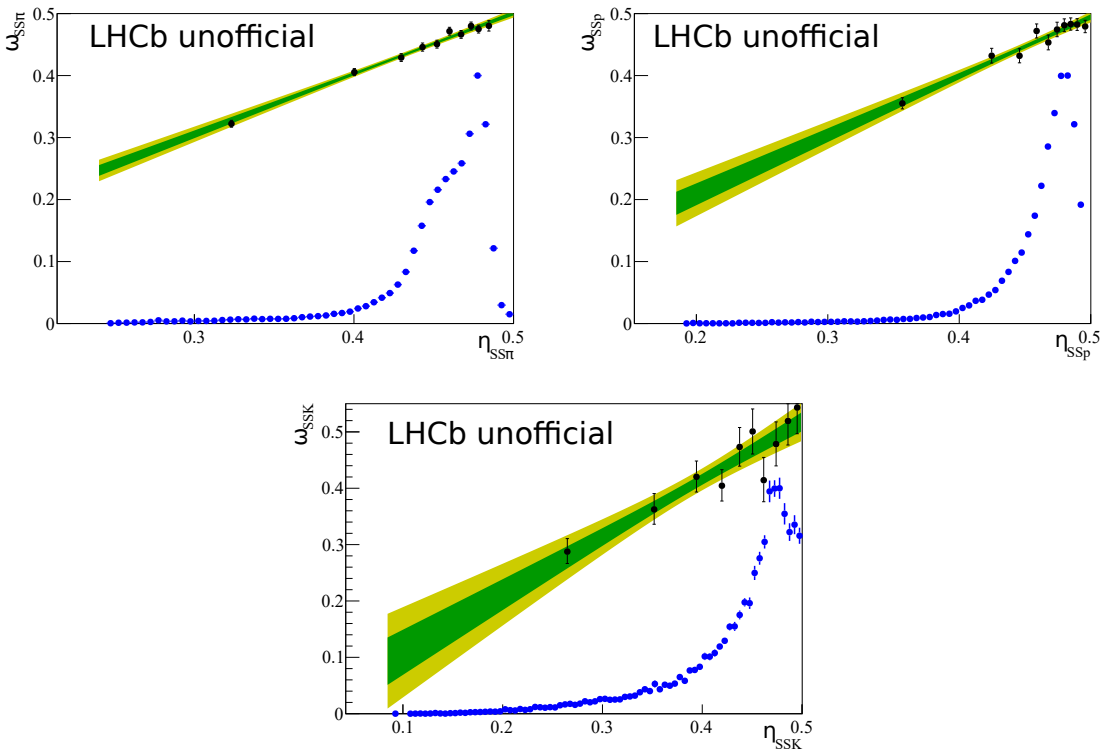

Figure 4.12: Calibration plots for the various SS taggers: from left to right $SS\pi BDT$, SSp and $SSkNN$. The calibrations of the $SS\pi$ and SSp taggers have been evaluated on a sample of $B^0 \to D^-\pi^+$ decays, while for the SSK algorithm the $B_s^0 \to D_s^-\pi^+$ is exploited. In both cases a kinematic reweighted, taking into account the p_T of the B meson and the $nSPD$ distribution, is performed. The data points represent the average observed mistag probability obtained in different bins of the predicted mistag (η). The η distribution is also shown.

Table 4.14: Tagging efficiency and tagging power of the various SS tagging algorithms. The performance of the $SS\pi$ & SSp and SSK taggers have been evaluated sample of $B^0 \to D^-\pi^+$ and $B_s^0 \to D_s^-\pi^+$ decays, respectively. In both cases a simultaneous reweighting on the p_T of the B meson and the $nSPD$ distribution is performed in order to correct the $B^0 \to D^-\pi^+$ and $B_s^0 \to D_s^-\pi^+$ phase space according to the one of the $B \to h^+h'^-$ decays.

Tagger	ε_{tag} [%]	ε_{eff} [%]
$SS\pi BDT$	76.09 ± 0.16	$1.034 \pm 0.005(stat) \pm 0.059(cal)$
SSp	38.42 ± 0.18	$0.439 \pm 0.004(stat) \pm 0.045(cal)$
$SSkNN$	49.88 ± 0.37	$1.587 \pm 0.019(stat) \pm 0.272(cal)$

4.6.2 Distributions of the predicted mistag

The final histograms describing the predicted mistag probability for the signal decay modes and cross-feed backgrounds are determined from the $H_b \to h^+h'^-$ Run 2 data sample reweighting the corresponding predicted mistag distributions according to the PID efficiency of the B meson as function of the momentum of the final state particles and SPD multiplicity. Regarding the predicted mistag distributions related to the combinatorial and partially reconstructed backgrounds, they are described by means of histograms filled with B candidates in the upper ($m > 5.6\,\text{GeV}/c^2$) and lower ($m < 5.2\,\text{GeV}/c^2$) invariant mass sideband, respectively. In the case of the partially reconstructed background, the residual contamination due to the combinatorial background in the lower invariant mass region is subtracted from the histogram. The amount of combinatorial background events to be removed is computed fitting the high invariant mass region with an exponential function and then extrapolating the number of expected events in the low invariant mass sideband. The final histograms of the η distributions in all three final states are reported in Section 6.4.

4.6.3 Flavour Tagging performance

The total tagging powers of the OS and SS algorithms are reported in Table 4.15.

Table 4.15: Summary of the tagging powers for the $B^0 \to \pi^+\pi^-$ and $B_s^0 \to K^+K^-$ Run 2 data samples.

Tagging algorithm	Tagging power [%]
OS	3.56 ± 0.10
$SScomb$	1.44 ± 0.08
SSK	1.59 ± 0.27

5

CP violation on $B \to h^+h'^-$ decays using Run 1 data

In this chapter both the CP-violating asymmetries in decay and in the interference in the $B^0 \to \pi^+\pi^-$ and $B_s^0 \to K^+K^-$ decays, described in Section 1.5.4, and the direct CP asymmetries in the $B^0 \to K^+\pi^-$ and $B_s^0 \to \pi^+K^-$ decays, discussed in Section 1.5.3, are measured. The measurement is performed using the data sample of pp collisions collected by LHCb during the Run 1 data taking, corresponding to an integrated luminosity of 3 fb^{-1}.

The CP-violating asymmetries are determined through an unbinned maximum likelihood fit performed on the B signal candidates selected through a complex chain of requirements, discussed in detail in Section 5.1. The fit is performed exploiting the classes of the RooFit package [124] and a set of ad-hoc functions and routines developed to fulfil all the analysis requirements. The set of observables used in the fit consists in: the invariant mass m, the decay-time t, the predicted decay-time error δ_t evaluated by reconstruction algorithms, the tagging decision d and the predicted mistag probability η evaluated by the OS and SS flavour tagging algorithms. The fit is performed simultaneously on three different final states: $\pi^+\pi^-$, K^+K^- and $K^\pm\pi^\mp$, determined by means of an optimised set of requirements on the PID of the two particles. The calibration of the PID efficiency, fundamental in such analysis, is described in Section 5.2.

The simultaneous fit allows to take into account the correlations among the parameters which are shared between the different decay modes, such as the calibration parameters of the flavour tagging algorithms and the asymmetries between the production decay rates of the B and $\bar{B}$ mesons. Each final state is fitted through a p.d.f. consisting in two parts: the first one describing the invariant mass distribution, discussed in Section 5.3, and the latter one describing the decay-time component where also the flavour tagging information play an important role, discussed in Section 5.4. The determination of the production asymmetries from the fit itself is a very important step in order to

reduce the systematics on the direct *CP* asymmetries on $B^0 \to K^+\pi^-$ and $B_s^0 \to \pi^+K^-$; indeed it allows to avoid to introduce in the fit fixed values for the production asymmetries taken by external measurements. Another advantage of fitting simultaneously all the final states is that in doing so it is possible to determinate accurately the cross-contamination due to misidentified $H_b \to h^+h'^-$ decays, relating the corresponding yields in the various final states using PID efficiency ratios.

The preliminary results of this measurement were already published in a conference note [70]. The work presented in this chapter represents an update of those results, consisting in an improvement of the event selection, in an additional contribution of the S*S* tagger algorithms and in a better determination of the decay-time acceptance functions. These improvements will be highlighted and discussed in the following sections.

5.1 Event selection

The measurement is performed using the data sample of pp collisions collected with LHCb detector at center-of-mass energy of 7 and 8 TeV during 2011 and 2012, the Run 1 data taking, corresponding to an integrated luminosity of 1 and 2 fb^{-1}, respectively. The event selection consists of different steps: the trigger selection, the event reconstruction, the stripping selection and finally the offline selection.

5.1.1 Trigger selection

The trigger system decides if an event has to be saved and written on tape, since it could be interesting for physics analyses. An event can be stored because of the positive response of one *trigger line* or another; the trigger line is a sequence of reconstruction and selection criteria used to select the event. The signal candidates, passing the trigger selection, can be classified in: *Triggered On Signal* (TOS), when the positive trigger decision is due to the signal candidate or its daughters, and *Triggered Independently on Signal* (TIS), when the event is triggered because of the some track in the event, completely independent from the signal candidate. An event can be selected by the firing of both a TOS and a TIS line at the same time, which allows to measure the trigger efficiencies. The TIS/TOS classification can be applied both for lines in the L0 trigger and in HLT.

The signal H_b candidates used in this analysis are required to pass the hadronic hardware trigger or to be unnecessary for a positive decision of any hardware trigger requirements. With respect to the previous analysis described in Reference [70] the set of trigger lines used to select the signal events has been enlarged in order to slightly increase the number of signal $H_b \to h^+h'^-$ candidates. The full list of trigger lines is reported in Table 5.1. The requirements applied in the Hlt2 lines, specific to this analysis, are listed in Table 5.2 and involves variables related to the mother candidate, the

Table 5.1: Trigger requirements applied to the $H_b \to h^+h'^-$ candidates

Trigger	Requirement
L0	L0Hadron_TOS OR L0Global_TIS
HLT1	Hlt1TrackAllL0Decision_TOS
HLT2	Hlt2B2HHDecision_TOS OR Hlt2Topo2BodyBBDTDecision_TOS

Table 5.2: Description of the Hlt2 trigger requirements applied to the $H_b \to h^+h'^-$ candidates

Requirements	Description
MotherCut	PT>1200.0 MeV & BPVIP() < 0.12 & BPVLTIME('PropertimeFitter/properTime:PUBLIC') > 0.0006
DaughterCut	TRCHI2DOF<3 & PT>1000.0 MeV & MIPDV(PRIMARY) > 0.12
CombinationCut	AM>4700.0 MeV & AM<5900.0 MeV & AMAXDOCA('') < 0.1

two daughters and also the combination itself. The mother candidate is required to have a large transverse momentum (PT), a small impact parameter with respect to the primary vertex (BPVIP) and a non null lifetime (BPVLTIME); the two daughter are required to have a small normalized χ^2/ (TRCHI2DOF), a large transverse momentum (PT) and a small value for the minimum impact parameter with respect to the primary vertex; finally the combination of the two tracks has to satisfy the request of an invariant mass (AM) in range [4700, 5900] MeV and a small distance of closest approach (AMAXDOCA).

5.1.2 Event reconstruction

The reconstruction of the decay chain occurs through a method, named *Decay Tree Fitter* (DTF) [125], which combines the particles in the final states to form their mother particle by constraining them to be originated from a common vertex. The momenta of all the particles and the positions of the vertices are the degrees of freedom of the decay chain and all the decay parameters are extracted simultaneously. The momentum conservation is required at each vertex and the relation between the decay vertex of a particle and the production vertex of its daughters determine the internal constraints that eliminate the redundant degrees of freedom. On the other hand the momentum vector of the reconstructed final state particles provides the external constraints. When the decay length of the mother particle is larger than (or at least comparable to) the vertex detector resolution, a parameter related to the decay time of the particle is provided. Otherwise the mother particle vertex coincides with the decay vertex position and the mother particle is classified as "resonance". The decay parameters and the related covariance matrix are determined from the constraints using a Kalman filter [104]. The DTF is used to reconstruct the $B \to h^+h'^-$ decays assuming different mass

hypothesis for the two particles in the final state. In this case, the DTF method constrains the two tracks in the final state to be originated from the same primary vertex. A graphical representation of the $H_b \to h^+h'^-$ decay topology is shown in Figure 5.1.

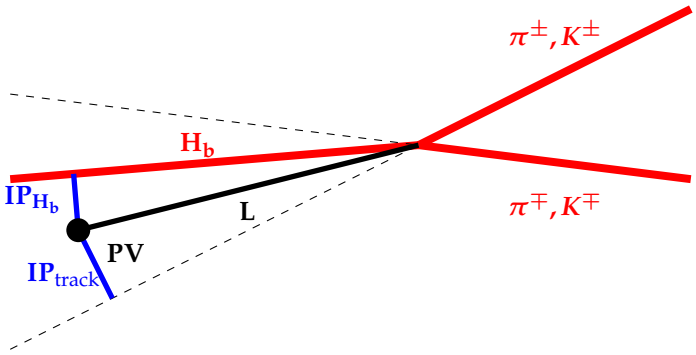

Figure 5.1: Sketch of the charmless two-body B decay topology. The impact parameters for both the tracks and the signal candidate are shown. In addition the flight distance of the signal B candidate is indicated with L.

5.1.3 Stripping selection

Before the final offline selection used to identify the $H_b \to h^+h'^-$ candidates, described in the next section, a central offline selection, named "stripping" within the LHCb collaboration, is performed with the aim to reduce the datasets to a manageable size. The stripping selection vary according to the signal B candidates of interest and in this case proceeds in two steps: firstly a preselection is applied on the pairs created combining oppositely charged tracks and assigning to them the pion mass hypothesis. In the second step a multivariate Boosted Decision Tree (BDT) classifier is used in order to enhance the purity of the sample. The preselection applies a set of requirements on the two tracks in the final state selecting only those with large transverse momentum (p_T^{track}), large impact parameter (d_{IP}^{track}) evaluated with respect to all the primary vertices (PVs), a small normalized χ^2 ($\chi^2/ndof$) and small probability to be a *ghost-track* (GhostProb), i.e. the probability for a track to be just a random combination of hits. The pairs of the two tracks are requested to have a small distance of closest approach (d_{CA}) in order to form a valid H_b candidate. In addition, only the candidates with a large decay-time ($t_{\pi\pi}$, computed by the DTF assuming the pion mass hypothesis for both the track in the final state), a large transverse momentum ($p_T^{H_b}$) and a small impact parameter with respect to all the PVs ($d_{IP}^{H_b}$) are selected. All the requirements applied in the preselection are reported in Table 5.3.

The second step consists in a BDT algorithm trained to discriminate the signal candidates from the combinatorial background contribution. The optimal value of the cut requested in the preselection to the BDT output has been set in order to reduce as much as possible the retention rate without

Table 5.3: Values of the cuts applied during the stripping preselection in order to form the $H_b \to h^+h'^-$ candidates.

Variable	Values
p_T^{track}	$> 1.0\,\text{GeV}/c$
d_{IP}^{track}	$> 120\,\mu\text{m}$
track $\chi^2/ndof$	< 3
GhostProb	< 0.5
d_{CA}	$< 100\,\mu\text{m}$
$p_T^{H_b}$	$> 1.2\,\text{GeV}/c$
$d_{IP}^{H_b}$	$< 120\,\mu\text{m}$
$t_{\pi\pi}$	> 0.6

affecting the signal selection efficiency. A detailed description of the BDT is reported in Appendix C.

5.1.4 Offline selection

Further offline selection criteria are applied to the events that pass the stripping line. It consists of two steps: in the first one the candidates are classified into three mutually exclusive samples corresponding to the different final state hypothesis ($\pi^+\pi^-$, K^+K^- and $K^\pm\pi^\mp$) by means of the particle identification DLL variables. In the second step, a multivariate BDT classifier is exploited to further suppress the combinatorial background.

Particle identification

The main source of background below the $B^0 \to \pi^+\pi^-$ and $B_s^0 \to K^+K^-$ invariant mass peaks is related to the $B^0 \to K^+\pi^-$ decay candidates where one of the final state particles is misidentified, named hereafter cross-feed [126]. Similarly, the main backgrounds under the invariant mass peak for the $B^0 \to K^+\pi^-$ decay are the $B^0 \to \pi^+\pi^-$ and $B_s^0 \to K^+K^-$ cross-feed contributions. Therefore an optimal set of requirements on the $\text{DLL}_{K\pi}$ variable is applied separating the different final states and reducing such cross-feed background to about 10% of the corresponding signal yields. As already demonstrated in previous measurements [127, 126], this level of cross-feed contamination allows to keep under control the systematic uncertainties related to the modelling of the cross-feed backgrounds.

The amount of $B^0 \to K^+\pi^-$ contamination in the $\pi^+\pi^-$ and K^+K^- final state hypothesis with

respect to the signal yields are evaluated as:

$$\begin{aligned} B_{K^+\pi^- \to \pi^+\pi^-} &= \frac{\varepsilon(K^+\pi^- \to \pi^+\pi^-)}{\varepsilon(K^+\pi^- \to K^+\pi^-)} \cdot \frac{BR(B^0 \to K^+\pi^-)}{BR(B^0 \to \pi^+\pi^-)} \\ B_{K^+\pi^- \to K^+K^-} &= \frac{\varepsilon(K^+\pi^- \to K^+K^-)}{\varepsilon(K^+\pi^- \to K^+\pi^-)} \cdot \frac{f_d}{f_s} \cdot \frac{BR(B^0 \to K^+\pi^-)}{BR(B_s^0 \to K^+K^-)} \end{aligned} \tag{5.1}$$

where ε stands for the PID efficiencies for a given final state to be identified or misidentified (described in Section 5.2, $f_{(d,s)}$ indicates the probabilities of a b-quark to hadronize into a B^0 or a B_s^0 meson and BR indicates for the branching fraction of the related decay. Analogously, the cross-feed contamination coming from the $B^0 \to \pi^+\pi^-$ and $B_s^0 \to K^+K^-$ decays in the $K^+\pi^-$ final state are calculated as:

$$\begin{aligned} B_{\pi^+\pi^- \to K^+\pi^-} &= \frac{\varepsilon(\pi^+\pi^- \to K^+\pi^-)}{\varepsilon(\pi^+\pi^- \to \pi^+\pi^-)} \cdot \frac{BR(B^0 \to \pi^+\pi^-)}{BR(B^0 \to K^+\pi^-)} \\ B_{K^+K^- \to K^+\pi^-} &= \frac{\varepsilon(K^+K^- \to K^+\pi^-)}{\varepsilon(K^+K^- \to K^+K^-)} \cdot \frac{f_s}{f_d} \cdot \frac{BR(B_s^0 \to K^+K^-)}{BR(B^0 \to K^+\pi^-)}. \end{aligned} \tag{5.2}$$

The PID efficiencies have been calibrated through a data-driven method using background subtracted samples of $D^{*+} \to D^0(K^-\pi^+)\pi^+$ and $\Lambda \to p\pi^-$, described in detail in Section 5.2. In the evaluation of the cross-feed contamination the ratios of the branching fractions are taken from [58]. The relative $B^0 \to K^+\pi^-$ yield with respect to the $B^0 \to \pi^+\pi^-$ and $B_s^0 \to K^+K^-$ decays as function of the cut applied on the $\mathrm{DLL}_{K\pi}$ PID variable are shown in Figure 5.2.

In order to suppress also other sources of cross-feed contamination, coming from $\Lambda_b^0 \to p\pi^-$ and $\Lambda_b^0 \to pK^-$ decays, an additional loose PID cut is applied to the signal B candidates requiring a $\mathrm{DLL}_{p\pi} < 5$ and $\mathrm{DLL}_{Kp} > -5$ for the $\pi^+\pi^-$ and K^+K^- final state, respectively. The final PID requirements for all the three final states are reported in Table 5.4.

Table 5.4: PID selection criteria used to identify the three final states $\pi^+\pi^-$, $K^\pm\pi^\mp$ and K^+K^- in the $B \to h^+h'^-$ Run1 analysis.

Daughter	$\pi^+\pi^-$	$K^+\pi^-$	K^+K^-
h^+	$DLL_{K\pi} < -3$ $DLL_{p\pi} < 5$	$DLL_{K\pi} > 5$ $DLL_{Kp} > -5$	$DLL_{K\pi} > 4$ $DLL_{Kp} > -5$
h^-	$DLL_{K\pi} < -3$ $DLL_{p\pi} < 5$	$DLL_{K\pi} < -5$ $DLL_{p\pi} < 5$	$DLL_{K\pi} > 4$ $DLL_{Kp} > -5$

BDT selection

The last step of the event selection is performed by means a BDT classifier [128], trained with the aim to reduce as much as possible the combinatorial background. The BDT is trained using two different selections: the first optimized for the $B^0 \to \pi^+\pi^-$ decay, indicated hereafter with $BDT_{\pi^+\pi^-}$,

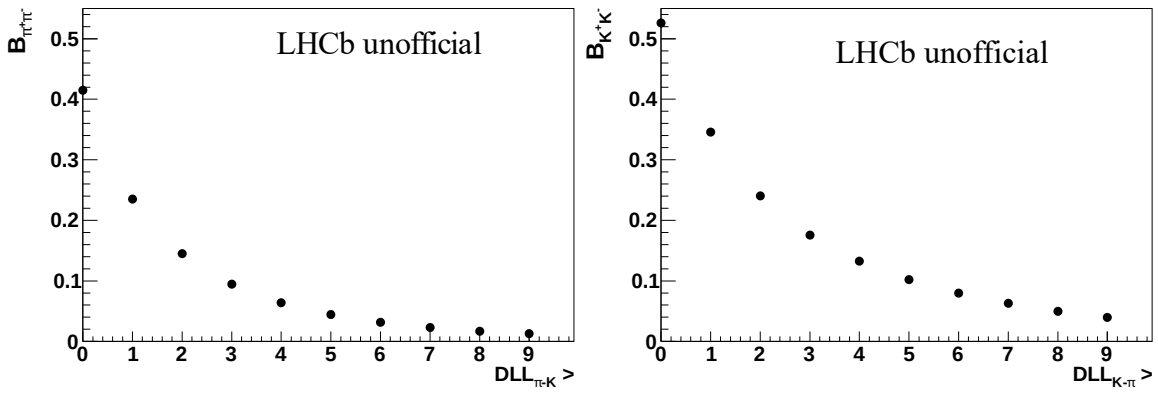

Figure 5.2: Relative yields of the $B^0 \to K^+\pi^-$ decay with respect to the $B^0 \to \pi^+\pi^-$ and $B_s^0 \to K^+K^-$ decays as function of the requirement on $\mathrm{DLL}_{K\pi}$ variable applied to both the daughter particles in the final state.

while the other chosen for the $B_s^0 \to K^+K^-$ decay optimization, referred to as $BDT_{K^+K^-}$. Both the selection consist of the PID requirements reported in Table 5.4 and the following description is valid for both the BDTs. The BDT is trained using an *Adaptive* boost and 100 independent trees, in order to stabilize the BDT response and reduce any possible source of overtraining. The variables used as input for the BDT training, summarized in Table 5.5, consist of the minimum and maximum p_T^{track} of the two final state daughters, the minimum and maximum quality of the impact parameter of the two tracks ($\chi^2(d_{IP}^{\text{track}})$), defined as reported in Section 5.1.3, the quality of the common vertex fit of the two tracks (χ^2_{vtx}), the distance of closest approach (d_{CA}) between the two tracks, the transverse momentum of the H_b candidate ($p_T^{H_b}$), the χ^2 of the H_b candidate impact parameter and flight distance calculated with respect the associated primary vertex ($\chi^2(d_{IP}^{H_b})$ and $\chi^2(FD)$, respectively). The BDT has been trained from the top with respect the one used in the previous analysis [70] since, in order to enhance the discrimination power between signal and background, a logarithmic transformation has been applied to the variables with a very narrow peak distribution, namely the $\chi^2(FD)$, $\min(\chi^2(d_{IP}^{\text{track}^+}), \chi^2(d_{IP}^{\text{track}^-})$ and $\max(\chi^2(d_{IP}^{\text{track}^+}), \chi^2(d_{IP}^{\text{track}^-})$, making their distributions more Gaussian-like. The distributions of the variables, both for signal and background

Table 5.5: Input variables used to train the both the $\mathrm{BDT}_{\pi^+\pi^-}$ and $\mathrm{BDT}_{K^+K^-}$ algorithms

Input variables		
$min(p_T^{\text{track}^+}, p_T^{\text{track}^-})$	$log(\min(\chi^2(d_{IP}^{\text{track}^+}), \chi^2(d_{IP}^{\text{track}^-})))$	
$max(p_T^{\text{track}^+}, p_T^{\text{track}^-})$	$\log(\max(\chi^2(d_{IP}^{\text{track}^+}), \chi^2(d_{IP}^{\text{track}^-})))$	
$\log(\chi^2(FD))$	d_{CA}	χ^2_{vtx}
	$p_T^{H_b}$	$\chi^2(d_{IP}^{H_b})$

samples, used for the training of the two BDT classifiers are shown in Figures 5.5 5.6, while the

their correlations are shown in Figures 5.3, 5.4. The signal component has been parametrised using a cocktail of $B \to h^+h'^-$ decays described in Section 5.1.3, while the events used to described the combinatorial background are taken from the real data sample requiring an invariant mass[1] greater than 5.6 GeV/c^2. The BDT has been trained using simultaneously the data collected during the 2011 and 2012, since no significant differences were found in the distributions and correlations of the input variables. The BDT selection is performed in two steps: the training of the BDT and optimisation of the requirement on the BDT output. However, in order to prevent any possible bias affecting the determination of the best BDT selection, it is important to avoid to apply the selected BDT requirement on the same events used for its optimisation. For this reason the signal and background samples have been randomly divided into three equivalent sub-samples. For each couple of independent sub-samples, firstly an instance of the BDT has been trained and then the requirements are applied on the second sub-sample for the determination of the optimal cut. Finally, the best BDT requirement is applied to select the events of the third statistically independent sub-sample while performing the final *CP* measurement. The distributions of the $BDT_{\pi^+\pi^-}$ and $BDT_{K^+K^-}$ output for all the three sub-samples are shown in Figure 5.7.

The optimisation is performed maximizing a figure of merit define as: $\xi = S/\sqrt{S+B}$, where S and B represent the number of signal and combinatorial background events[2], respectively. The number of signal and background events are determined by means of an unbinned maximum likelihood fit to the invariant mass distribution in a range between 5.0 GeV/c^2 and 5.8 GeV/c^2. Different components have to be parametrised in order to describe correctly the invariant mass shape: the signal $B^0 \to \pi^+\pi^-$ and $B_s^0 \to K^+K^-$ decays, the cross-feed background due to the $B^0 \to K^+\pi^-$ decay, the combinatorial background and the partially reconstructed 3-body decays ($B \to h^+h'^-X$). The modelling of all these components is the same as the one used in the final fit and described in Section 5.3. The dependence of the figure of merit ξ on the $\mathrm{BDT}_{\pi^+\pi^-}$ and $\mathrm{BDT}_{K^+K^-}$ output requirement is shown in Figure 5.8. The optimal value of ξ is reached requiring a BDT value greater than 0.1 and -0.1 for the $\mathrm{BDT}_{\pi^+\pi^-}$ and $\mathrm{BDT}_{K^+K^-}$, respectively. The optimised cut on the BDT optimised for the $B^0 \to \pi^+\pi^-$ selection corresponds to a signal efficiency of $83.3 \pm 1.2\%$ and to a background efficiency of $6.57 \pm 0.07\%$. The efficiencies corresponding to the BDT optimised for the $B_s^0 \to K^+K^-$ selection are $93.9 \pm 0.8\%$ and $19.2 \pm 0.3\%$ for signal and combinatorial background, respectively. In order to compare the performance of the two different BDT selections, the optimal requirements are applied both to the $B^0 \to \pi^+\pi^-$ and $B_s^0 \to K^+K^-$ decays. The values of the figure of merit ξ obtained

[1] From hereafter the invariant mass (m) has to be meant as evaluated under the right final state hypothesis according to considered signal.

[2] The background events are taken within a range of ± 60 GeV/c^2, corresponding to about $\pm$ 3 standard deviations, around the B^0 and B_s^0 meson masses.

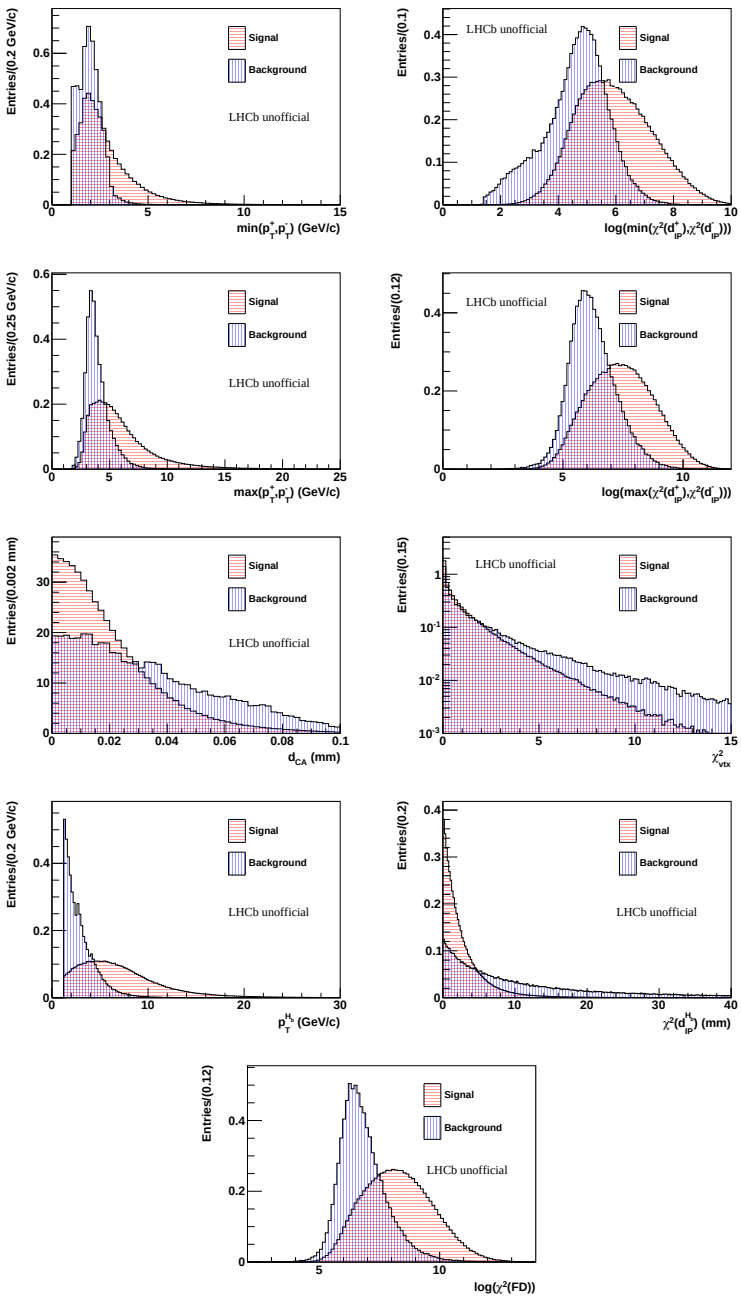

Figure 5.3: Distribution of the variables used in the training of the BDT classifier for $B^0 \to \pi^+\pi^-$ decays (red histogram) and high invariant mass sideband events (blue histogram).

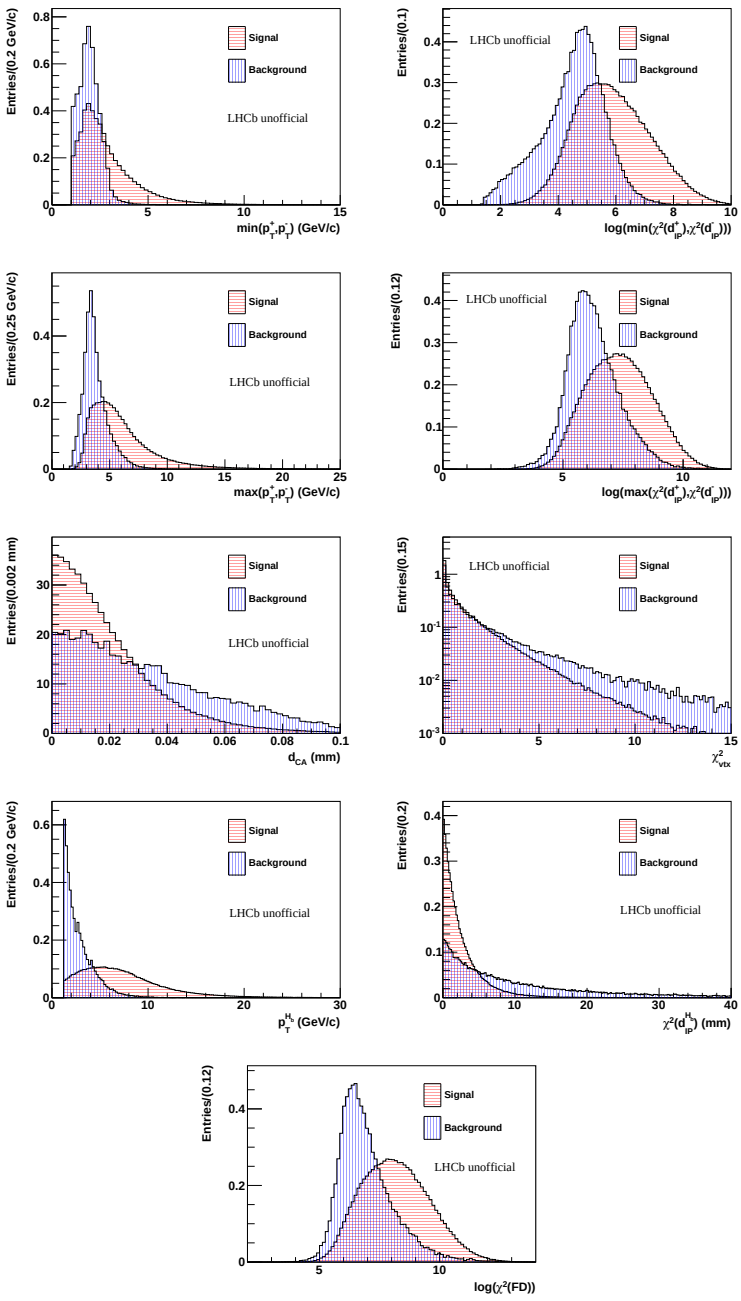

Figure 5.4: Distribution of the variables used in the training of the BDT algorithms for $B_s^0 \to K^+K^-$ decays (red histogram) and high invariant mass sideband events (blue histogram).

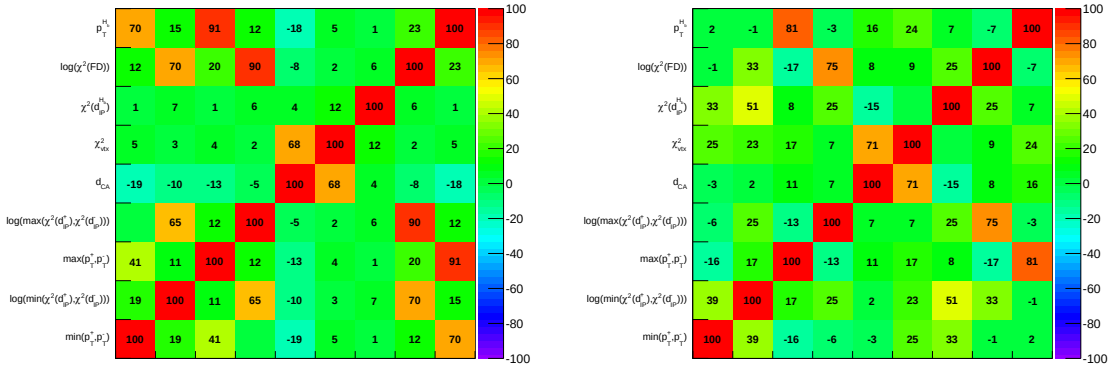

Figure 5.5: Correlation among the variables used to train the BDT algorithms for $B^0 \to \pi^+\pi^-$ simulated events (left) and high invariant mass sideband (right).

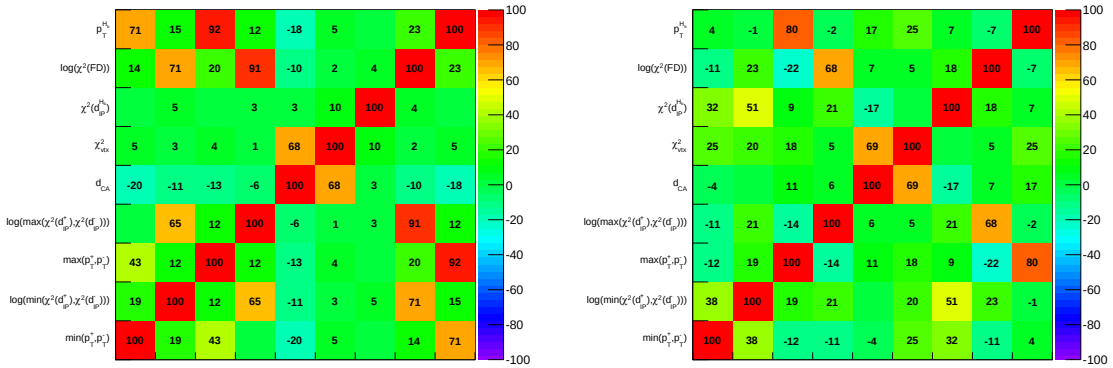

Figure 5.6: Correlation among the variables used to train the BDT algorithms for $B_s^0 \to K^+K^-$ simulated events (left) and high invariant mass sideband (right).

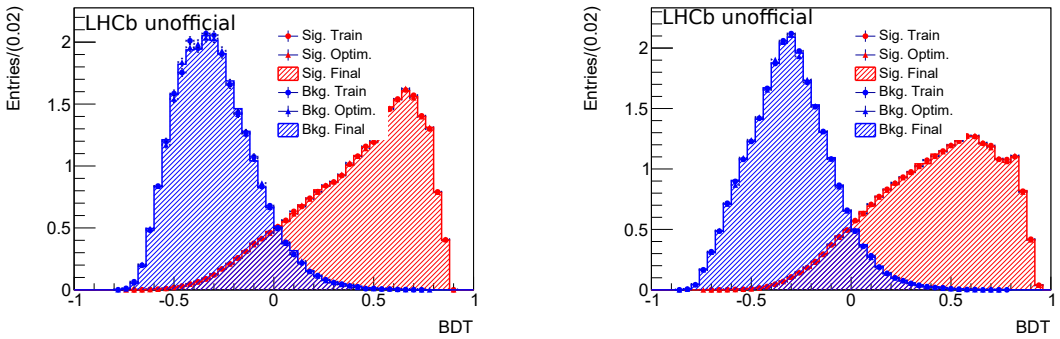

Figure 5.7: Distribution of the BDT response optimised for the $B^0 \to \pi^+\pi^-$ (left) and $B_s^0 \to K^+K^-$ (right) decays. The signal distribution is depicted in red, while the background-like events, shown in blue, have been selected applying the PID cut optimised for the corresponding final state hypothesis, on top of the stripping preselection and the requirement $m_{(K^+K^-,\pi^+\pi^-)} > 5.6\,\text{GeV}/c^2$. The BDT output distribution is reported for all the subsamples used for the optimisation procedure, as described in the text. The Circles represent the the plot of the BDT in the training samples, the triangles represent the BDT in the samples used for the optimisation and the filled histograms indicate the BDT distribution in the final samples.

for the BDTs and both the signal decays are reported in Table 5.6.

Table 5.6: Values of the figure of merit $\xi = S/\sqrt{S+B}$ for $BDT_{\pi^+\pi^-}$ and $BDT_{K^+K^-}$ evaluated on both the $B^0 \to \pi^+\pi^-$ and $B_s^0 \to K^+K^-$ decays. The number of signal and combinatorial background events is estimated by means of an unbinned maximum likelihood fit. The combinatorial yield is calculated around a region of $\pm 60\,\text{MeV}/c^2$ around the signal peak.

Selection	$B^0 \to \pi^+\pi^-$	$B_s^0 \to K^+K^-$
$\text{BDT}_{\pi^+\pi^-}$	150.024	189.012
$\text{BDT}_{K^+K^-}$	146.668	195.869

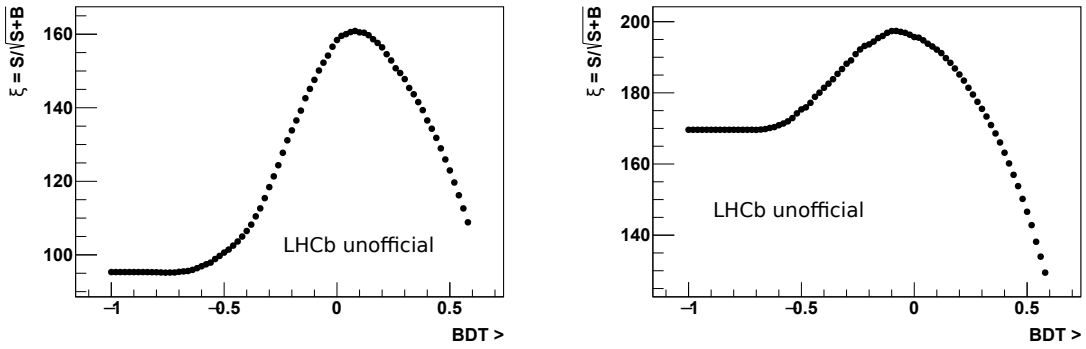

Figure 5.8: Estimated value of $\xi = S/\sqrt{(S+B)}$ as a function on the requirement applied on the BDT output for the $B^0 \to \pi^+\pi^-$ decays (left) and for the $B_s^0 \to K^+K^-$ decays (right).

Since the BDT requirement allows to highly reduce the combinatorial background in the $\pi^+\pi^-$ final state, a further component, describing the $B_s^0 \to \pi^+\pi^-$ decay, has been introduced in the invariant mass fit in order to obtain a more reliable estimation of the $B^0 \to \pi^+\pi^-$ yield. The invariant mass distributions for both the $\pi^+\pi^-$ and K^+K^- final state before and after having applied the two BDT requirements are shown in Figure 5.9.

Comparing the figure of merit corresponding to the optimal BDT requirements, it can be noted that their values differ by about a relative 10%. Since such level of discrepancy will not affect significantly the final errors on the *CP* parameters, it has been decided to use the same BDT and to apply a unique selection for both the decays: in particular the BDT and the selection optimised for the $B^0 \to \pi^+\pi^-$ decay. On one hand, this decision allows to simplify the analysis avoiding the repetition of several studies in spite of a small loss in the final precision in the *CP* parameters related to the $B_s^0 \to K^+K^-$ decay. On the other hand, the lower amount of combinatorial background allows a better description of the distributions of the various components in the final fit. In addition it resolve the not trivial problem of taking under control the correlations among the relevant variables determined using two different selections. The final yields estimated through the unbinned likelihood fit

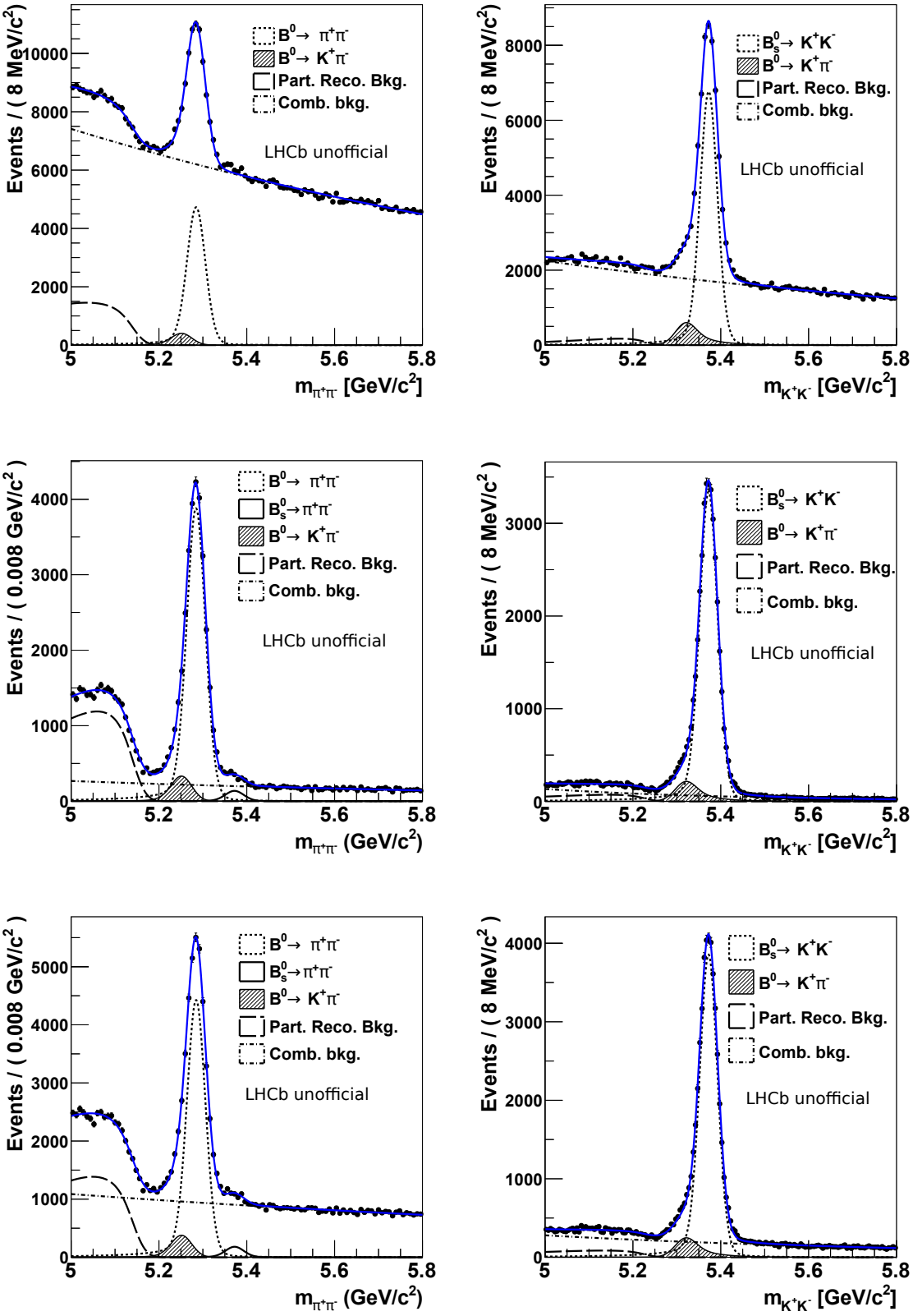

Figure 5.9: Invariant mass fits to the $\pi^+\pi^-$ (left) and to the K^+K^- (right) mass hypothesis before to apply any BDT selection (top) and related to the events surviving the BDT requirement of $BDT_{\pi^+\pi^-}$ (middle) and of $BDT_{K^+K^-}$ (bottom). The model used to fit the data is described in the Section 5.3.

before and after applying the BDT selection are shown in Table 5.7.

Table 5.7: Values of the number of events of the $B^0 \to \pi^+\pi^-$ and $B_s^0 \to K^+K^-$ decays before and after having applied the $\text{BDT}_{\pi^+\pi^-}$ requirement. The number of signal and combinatorial background events is estimated by means of an unbinned maximum likelihood fit. The combinatorial yield is calculated around a region of $\pm 60\,\text{MeV}/c^2$ around the signal peak.

Selection	$B^0 \to \pi^+\pi^-$	$B_s^0 \to K^+K^-$
no BDT	33 600	45 000
$\text{BDT}_{\pi^+\pi^-}$	28 600	36 800

5.1.5 Monte Carlo samples

Simulated samples are very useful ingredient for the *CP* measurement in $H_b \to h^+h'^-$ decays. In order to have events as much similar to the real data, the simulated samples have been reproduced using the same data taking conditions, trigger, reconstruction, stripping and Flavour Tagging used for the processing of the real data. The statistics of each sample is such to reproduce correctly the observed ratios between the integrated luminosities collected with the different data taking conditions. The number of generated events for the different $H_b \to h^+h'^-$ decays, separated by data taking conditions, is reported in Table 5.8.

Table 5.8: Number of events available in fully-simulated samples for the various $H_b \to h^+h'^-$ decay modes generated with 2011 and 2012 data taking conditions.

Decays	Number of 2011 events	Number of 2012 events
$B^0 \to K^+\pi^-$	1 541 196	3 068 989
$B^0 \to \pi^+\pi^-$	1 527 244	3 067 742
$B_s^0 \to \pi^+K^-$	1 532 248	3 052 242
$B_s^0 \to K^+K^-$	1 514 494	3 071 739
$B_s^0 \to \pi^+\pi^-$	1 024 500	2 030 741

The mass model used for the various components, described in detail in Section 5.3, relies on Monte Carlo (MC) input. In particular some parameters related to the shape of the signal p.d.f. are taken from fully Simulated data and fixed during the fit. The complete list of the parameters is reported in Table 5.9. The invariant mass distributions for the various $H_b \to h^+h'^-$ decays are shown in Figure 5.10. The result of the best fit of the model is superimposed. In addition the shape of the different cross-feed backgrounds is also determined from the MC samples, applying the same PID selections used for separate the three final states in real data. Similarly to the mass model, also

the decay time model benefits from the use of simulated samples, both for the determination of the decay-time resolution, described in Section 5.4.1, and of the decay-time acceptance, discussed in Section 5.4.2.

Table 5.9: Parameters governing the signal mass shape of the p.d.f. reported in Equation (5.11), obtained from unbinned maximum likelihood fits to simulated $H_b \to h^+h'^-$ decays, which will be fixed in the fit to data.

Decay	f_{tail}	α_1	α_2
$B^0 \to K^+\pi^-$	0.1506 ± 0.0047	0.703 ± 0.018	0.5423 ± 0.0089
$B_s^0 \to \pi^+K^-$	0.1482 ± 0.0038	0.719 ± 0.015	0.5261 ± 0.0074
$B^0 \to \pi^+\pi^-$	0.1743 ± 0.0042	0.773 ± 0.016	0.5289 ± 0.0076
$B_s^0 \to \pi^+\pi^-$	0.1863 ± 0.0050	0.745 ± 0.016	0.5373 ± 0.0076
$B_s^0 \to K^+K^-$	0.1184 ± 0.0033	0.639 ± 0.015	0.5122 ± 0.0082
$B^0 \to K^+K^-$	0.1336 ± 0.0076	0.603 ± 0.014	0.5037 ± 0.0103

5.1.6 Background subtracted $H_b \to h^+h'^-$ sample

In order to extract reliable templates for describing the distribution of some observables, playing an important role in the final fit, a background subtracted $H_b \to h^+h'^-$ decay sample is created exploiting the *sPlot* technique [122]. This technique allows to unfold the background and signal contributions by applying a per-event weight. Such weights are obtained from an unbinned maximum likelihood fit to the invariant mass, calculated assuming that both the particles in the final state were pions.The events have been selected applying the full selection described in this section. This fit is different from the final *CP* fit, described in the following sections, where the *sPlot* technique is not used and the fit observables include also the decay-time, the decay-time error and the tagging information. The shape of the $H_b \to h^+h'^-$ contributions have been parametrised by means of a Kernel Estimation Method [129] to the invariant mass distribution of fully simulated decays. The mass distribution is then convolved with a Gaussian resolution model, leaving free both the mean (μ) and the width (σ). The relative fractions among the various $H_b \to h^+h'^-$ modes are fixed to the values measured by LHCb in Reference [58], except for the Λ_b^0 decays where the branching ratios evaluated by HFLAV are used instead. The Λ_b^0 hadronization fraction is taken from a previous measurement of $f_{\Lambda_b^0}/(f_d + f_u)$ performed by LHCb [130] (assuming $f_d \approx f_u$). The measurement is dominated by the external input of the $\Lambda_c^+ \to pK^-\pi^+$, and the central value is inversely proportional to this branching ratio. Thus the value of $f_{\Lambda_b^0}/(f_d + f_u)$ is rescaled by the ratio between the input used in the LHCb measurement and the updated value reported by Belle in Reference [131]. The contribution to the

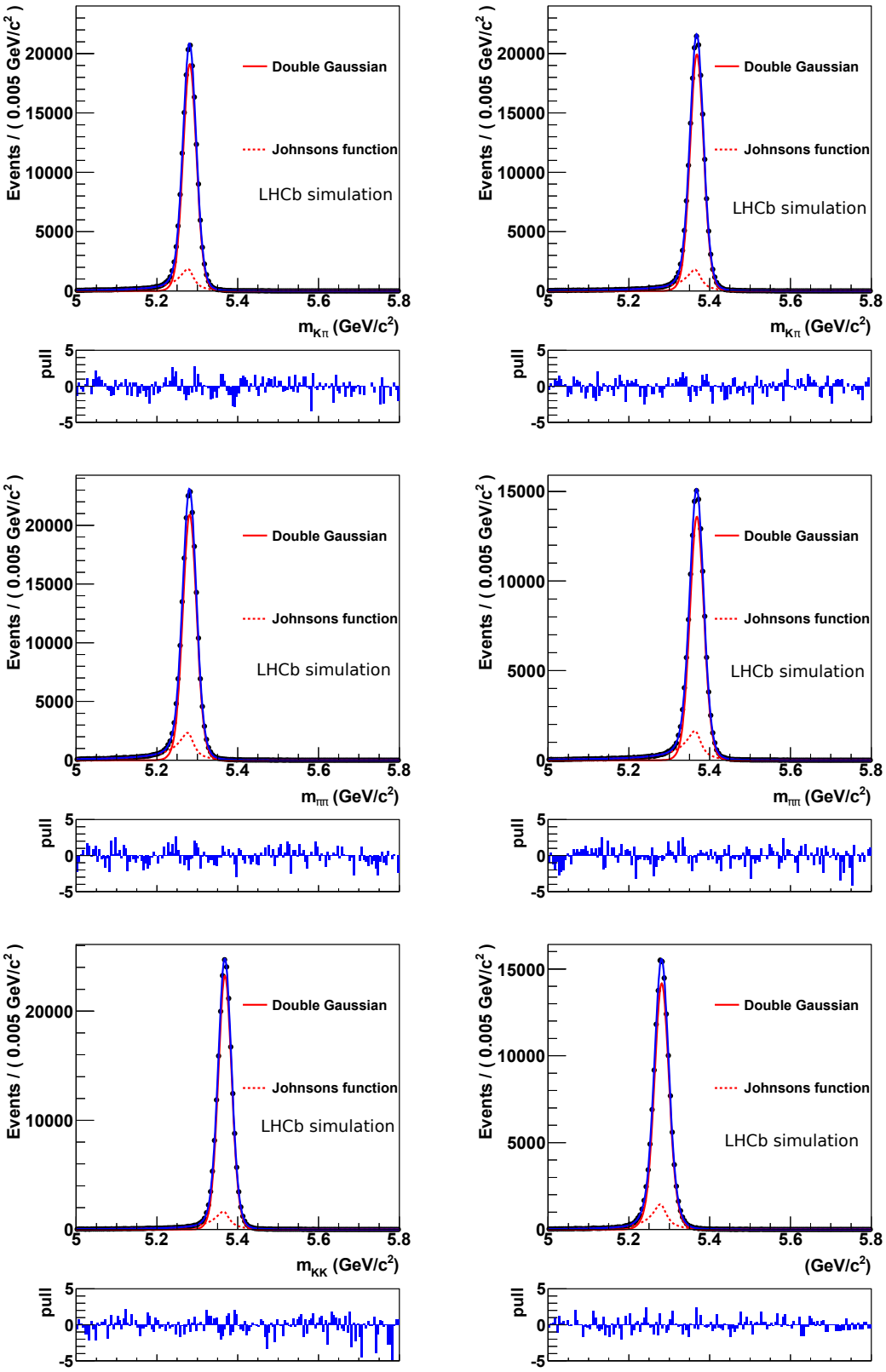

Figure 5.10: Invariant mass distributions for $B^0 \to K^+\pi^-$, $B_s^0 \to \pi^+K^-$, $B^0 \to \pi^+\pi^-$, $B_s^0 \to \pi^+\pi^-$, $B_s^0 \to K^+K^-$ and $B^0 \to K^+K^-$ simulated decays (from top left to bottom right). The result of the best fit of the model described in Equation (5.11) are also superimposed.

combinatorial and partially reconstructed backgrounds are parametrised, respectively, with a simple exponential and an ARGUS [132] function convolved with the same Gauss resolution used for the signal:

$$f(m) = A \cdot \left[m' \sqrt{1 - \frac{m'^2}{m_0^2}} \Theta(m_0 - m') \exp(c \frac{m'}{M_0}) \right] \otimes G(m - m', \mu, \sigma), \tag{5.3}$$

where A is a normalization factor, m_0 is the ARGUS end-point, c is parameter related to the shape of the Argus function, Θ stands for a step function which is equal to 1 if $m_0 > m'$ and to 0 otherwise, the symbol $\otimes$ indicates the convolution product and G stands for the the Gaussian resolution model. The invariant mass ($m_{\pi\pi}$) distribution and the result of the fit are shown in Figure 5.11.

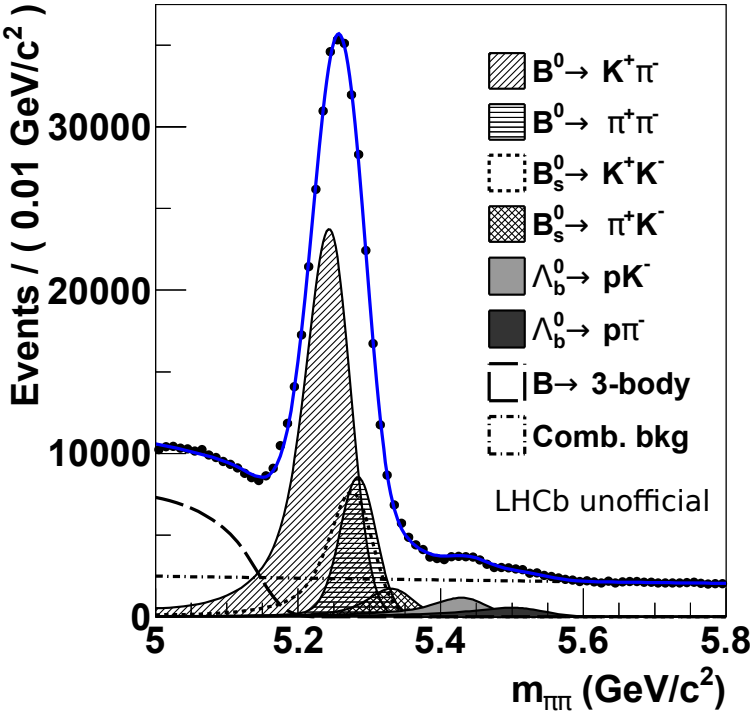

Figure 5.11: Distribution of invariant mass under the $\pi^+\pi^-$ final state hypothesis for the events surviving the full event selection. The result of the fit used to extract the $H_b \to h^+h'^-$ weights, exploiting the *sPlot* technique, is also shown.

5.2 PID calibration

Another fundamental ingredient of such an analysis is the PID calibration. As mentioned in Section 5.1 all signal decays contribute with peaking shapes to the same invariant mass region. The $\Delta \log \mathcal{L}$ variables [133] are used to discriminate between pions, kaons and protons. The choice of using the $\Delta \log \mathcal{L}$ variables has been driven by a studied reported in Reference [134].The PID effi-

ciencies have been calibrated through a data-driven method using background subtracted samples of $D^{*+} \to D^0(K^-\pi^+)\pi^+$ and $\Lambda \to p\pi^-$, where the background contamination has been removed by means of the *sPlot* technique [122].

5.2.1 Calibration of the PID efficiencies

The procedure used for the PID efficiency calibration is based on the following considerations:

- the values of $\Delta \log \mathcal{L}$ variables mostly depend on the the momentum p of the final-state particle due to its relation with the emission angle of Cherenkov photons;
- the $\Delta \log \mathcal{L}$ values depend also on the pseudorapidity η of the particle since the RICH detectors, described in Section 3.2, have been designed with different angular acceptances and optimised for different momentum regions;
- PID performances depend also on the event occupancy, i.e. the track multiplicity in the event *nTracks*;

The calibration procedure consists on two steps. In the first place the PID efficiencies are evaluated with maps in bins of p, η and *nTracks*. This is done applying PID requirements to the calibration events falling in a particular bin and computing the efficiency as the number of candidates surviving the cuts divided by the total number of candidates inside the bin. The binning scheme used in this procedure is:

- p: 2 bins in [0, 10 GeV/c], 45 bins in [10 GeV/c, 100 GeV/c], 20 bins in [100 GeV/c, 150 GeV/c], 4 bins in [150 GeV/c, 500 GeV/c];
- η: 10 bins in [1, 6];
- *nTracks*: 4 bins in [0, 400] and 1 bin in [400, 600].

Since the track multiplicity and the kinematic of the final-state particle are uncorrelated quantities, the dependence of the PID efficiency on the former one is integrated out. Defining the functional relation between the PID efficiency and p, η and *nTracks* as $\varepsilon(p, \eta, nTracks)$, and the distribution of *nTracks* for the $H_b \to h^+h'^-$ sample as $f(nTracks)$, the procedure could be formalised by means of the following equation:

$$\bar{\varepsilon}(p, \eta) = \int \varepsilon(p, \eta, nTracks) \cdot f(nTracks) dnTracks, \tag{5.4}$$

where $\bar{\varepsilon}(p, \eta)$ is the PID efficiency as function of p and η for a final-state particle in the occupancy regime observed in the $H_b \to h^+h'^-$ data sample. The integration in Equation 5.4 can be discretized

as:

$$\bar{\varepsilon}(p_i, \eta_j) = \frac{1}{N} \sum_{k=1}^{N} \varepsilon(p_i, \eta_j, nTracks_k), \tag{5.5}$$

where $\bar{\varepsilon}(p_i, \eta_j)$ is the final PID efficiency corresponding to the $i-$th bin of particle momentum and $j-$th bin of particle pseudorapidity, $\varepsilon(p_i, \eta_j, nTracks_k)$ is the PID efficiency corresponding to the $i-$th bin of particle momentum, $j-$th bin of particle pseudorapidity and $k-$th bin of track multiplicity and N represents a sufficiently large number to avoid any significant statistical fluctuation in the average (as reported in Reference [134], $N = 200000$ is a good value balancing the request of high statistics and the need of using reasonable computing resource). For each term of the sum the value of $nTracks_k$ is randomly extracted according to the track multiplicity distribution in the $H_b \to h^+h'^-$ data sample. The background subtracted distributions of $nTracks$ for the calibration and the $H_b \to h^+h'^-$ samples are shown in Figure 5.12. The result of such a procedure are the maps of PID efficiencies in bin of p and η for the final-state particle of the $H_b \to h^+h'^-$ decays.

The PID efficiency maps for protons are determined only for particles in the "*fiducial region*" defined using the same set of requirements optimised in Reference [134]:

$$\begin{aligned} &(\eta > 2 \; AND \; p < 25\,\text{GeV}/c) \; OR \\ (\eta > p \cdot m_2 + q_2 \; AND \; p \geq 25\,\text{GeV}/c \; AND \; &p < 120\,\text{GeV}/c) \; OR \\ &(\eta > p \cdot m_3 + q_3 \; AND \; p \geq 120\,\text{GeV}/c), \end{aligned} \tag{5.6}$$

where $m_2 = 0.0184\,c/GeV$, $q_2 = 1.539$, $m_3 = 0.150\,c/GeV$ and $q_3 = -14.25$. The remaining part of the $p - \eta$ plane is referred to "*non-fiducial region*" hereafter. Such a separation is due to the fact that the calibration sample for protons, differently than the calibration samples for pions and kaons, does not cover the whole $p - \eta$ phase space occupied by the $H_b \to h^+h'^-$ decay mode.

5.2.2 Determination of PID efficiencies for $H_b \to h^+h'^-$ decays

The probability for a given $H_b \to h^+h'^-$ candidate to survive a certain PID requirement can be written as:

$$\varepsilon_{h^+h'^-}(p_i^+, \eta_i^+, p_i^-, \eta_i^-) = \bar{\varepsilon}_{h^+}(\pi_i^+, \eta_i^+) \cdot \bar{\varepsilon}_{h'^-}(\pi_i^-, \eta_i^-), \tag{5.7}$$

where $\bar{\varepsilon}_{h^+}$ and $\bar{\varepsilon}_{h'^-}$ represent the PID efficiencies, as determined in Equation 5.5, for the positive (h^+) and negative (h'^-) charged particle, i.e pions, kaons or protons, respectively. The parameters $p_i^\pm$ and $\eta_i^\pm$ stand for the momentum and pseudorapidity of a positive or negative particle in the $H_b \to h^+h'^-$ final state. Given a certain test sample of $H_b \to h^+h'^-$ decays, containing N candidates, the total PID efficiency corresponding to a particular PID requirement can be evaluated as:

$$\hat{\varepsilon}_{h^+h'^-} = \frac{1}{N} \sum_{i=1}^{N} \varepsilon_{h^+h'^-}(p_i^+, \eta_i^+, p_i^-, \eta_i^-). \tag{5.8}$$

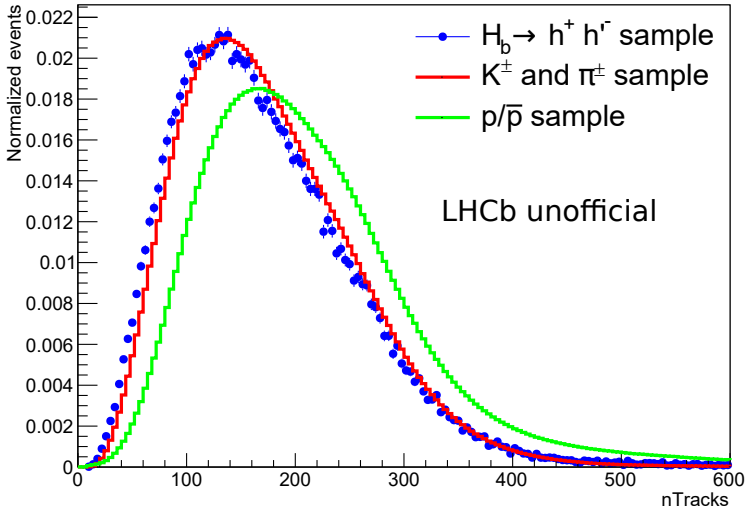

Figure 5.12: Background subtracted distributions of track multiplicity, *nTracks*, for $H_b \to h^+h'^-$ decays (blue dots) and PID calibration samples of $D^{*+} \to D^0(\to K^-\pi^+)\pi^+$ decays (red filled histogram) and $\Lambda \to p\pi^-$ (green histogram).

In the first step of the offline event selection, described in Section 5.1, the optimisation procedure is performed using the total PID efficiency as figure of merit, extracting the $H_b \to h^+h'^-$ candidates from a fully simulated $H_b \to h^+h'^-$ sample.

Determination of PID efficiencies for $\Lambda_b^0 \to pK^-$ and $\Lambda_b^0 \to p\pi^-$ decays

The determination of the PID efficiencies for $\Lambda_b^0 \to pK^-$ and $\Lambda_b^0 \to p\pi^-$ decays results to be slightly more difficult with respect to the other $H_b \to h^+h'^-$ decay modes. The reason lies in the distinction in the $p - \eta$ phase space between *fiducial* and *non-fiducial* regions. Firstly the total PID efficiency is computed for the candidates having protons in the *fiducial* region, as shown in Equation 5.7. Since the *non-fiducial* region is not covered by the calibration sample, the corresponding PID efficiency is determined applying the requirements on the variables of fully simulated samples. Then the so obtained efficiency is rescaled taking into account the different PID performances between fully simulated and real events. The rescaling factor $\mathcal{K}_F$ is evaluated as:

$$\mathcal{K}_F = \frac{\varepsilon_F}{\varepsilon_F^{MC}}, \tag{5.9}$$

where ε_F and ε_F^{MC} are the PID efficiency in the fiducial region determined on real data, applying the calibration procedure formalised in Equation 5.7, and on fully simulated sample, respectively. A dependence of the $\mathcal{K}_F$ factor on both the final state hypothesis and the applied PID requirements is found. Finally, assuming the same scale factor between *fiducial* and *non-fiducial* regions the final PID

efficiency is calculated as:

$$\hat{\varepsilon} = f \cdot \varepsilon_F + (1 - f) \cdot \mathcal{K}_F \varepsilon_{noF}^{MC}, \tag{5.10}$$

where f is the fraction of test candidates within the fiducial region and the ε_{noF}^{MC} represents the PID efficiency corresponding to the *non-fiducial* region, as determined from fully simulated events.

5.3 Invariant mass fit

The first important ingredient of the analysis is the fit to the invariant mass distribution, used to discriminate between signal and background candidates. Indeed the strategy adopted for the optimisation of the event selection, reported in Section 5.1, is based on the knowledge of the various models adopted to fit the invariant mass distribution of the selected candidates. Four different components are identified to contribute to the invariant mass spectrum:

- **signal**: $H_b \to h^+h'^-$ decays in which the final state particles have been correctly identified by the PID selection requirements;
- **cross-feed background**: $H_b \to h^+h'^-$ decays where at least one of the final state particles has been mis-identified. This type of background is particularly dangerous since it lies just under the signal peak;
- **combinatorial background**: candidates composed by pairs of oppositely charged particles coming from different decay chains;
- **partially reconstructed 3-body decay**: $H_b \to h^+h'^-X$ decays where only two of the three daughters have been reconstructed and used to form the H_b hadron.

In the following, the models used to describe these four components are reported in detail.

5.3.1 Invariant mass model for signal decay

The invariant mass (m) model of the signal component is studied using fully simulated events. It is described as:

$$P_{sig}(m) = (1 - f_{tail})[f_g \cdot G_1(m, \mu + \delta, \sigma_1) + (1 - f_g) \cdot G_2(m, \mu + \delta, \sigma_2)] + f_{tail} \cdot J(m, \mu, \delta, \sigma_1, \alpha_1, \alpha_2) \tag{5.11}$$

where $G(m, \mu + \delta, \sigma_1)$ and $G(m, \mu + \delta, \sigma_2)$ are two Gaussian functions with the same mean, equal to $\mu + \delta$, and widths σ_1 and σ_2, respectively; the parameter μ is fixed to the B meson mass taken from the PDG [15], while the parameter δ is left free to vary in order to take into account any possible offset in the invariant mass. The parameter f_g represents the relative fraction between the two Gaussian

functions. In order to describe correctly the asymmetric tails of the signal distribution, a Johnson function, $J(m, \mu, \delta, \sigma_1, \alpha_1, \alpha_2)$ is used, which can be written as:

$$J(m, \mu, \delta, \sigma_1, \alpha_1, \alpha_2) = \frac{\alpha_2}{\sigma_1 \sqrt{2\pi(1+z^2)}} \exp[-\frac{1}{2}(\alpha_1 + \alpha_2 \sinh^{-1} z)^2], \tag{5.12}$$

where z is defined as:

$$z \equiv \left[\frac{m - (\mu + \delta)}{\sigma_1}\right]. \tag{5.13}$$

Finally the parameter f_{tail} is the relative fraction between the sum of the two Gaussian functions and the Johnson function.

In the final fit all the parameters are left free to vary except for the parameters describing the shape of the signal tails (α_1, α_2, f_{tails}), which are fixed to the values determined from a fit to the invariant mass distribution of fully simulated samples. The values of these fixed parameters for the various $H_b \to h^+h'^-$ decays are reported in Table 5.9. The invariant mass distributions of the fully simulated sample are shown in Figure 5.10, with the results of the best fit superimposed.

5.3.2 Invariant mass model for cross-feed background

The invariant mass models for the cross-feed background are determined by means of a kernel estimation method [129] applied to the fully simulated signal decays. The simulated dataset has been created applying the same selection used for the real data and reported in Section 5.1. In order to describe correctly the shape of the cross-feed contribution, the effect of the PID requirements has to be taken into account. Indeed, since the application of PID requirements alters the momentum distribution of the two tracks, the invariant mass could turn out to be deformed with respect to the original shape. For this reason, a per-event weight is assigned to each MC candidate corresponding to:

$$w_i = \varepsilon_{h^+}(p_i^+, \eta_i^+)\varepsilon_{h'^-}(p_i^-, \eta_i^-) \tag{5.14}$$

where the symbol $\varepsilon_{h^\pm}$ indicates the PID efficiencies of the positive and negative track in the final state, $p^\pm$ and $\eta^\pm$ represent the momentum and the pseudorapidity of the two final state particles related to the i-th event. The kernel estimation method is then applied to these weighted samples in order to determine a non-parametric p.d.f, which will be convolved with the same invariant mass resolution used for the signal in the final fit to the invariant mass. A dedicated study performed to validate the kernel method is described in the Appendix B of the Reference [134], however it is not reported in this section since it goes beyond the scope of this thesis.

The amount of each cross-feed background component is evaluated as:

$$N_{\hat{h}^+\hat{h}'^-}(H_b \to h^+h'^-) = N(H_b \to h^+h'^-) \cdot \frac{\varepsilon_{\hat{h}^+\hat{h}'^-}(H_b \to h^+h'^-)}{\varepsilon_{h^+h'^-}(H_b \to h^+h'^-)}, \tag{5.15}$$

where $N_{\hat{h}^+\hat{h}'^-}(H_b \to h^+h'^-)$ is the number of $H_b \to h^+h'^-$ candidates under the $\hat{h}^+\hat{h}'^-$ hypothesis, $N(H_b \to h^+h'^-)$ represents the number of $H_b \to h^+h'^-$ events correctly identified by the PID requirements. The parameters $\varepsilon_{\hat{h}^+\hat{h}'^-}(H_b \to h^+h'^-)$ and $\varepsilon_{h^+h'^-}(H_b \to h^+h'^-)$ represent the probabilities to assign the $\hat{h}^+\hat{h}'^-$ and the correct mass hypothesis to the $H_b \to h^+h'^-$ decay, respectively. These PID variables are computed using as proxy for the kinematics of the final state particles the background subtracted samples of $H_b \to h^+h'^-$ decays, mentioned in Section 5.1.6, and their values are fixed in the final fit to data.

5.3.3 Invariant mass model for combinatorial background

For each final state hypothesis f ($f = \pi^+\pi^-, K^+\pi^-, K^+K^-$), the combinatorial background component has been modelled with a simple exponential function:

$$P_f(m) = B_f \exp(-k_f m) \tag{5.16}$$

where k_f is the exponential slope and B_f is just a normalization factor. Both the parameters for all the final states are left free to vary in the final fit to data.

5.3.4 Invariant mass model for partially reconstructed 3-body decay

The partially reconstructed 3-body decay component related to the $\pi^+\pi^-$ and K^+K^- mass hypothesis is parametrised by an Argus [132] function convolved with a double Gaussian resolution function, while for the $K^+\pi^-$ final state hypothesis this contribution is described convolving the sum of two Argus functions with a Gaussian resolution function:

$$\begin{aligned} P_{\pi^+\pi^-,K^+K^-}(m) =& A \cdot \left[m' \sqrt{1 - \frac{m'^2}{m_0^2}} \cdot \exp(c(1 - \frac{m'^2}{m_0^2})) \otimes G_2(m - m', \delta, f_g, \sigma_1, \sigma_2) \right], \\ P_{K^+\pi^-}(m) =& A \cdot \left[m' \left(\sqrt{1 - \frac{m'^2}{m_{0,B^0}^2}} \cdot \exp(c(1 - \frac{m'^2}{m_{0,B^0}^2})) + \sqrt{1 - \frac{m'^2}{m_{0,B_s^0}^2}} \cdot \exp(c(1 - \frac{m'^2}{m_{0,B_s^0}^2})) \right) \right. \\ & \left. \otimes G_1(m - m', \delta, \sigma_1) \right], \end{aligned} \tag{5.17}$$

The usage of two Argus function in the $K^+\pi^-$ mass hypothesis allows to better describe this component taking into account both the main contribution due to B^0 meson and the lower fraction of 3-body B_s^0 decay. The endpoints (m_0) of the Argus functions are fixed to the values $m_{B^0} - m_{\pi^0}$ and $m_{B_s^0} - m_{\pi^0}$ for the B^0 and B_s^0 partially reconstructed decay respectively, where the values of m_{B^0}, m_{π^0} and $m_{B_s^0}$ are taken from the PDG [15]. As documented in Reference [134] this model provides a good empirical parametrisation of this kind of background component. In the final fit, the widths of the Gaussian resolution functions and the parameter δ are in common with the ones used for the parametrisation of the signal model.

5.4 Decay-time fit

The unbinned maximum likelihood fit used to extract the values of the *CP* parameters is performed simultaneously on the invariant mass and the decay time observables. The models related to the invariant mass for the signal and the various background contributions have been already described in Section 5.3. In the following the decay-time models for both for signal and backgrounds, contributing to all the three final state hypothesis ($\pi^+\pi^-$, $K^+\pi^-$ and K^+K^-), are reported.

5.4.1 Decay-time resolution

The decay time resolution is a consequence of the finite vertex and momentum resolution and it is a very important effect to be taken into account since it dilutes the observed *CP* asymmetries by a factor equal to:

$$D_{\sigma_t} = \exp\left(-\frac{\Delta m_{d,s}^2 \cdot \sigma_t^2}{2}\right), \tag{5.18}$$

where $\Delta m_{d,s}$ is the oscillation frequency for the B^0 and B_s^0 meson respectively and σ_t is the decay-time resolution [135]. For the B^0 meson, the value of Δm_d is sufficiently small that the deviation of the observed *CP* violation parameters with respect to their real value is below 1%, even for large decay-time resolution. On the other hand, for the B_s^0 meson, due to the large value of Δm_s, the decay-time resolution plays a crucial role. For this reason a correct determination of the decay-time resolution is required in order to obtain a correct estimation of the *CP* asymmetries. The determination of the decay time resolution for the $H_b \to h^+h'^-$ decays is divided in two steps

- determination of the decay time resolution model,
- calibration of decay time resolution in data using tagged time-dependent fits.

These steps are described in detail in the following paragraphs.

Table 5.10: Calibration parameters describing the linear relation between predicted decay time error δ_t and RMS(τ_{err}) for fully simulated $B_s^0 \to \pi^+K^-$, $B_s^0 \to K^+K^-$ and $B_s^0 \to D_s^-\pi^+$ decays.

Decay	Unweighted			Weighted		
	q_0	q_1	$\rho(q_0, q_1)$	q_0	q_1	$\rho(q_0, q_1)$
$B_s^0 \to \pi^+K^-$	38.97 ± 0.05 fs	1.136 ± 0.006	0.13	38.44 ± 0.08 fs	1.113 ± 0.010	-0.19
$B_s^0 \to K^+K^-$	38.26 ± 0.05 fs	1.140 ± 0.006	0.11	38.00 ± 0.08 fs	1.120 ± 0.010	-0.16
$B_s^0 \to D_s^-\pi^+$	40.07 ± 0.05 fs	1.174 ± 0.005	0.10	40.05 ± 0.06 fs	1.195 ± 0.006	-0.23

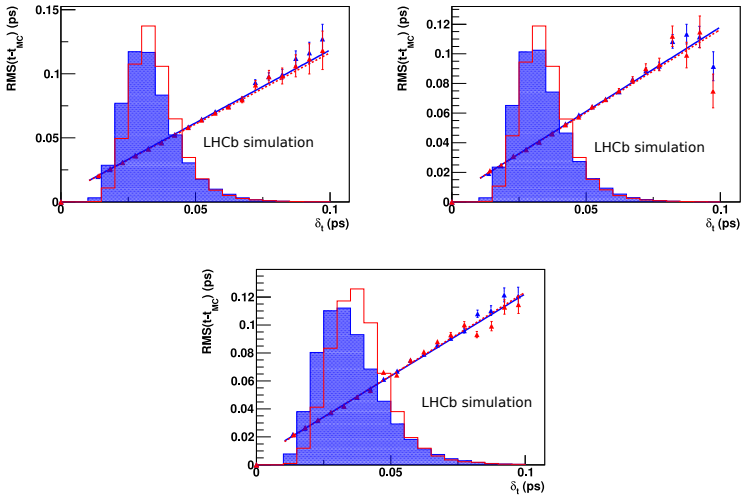

Figure 5.13: Dependency between δ_t and the $RMS(\tau_{err})$ (triangles) for fully simulated $B_s^0 \to \pi^+K^-$ (left), $B_s^0 \to K^+K^-$ (middle) and $B_s^0 \to D_s^-\pi^+$ (right) decays. Red and blue triangles represent the case where PID effect and kinematic reweighting have or not been applied, respectively. The dashed red (solid blue) line represent the best fit to the red (blue) triangles using a linear function. The red and the blue filled histograms represent the distribution of δ_t for weighted and unweighted samples, respectively.

Determination of the decay time resolution model

The model describing the predicted decay time resolution is determined from a bi-dimensional unbinned maximum likelihood fit to the distributions of the predicted decay time error δ_t, evaluated by means of the DTF, and the quantity τ_{err} exploiting fully simulated $B_s^0 \to \pi^+K^-$ and $B_s^0 \to D_s^-\pi^+$ events. The variable τ_{err} is defined as the difference between the reconstructed decay time t and the true decay time t_{MC} of the generated B meson. For the $B_s^0 \to \pi^+K^-$ sample the same selection reported in Section 5.1 is applied, while for the $B_s^0 \to D_s^-\pi^+$ events the D meson is forced to decay to the $K^+K^-\pi^-$ final state. A weight, corresponding to the PID efficiencies and defined as function of the momentum and pseudorapidity of the final state particles, is applied to the $B_s^0 \to \pi^+K^-$ decay on a per-event basis in order to take into account any possible effect related to their kinematic. Similarly the simulated $B_s^0 \to D_s^-\pi^+$ decay has been reweighted according to the momentum and pseudorapidity distributions of the $B_s^0 \to \pi^+K^-$ decay.

The δ_t and τ_{err} distributions are modelled through the conditional p.d.f. which represents the probability distribution of τ_{err} when δ_t is known to be a specific value:

$$T(\delta_t, \tau_{err}) = R(\tau_{err}|\delta_t) \cdot g(\delta_t) = [f_\tau \cdot G(\tau_{err}, \mu, \sigma_1(\delta_t)|\delta_t) + (1 - f_\tau) \cdot G(\tau_{err}, \mu, \sigma_2(\delta_t)|\delta_t)] \cdot g(\delta_t), \tag{5.19}$$

where $G(\tau_{err}, \mu, \sigma_{1,2}(\delta_t)|\delta_t)$ are two Gaussian functions with a common mean μ and width equal to

σ_1 and σ_2 respectively, and $g(\delta_t)$ represents the δ_t distribution. This conditional p.d.f. gives the possibility to take into account and correctly describe the correlation between the δ_t and τ_{err}. The two Gaussian widths are parametrised as function of the decay time error and their functional dependence is defined as:

$$\begin{aligned} \sigma_1(\delta_t) &= q_0 + q_1 \cdot (\delta_t - \hat{\delta}_t), \\ \sigma_2(\delta_t) &= r_\sigma \cdot \sigma_1(\delta_t). \end{aligned} \tag{5.20}$$

where $\hat{\delta}_t$ is fixed and represents the average of the decay time distribution ($\sim$ 30 fs) while r_σ is a scale coefficient free to vary in the fit.

The linear dependence between the τ_{err} and δ_t, expressed in the $\sigma_{1,2}$ definition, has been verified splitting the two samples, in 20 equivalent subsamples of δ_t and evaluating in each of them the Root Mean Square (RMS) of τ_{err}. In this check also a sample of fully simulated $B_s^0 \to K^+K^-$ events is taken into account, after having applied both the selection reported in Section 5.1 and the PID reweighting. The results of this test show a significant dependence of the δ_t distribution on the PID and kinematic reweighting, however the linearity of the relation remains untouched. The calibration parameters q_0 and q_1, obtained for the three decay modes with and without the weight application, are reported in Table 5.10 while the functional dependencies between the δ_t and the $RMS(\tau_{err})$ along with δ_t distributions are shown in Figure 5.13.

Finally, the results of the bi-dimensional fit are reported in Table 5.11 while the distributions of τ_{err} are shown in Figure 5.14. No significant deviation of μ from 0 are observed, and the f_τ and r_σ parameters are in good agreement between the two decay modes.

Table 5.11: Calibration parameters of the decay time resolution for fully simulated $B_s^0 \to \pi^+K^-$ and $B_s^0 \to D_s^-\pi^+$ decays. The results are obtained from the unbinned maximum likelihood fit, using the model reported in Equation 5.19, to the distributions of fully simulated candidates.

Parameter	$B_s^0 \to \pi^+K^-$	$B_s^0 \to D_s^-\pi^+$
μ	0.07 ± 0.05 fs	-0.07 ± 0.07 fs
q_0	35.1 ± 0.1 fs	36.7 ± 0.1 fs
q_1	1.10 ± 0.01	1.16 ± 0.01
r_σ	3.08 ± 0.03	2.98 ± 0.04
f_τ	0.971 ± 0.001	0.971 ± 0.001

Calibration of decay time resolution in data

The calibration of the decay time resolution in data is performed by means of fits to the tagged time-dependent decay rates of the flavour specific $B^0 \to D^-\pi^+$ and $B_s^0 \to D_s^-\pi^+$ decays. The two

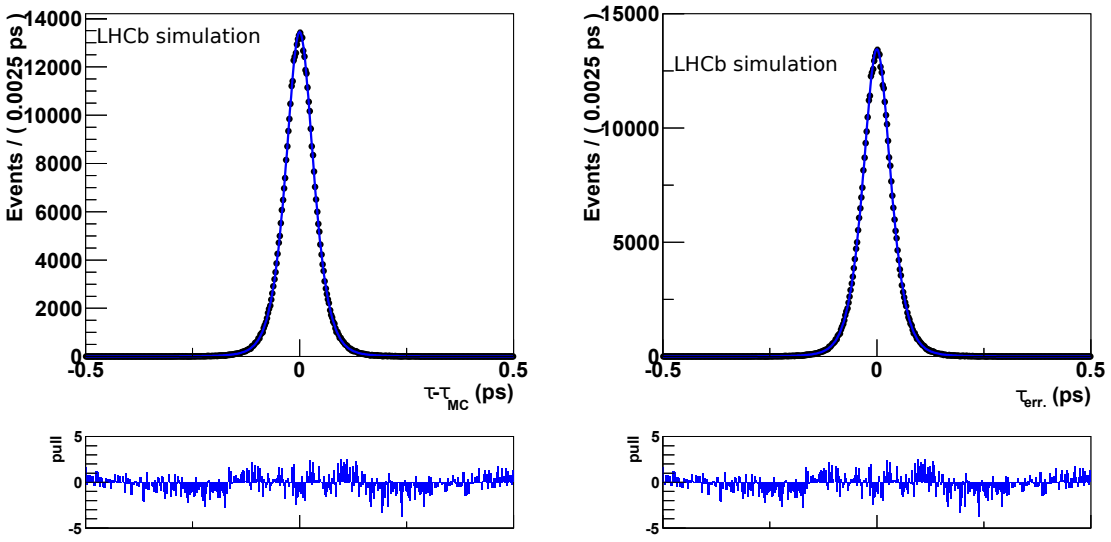

Figure 5.14: Distribution of τ_{err} for fully simulated $B_s^0 \to \pi^+K^-$ and $B_s^0 \to D_s^-\pi^+$ decays on the left and right, respectively. The result of the fit, using the model reported in Equation 5.19, is superimposed.

background subtracted samples have been fitted simultaneously using the model described in Equation 5.22 with the decay time resolution R parametrised as reported in Equation 5.19. The calibration parameters q_0 and q_1 of the decay time resolution are shared between the two decay modes. The values of the decay widths $\Gamma_{d,s}$ and of the differences of the decay widths $\Delta\Gamma_{d,s}$ are fixed to the HFLAV averages [71]. The coefficient of the cubic spline polynomial, describing the decay time acceptance, are free to vary in the fit as well as the oscillation frequency parameters $\Delta m_{d,s}$. The fit is performed using only the OS tagger and the parameters governing its calibration are shared among the two decay modes since, as mentioned in Chapter 4, the OS tagging performance are compatible for both B^0 and B_s^0 mesons. Since the effect of the decay time resolution is negligible for the $B^0 \to D^-\pi^+$ decay, it is possible to determine the calibration of the flavour tagging fixing the dilution factor of the oscillation amplitude to the mistag probability. The calibration of the decay time resolution is hence determined measuring the additional dilution of the oscillation amplitude in the $B_s^0 \to D_s^-\pi^+$ decay. The value of μ, f_τ and r_σ are fixed to 0, 0.971 and 3 respectively, according to the value reported in Table 5.11. The results of the fit for the parameters governing the calibration of the decay time resolution are $q_0 = 46.1 \pm 2.5$ fs and $q_1 = 0.81 \pm 0.23$, with a correlation equal to $\rho_{q_0,q_1} = -0.32$. The decay time distributions and the time-dependent asymmetries, both for the $B^0 \to D^-\pi^+$ and $B_s^0 \to D_s^-\pi^+$ decays, are shown in Figure 5.15.

The validity of this procedure, used to determine the parameters governing the calibration of the decay time resolution, has been verified using fully simulated samples of $B_s^0 \to \pi^+K^-$ and $B_s^0 \to D_s^-\pi^+$ decays, as described in Appendix D.

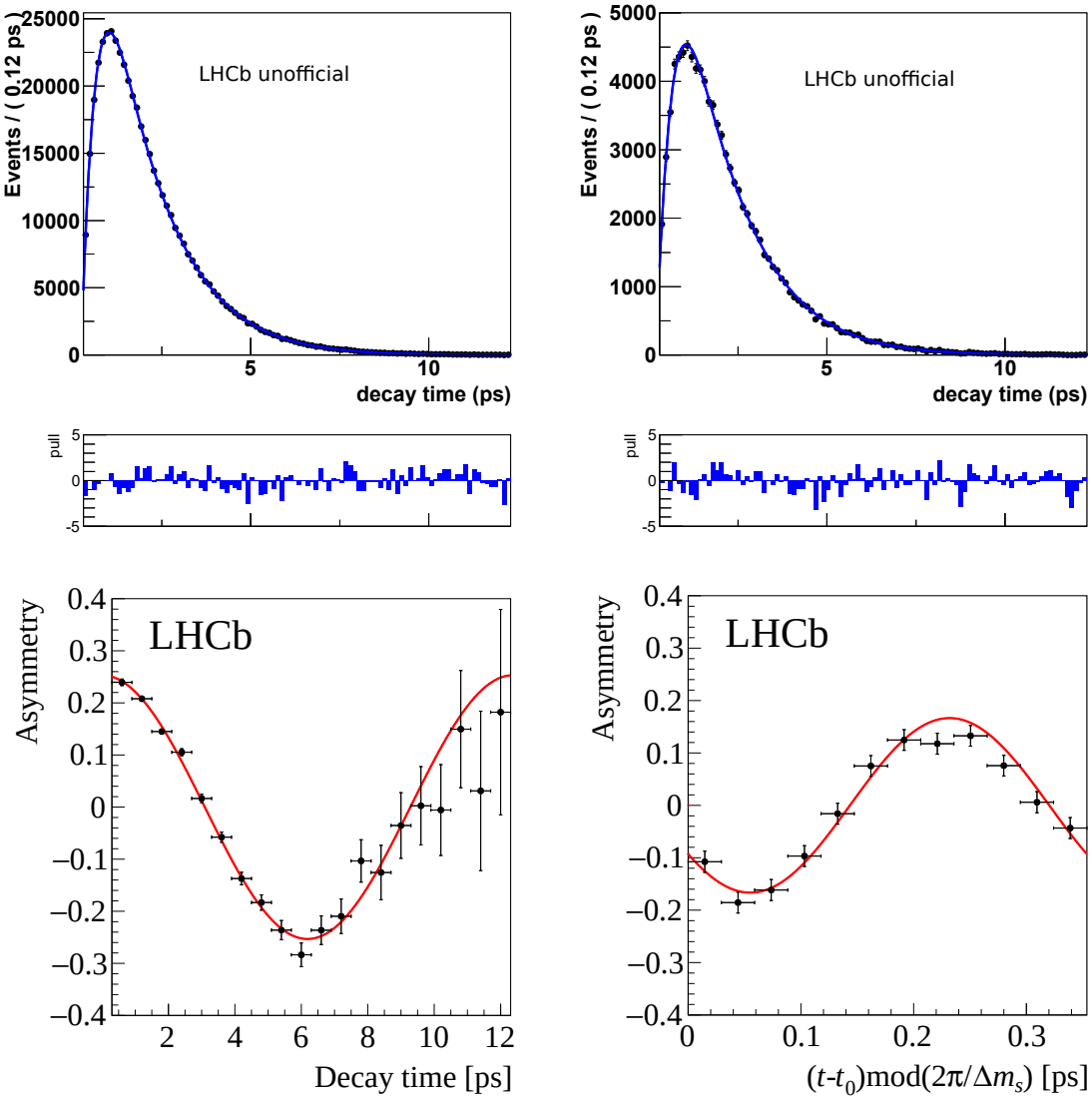

Figure 5.15: Distribution of the decay time (top) and time-dependent asymmetry (bottom) for $B^0 \to D^-\pi^+$ (left) and $B_s^0 \to D_s^-\pi^+$ (right) decays. The result of the best fit are superimposed on data points.

Parametrisation of the δ_t distribution

Another important ingredient to be used in the final fit regards the correct description of the δ_t distribution for all the components contributing to the three final states. For the signal and the cross-feed backgrounds the distribution of δ_t is described by means of templates taken from a background subtracted sample of $H_b \to h^+h'^-$ decays, obtained as described in Section 5.1.6. Since the PID requirement can affect significantly the δ_t distribution, the *sWeight* associated to each B meson, obtained by means of the *sPlot* technique, is multiplied by the PID efficiency evaluated as function of the momentum and pseudorapidity of the two daughters in the final state. The templates for the combinatorial backgrounds are obtained from histograms filled with B candidates taken from the upper invariant mass sidebands ($m > 5.6\,\text{GeV}/c^2$) for the different final states. Similarly the templates of the partially reconstructed 3-body backgrounds are obtained from histograms filled with B candidates taken from the lower invariant mass sidebands ($m < 5.2\,\text{GeV}/c^2$), subtracting the residual contamination due to the combinatorial background. The amount of the contamination is estimated by fitting the upper mass sideband ($m > 5.6\,\text{GeV}/c^2$) with an exponential function and rescaling the yield obtained to what expected in the lower invariant mass region. The histograms parametrising the δ_t distribution for the combinatorial background component are then subtracted, according to the estimated amount of the contamination, from those obtained from the B candidate in the lower invariant mass sideband.

5.4.2 Decay-time acceptance

Some of the criteria used for the event selection can affect the reconstruction efficiency introducing a distortion of the decay time distribution of the signal $H_b \to h^+h'^-$ decays. Because of this effect the signal decay time distribution can not be parametrised as a simple exponential and an acceptance function has to be included in the model. The determination of the acceptance functions for the $H_b \to h^+h'^-$ decay modes has been completely revisited with respect to the one used in the previous analysis [70]. The decay acceptance has been determined using the data of the $B^0 \to K^+\pi^-$ decay. In this case, due to the small value of $\Delta\Gamma_d$, the untagged time dependent decay rate can be described by a pure exponential with $\Gamma_d = 0.65588 \pm 0.0017\,\text{ps}^{-1}$ [71]. The $B^0 \to K^+\pi^-$ decay time distribution in the $K^+\pi^-$ mass hypothesis is splitted in 27 equivalent subsamples. In each subsample an unbinned maximum likelihood fit is performed, using the models given in Section 5.3, in order to estimate the yields of the signal. The yields obtained from the fits are then used to build an histogram representing the decay-time distribution for the $B^0 \to K^+\pi^-$ decay. The $B^0 \to K^+\pi^-$ acceptance function is determined from the ratio between the histogram of the decay time distribution and an histogram representing the true decay time distribution if all the events were reconstructed.

This second histogram is built using simulated events generated according to a pure exponential with a constant equal to Γ_d.

The decay time acceptance function for all the other signal modes is determined from the $B^0 \to K^+\pi^-$ acceptance. Firstly, the acceptance of each mode is determined using fully simulated events and then the ratio with respect to the acceptance of fully simulated $B^0 \to K^+\pi^-$ decay is evaluated. Each simulated event is reweighted according to the PID efficiencies in order to take into account any possible discrepancy introduced by the PID requirements used for the final state selection. Finally, the $B^0 \to K^+\pi^-$ decay time acceptance, obtained from the data as described before, is rescaled by the ratio of the decay-time acceptances in order to obtain the observed decay time acceptance for each mode.

An effective function is used to parametrise the obtained decay time acceptance for all the modes:

$$\varepsilon_{acc}^{\text{sig}} = [a_0 - \text{erf}\,(a_1 t^{a_2})]\,(1 - a_3 t)\,, \tag{5.21}$$

where the a_i parameters are left free to vary in the fit. The acceptance histograms for the $H_b \to h^+h'^-$ decays in the three mass hypotheses are shown in Figures 5.16, 5.17, and 5.18. The result of the fit is superimposed and the bands corresponding to one and two standard deviation confidence regions are also shown. As last step, very high statistics samples are generated from the best fit results and are used to fill histograms, which will be interpolated with cubic spline polynomial functions in the final fit to data. The so-obtained decay time acceptance functions, used to describe the decay-time distribution for the various signal components, are used also to determine the decay-time distribution of the corresponding cross-feed backgrounds.

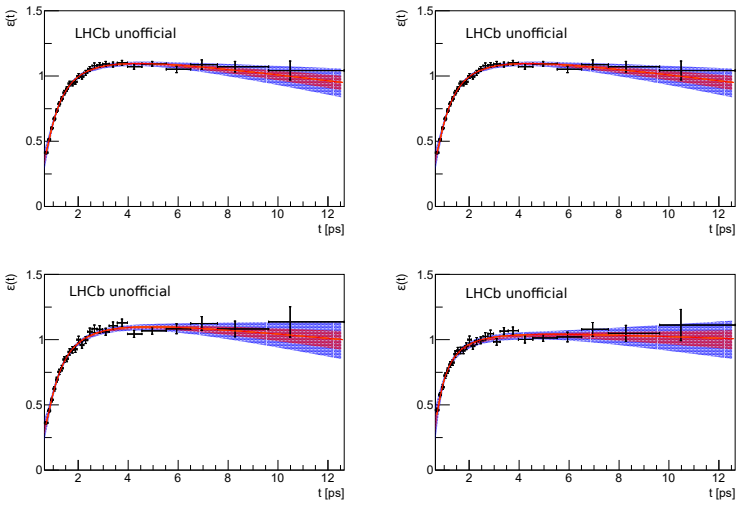

Figure 5.16: Decay-time acceptance for the $H_b \to h^+h'^-$ decay modes contributing to the $K^+\pi^-$ spectrum obtained as described in the text. From top left to bottom right: the $B^0 \to K^+\pi^-$, the $B_s^0 \to \pi^+K^-$, the $B^0 \to \pi^+\pi^-$ and the $B_s^0 \to K^+K^-$ reconstructed under the $K^+\pi^-$ hypothesis.

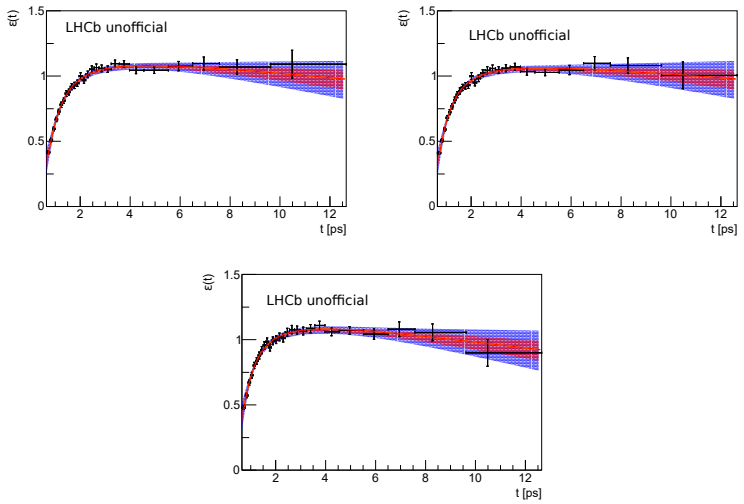

Figure 5.17: Decay-time acceptance for the $H_b \to h^+h'^-$ decay modes contributing to the $\pi^+\pi^-$ spectrum obtained as described in the text. From left to right: the $B^0 \to \pi^+\pi^-$, the $B_s^0 \to \pi^+\pi^-$ and the $B^0 \to K^+\pi^-$ reconstructed under the $\pi^+\pi^-$ hypothesis.

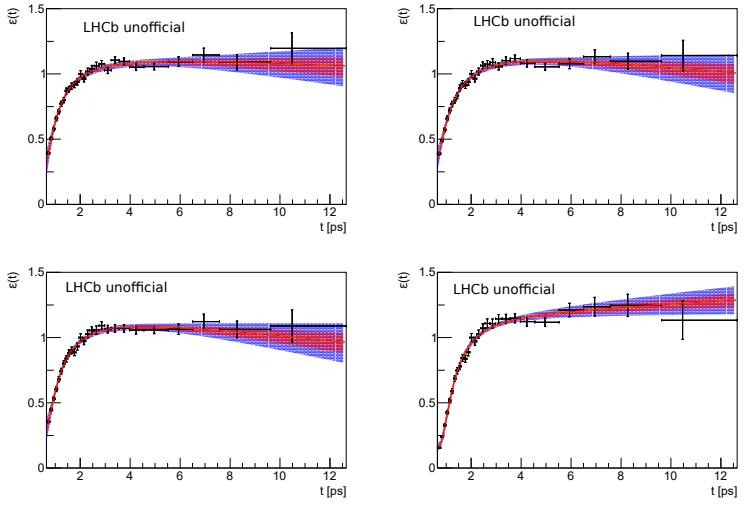

Figure 5.18: Decay-time acceptance for the $H_b \to h^+h'^-$ decay modes contributing to the K^+K^- spectrum obtained as described in the text. From left to right: the $B_s^0 \to K^+K^-$, the $B^0 \to K^+K^-$, the $B^0 \to K^+\pi^-$ and the $\Lambda_b^0 \to pK^-$ reconstructed under the K^+K^- hypothesis.

5.4.3 Decay-time model for signal decay

The decay time model for the signals consists of various ingredients that have been described in detail in the previous sections, namely the decay-time resolution (Section 5.4.1), the decay-time acceptance (Section 5.4.2) and the flavour tagging observables (Section 4). The description of the model change according to the nature of the decay: i.e. if it is flavour specific or a *CP* eigenstate.

Flavour specific B decays

For a flavour specific decay, such as the $B^0 \to K^+\pi^-$ and $B_s^0 \to \pi^+K^-$, where the the final state f and its *CP* conjugate $\overline{f}$ are different, the dependence on time of the decay rate can be expressed as:

$$\begin{aligned} f(\overrightarrow{\theta}) =& K^{-1}(1-\psi A_{CP})(1-\psi A_f)\cdot \\ & \Big\{ \Big[(1-A_p)\Omega_{\rm sig}(\overrightarrow{\theta}_{\rm tag}) + (1+A_p)\overline{\Omega}_{\rm sig}(\overrightarrow{\theta}_{\rm tag})\Big] H_+(t,\delta_t) + \\ & \psi \Big[(1-A_p)\Omega_{\rm sig}(\overrightarrow{\theta}_{\rm tag}) - (1+A_p)\overline{\Omega}_{\rm sig}(\overrightarrow{\theta}_{\rm tag})\Big] H_-(t,\delta_t)\Big\}, \end{aligned} \tag{5.22}$$

where $\overrightarrow{\theta} = (t, \delta_t, \psi, d_{OS}, \eta_{OS}, d_{SS}, \eta_{SS})$ is the set observables of the fit: the variables t and δ_t represent the decay time and its uncertainty, ψ indicates the final state tag which can assume the value of 1 and -1 for the final state f and $\overline{f}$ respectively, d_{tag} and η_{tag} are the flavour tagging decision and the predicted mistag probability respectively, assigned to the B candidates, where tag stands for OS and SS tagger; the parameter K is a normalization factor equal to:

$$K = 4(1+A_{CP}A_f)\iint H_+(t'\delta_t')dt'd\delta_t' + 4A_P(A_{CP}+A_f)\iint H_-(t'\delta_t')dt'd\delta_t'; \tag{5.23}$$

the parameters $\Omega_{\rm sig}$ and $\overline{\Omega}_{\rm sig}$ represent the probability functions for the flavour tagging observables, as reported in Chapter 4, where $\overrightarrow{\theta}_{\rm tag} = (d_{OS}, \eta_{OS}, d_{SS}, \eta_{SS})$; A_{CP}, A_f, A_P are the direct *CP* asymmetry, the asymmetry of the final state reconstruction efficiencies and the B meson production asymmetry, defined as:

$$\begin{aligned} A_{CP} &= \frac{\mathcal{B}(\overline{B}\to\overline{f}) - \mathcal{B}(B\to f)}{\mathcal{B}(\overline{B}\to\overline{f}) + \mathcal{B}(B\to f)} \\ A_f &= \frac{\varepsilon_{tot}(\overline{f}) - \varepsilon_{tot}(f)}{\varepsilon_{tot}(\overline{f}) + \varepsilon_{tot}(f)} \\ A_P &= \frac{\mathcal{R}(\overline{B}) - \mathcal{R}(B)}{\mathcal{R}(\overline{B}) + \mathcal{R}(B)} \end{aligned} \tag{5.24}$$

where $\mathcal{B}$ indicates the branching fraction, ε_{tot} stands for the total efficiency in the reconstruction and selection of the final state (f or $\overline{f}$), and $\mathcal{R}$ is the production rate of the given B or $\overline{B}$ meson; finally the functions $H_+(t,\delta_t)$ and $H_-(t,\delta_t)$ can be written as:

$$\begin{aligned} H_+(t,\delta_t) &= \left[\exp(-\Gamma t')\cosh\left(\frac{\Delta\Gamma}{2}t'\right)\right] \otimes R(t-t'|\delta_t)\cdot g(\delta_t)\cdot \varepsilon_{\rm sig}^{acc}(t), \\ H_-(t,\delta_t) &= \left[\exp(-\Gamma t')\cos(\Delta m t')\right] \otimes R(t-t'|\delta_t)\cdot g(\delta_t)\cdot \varepsilon_{\rm sig}^{acc}(t), \end{aligned} \tag{5.25}$$

where Γ is the average width of the B meson decay, $\Delta\Gamma$ and Δm are the decay width and mass difference between the mass eigenstates, R stands for the decay-time resolution model defined on per-event basis depending on δ_t, $g(\delta_t)$ and ε_{acc} represent the distribution of the δ_t variable and the decay time acceptance, respectively.

It is important to notice that using the model described by Equation 5.22 in the final fit do not allow the discrimination between A_{CP} and A_f asymmetry, which therefore will be estimated as a unique raw asymmetry: $A_{raw} = A_{CP} + A_f$. The determination of A_f, essential for the extraction of the A_{CP} asymmetry, is described in Section 5.5.1.

CP **eigenstate** B **decays**

For a no-flavour specific decay, the two final states f and $\overline{f}$ are the same thus the ψ variable is removed from the $\overrightarrow{\theta}$ set of observables, since there is no need to use it in the model description. The time-dependent decay rate can be written as:

$$\begin{aligned} f(\overrightarrow{\theta}) = K^{-1}\Big\{ &\Big[(1-A_P)\Omega(\overrightarrow{\theta}_{\text{tag}}) + (1+A_P)\overline{\Omega}(\overrightarrow{\theta}_{\text{tag}})\Big] I_+(t,\delta_t) + \\ &\Big[(1-A_P)\Omega(\overrightarrow{\theta}_{\text{tag}}) - (1+A_P)\overline{\Omega}(\overrightarrow{\theta}_{\text{tag}})\Big] I_-(t,\delta_t)\Big\}, \end{aligned} \tag{5.26}$$

where the normalization factor K is defined as:

$$K = 2\iint I_+(t',\delta_t')dt'd\delta_t' - 2A_P \iint I_-(t',\delta_t')dt'd\delta_t', \tag{5.27}$$

and the two functions $I_+(t,\delta_t)$ and $I_-(t,\delta_t)$ are:

$$\begin{aligned} I_+(t,\delta_t) =& \Big\{ \exp(-\Gamma t') \left[\cosh\left(\frac{\Delta\Gamma}{2}t'\right) - A_f^{\Delta\Gamma}\sinh\left(\frac{\Delta\Gamma}{2}t'\right)\right] \Big\} \otimes R(t-t'|\delta_t)\cdot g(\delta_t)\cdot \varepsilon_{\text{sig}}^{acc}(t), \\ I_-(t,\delta_t) =& \Big\{ \exp(-\Gamma t') \Big[C_f\cos(\Delta m t') - S_f\sin(\Delta m t')\Big] \Big\} \otimes R(t-t'|\delta_t)\cdot g(\delta_t)\cdot \varepsilon_{\text{sig}}^{acc}(t). \end{aligned} \tag{5.28}$$

The parameters C_f, S_f and $A_f^{\Delta\Gamma}$ satisfy the following relation: $|C_f|^2 + |S_f|^2 + |A_f^{\Delta\Gamma}|^2 = 1$. They are left free to vary in the final fit, except for $A^{\Delta\Gamma}_{\pi^+\pi^-}$ which is fixed to 0 since it can not be measured because the value of $\Delta\Gamma_d$ is too small.

5.4.4 Decay-time model for cross-feed background

The decay time p.d.f.'s for the cross-feed background components have been determined assuming that the decay time calculated under the wrong mass hypothesis is not significantly different from the correct one. This assumption has been verified by means of full simulations, as already proved in Reference [136]. The considered cross-feed contributions are:

- the $B^0 \to \pi^+\pi^-$ and $B_s^0 \to K^+K^-$ decays misidentified as $K^+\pi^-$ final states;
- the $B^0 \to K^+\pi^-$ decay misidentified as $\pi^+\pi^-$ and K^+K^- final states.

- the $\Lambda_b^0 \to pK^-$ decay misidentified as K^+K^- final state.

Additional components, due to the misidentification of both the daughters in the final state, are found to be negligible given the PID requirements used to separate the $K^+\pi^-$, $\pi^+\pi^-$ and K^+K^- mass hypothesis.

$B^0 \to \pi^+\pi^-$ and $B_s^0 \to K^+K^-$ decays under the $K^+\pi^-$ hypothesis

Since the final states of $B^0 \to \pi^+\pi^-$ and $B_s^0 \to K^+K^-$ decays are CP eigenstates, the decay rate does not depend explicitly on ψ. Therefore the p.d.f. can be written as:

$$\begin{aligned} f\left(\overrightarrow{\theta}\right) = K^{-1}\Big\{ &\left[(1-A_P)\,\Omega_{\text{sig}}\left(\overrightarrow{\theta}_{\text{tag}}\right) + (1+A_P)\,\overline{\Omega}_{\text{sig}}\left(\overrightarrow{\theta}_{\text{tag}}\right)\right] I_+\left(t,\delta_t\right) + \\ &\left[(1-A_P)\,\Omega_{\text{sig}}\left(\overrightarrow{\theta}_{\text{tag}}\right) - (1+A_P)\,\overline{\Omega}_{\text{sig}}\left(\overrightarrow{\theta}_{\text{tag}}\right)\right] I_-\left(t,\delta_t\right)\Big\}, \end{aligned} \tag{5.29}$$

where $\overrightarrow{\theta} = \left\{t, \delta_t, \psi, d_{\text{OS}}, d_{\text{SS}}, \eta_{\text{OS}}, \eta_{\text{SS}}\right\}$, but the dependence on ψ is implicit as $B^0 \to \pi^+\pi^-$ and $B_s^0 \to K^+K^-$ can be misidentified as both $K^+\pi^-$ and $K^-\pi^+$ final states. The normalization factor K is given by

$$K = 4\int\int I_+\left(t',\delta_t'\right)dt'd\delta_t' - 4A_P\int\int I_+\left(t',\delta_t'\right)dt'd\delta_t'. \tag{5.30}$$

and the functions $I_+(t,\delta_t)$ and $I_-(t,\delta_t)$ are the ones reported in Section 5.4.3

$B^0 \to K^+\pi^-$ decays with final state identified as $\pi^+\pi^-$ or K^+K^-

In this case the information provided by the observation of the two $K^+\pi^-$ and $K^-\pi^+$ final states is lost. This effect is equivalent to integrate on ψ the p.d.f. written in Equation (5.22). This cross-feed background can be parametrised as:

$$\begin{aligned} f\left(\overrightarrow{\theta}\right) = K^{-1}\Big\{ &\left(1+A_{CP}A_f\right)\left[(1-A_P)\,\Omega_{\text{sig}}\left(\overrightarrow{\theta}_{\text{tag}}\right) + (1+A_P)\,\overline{\Omega}_{\text{sig}}\left(\overrightarrow{\theta}_{\text{tag}}\right)\right] H_+(t,\delta_t) - \\ &\left(A_{CP}+A_f\right)\left[(1-A_P)\,\Omega_{\text{sig}}\left(\overrightarrow{\theta}_{\text{tag}}\right) - (1+A_P)\,\overline{\Omega}_{\text{sig}}\left(\overrightarrow{\theta}_{\text{tag}}\right)\right] H_-(t,\delta_t)\Big\}, \end{aligned} \tag{5.31}$$

where the variable ψ is removed from $\overrightarrow{\theta}$ and the normalization factor K is

$$K = 2\left(1+A_{CP}A_f\right)\int\int H_+\left(t',\delta_t'\right)dt'd\delta_t' + 2A_P\left(A_{CP}+A_f\right)\int\int H_-\left(t',\delta_t'\right)dt'd\delta_t', \tag{5.32}$$

and the functions $H_+(t,\delta_t)$ and $H_-(t,\delta_t)$ are the ones reported in Section 5.4.3

$\Lambda_b^0 \to pK^-$ decays with final state identified as K^+K^-

Also in this latest case, the information provided by the observation of the two pK^- and $\overline{p}K^+$ final states is lost. Since the time-dependent decay rate of the Λ_b^0 baryon is a pure exponential, the decay time distribution of $\Lambda_b^0 \to pK^-$ misidentified as K^+K^- final state is given by:

$$\begin{aligned} f\left(\overrightarrow{\theta}\right) = &K^{-1}\Big[(1-A_P)\left(1-A_f\right)(1-A_{CP})\,\Omega_{\text{sig}}\left(\overrightarrow{\theta}_{\text{tag}}\right) + \\ &(1+A_P)\left(1+A_f\right)(1+A_{CP})\,\overline{\Omega}_{\text{sig}}\left(\overrightarrow{\theta}_{\text{tag}}\right)\Big]\,T\left(t,\delta_t\right) \end{aligned} \tag{5.33}$$

where K is the normalization factor,

$$K = 2\left(1 + A_{CP}A_f + A_{CP}A_P + A_fA_P\right)\int\int T\left(t', \delta_t'\right)dt'd\delta_t', \tag{5.34}$$

A_P is the production asymmetry of the Λ_b^0 baryon, A_f is the detection asymmetry of the pK^- and $\overline{p}K^+$ final states, A_{CP} is the CP asymmetry of the $\Lambda_b^0 \to pK^-$ decay, the functions $\Omega_{\text{sig}}\left(d, \eta\right)$ and $\overline{\Omega}_{\text{sig}}\left(d, \eta\right)$ represent the probability of a Λ_b^0 baryon to be tagged as a B meson or a $\overline{B}$ meson respectively, $T\left(t, \delta_t\right)$ is defined as:

$$T\left(t,\, \delta_t\right) = e^{-\Gamma t'} \otimes R\left(t - t'|\delta_t\right) \cdot g\left(\delta_t\right) \cdot \varepsilon_{acc}\left(t\right), \tag{5.35}$$

where Γ is the decay width of the Λ_b^0 baryon, $g\left(\delta_t\right)$ is the distribution of δ_t and ε_{acc} is the decay time-acceptance function.

5.4.5 Decay-time model for combinatorial background

The decay time of the combinatorial background has been parametrised using the events in the high invariant mass sideband, defined requiring $m > 5.6\,\text{GeV}/c^2$. The parametrisation of the p.d.f can be written as:

$$\begin{aligned} f(\overrightarrow{\theta}) =& K^{-1}(1 - \psi A_{CP}^{\text{comb}})\Omega_{\text{comb}}(\overrightarrow{\theta}_{\text{tag}})g_{\text{comb}}(\delta_t)\times \\ & [f^{\text{comb}}\exp(-\Gamma_1^{\text{comb}}t)\varepsilon_{\text{comb}}^{acc}(t) + (1 - f^{\text{comb}})\exp(-\Gamma_2^{\text{comb}}t)\varepsilon_{\text{comb}}^{acc}(t)], \end{aligned} \tag{5.36}$$

where $\overrightarrow{\theta}$ is the same set of observables defined in Section 5.4.3, K is the normalization factor defined as:

$$K = 2\int g_{\text{comb}}(\delta_t')d\delta_t' \int \left[f^{\text{comb}}\exp(-\Gamma_1^{\text{comb}}t)\varepsilon_{\text{comb}}^{acc}(t) + (1 - f^{\text{comb}})\exp(-\Gamma_2^{\text{comb}}t)\varepsilon_{\text{comb}}^{acc}(t)\right]dt', \tag{5.37}$$

A_{CP} is the charge asymmetry of the combinatorial background, $\Omega_{\text{comb}}(\overrightarrow{\theta}_{\text{tag}})$ is the probability function for the flavour tagging variables described in Chapter 4, $g_{\text{comb}}(\delta_t)$ represents the distribution of the decay-time error for the combinatorial background, $\varepsilon_{\text{comb}}^{acc}(t)$ is an effective function covering the place of the acceptance function for the signal decays, defined as:

$$\varepsilon_{\text{comb}}^{acc}(t) = \frac{1}{2}\left[1 - \text{erf}\left(\frac{a - t}{a \cdot t}\right)\right] \tag{5.38}$$

where the parameters a together to the remaining parameters f^{comb}, Γ_1^{comb} and Γ_2^{comb} are free parameters to be determined in the fit. For all the three mass hypothesis a good agreement between the model and the decay time distribution in the high invariant mass sideband has been found. In case of the $\pi^+\pi^-$ and K^+K^- mass hypothesis, the parametrisation does not depend on the two different charge conjugate final states.

5.4.6 Decay-time model for partially reconstructed 3-body decay

The parametrisation of the decay time distribution for the partially reconstructed 3-body B decay in the $\pi^+\pi^-$ and K^+K^- final state has been defined as:

$$f(\overrightarrow{\theta}) = K^{-1}\Omega_{\text{phys}}(\overrightarrow{\theta}_{\text{tag}}) \cdot g_{\text{phys}}(\delta_t) \cdot \exp(-\Gamma_{\text{phys}}t)\varepsilon^{acc}_{\text{phys}}(t), \tag{5.39}$$

where K is the normalization factor, $\Omega_{\text{phys}}(\overrightarrow{\theta}_{\text{tag}})$ is the probability function for the flavour tagging observables described in Section 4, g_{phys} is the decay time error distribution for the partially reconstructed backgrounds and $\varepsilon^{acc}_{\text{phys}}$ is an effective function describing the decay time acceptance defined as:

$$\varepsilon^{acc}_{\text{phys}}(t) = \frac{1}{2}\left[1 - \text{erf}\left(\frac{b-t}{b\cdot t}\right)\right], \tag{5.40}$$

where b is a free parameter of the final fit. The decay time distribution in the $K^+\pi^-$ mass hypothesis is the same used to describe the $B^0 \to K^+\pi^-$ decay, with independent flavour tagging parameters and leaving the oscillation frequency Δm free to vary. The change in the decay model description for the partially reconstructed 3-body B decay in the $K^+\pi^-$ final state is due to the observation of a time-dependent asymmetry in the low-mass region. In both the cases, the acceptance function is described by a cubic splines polynomial [137] whose parameters are left free in the fit, while the parameter Γ is fixed to $0.6\,\text{ps}^{-1}$ [15].

5.5 Fit results

All the ingredients described in the previous sections are then combined together in order to perform the final unbinned maximum likelihood fit to data. The parameters fixed in the fit comprise:

- the parameters governing the tails of the signal mass models, as mentioned in Section 5.3. Their value are reported in Table 5.9;
- the endpoints of the ARGUS functions describing the mass distributions of the partially reconstructed 3-body background components are fixed to the difference between the B meson and pion masses. In particular, the endpoint governing the contribution due to B^0 meson is set to $5.1446\,\text{GeV}/c^2$ [15], while the endpoint for the partially reconstructed background coming from the B^0_s meson is fixed to $5.2318\,\text{GeV}/c^2$ [15];
- the PID efficiencies related to the yields of the correctly identified and misidentified $H_b \to h^+h'^-$ decays contributing to the different mass hypotheses;
- the calibration parameters of the per-event decay-time resolution are fixed to $q_0 = 46.1 \pm 2.5\,\text{fs}$ and $q_1 = 0.81 \pm 0.23$, as reported in Section 5.4.1. The parameters μ, f_τ and r_σ governing the

decay time resolution model are fixed as well to 0, 3, and 0.971, respectively;

- the shapes of the signal decay-time acceptances are fixed using the templates taken from the histograms, as described in Section 5.4.2;
- the calibration parameters of the flavour tagging SSπBDT and SSp algorithms, combined to obtain a unique SS*comb* tagger, as well as the SSkNN algorithm are fixed to the values reported in Tables 4.2, 4.6.
- the values of the mixing oscillation frequencies, the differences of the decay widths for B^0 and B_s^0 mesons and the decay width of the B_s^0 mesons are fixed to the HFLAV averages [71] summarized in Table 5.12.

The decay width of the B^0 meson is left free to vary in the fit in order to provide a validity cross-check of strategy used to describe the signal decay-time acceptances. The values of the calibration parameters related to the OS and SS*comb* taggers obtained from the fit are reported in Table 5.13.

Table 5.12: The values of the parameters Δm_d, $\Delta\Gamma_d$, Δm_s, Γ_s and $\Delta\Gamma_s$ that are taken from HFLAV [71] and fixed in the fit to data. The parameter errors are used to determine the systematic uncertainty. The correlation between Γ_d and $\Delta\Gamma_d$, as well as between Γ_s and $\Delta\Gamma_s$, is also reported.

Parameter	Value
Δm_d	$0.5065 \pm 0.0019\,\text{ps}^{-1}$
$\Delta\Gamma_d$	$0\,\text{ps}^{-1}$
$\rho(\Gamma_d, \Delta\Gamma_d)$	0
Δm_s	$17.757 \pm 0.021\,\text{ps}^{-1}$
Γ_s	$0.6654 \pm 0.0022\,\text{ps}^{-1}$
$\Delta\Gamma_s$	$0.083 \pm 0.007\,\text{ps}^{-1}$
$\rho(\Gamma_s, \Delta\Gamma_s)$	-0.292

The results of the *CP* asymmetries are

$$\begin{aligned} C_{\pi^+\pi^-} &= -0.3367 \pm 0.0623 \\ S_{\pi^+\pi^-} &= -0.6261 \pm 0.0538 \\ C_{K^+K^-} &= 0.1968 \pm 0.0584 \\ S_{K^+K^-} &= 0.1816 \pm 0.0586 \\ A_{K^+K^-}^{\Delta\Gamma} &= -0.7876 \pm 0.0730 \\ A_{raw}(B^0 \to K^+\pi^-) &= (-9.338 \pm 0.396)\% \\ A_{raw}(B_s^0 \to \pi^+K^-) &= (22.27 \pm 1.53)\% \end{aligned} \tag{5.41}$$

Table 5.13: Calibration parameters of the flavour tagging obtained from the fits. The calibration parameters have been determined from the fits using OS only, S*Scomb* only and OS+S*Scomb* only information.

Parameter	OS	S*Scomb*	OS +S*Scomb*
$\hat{\varepsilon}^{sig}_{OS}$	0.33693 ± 0.00162	–	0.33679 ± 0.00162
$\Delta\varepsilon^{sig}_{OS}$	0.00973 ± 0.00713	–	0.01013 ± 0.00712
$\hat{p}^{OS}_0$	0.38541 ± 0.00431	–	0.38512 ± 0.00424
Δp^{OS}_0	0.01823 ± 0.00650	–	0.01570 ± 0.00639
$\hat{p}^{OS}_1$	1.0035 ± 0.0452	–	1.0212 ± 0.0444
Δp^{OS}_1	0.0223 ± 0.0250	–	0.0285 ± 0.0244
$\hat{\eta}_{OS}$	0.37	–	0.37
$\hat{\varepsilon}^{sig}_{SScomb}$	–	0.76528 ± 0.00144	0.76477 ± 0.00144
$\Delta\varepsilon^{sig}_{SScomb}$	–	-0.00463 ± 0.00365	-0.00294 ± 0.00303
$\hat{p}^{SScomb}_0$	–	0.43727 ± 0.00312	0.43826 ± 0.00294
Δp^{SScomb}_0	–	-0.00200 ± 0.00453	0.00152 ± 0.00420
$\hat{p}^{SScomb}_1$	–	0.9593 ± 0.0749	0.9613 ± 0.0710
Δp^{SScomb}_1	–	-0.0003 ± 0.0447	-0.0298 ± 0.0428
$\hat{\eta}_{SScomb}$	–	0.44	0.44

where the parameters related to the B^0 meson are obtained using both the OS and the S*Scomb* tagging algorithms, while the *CP* observables corresponding to the B^0_s meson come from the fit performed using both the OS and the S*SkNN* taggers. In Table 5.14 the statistical correlations among the various *CP* violating parameters are reported. The corrections required to obtain the *CP* asymmetries for the $B^0 \to K^+\pi^-$ and $B^0_s \to \pi^+K^-$ decays from the corresponding raw asymmetries are discussed in Section 5.5.1. The raw time-dependent asymmetries of the $K^\pm\pi^\mp$ spectrum related to the B candidates lying under the signal region, defined requiring an invariant mass ($m_{K^\pm\pi^\mp}$) in range [5.20, 5.32] GeV/c^2, are shown in Figure 5.19. The raw time-dependent asymmetries for the $\pi^+\pi^-$

Table 5.14: Statistical correlations among the *CP* violation parameters are determined from the fit.

	$C_{\pi^+\pi^-}$	$S_{\pi^+\pi^-}$	$C_{K^+K^-}$	$S_{K^+K^-}$	$A^{\Delta\Gamma}_{K^+K^-}$	$A_{raw}(B^0 \to K^+\pi^-)$	$A_{raw}(B^0_s \to \pi^+K^-)$
$C_{\pi^+\pi^-}$	1.000	0.448	−0.006	−0.009	0.000	−0.009	0.003
$S_{\pi^+\pi^-}$	0.448	1.000	−0.040	−0.006	0.000	0.008	0.000
$C_{K^+K^-}$	−0.006	−0.040	1.000	−0.014	0.025	0.006	0.001
$S_{K^+K^-}$	−0.009	−0.006	−0.014	1.000	0.028	−0.003	0.000
$A^{\Delta\Gamma}_{K^+K^-}$	0.000	0.000	0.025	0.028	1.000	0.001	0.000
$A_{raw}(B^0 \to K^+\pi^-)$	−0.009	0.008	0.006	−0.003	0.001	1.000	0.043
$A_{raw}(B^0_s \to \pi^+K^-)$	0.003	0.000	0.001	0.000	0.000	0.043	1.000

and K^+K^- final states, observed in signal invariant mass regions corresponding to $5.20\,\text{GeV}/c^2 < m_{\pi^+\pi^-} < 5.35\,\text{GeV}/c^2$ and $5.30\,\text{GeV}/c^2 < m_{K^+K^-} < 5.44\,\text{GeV}/c^2$ respectively, are shown in Figure 5.20. The distributions of all the observables used in the fit for all the three final states are reported in Figures 5.21, 5.22 and 5.23. The production asymmetries are also estimated during the fit in order to reduce the systematic uncertainties on the *CP* asymmetries in the $K^+\pi^-$ mass hypothesis. Their values for the B^0 and B_s^0 mesons are found to be $A_P(B^0) = (0.2 \pm 0.6)\%$ and $A_P(B_s^0) = 2.4 \pm 2.1)\%$, respectively.

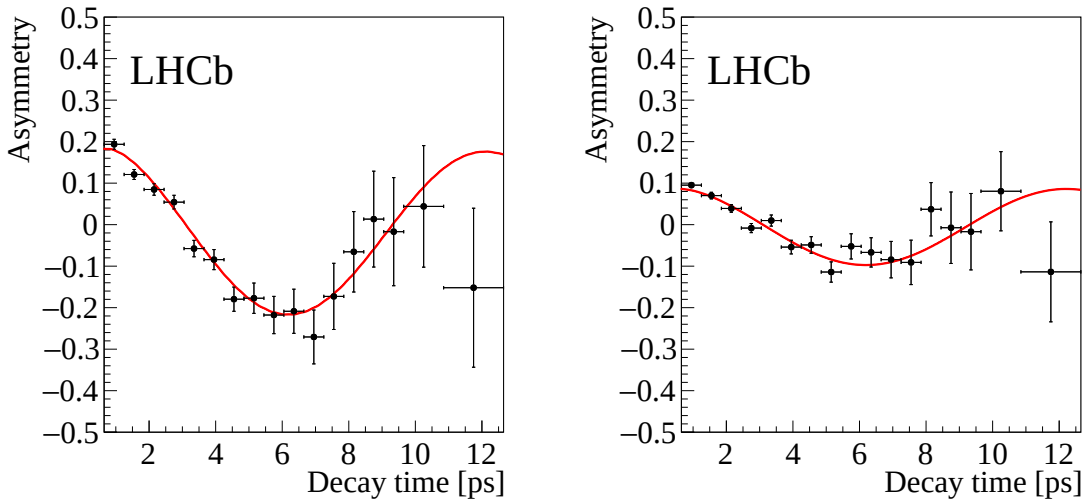

Figure 5.19: Raw time-dependent asymmetry for the $K^\pm\pi^\mp$ final state from the invariant mass region corresponding to $5.20\,\text{GeV}/c^2 < m < 5.32\,\text{GeV}/c^2$ dominated by the $B^0 \to K^+\pi^-$ decay. On the left the asymmetry observed using the OS tagger is shown while on the right the same asymmetry obtained using only the SS*comb* tagging information is reported.

5.5.1 Corrections to $A_{CP}(B^0 \to K^+\pi^-)$ and $A_{CP}(B_s^0 \to \pi^+K^-)$

As mentioned in Section 5.4.3, in order to determine the correct *CP* asymmetries, $A_{CP}(B^0 \to K^+\pi^-)$ and $A_{CP}(B_s^0 \to \pi^+K^-)$, it is necessary to apply some corrections to the corresponding raw asymmetries observed in data. The measured raw asymmetries (A_{raw}) represent the sum of the *CP* asymmetries (A_{CP}) and the asymmetries of the final state reconstruction efficiencies (A_f). The spurious asymmetry A_f can be written as:

$$A_f = A_D^{K\pi} + A_{\text{PID}}^{K\pi}, \tag{5.42}$$

where A_D stands for the asymmetry between the reconstruction efficiencies of the $K^+\pi^-$ and π^+K^- final states and $A_{\text{PID}}^{K\pi}$ represents the asymmetry between the efficiencies of the PID requirements applied in the selection of the candidates in the $K^\pm\pi^\mp$ final state. These two asymmetries are defined

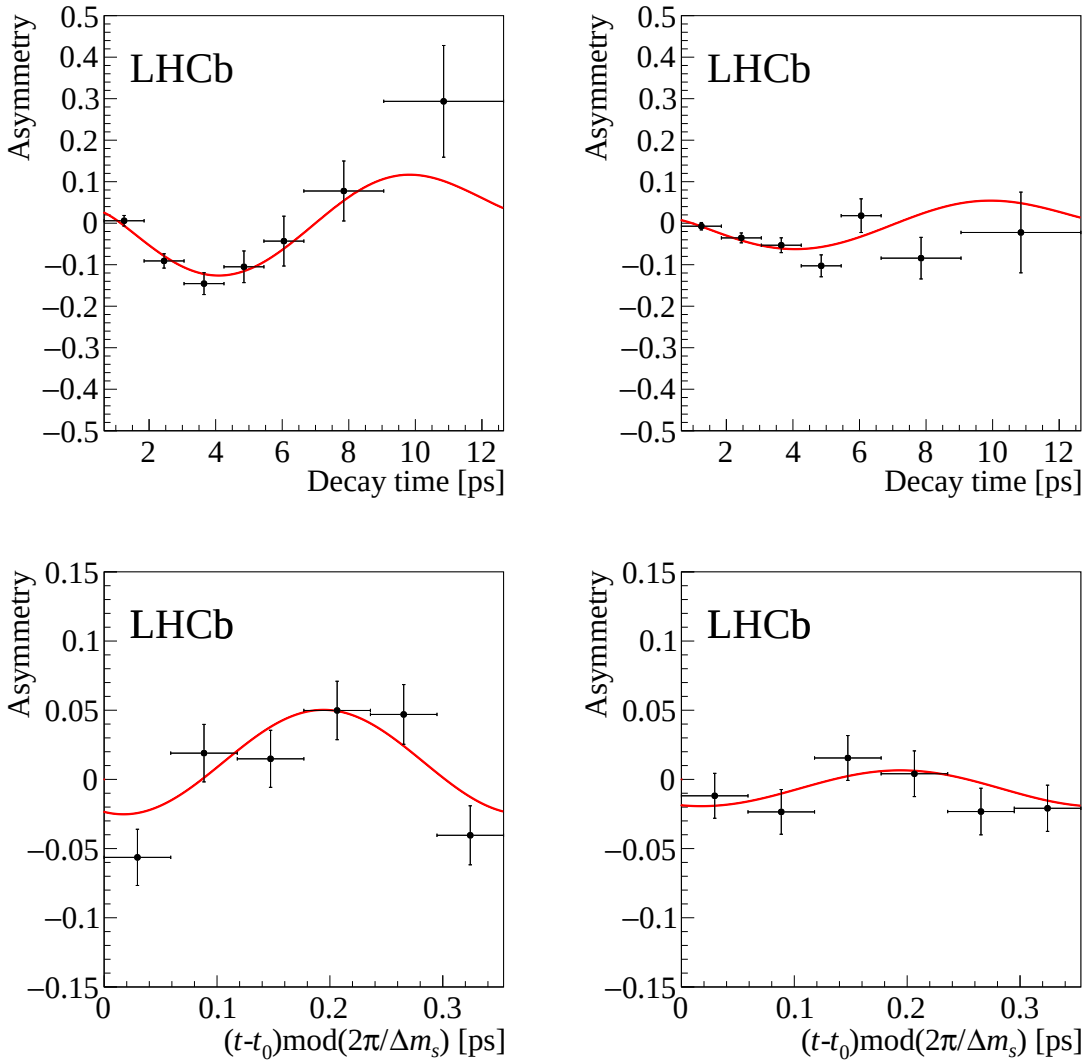

Figure 5.20: Raw time-dependent asymmetry for the $\pi^+\pi^-$ (top) and K^+K^- (bottom) final states from the invariant mass regions corresponding to $5.20\,\text{GeV}/c^2 < m < 5.35\,\text{GeV}/c^2$ and $5.30\,\text{GeV}/c^2 < m < 5.44\,\text{GeV}/c^2$, respectively. On the left the asymmetries obtained using the OS tagging information while on the right the asymmetries observed using the SS*comb* (for the $\pi^+\pi^-$ spectrum) and the SS*kNN* (for the K^+K^- spectrum).

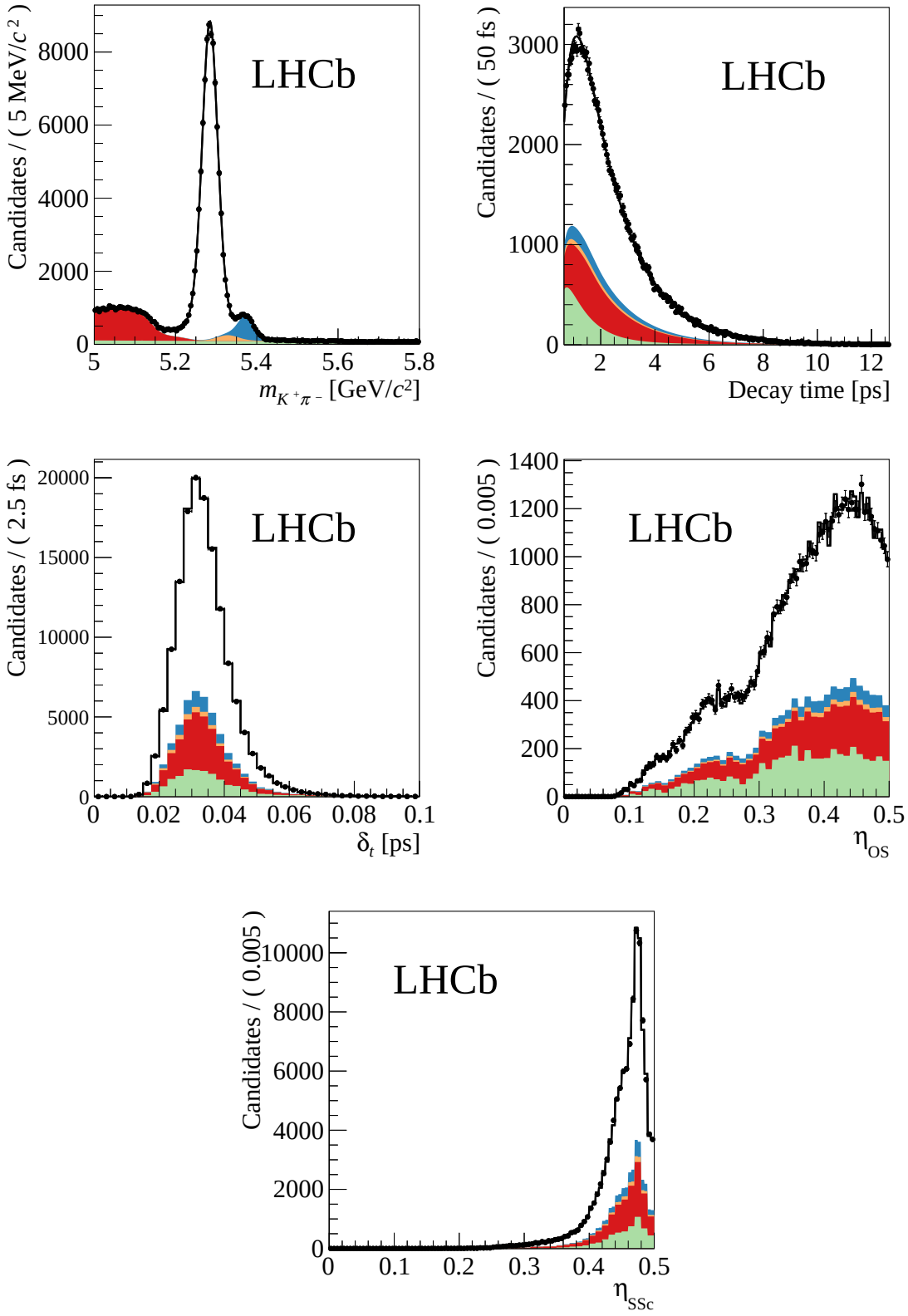

Figure 5.21: Distributions of the fit observables (invariant mass, decay-time, decay-time error, OS mistag and SS*comb* mistag) in the $K^\pm\pi^\mp$ final state. The result of the simultaneous fit is superimposed to data points.

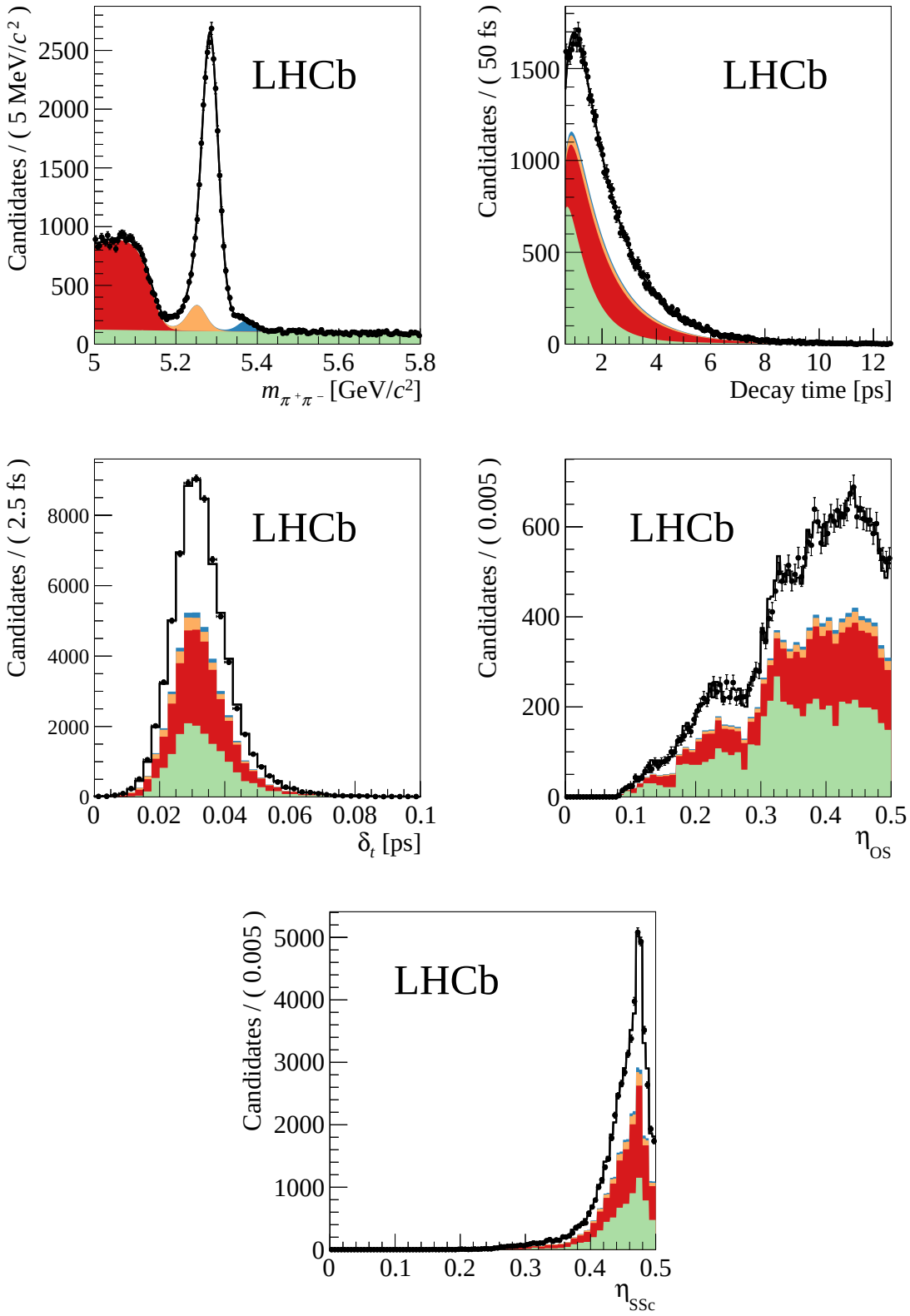

Figure 5.22: Distributions of the fit observables (invariant mass, decay-time, decay-time error, OS mistag and SS*comb* mistag) in the $\pi^+\pi^-$ final state. The result of the simultaneous fit is superimposed to data points.

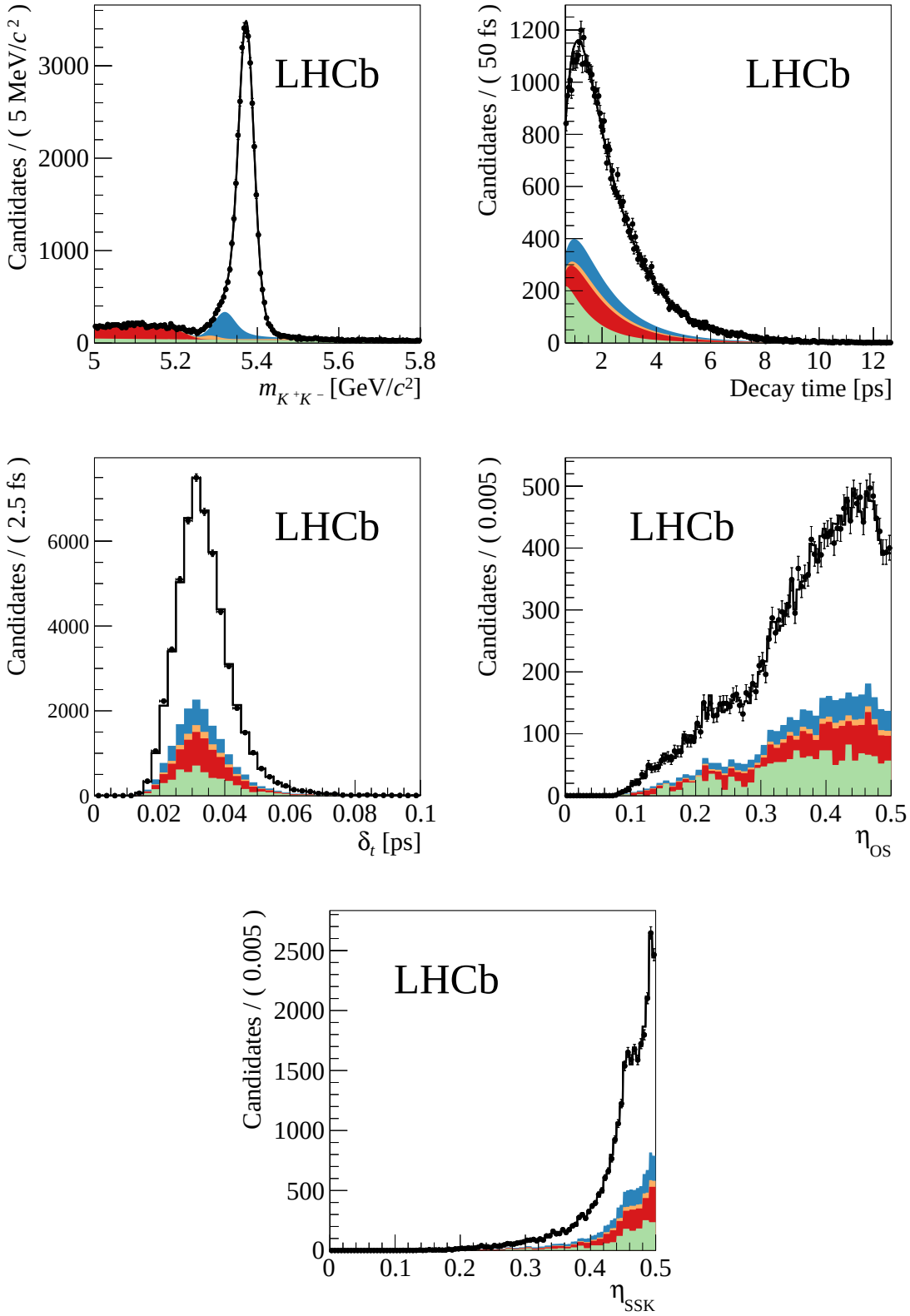

Figure 5.23: Distributions of the fit observables (invariant mass, decay-time, decay-time error, OS mistag and SSkNN mistag) in the K^+K^- final state. The result of the simultaneous fit is superimposed to data points.

as:

$$\begin{aligned} A_D^{K\pi} &= \frac{\varepsilon_D(\pi^+K^-) - \varepsilon_D(K^+\pi^-)}{\varepsilon_D(\pi^+K^-) + \varepsilon_D(K^+\pi^-)} \\ A_{\text{PID}}^{K\pi} &= \frac{\varepsilon_{\text{PID}}(\pi^+K^-) - \varepsilon_{\text{PID}}(K^+\pi^-)}{\varepsilon_{\text{PID}}(\pi^+K^-) + \varepsilon_{\text{PID}}(K^+\pi^-)} \end{aligned} \tag{5.43}$$

where ε_D and ε_{PID} are the reconstruction and PID efficiencies, respectively. Since $A_{CP}(B_s^0 \to \pi^+K^-)$ is defined with the opposite order with respect to Equation 5.43, the *CP* asymmetries for the two $B^0 \to K^+\pi^-$ and $B_s^0 \to \pi^+K^-$ are defined in the following as:

$$A_{CP} = A_{raw} + \zeta A_f, \tag{5.44}$$

where ζ will be equal to -1 for the B^0 mode and +1 for the B_s^0 mode, respectively.

Asymmetry of the reconstruction efficiencies

The asymmetry related to the reconstruction efficiencies, also called *final-state detection asymmetry*, has been estimated by means of $D^+ \to K^-\pi^+\pi^+$ and $D^+ \to \bar{K}^0\pi^+$ control samples. The strategy chosen to determine such asymmetry has been already used and validate in the previous measurement performed by LHCb and it is reported in detail in Reference [138]. The method consists in measuring and combining the raw *CP* asymmetries for these two modes. The raw asymmetries are defined as:

$$\begin{aligned} A_{raw}^{K\pi\pi} &= A_P^{D^+} + A_D^{K\pi} + A_D^{\pi}, \\ A_{raw}^{K^0\pi} &= A_P^{D^+} + A_D^{\pi} - A_D^{K^0}, \end{aligned} \tag{5.45}$$

where $A_P^{D^+}$ represents the production asymmetry of the D^+ meson and the A_D asymmetries are the final-state detection asymmetries for the various particles. From the difference between the relations reported in Equation 5.45 the value of $A_D^{K\pi}$ can be estimate:

$$A_D^{K\pi} = A_{raw}^{K\pi\pi} - A_{raw}^{K^0\pi} - A_D^{K^0}. \tag{5.46}$$

The final-state detection asymmetry for the K^0 meson is taken as an external input from a previous LHCb measurement [139] and it is equal to $A_D^{K^0} = (0.054 \pm 0.014)\%$. This measurement includes both the *CP* violation of the $K^0 \to \pi^+\pi^-$ decay and the different interaction rates of the K^0 and $\bar{K}^0$ mesons with the LHCb detector. A kinematic reweight is applied simultaneously on the momentum and the transverse momentum of the D^+ and π^+ mesons in order to guarantee a perfect cancellation of $A_P^{D^+}$ and A_D^{π} between the two decay modes. Finally, since the interaction cross-section of the K^+ and K^- mesons with the detector material vary according to the kaon momentum, the value of $A_D^{K\pi}$ has been measured in different ranges of the kaon momentum, as shown in Figure 5.24. The final value of the detection asymmetry is calculated convolving the values of $A_D^{K\pi}$, reported in

Figure 5.24 with kaon momentum distribution of the $B^0 \to K^+\pi^-$ and $B_s^0 \to \pi^+K^-$ decays taken from background subtracted samples. These samples are obtained by means of the *sPlot* technique as described in Section 4.4. However, the kaon momentum distribution for the $H_b \to h^+h'^-$ modes extends up 150 GeV/c while the measurement of the kaon detection asymmetry from the D^+ decay modes is performed up to 70 GeV/c. Thus an additional bin in range [70, 150] GeV/c is taken into account, using the same mean value and doubling the error of the last bin depicted in Figure 5.24. The final values of the final state detection asymmetries, obtained convolving the asymmetries shown in Figure 5.24 with the final state particle momentum distributions, are:

$$\begin{aligned} A_D^{K\pi}(B^0 \to K^+\pi^-) &= (-0.900 \pm 0.141)\%, \\ A_D^{K\pi}(B_s^0 \to \pi^+K^-) &= (-0.924 \pm 0.142)\%, \end{aligned} \tag{5.47}$$

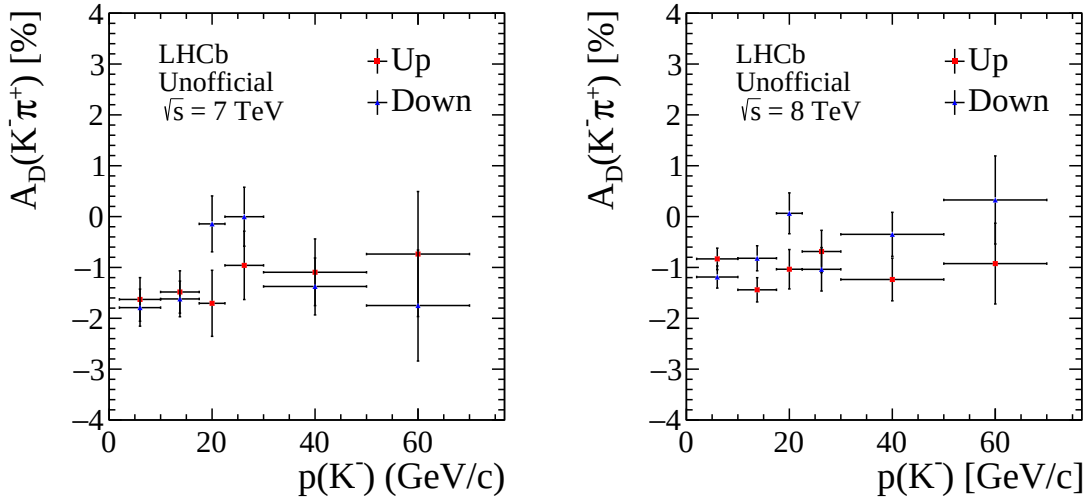

Figure 5.24: Values of $AD^{K\pi}$ for (left) 2011 and (right) 2012 data as function of the kaon momentum. Different histograms are shown for different magnet polarities.

Asymmetry of the PID requirements efficiencies

The correction for the *CP* asymmetries due to the PID requirements is evaluated using the strategy reported in Reference [134]. The PID efficiencies are calculated for kaons and pions splitting a calibration sample of $D^{*+} \to D^0(K^-\pi^+)\pi^+$ decays in different bins of track momentum (p), pseudorapidity (η), azimuthal angle (ϕ) and number of tracks in the event. The maps of the PID efficiencies are used to evaluate the corresponding PID asymmetries as function of the final state particle kinematic. Then the PID asymmetry for the $K\pi$ final state as function of the track kinematic is defined as:

$$A_{\rm PID}^{K\pi}(p_K, \eta_K, \phi_K, p_\pi, \eta_\pi, \phi_\pi) = \frac{A_{\rm PID}^{K}(p_K, \eta_K, \phi_K) - A_{\rm PID}^{\pi}(p_\pi, \eta_\pi, \phi_\pi)}{1 - A_{\rm PID}^{K}(p_K, \eta_K, \phi_K) A_{\rm PID}^{\pi}(p_\pi, \eta_\pi, \phi_\pi)} \tag{5.48}$$

where $A^K_{\rm PID}(p_K, \eta_K, \phi_K)$ and $A^\pi_{\rm PID}(p_\pi, \eta_\pi, \phi_\pi)$ represent the PID asymmetries of kaons and pions as function of their kinematic. The dependence on the number of tracks in the event has been integrated out in order to correct the effect of the different occupancy between the $H_b \to h^+h'^-$ and the calibration samples. As last step, the correct integrated value of the PID asymmetry $A^{K\pi}_{\rm PID}$ is obtained by means of a convolution with the phase space of the $H_b \to h^+h'^-$ decays. Two sources of uncertainties are taken into account: the first, related to statistics available in the calibration and $H_b \to h^+h'^-$ samples, is evaluated propagating the statistical errors of the amount of signal and the efficiency maps in each bin used to split the phase space. The second source, related to the binning scheme used to map the phase space, is computed changing the number and range of the various bins. The nominal binning scheme consists in 71 bins in momentum, 10 bins in pseudorapidity and 8 bins in azimuthal angle. A set of 27 different bin configurations are taken into account doubling and halving the number of bins of all the three variables in turn. This second source of uncertainty results to be largely dominant with respect to the former one. At the end the average and the root mean square of the results are used as mean value and uncertainty for the final PID asymmetry $A^{K\pi}_{\rm PID}$, which is found to be:

$$A^{K\pi}_{\rm PID} = (-0.04 \pm 0.25)\% \tag{5.49}$$

Extraction of the time-integrated *CP* asymmetries

Finally the extraction of the real *CP* asymmetries for the $B^0 \to K^+\pi^-$ and $B^0_s \to \pi^+K^-$ decays can be performed. The values reported in Equation 5.41 are corrected by $A^{K\pi}_D$ in Equation 5.47 and $A^{K\pi}_{\rm PID}$ in Equation 5.49. The final values of $A_{CP}(B^0 \to K^+\pi^-)$ and $A_{CP}(B^0_s \to \pi^+K^-)$ are:

$$\begin{aligned} A_{CP}(B^0 \to K^+\pi^-) &= (-8.40 \pm 0.40 \pm 0.14 \pm 0.25)\% \\ A_{CP}(B^0_s \to \pi^+K^-) &= (21.31 \pm 1.53 \pm 0.14 \pm 0.25)\% \end{aligned} \tag{5.50}$$

where the first error is the statistical uncertainty, the second error comes from the $K^\pm\pi^\mp$ final state detection asymmetry and the third one comes from the uncertainty on the $A^{K\pi}_{\rm PID}$ asymmetry.

The measurements of $A_{CP}(B^0 \to K^+\pi^-)$ and $A_{CP}(B^0_s \to \pi^+K^-)$ allow to perform a test of the validity of the SM, as suggested in Reference [140] by checking the equality:

$$\Delta = \frac{A_{CP}(B^0 \to K^+\pi^-)}{A_{CP}(B^0_s \to \pi^+K^-)} + \frac{\mathcal{B}(B^0_s \to \pi^+K^-)}{\mathcal{B}(B^0 \to K^+\pi^-)}\frac{\tau_d}{\tau_s} = 0. \tag{5.51}$$

where $\mathcal{B}(B^0 \to K^+\pi^-)$ and $\mathcal{B}(B^0_s \to \pi^+K^-)$ are the *CP* averaged branching fractions while τ_d and τ_s represent the mean lifetimes of the B^0 and B^0_s mesons, respectively. Using the results obtained in this analysis for the $\mathcal{A}^{CP}$ values, the world average values [71] for the B^0 and B^0_s mean lifetimes and for the quantity $f_s/f_d \times \mathcal{B}(B^0_s \to \pi^+K^-)/\mathcal{B}(B^0 \to K^+\pi^-)$ and the measurement of f_s/f_d reported in Reference [141], the value of $\Delta = 0.11 \pm 0.04 \pm 0.03$ is obtained where the first uncertainty is

related to the measurements of the *CP* asymmetries and the second comes from the input values of the remaining parameters. No evidence for a deviation from the expectation is observed with the present experimental precision.

5.6 Systematic uncertainties and validation tests

In this section the single contribution to the total systematic uncertainty on the *CP* violating parameters for all the three final state hypotheses are described. In addition the cross-checks performed to validate the stability and the reliability of the measurement are discussed.

5.6.1 Systematic uncertainties

The various relevant sources of systematic uncertainties affecting the measurement of the *CP* observables are discussed in the following. The main sources are related to the invariant mass and the decay time model used to describe the signal and the background contributions in the fit, the decay-time resolution, the flavour tagging algorithms and the parameters fixed in the fit to data. These systematics have been determined following two main strategies. The first strategy consists in repeating multiple times the fit procedure changing the values of the fixed parameters or the fitting models. In this case the final uncertainty is evaluated as the RMS of the difference between the nominal fit and the results of the fit to data with the changed parameters. The second method consists in a generation of multiple samples simulated according to the nominal model, so-called "pseudo-experiments", which will be fitted using the modified models. The systematic uncertainty will be computed as the RMS of the distribution representing the difference between the nominal results and the ones obtained from the pseudo-experiments. All the systematic uncertainties taken into account are briefly described in the next subsections and they are summarized in Table 5.15. Also the uncertainties due to the PID and detection asymmetries, described in Section 5.5.1, are reported in Table 5.15. Since the different sources of systematic errors are expected to be completely uncorrelated, the single effects are evaluated separately and the overall systematic uncertainty on the *CP* asymmetries is computed as a sum in quadrature of the single contributions.

Invariant mass model

The effect of the invariant mass models used in the final fit, describing both the signal and background components, on the *CP* observables is investigated. The study is performed by means of 100 pseudo-experiments generated with the nominal model, described in Section 5.3. The pseudo-experiments are then fitted using a modified model obtained changing in turn:

Table 5.15: List of the systematic uncertainties on the *CP* asymmetries taken into account.

Parameter	$C_{\pi^+\pi^-}$	$S_{\pi^+\pi^-}$	$C_{K^+K^-}$	$S_{K^+K^-}$	$A^{\Delta\Gamma}_{K^+K^-}$	$A_{CP}(B^0 \to K^+\pi^-)$	$A_{CP}(B^0_s \to \pi^+K^-)$
Signal mass model (reso.)	0.0027	0.0025	0.0015	0.0015	0.0023	0.0001	0.0041
Signal mass model (tails)	0.0007	0.0008	0.0013	0.0013	0.0016	negligible	0.0003
Comb. bkg. mass model	0.0001	0.0003	0.0002	0.0002	0.0016	negligible	0.0001
Time acceptance	0.0011	0.0004	0.0020	0.0017	0.0778	0.0004	0.0002
Cross-feed time model	0.0075	0.0059	0.0022	0.0024	0.0003	0.0001	0.0001
Comb. bkg. time model	0.0016	0.0016	0.0004	0.0002	0.0019	0.0001	0.0005
3Body bkg.	0.0070	0.0056	0.0044	0.0043	0.0304	0.0008	0.0043
Time resolution calibration	0.0014	0.0013	0.0108	0.0119	0.0051	0.0001	0.0001
Time resolution model	0.0001	0.0005	0.0002	0.0002	0.0003	negligible	negligible
OS Tagging calibration	0.0018	0.0021	0.0018	0.0019	0.0001	negligible	negligible
SS*kNN* Tagging calibration	–	–	0.0076	0.0098	0.0004	–	–
SS*comb* Tagging calibration	0.0015	0.0017	–	–	–	negligible	negligible
Input parameters	0.0025	0.0024	0.0092	0.0107	0.0480	negligible	0.0001
PID asymmetry	–	–	–	–	–	0.0025	0.0025
Detection asymmetry	–	–	–	–	–	0.0014	0.0014
Total	0.0115	0.0095	0.0165	0.0191	0.0966	0.0009	0.0060

- the mass resolution for both the signals and the cross-feed backgrounds with a single Gaussian function ("Signal mass model (reso.)");
- a unique shape describing the signal tails is used for all the decay modes, fixing the parameters of the Johnson functions to the values of the $B^0 \to K^+\pi^-$ decay ("Signal mass model (tails)");
- the exponential function describing the invariant mass of the combinatorial background is substituted with a first order polynomial("Comb. bkg. mass model").

Decay-time model

Because of the complexity of the decay time model used to extract the *CP* observables, different possible sources of systematic uncertainties are considered. The first source of systematic is related to decay-time acceptance used to describe the signals and the cross-feed backgrounds ("Time acceptance"). For each $H_b \to h^+h'^-$ decay a set of 100 different acceptance histograms with high statistic is built, where each histogram is generated by means of a random variation of the effective function parameters, as reported in Equation 5.21, according to a multidimensional Gaussian model taking into account their errors and correlations. Then the acceptance histograms are interpolated in the fit to data using a polynomial cubic splines, as described in Section 5.4.2, and the systematic uncertainty is determined as the RMS of the distribution of the fitted *CP* parameters.

A further study is performed to validate the consistency of the systematic uncertainty associated

to the decay-time acceptance fixing to 0 the value of the parameter a_3 in the effective function, given in Equation 5.21, for all the $H_b \to h^+h'^-$ decays. The fit to data is repeated with the new acceptance function and no significant variations are observed in the *CP* parameters with respect to the nominal value, as shown in Table 5.16. Thus no additional systematic is associated to the decay-time acceptance.

Table 5.16: Result of the further study regarding the parametrization of the decay-time acceptance function, fixing the a_3 parameter to 0.

Parameter	Nominal	$a_3 = 0$	Variation
$C_{\pi^+\pi^-}$	-0.3367 ± 0.0623	-0.3374 ± 0.0624	-0.0007
$S_{\pi^+\pi^-}$	-0.6261 ± 0.0538	-0.6263 ± 0.0539	-0.0002
$C_{K^+K^-}$	0.1968 ± 0.0584	0.1984 ± 0.0582	$+0.0016$
$S_{K^+K^-}$	0.1816 ± 0.0586	0.1805 ± 0.0582	-0.0011
$A^{\Delta\Gamma}_{K^+K^-}$	-0.7876 ± 0.0730	-0.8298 ± 0.0715	-0.0422
$A_{raw}(B^0 \to K^+\pi^-)$	-0.0934 ± 0.0040	-0.0933 ± 0.0040	$+0.0001$
$A_{raw}(B^0_s \to \pi^+K^-)$	0.2227 ± 0.0153	0.2228 ± 0.0154	$+0.0001$

Another source of uncertainty comes from the parametrization of the cross-feed backgrounds. It has been estimated removing the oscillating components in the fit: i.e. fixing to 0 the *CP* asymmetry related to the $B^0 \to K^+\pi^-$ decays in the $\pi^+\pi^-$ and K^+K^- final states hypotheses and to the $B^0 \to \pi^+\pi^-$ and $B^0_s \to K^+K^-$ decay modes in the $K^\pm\pi^\mp$ spectrum. A set of 100 pseudo-experiments is generated in order to determine the value of the systematic uncertainty ("Cross-feed time model").

A final study is done in order to quantify the systematic uncertainty related to the combinatorial background model ("Comb. bkg. time model"). A set of 100 pseudo-experiments is built and the fit is repeated removing the acceptance function from the combinatorial decay time model.

Partially reconstructed 3-body background

The impact of the presence of the partially reconstructed 3-body background on the *CP* asymmetries is studied. Also in this case, a set of 100 pseudo-experiments, generated using the nominal model, is used to determine the systematic uncertainty ("3Body bkg."). The modified model is obtained removing the components describing the partially reconstructed 3-body background for all the three final state hypotheses and fitting the pseudo-experiments in an invariant mass range between [5.2,5.8] GeV/c^2.

Decay-time resolution

The decay-time resolution can introduce systematic uncertainties due to the calibration parameters q_0 and q_1 ("Time resolution calibration") and to the model used to describe its distribution ("Time resolution model"). The systematic related to the calibration parameters is quantified repeating the fit to data 100 times, where in each fit the values of q_0 and q_1 are varied by means of a bi-dimensional Gaussian model according to their errors and correlation. The values considered to constraint the Gaussian model are: $q_0 = 46.1 \pm 4.1$ fs, $q_1 = 0.81 \pm 0.38$ and $\rho(q_0, q_1) = -0.32$. The errors of the two parameters are different with respect the ones reported in Section 5.4.1, since they have been inflated in order to take into account both the differences between the calibrations in the $B_s^0 \to \pi^+K^-$ and $B_s^0 \to D_s^-\pi^+$ decays, which are found to be equal to 1.1 fs for q_0 and 0.1 for q_1, and the differences between data and fully simulated samples, which are approximately of 1 fs for q_0 and 0.05 for q_1.

The systematic related to the decay-time resolution model is quantified adding a third Gaussian function in order to describe the large tails of the τ_{err} distributions, shown in Figure 5.14. The new model can be written as:

$$\begin{aligned} R(t-t'|\delta_t) =& (1-f_{tail})[f_\tau \cdot G(t-t', \mu, \sigma_1(\delta_t)|\delta_t) + (1-f_\tau) \cdot G(t-t', \mu, \sigma_2(\delta_t)|\delta_t)] \\ &+ f_{tail} \cdot G(t-t', \mu, \sigma_3(\delta_t)|\delta_t), \end{aligned} \tag{5.52}$$

where σ_1 and σ_2 are defined as in Section 5.4.1 and $\sigma_3 = r_{tail} \cdot \sigma_1(\delta_t)$. The results of the new unbinned maximum likelihood fit are reported in Table 5.17, while the distribution of τ_{err} with the fit result superimposed is shown in Figure 5.25. A set of 100 pseudo-experiments, generated according to the nominal model, is fitted using both the nominal and the modified models. The central value and the RMS of the distributions of the variations between the *CP* parameters obtained with the two fit methods are used as systemic uncertainties.

Table 5.17: Calibration parameters of the decay time resolution for fully simulated $B_s^0 \to \pi^+K^-$ decays, obtained by means of a unbinned maximum+ likelihood fit, using the model described in Equation 5.52.

Parameter	$B_s^0 \to \pi^+K^-$
μ	0.076 ± 0.052 fs
q_0	32.68 ± 0.13 fs
q_1	1.0117 ± 0.0058
r_σ	1.776 ± 0.031
f_τ	0.8844 ± 0.0080
r_{tail}	5.20 ± 0.16
f_{tail}	0.0062 ± 0.0005

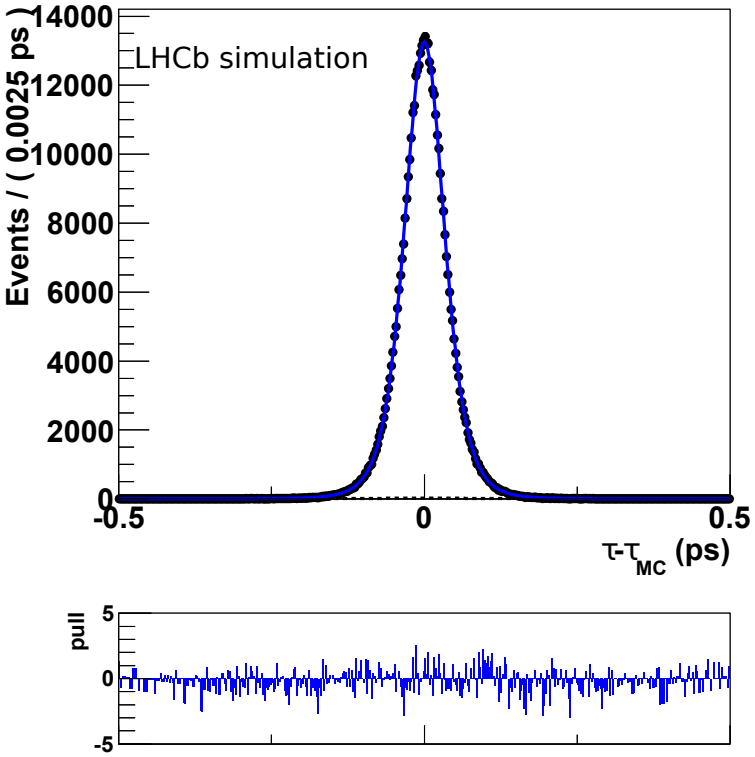

Figure 5.25: Distribution of τ_{err} for fully simulated $B_s^0 \to \pi^+K^-$ along with the result of the best fit, using the model described in Equation 5.52.

Finally, the systematic due to the model of the δ_t distribution has been investigated. Alternative histograms are obtained from fully simulated decays reweighted by the PID efficiencies on a per-event basis. The decay-time error distributions of the combinatorial and partially reconstructed backgrounds are substituted with the same histogram used to parametrize the $B^0 \to K^+\pi^-$ decay in the $K^\pm\pi^\mp$ final state hypothesis. The variation of the *CP* parameters between the fit with the nominal and the modified models are taken as systematics.

Flavour tagging

Flavour tagging can represent an important systematic to be taken into account since often the calibration of the tagging algorithm is performed on decay channels with a different kinematic with respect to the decay of interest. However, in this analysis, most of the systematic uncertainties related to the O*S* and S*Scomb* taggers are expected to cancel out, since the two algorithms are calibrated using the $B^0 \to K^+\pi^-$ decay which shares the same topology and selection of the signal decays. A significant effect could come from the linear dependence used to describe the relation between the predicted (η) and the observed mistag (ω) ("O*S* Tagging calibration" and "S*Scomb* Tagging calibration"). In order to quantify this effect a set of 100 pseudo-experiments is generated and the fit is repeated substituting the linear function with a second order polynomial:

$$\omega = p_0 + p_1 \cdot (\eta - \hat{\eta}) + p_2 \cdot (\eta - \hat{\eta})^2. \tag{5.53}$$

Regarding the $B_s^0 \to K^+K^-$ decay, an additional systematic uncertainty can come from a contamination of kaons, generated during the B_s^0 hadronization, affecting the OS tagger performance. Thus the calibration of the O*S* algorithm could be different between the B^0 and B_s^0 decay modes. In order to quantify this effect, the O*S* tagger is re-calibrated on a $B_s^0 \to D_s^-\pi^+$ sample, after a full kinematic and occupation reweighting, as described in Section 4.4. Since the calibration parameters are found to be in very good agreement with the ones obtained in the nominal fit (as shown in Table 5.18), no systematic uncertainty is added.

Table 5.18: Result of the additional cross-check on the O*S* calibration parameters in B_s^0 decay modes.

Parameter	B^0 mode	B_s^0 mode	Variation
$\hat{p}_0^{OS}$	0.3854 ± 0.0043	0.3749 ± 0.0060	-0.0105
$\hat{p}_1^{OS}$	1.004 ± 0.045	0.993 ± 0.061	-0.011

The calibration of S*SkNN* tagger is taken from a sample of $B_s^0 \to D_s^-\pi^+$ sample after a kinematic reweighting, thus its systematic uncertainty could be larger than the other tagging algorithms. The uncertainty is evaluate repeating the fit to data 100 times, varying the calibration parameters ac-

cording to a multidimensional Gaussian model according to the errors and correlations reported in Tables 4.6, 4.7. The RMS of the *CP* parameter distributions are taken as systematic uncertainties.

As last study, the fit is repeated using the calibration parameters related to the full reweighting (kinematic and occupancy), reported in Table 4.4. The variations between the results of this fit with respect to the nominal fit are summed in quadrature with the uncertainties coming from the previous check in order to obtain the final systematic uncertainty for the SS*kNN* tagger ("SS*kNN* Tagging calibration").

Fixed parameters

The effect of fixing the parameters Γ_s, $\Delta\Gamma_s$, Δm_d and Δm_s on the *CP* violating parameters is evaluated repeating the fit to data 100 times ("Input parameters"). Each time the values of these parameters are randomly extracted according to the values and errors reported in Table 5.12.

5.6.2 Cross-check and validations

Various cross-checks are performed in order to ensure the validity and the stability of the results. In the following a short description of the cross-checks performed is report, while the corresponding plots and detail are reported in Reference [142].

A first check of the best fit results is done comparing the values of the *CP* asymmetries obtained using the OS, the SS*comb* and the SS*kNN* tagging algorithm one at a time. The outcome of the cross-check is reported in Table 5.19. No significant discrepancies with respect to the *CP* violating parameters obtained in the nominal fit are found.

Table 5.19: Values of the *CP*-violation parameters obtained from the fits using only OS tagging information, using only SS*comb* tagging information, using only SS*kNN* tagging information, using OS +SS*comb* tagging information, and using OS +SS*kNN* tagging information.

Parameter	OS	SS*comb*	SS*kNN*	OS +SS*comb*	OS +SS*kNN*
$C_{\pi^+\pi^-}$	-0.3392 ± 0.0711	-0.3924 ± 0.1303	–	-0.3367 ± 0.0623	–
$S_{\pi^+\pi^-}$	-0.6884 ± 0.0632	-0.5023 ± 0.1070	–	-0.6261 ± 0.0538	–
$C_{K^+K^-}$	0.2191 ± 0.0654	–	0.057 ± 0.141	–	0.1968 ± 0.0584
$S_{K^+K^-}$	0.2170 ± 0.0653	–	0.099 ± 0.148	–	0.1816 ± 0.0586
$A^{\Delta\Gamma}_{K^+K^-}$	-0.7857 ± 0.0731	–	-0.7966 ± 0.0730	–	-0.7876 ± 0.0730

The stability of the fit is verified exploiting two set of about 500 pseudo-experiments: the first reproducing the fit including the OS and SS*comb* tagging algorithms, while the second including the OS and SS*kNN* tagging information. The quality of the fit model is checked by means of the distributions of the so-called *pulls*. For *i*-th pseudo-experiment the corresponding pull related to one

of *CP* parameters is defined as: $(O_i - E)/\sigma_i$, where O_i and E are the observed and expected value for the *CP* observable and σ_i indicates the statistical uncertainty of the observed measurement. The relevant information which can be extracted from a pull distribution are: the shape, the central value and the pull width. For a good estimation of the parameter of interest, the shape of its distribution is expected to be Gaussian-like. If this is not the case, the likelihood used for the fit is not considered a good estimator for the parameter. The central value of the distribution is expected to be null for an unbiased fit. Any discrepancies from 0 represents a hint of a systematic overestimation or underestimation. Finally the pull width should be compatible with 1 if the parameter is correctly estimated. A smaller or larger value indicates that the parameter error is systematically overestimated or underestimated. The results of the study are shown in Figure 5.26.The pulls of all the *CP* violating parameters are found to have reliable shapes, central values and widths.

As final cross-check, the fit is performed on a fully simulated sample in order to check if the neglected correlations between the variables can have any effect on the *CP* measurement. The sample has been built in such a way to reproduce exactly the proportions between the $H_b \to h^+h'^-$ modes observed in the Run 1 data set. The complete procedure used for building such MC data set consists in the following steps:

- a sample of fully simulated $B^0 \to K^+\pi^-$ decays is divided in three subsamples, where the final state particles are reconstructed as $K^\pm\pi^\mp$, $\pi^+\pi^-$ and K^+K^-, keeping the relative amount of candidates in each subsample the same as observed in data;
- the other $H_b \to h^+h'^-$ decay modes are jointed to the three subsamples, adding a relative amount of fully simulated candidates corresponding to the relative amounts observed in data;
- PID requirements are not applied, since that will lower significantly the amount of available simulated candidates affecting the test precision.

A total amount of about 360 000, 11 000 and 18 000 $B^0 \to K^+\pi^-$ candidates populate the $K^\pm\pi^\mp$, $\pi^+\pi^-$ and K^+K^- subsamples, respectively. The best fit results to the fully simulated sample are reported in Table 5.20 together to the values of the *CP* parameters used in the MC simulation. Since the *CP* parameters obtained are well in agreement with the generated values, the absence in the model of the correlation among the observables appears to have a negligible impact on the CP parameters.

5.6.3 Comparison with previous preliminary results

A consistency check has been performed with respect to the preliminary results obtained in Reference [70]. The main differences between the two measurements lie in the event selection, related to the trigger requirements, and in addition of the flavour tagging S*Scomb* algorithm in this up-

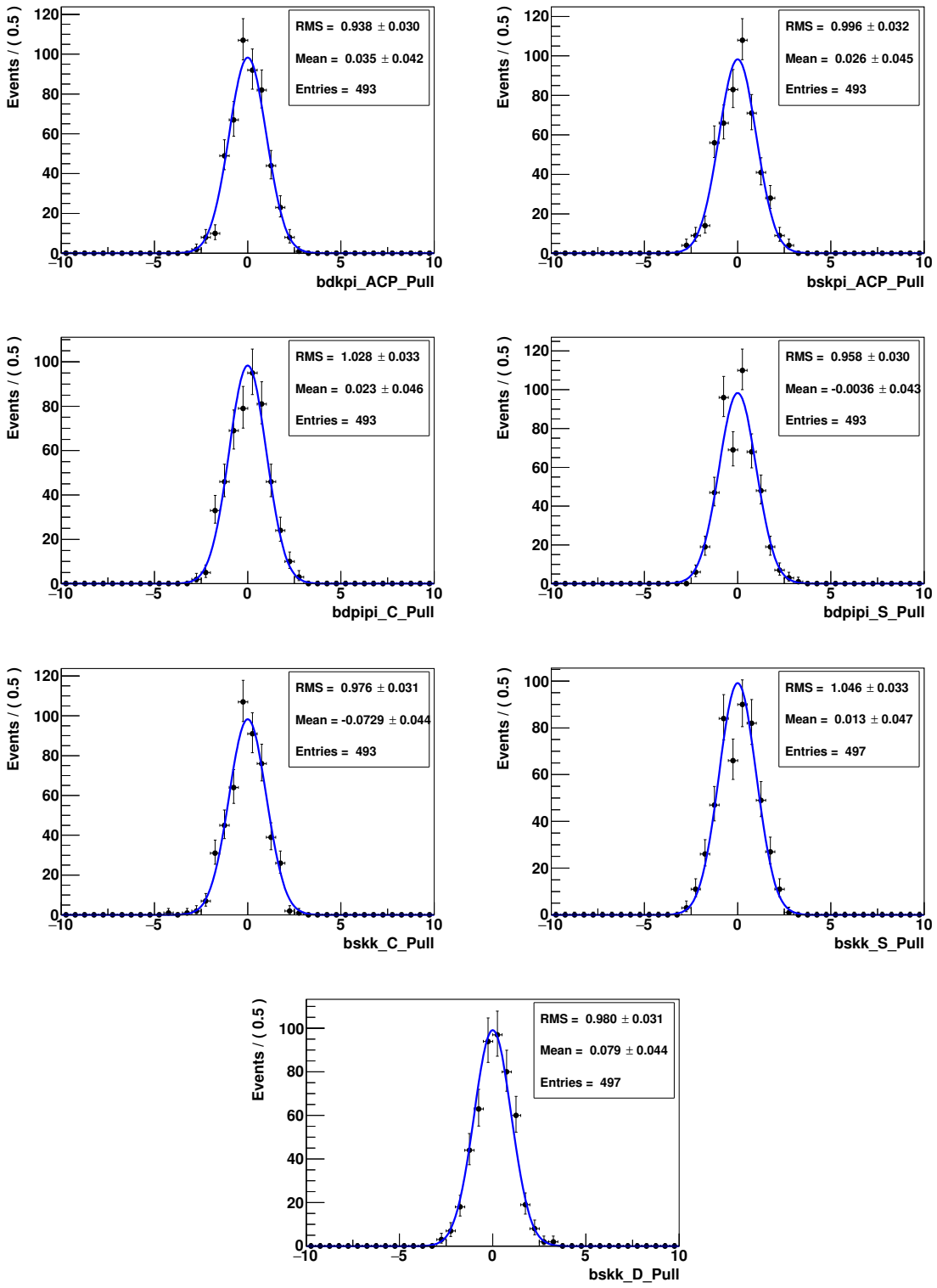

Figure 5.26: From top left to bottom right: pull distributions for $A_{CP}(B^0 \to K^+\pi^-)$ and $A_{CP}(B_s^0 \to \pi^+K^-)$ (first row), $C_{\pi^+\pi^-}$ and $S_{\pi^+\pi^-}$ (second row), $C_{K^+K^-}$ and $S_{K^+K^-}$ (third row) and $A_{K^+K^-}^{\Delta\Gamma}$.

Table 5.20: Results of the parameters $C_{\pi^+\pi^-}$, $S_{\pi^+\pi^-}$, $C_{K^+K^-}$, $S_{K^+K^-}$ and $A^{\Delta\Gamma}_{K^+K^-}$ obtained from the fit to a fully simulated samples of $H_b \to h^+h'^-$ decays.

Parameter	From fit	From simulation
$C_{\pi^+\pi^-}$	-0.3878 ± 0.0242	-0.3846
$S_{\pi^+\pi^-}$	-0.6410 ± 0.0220	-0.6403
$C_{K^+K^-}$	0.1311 ± 0.0185	0.1327
$S_{K^+K^-}$	0.2488 ± 0.0185	0.2356
$A^{\Delta\Gamma}_{K^+K^-}$	-0.9708 ± 0.0461	-0.9627
$A_{CP}(B^0 \to K^+\pi^-)$	-0.1024 ± 0.0020	-0.10
$A_{CP}(B^0_s \to \pi^+K^-)$	0.3938 ± 0.0069	0.39

dated analysis. A relevant discrepancy is found in the value of $C_{\pi^+\pi^-}$ observable, while all the other parameters are in good agreement. Different alternative fitting models have been used in the two subsamples without finding any variation in the $C_{\pi^+\pi^-}$ value. In the end this discrepancy is found to be due only to a statistical fluctuation as proved in Reference [142].

6

CP violation on $B \to h^+h'^-$ decays using Run 2 data

In this chapter an update of the analysis presented in Chapter 5 is described. The aim of the analysis is to provide a new measurement of the *CP*-violating asymmetries in the decay and in the interference between mixing and decay in the $B^0 \to \pi^+\pi^-$ and $B_s^0 \to K^+K^-$ decays as well as of the direct *CP* asymmetries in the $B^0 \to K^+\pi^-$ and $B_s^0 \to \pi^+K^-$ decays. The measurement is performed using the data sample of pp collisions collected by LHCb during the first period of the Run 2 data taking, corresponding to an integrated luminosity of about 2 fb^{-1}.

The *CP*-violating asymmetries are determined following the same workflow used in the Run 1 analysis, i.e. an unbinned maximum likelihood fit is performed simultaneously on the B signal candidates selected in three different final states: $\pi^+\pi^-$, K^+K^- and $K^\pm\pi^\mp$. The set of observables used in the fit is still the same as in Run 1: the invariant mass m, the decay-time t, the predicted decay-time error δ_t evaluated by reconstruction algorithms, the tagging decision d and the predicted mistag probability η evaluated by the OS and SS flavour tagging algorithms.

Many steps of the analysis have been revisited in order to achieve a better precision of the final *CP* asymmetries. In particular the offline event selection has been completely redesigned, as it is described in Section 6.1. The decay time resolution has been calibrated exploiting a data sample of $J/\psi \to \mu\mu$ decays instead of samples of $B^0 \to D^-\pi^+$ and $B_s^0 \to D_s^-\pi^+$ candidates, as reported in Section 6.3.1. In addition, this analysis makes use of the new flavour tagging algorithms optimised on Run 2 data, already discussed in Section 4.6.

6.1 Event selection

The measurement is performed using the data sample of pp collisions collected with LHCb detector at center-of-mass energy of 13 TeV during 2015 and 2016, corresponding to an integrated luminosity of about 2 fb^{-1}. Similarly to the Run 1 analysis, the event selection consists of different steps: the trigger selection, the event reconstruction, the stripping selection and finally the offline selection. The event reconstruction is entrusted to the DTF algorithm, which has been already briefly described in Section 5.1.2.

6.1.1 Trigger and stripping selections

The trigger lines have been changed with respect to the Run 1 analysis in order to improve the expected signal yield. In particular the lines at the level of the software trigger: the Hlt1 lines have been altered into the logical disjunction between the "Hlt1TwoTrackMVA" and "Hlt1TrackMVA" lines while the Hlt2 requirements have been restricted to the new "Hlt2B2HH" line, which differs from the old one for some requirements which are shown in Table 6.1. On the other hand the L0 trigger lines are remained mostly untouched. The full list of trigger lines that are requested to be passed by each H_b candidate, reported in Table 6.2. The description of the Hlt2 trigger lines is reported in Table 6.1, where the requirements involves some different variables with respect to the Run 1 analysis: the mother candidate is now requested to have a large transverse momentum (p_T), a large cosine of the angle between the momentum and the direction of flight (BPVDIRA), a small χ^2 of the impact parameter with respect the PV (BPVIPCHI2) and a large χ^2 distance from the related PV; the requirements on the two daughters are the same as used in Run 1, but the MIPDV has been replaced with the χ^2 of the distance of a particles' trajectory to the PV; finally for the combination the range of AM has been enlarged with respect the Run 1 analysis, the requirement on the variable AMAXDOCA has been replaced by the request to have a small χ^2 of the distance of closest approach (ACUTDOCACHI2) and a further requirement on the scalar sum of the transverse momentum of the two tracks (p_{T1}+p_{T2}) is added. The stripping selection has been changed with respect to the one exploited in the Run 1 analysis. The BDT requirement has been removed and the new stripping line simply applies the requirements used in the Hlt2, but on the quantities reconstructed offline.

6.1.2 Offline selection

The offline selection, applied to the events that pass the stripping line, has been completely revisited with respect to the previous analysis. The sensitivity to the time-dependent *CP* asymmetries depends mostly on:

Table 6.1: Description of the Hlt2 trigger requirements applied to the $H_b \to h^+h'^-$ candidates in Run 2 analysis

Requirements	Description
MotherCut	PT>1200.0 MeV & BPVDIRA>0.99 & BPVIPCHI2()<9 & BPVVDCHI2>100
DaughterCut	TRCHI2DOF<3 & PT>1000.0 MeV & MIPCHI2DV(PRIMARY) > 16
CombinationCut	(PT1+PT2)>4500.0 MeV & AM>4700.0 MeV & AM<6200.0 MeV & ACUTDOCACHI2(9,")

Table 6.2: Trigger requirements applied to the $H_b \to h^+h'^-$ candidates in Run 2 analysis

Trigger	Lines
L0	L0Hadron_TOS OR L0Global_TIS
HLT1	Hlt1TrackMVADecision_TOS OR Hlt1TwoTrackMVADecision_TOS
HLT2	Hlt2B2HHDecision_TOS

- the signal yields;
- the background contamination;
- the total effective tagging power;
- the dilution from the decay-time resolution (negligible for the B^0 meson);
- the decay-time acceptance.

In order to take into account all these contributions, which significantly affect the final results, the optimisation of event selection has been improved in such a way to minimize the statistical error on the time-dependent *CP* asymmetries.

BDT classifier

Similarly to what done in the Run 1 analysis, a multivariate (MVA) classifier based on a Boost Decision Tree [128] is exploited in order to reduce the level of combinatorial background contamination. Two different BDTs are trained with the aim to optimally select both the $B^0 \to \pi^+\pi^-$ and $B_s^0 \to K^+K^-$ decays. The BDT specialized in the $B^0 \to \pi^+\pi^-$ selection, named hereafter $BDT_{\pi^+\pi^-}$, has been trained using a fully-simulated sample of $B^0 \to \pi^+\pi^-$ candidates as signal. Analogously the BDT developed for the $B_s^0 \to K^+K^-$ selection, $BDT_{K^+K^-}$, exploits a fully-simulated sample of such decays for learning the signal characteristics and correlations. The description of the background is taken from data for both the BDTs, using only the events with an invariant mass greater than $5.6\,\text{GeV}/c^2$. Both the BDTs are trained using an *Adaptive* boost and 850 independent trees in order to stabilize the BDTs response and reduce any possible source of overtraining. The BDTs are

trained using the variables summarized in Table 6.3 as input. Few variables are changed with respect the ones used in the BDT training in Run 1 analysis: they are the cosine of the angle comprised between the momentum of the H_b candidate and its direction of flight vectors ($DIRA$), the χ^2 of the H_b candidate primary vertex (χ^2(vtx)), the χ^2 of the H_b candidate primary vertex (χ^2(vtx)). Given this new set of input variables the signal efficiency has been increased from 87.4% to 89.1% while the background contamination has been decreased from 9.6% to 8.3% for the $B^0_s \to K^+K^-$ optimisation (while is remained unchanged for the $B^0 \to \pi^+\pi^-$ optimisation). The distribution of the input variables for both the signal and background categories are shown in Figures 6.1, 6.2 while their correlations are shown in Figure 6.3.

Table 6.3: Input variables used to train both the $BDT_{\pi^+\pi^-}$ and $BDT_{K^+K^-}$ classifiers. The description of the variables is reported in text.

Input variables		
χ^2(vtx)	$\chi^2(FD)$	$DIRA$
$min(p_T^{\text{track}^+}, p_T^{\text{track}^-})$	$log(\min(\chi^2(d_{IP}^{\text{track}^+}), \chi^2(d_{IP}^{\text{track}^-})))$	$log(\min(\chi^2(\text{track}^+), \chi^2(\text{track}^-)))$
$max(p_T^{\text{track}^+}, p_T^{\text{track}^-})$	$\log(\max(\chi^2(d_{IP}^{\text{track}^+}), \chi^2(d_{IP}^{\text{track}^-})))$	$log(\max(\chi^2(\text{track}^+), \chi^2(\text{track}^-)))$

The responses of the $BDT_{\pi^+\pi^-}$ classifier is shown in Figure 6.4. In order to prevent any possible bias affecting the determination of the best BDT requirement, discussed in Section 6.1.2, two different instances of BDT for each final state are created. The former of the two instance is trained using only the even numbered events, and then will be applied to the odd numbered events, while the latter instance will be trained on the odd events and then applied to the even events.

Strategy of the selection optimisation

Similarly to the Run 1 analysis the signal candidates of interest are identified by means of two selections: one based on particle identification criteria and the second consisting of a BDT classifier. However, in order to take into account the correlation between the PID and BDT requirements, the two selections are now optimised simultaneously. Only the requirement on the $DLL_{K\pi}$ variable, the most important for this kind of analysis, takes place in such optimisation. The $DLL_{p\pi}$ and DLL_{Kp} requirements, used just to reduce the contribution of the $\Lambda^0_b \to p\pi^-$ and $\Lambda^0_b \to pK^-$ decays, are determined separately and their values are reported in Table 6.4. The same PID requirements used in Run 1 are exploited for the identification of the $K^\pm\pi^\mp$ final state. Two different optimisations are determined for the $B^0 \to \pi^+\pi^-$ and $B^0_s \to K^+K^-$ decays, respectively and for each one several different combinations of $DLL_{K\pi}$ and BDT requirements are considered:

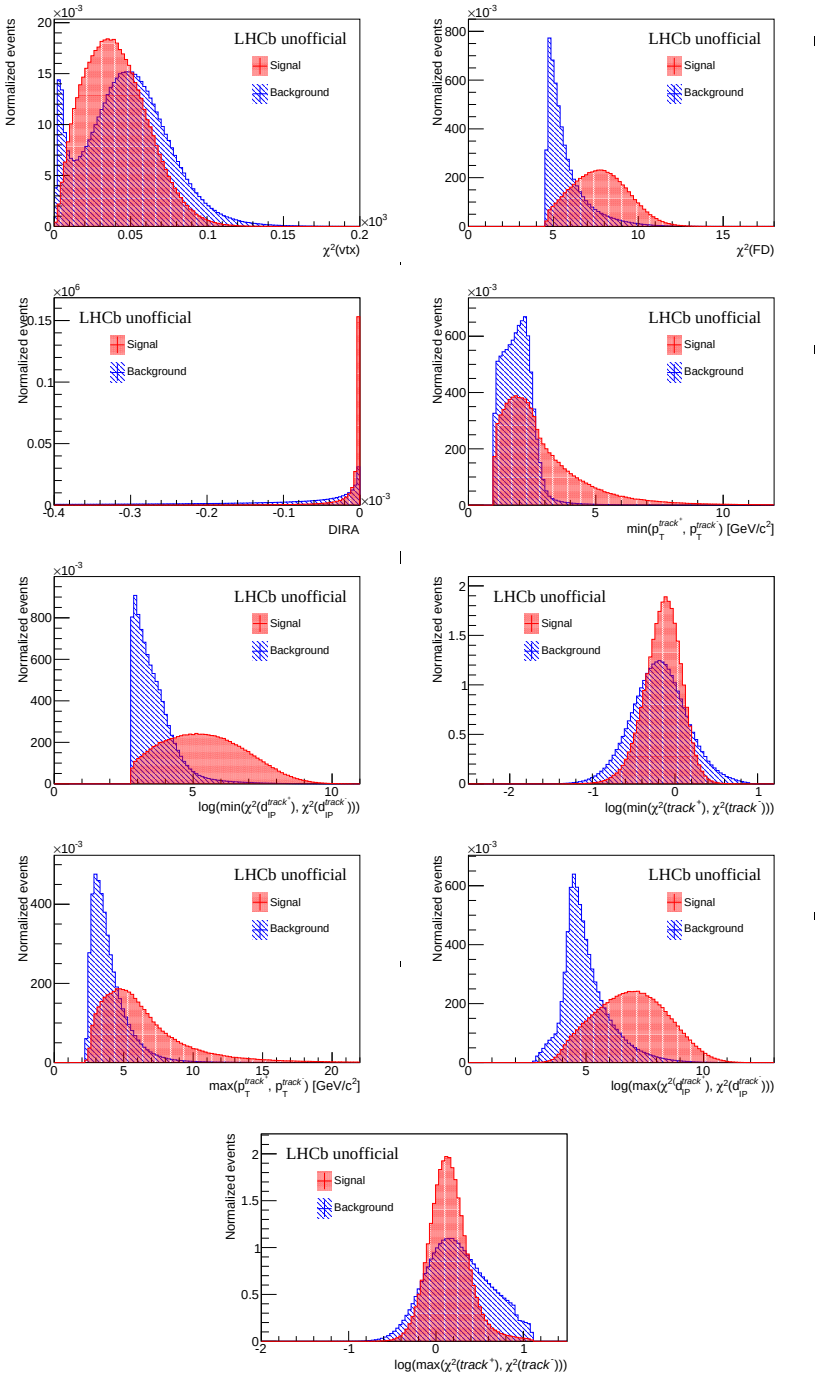

Figure 6.1: Distributions of the input variables used in the training of the $BDT_{\pi^+\pi^-}$ classifier. The distributions related to the signal (red) are obtained from fully-simulated $B^0 \to \pi^+\pi^-$ decays, while the distributions corresponding to the background (blue) are taken from data applying a requirement to the invariant mass of the H_b candidates to be greater than 5.6 GeV/c^2. From left to right the variables are: $\chi^2(\text{vtx})$, $\chi^2(FD)$, $DIRA$,$min(p_T^{\text{track}^+}, p_T^{\text{track}^-})$, $log(\min(\chi^2(d_{IP}^{\text{track}^+}), \chi^2(d_{IP}^{\text{track}^-})))$, $log(\min(\chi^2(\text{track}^+), \chi^2(\text{track}^-)))$, $max(p_T^{\text{track}^+}, p_T^{\text{track}^-})$, $\log(\max(\chi^2(d_{IP}^{\text{track}^+}), \chi^2(d_{IP}^{\text{track}^-})))$, $log(\max(\chi^2(\text{track}^+), \chi^2(\text{track}^-)))$. The description of the variables is reported in the text. For the sake of clarity a logarithm transformation is applied to the variables $\chi^2(FD)$ and $DIRA$.

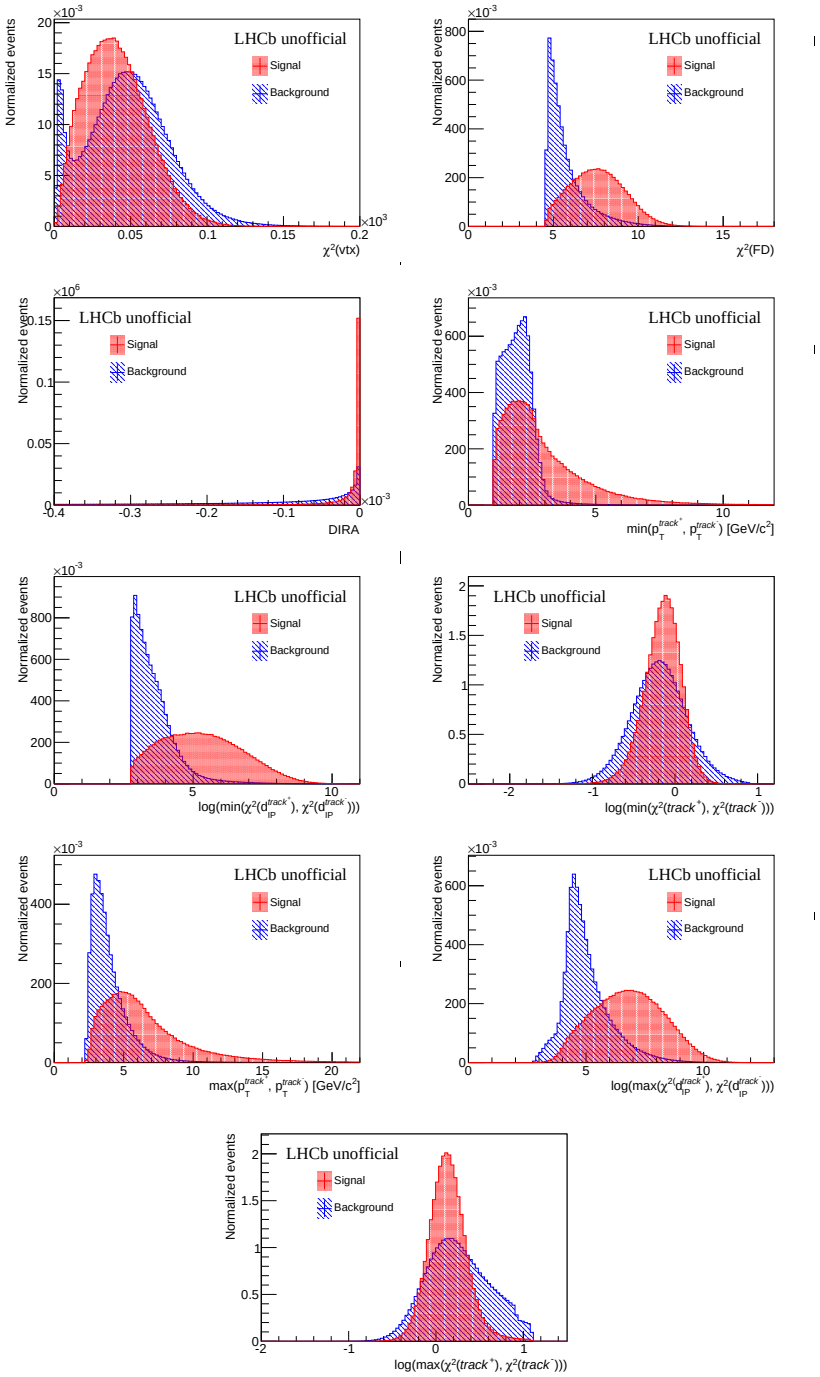

Figure 6.2: Distributions of the input variables used in the training of the $BDT_{K^+K^-}$ classifier. The distributions related to the signal (red) are obtained from fully-simulated $B^0_s \to K^+K^-$ decays, while the distributions corresponding to the background (blue) are taken from data applying a requirement to the invariant mass of the H_b candidates to be greater than 5.6 GeV/c^2. From left to right the variables are: $\chi^2(\text{vtx})$, $\chi^2(FD)$, $DIRA$,$min(p_T^{\text{track}^+}, p_T^{\text{track}^-})$, $log(\min(\chi^2(d_{IP}^{\text{track}^+}),\chi^2(d_{IP}^{\text{track}^-})))$, $log(\min(\chi^2(\text{track}^+),\chi^2(\text{track}^-)))$, $max(p_T^{\text{track}^+}, p_T^{\text{track}^-})$, $\log(\max(\chi^2(d_{IP}^{\text{track}^+}),\chi^2(d_{IP}^{\text{track}^-})))$, $log(\max(\chi^2(\text{track}^+),\chi^2(\text{track}^-)))$. The description of the variables is reported in the text. For the sake of clarity a logarithm transformation is applied to the variables $\chi^2(FD)$ and $DIRA$.

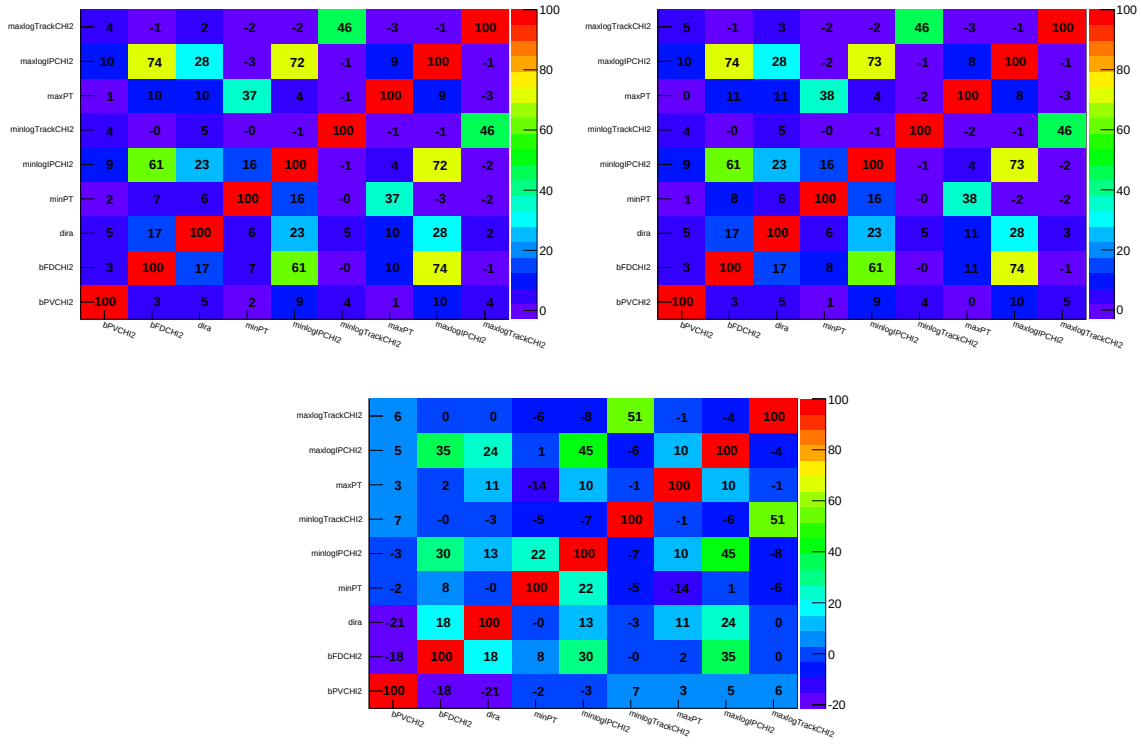

Figure 6.3: Correlation among the variables used to train the BDT algorithms for $B^0 \to \pi^+\pi^-$ simulated events (top left), $B_s^0 \to K^+K^-$ simulated events (top right) and high invariant mass sideband (bottom).

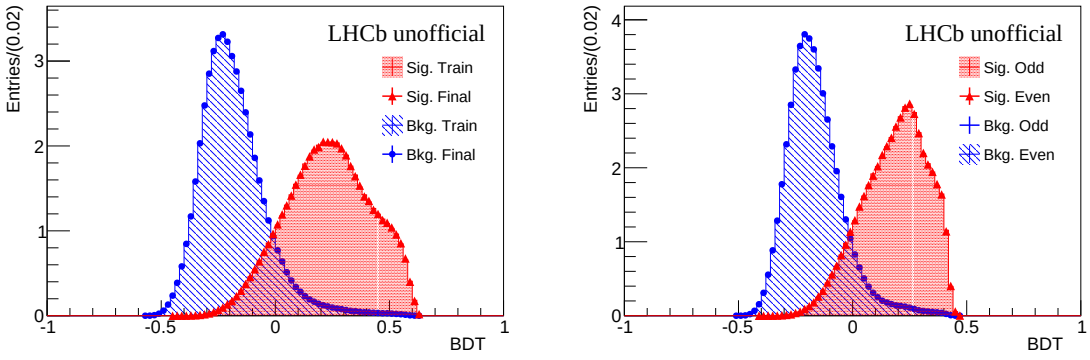

Figure 6.4: Distribution of the BDT response optimised for the $B^0 \to \pi^+\pi^-$ (left) and $B_s^0 \to K^+K^-$ (right) decays. The signal distribution is depicted in red, while the background-like events is shown in blue.

- $\pi^+\pi^-$ spectrum: $DLL_{K\pi}$ requirement varied in range [-9, 0] with step equal to 1;
  $BDT_{\pi^+\pi^-}$ requirement varied in [-0.1, 0.1] with step equal to 0.02;
- K^+K^- spectrum: $DLL_{K\pi}$ requirement varied in range [0, 9] with step equal to 1;
  $BDT_{K^+K^-}$ requirement varied in [-0.16, 0.06] with step equal to 0.02.

The best configuration is chosen as the one which leads to the minimal statistical error on the final time-dependent *CP* asymmetries. The determination of such asymmetries is performed by means of an unbinned maximum likelihood fit to pseudoexperiments. The observables used in this *CP* fit are the same which will be used in the final fit of the analysis: the invariant mass m, the decay time t, the decay time error and the tagging decision and mistag rate of both OS and SS tagging algorithms.

Construction of the pseudoexperiments

The pseudoexperiments are built in such a way to replicate as close as possible the data distributions and are generated for each configuration of PID and BDT requirements indicated previously. The different points to take into account are: determination of the yields of the various signal and background components, the determination of the decay-time acceptances and the construction of the template both for the tagging mistag rates. The determination of all these ingredients is described in detail in the following paragraphs.

Determination of the yields The yield of each signal and background component is determined from an unbinned maximum likelihood fit to the invariant mass distribution observed in data. To the $\pi^+\pi^-$ final state the following contributions are taken into account: $B^0 \to \pi^+\pi^-$, $B_s^0 \to \pi^+\pi^-$, $B^0 \to K^+\pi^-$, where the kaon is mis-identified with a pion, the combinatorial and the partially reconstructed 3-body backgrounds. On the other hand, the $B_s^0 \to K^+K^-$, $B^0 \to K^+K^-$, $B^0 \to K^+\pi^-$ and $B_s^0 \to \pi^+K^-$, where the pion is mis-identified with a kaon, along with the combinatorial and the partially reconstructed 3-body backgrounds contribute to the K^+K^- final state. The p.d.f. used in the fit for describing the several components are the same used in the Run 1 analysis, whose expressions are reported in Section 5.3. The cross-feed backgrounds are determined using the kernel estimation method applied to fully simulated signal decays generated in Run 2 conditions. Also the parameters describing the shape of the signal tails have been fixed to the values determined from a fit to the invariant mass distribution of the same simulated Run 2 samples. An example of invariant mass distribution, related to the $\pi^+\pi^-$ final state selected requiring $DLL_{K\pi} < -3$ and $BDT_{\pi^+\pi^-} > 0.04$, is shown in Figure 6.5.

Determination of the decay-time acceptances The decay-time acceptances for all the $H_b \to h^+h'^-$ decay modes, including the $B^0 \to K^+\pi^-$ decay channel, have been determined by means of fully-

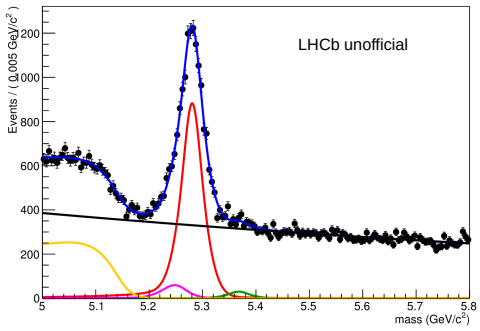

Figure 6.5: Invariant mass distribution for the $\pi^+\pi^-$ final state, selected requiring $DLL_{K\pi} < -3$ and $BDT_{\pi^+\pi^-} > 0.04$. The results of the unbinned maximum likelihood fit is superimposed. The different contributions are also shown: the $B^0 \to \pi^+\pi^-$ decay (red), the $B_s^0 \to \pi^+\pi^-$ decay (green), the $B^0 \to K^+\pi^-$ with a kaon mis-identified with a pion (violet), the combinatorial background (black) and the partially reconstructed 3-body background (yellow).

simulated samples using a strategy similar to what described in Section 5.4.2. In this case, the decay-time acceptances have been parametrised according to a different effective function:

$$\varepsilon_{acc}^{\text{sig}} = a_0 \left[1 - \text{erf}\left(a_1 t^{a_2}\right)\right] \left(1 - a_3 t\right), \tag{6.1}$$

in order to obtain a better agreement with the Run 2 simulated samples. As an example the acceptance histogram for the $B^0 \to \pi^+\pi^-$ decay, obtained applying the $DLL_{K\pi} < -3$ and $BDT_{\pi^+\pi^-} > 0.04$ requirements, and the corresponding high-statistics sample are shown in Figure 6.6.

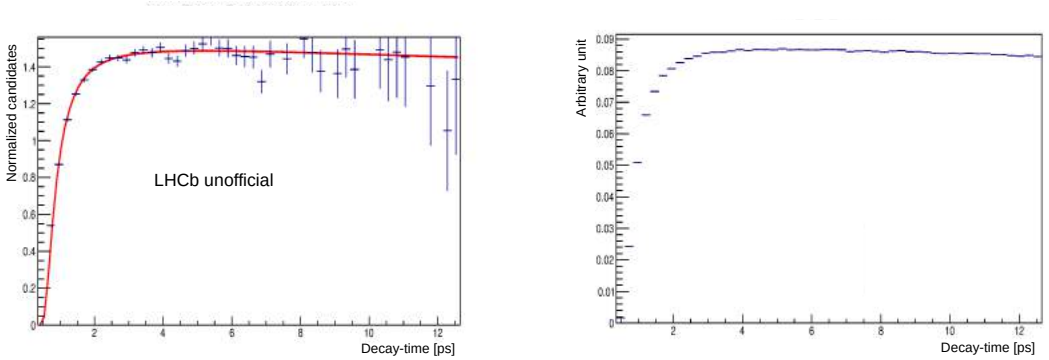

Figure 6.6: The decay-time acceptance for the $B^0 \to \pi^+\pi^-$ decay model (left), obtained as described in the text, and the corresponding high-statistics histogram (right) are shown. In the *CP* fit the histogram will be interpolated with a cubic spline polynomial functions.

The decay-time acceptance for the combinatorial and partially reconstructed 3-body background have been determined with a data-driven method, as described in Section 5.4.1. The decay-time distributions related to the events taken from the high- and low-mass sidebands are shown in Figure 6.7

with the results of the fit to the decay-time distribution are superimposed.

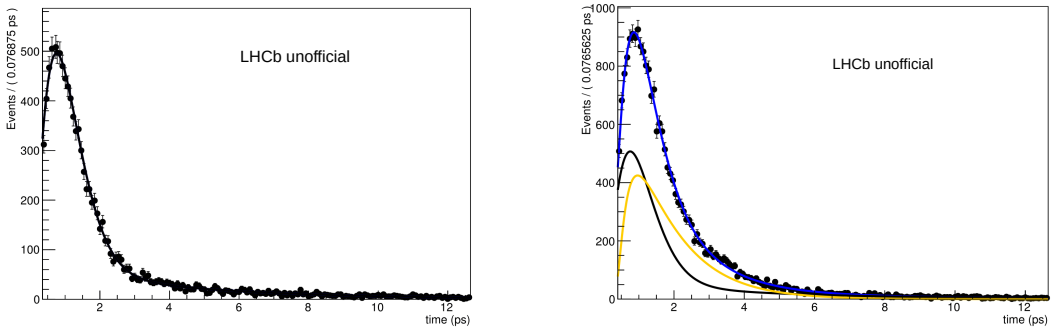

Figure 6.7: The decay-time distributions related to the events taken from the high- (left) and low-mass sidebands (right), corresponding to an invariant mass higher than 5.6 GeV and lower than 5.2 GeV respectively, are shown. The results of the fit to the decay-time distribution are superimposed. The so-obtained template will be used in the *CP* fit to describe the background decay-time acceptances.

Determination of the signal and background templates The last ingredient in order to generate a set of pseudoexperiments identically replicating the Run 2 data, consists in the determination of the decay-time error, computed by the DTF, and O*S* and S*S* mistag rate templates for all the signal and background components. The templates for the signal decay modes are obtained exploiting a data sample of $B^0 \to D^-\pi^+$ and $B_s^0 \to D_s^-\pi^+$ events. The background contamination is subtracted by means of the *sPlot* technique [122]. In addition both the samples are reweighted in order to take into account the different kinematic with respect to the $H_b \to h^+h'^-$ sample.

Similarly to the procedure followed in the previous paragraph regarding the determination of the decay-time acceptance, the templates for the two background sources are determined using the high- and low-mass sidebands. In the case of the low-mass region the residual contamination of the combinatorial background has to be subtracted in order to obtain the correct templates for the 3-body background. Such subtraction is performed using the templates obtained in the high-mass region and removing an amount of combinatorial background events equal to expected events in the low-mass region. This quantity is extrapolated, as already described in Section 4.4, by means of a fit to invariant high-mass distribution with a pure exponential function.

Generation of the pseudoexperiments In the previous paragraph the different steps required to parametrise the variable of each component have been described. From the combination of these various ingredients with the mass and decay-time p.d.f., described in Sections 5.3 and 5.4, the pseudoexperiments replicating the Run 2 $H_b \to h^+h'^-$ data can be generated. In order to reduce any significant statistical fluctuation of the results, for each configuration of PID and BDT requirement,

indicated at the beginning of this subsection a set of 10 pseudoexperiments is built. For each pseudoexperiment all the observables, necessary to perform the *CP* fit, are generated. In the generation, the *CP* parameters have been fixed to the values obtained with the Run 1 analysis, reported in Section 5.5, while the values of $\Delta m_{d,s}$, $\Gamma_{d,s}$ and $\Delta\Gamma_{d,s}$ are fixed to the PDG values [15]. As an example the invariant mass and the decay-time distribution related to the $\pi^+\pi^-$ final state, selected requiring $DLL_{K\pi} < -3$ and $BDT_{\pi^+\pi^-} > 0.04$, are shown in Figure 6.8.

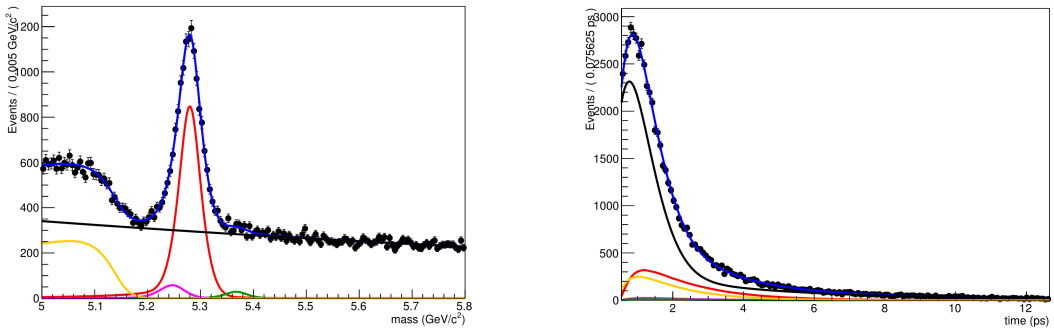

Figure 6.8: Invariant mass (left) and decay-time (right) distribution under the $\pi^+\pi^-$ final state hypothesis, using the configuration $DLL_{K\pi} < -3$ and $BDT_{\pi^+\pi^-} > 0.04$. The result of the *CP* fit is superimposed. The different components are shown: $B^0 \to \pi^+\pi^-$ (red), $B_s^0 \to \pi^+\pi^-$ (green), $B^0 \to K^+\pi^-$ (violet), the combinatorial background (black) and the partially reconstructed 3-body decays (yellow).

CP fit to the pseudoexperiments

Performing a *CP* fit to these pseudoexperiments it is possible to determine the *CP*-violating parameters and their corresponding statistical uncertainties. For each configuration, the statistical uncertainties of the *CP* asymmetries obtained repeating the *CP* fit 10 times, one for each pseudoexperiment generated with that configuration, are averaged in order to obtain a more reliable value.

The results of the optimisation for the $B^0 \to \pi^+\pi^-$ decay are shown in Figure 6.9, where the average statistical uncertainties of the $C_{\pi^+\pi^-}$ and $S_{\pi^+\pi^-}$ parameters, obtained for each configuration of PID and BDT requirements, are reported. In addition, the distributions of the signal S and background B yields, as well as of the quantity $S/\sqrt{S+B}$, which was used as figure of merit in the Run 1 selection optimisation, are reported for each configuration taken into account in Figure 6.10. In this case only the combinatorial background lying under the signal mass peak is taken into account. Similarly the same distributions related to the optimisation of the $B_s^0 \to K^+K^-$ decay are shown in Figures 6.11, 6.12.

It is worth to be noticed that the configuration leading to the minimal statistical uncertainty on the *CP* parameters it is not the same as the one with the highest $S/\sqrt{S+B}$ value. The reason lies in

the fact that using the $S/\sqrt{S+B}$ quantity as figure of merit do not take into account the effect of the total tagging power available and the effects of the decay-time error and decay-time acceptances, which play a role on the sensitivity to the various *CPV* parameters.

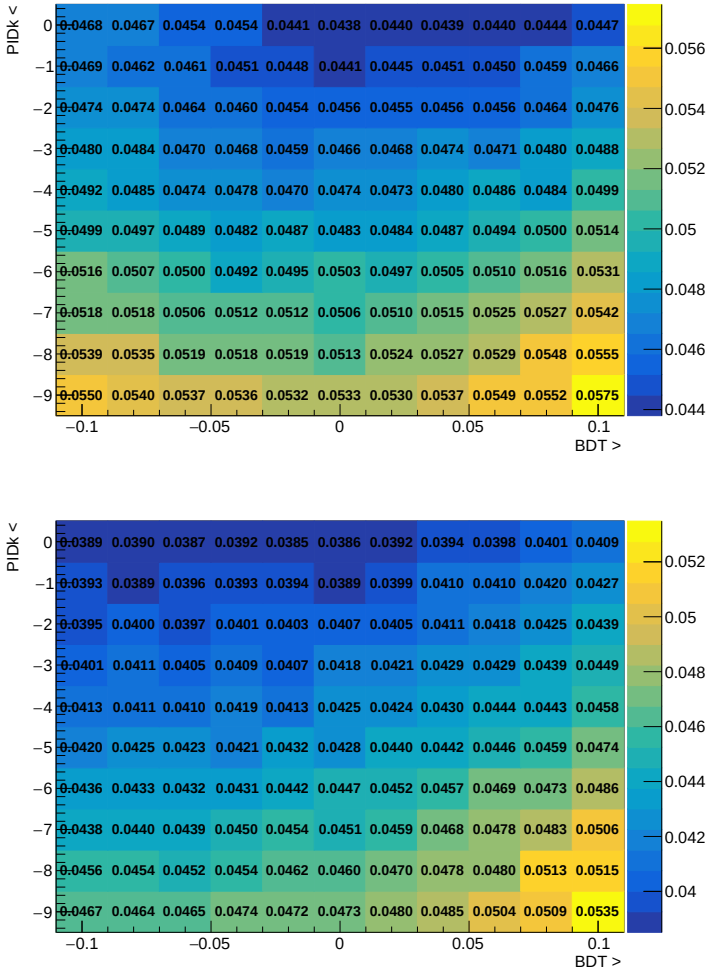

Figure 6.9: Distribution of the statistical uncertainty related to the $C_{\pi^+\pi^-}$ and $S_{\pi^+\pi^-}$ parameters in the scanned range of $DLL_{K\pi}$ and $BDT_{\pi^+\pi^-}$. The value in each bin corresponds to the average of the statistical uncertainty on the *CP* parameters obtained performing the *CP* fit to the 10 pseudoexperiments generated for each configuration.

Final selections

The study described in the previous paragraphs allows to determine which configuration of PID and BDT requirements leads to the maximal sensitivity on the *CP*-violating parameters. Looking at the distributions, shown in Figures 6.9, 6.11, it seems that the best selection is obtained using very loose $DLL_{K\pi}$ requirements. In addition it seems that the minimal statistical uncertainty on the *CP* parameters does not correspond to a very specific configuration, but it can be achieved using

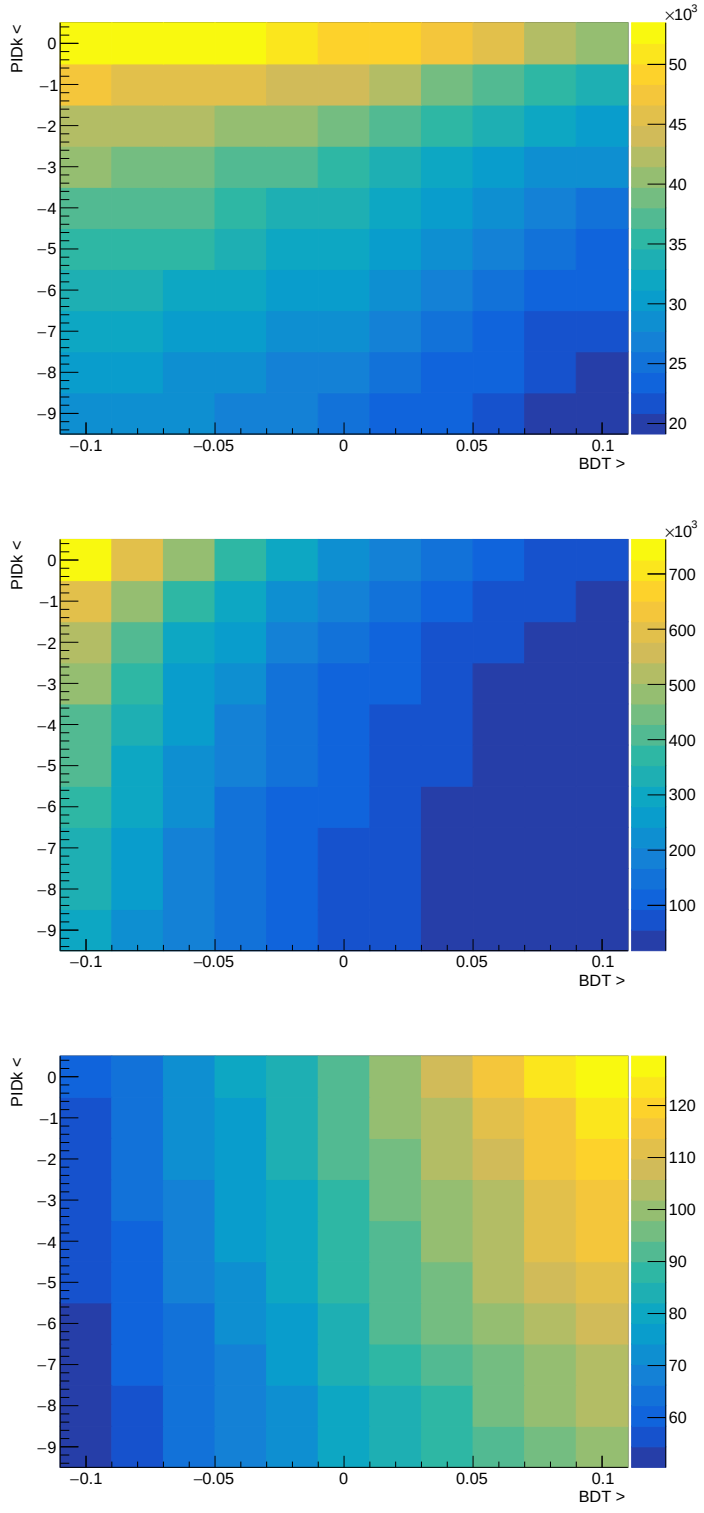

Figure 6.10: Distribution of the yields related to the $B^0 \to \pi^+\pi^-$ decay (top) and the combinatorial background (middle) obtained by means of a fit to the invariant mass spectrum for each configuration of $DLL_{K\pi}$ and $BDT_{\pi^+\pi^-}$ requirements. A similar distribution for the figure of merit $S/\sqrt{S+B}$ is also shown (bottom). Only the combinatorial background events lying under the signal mass peak are taken into account.

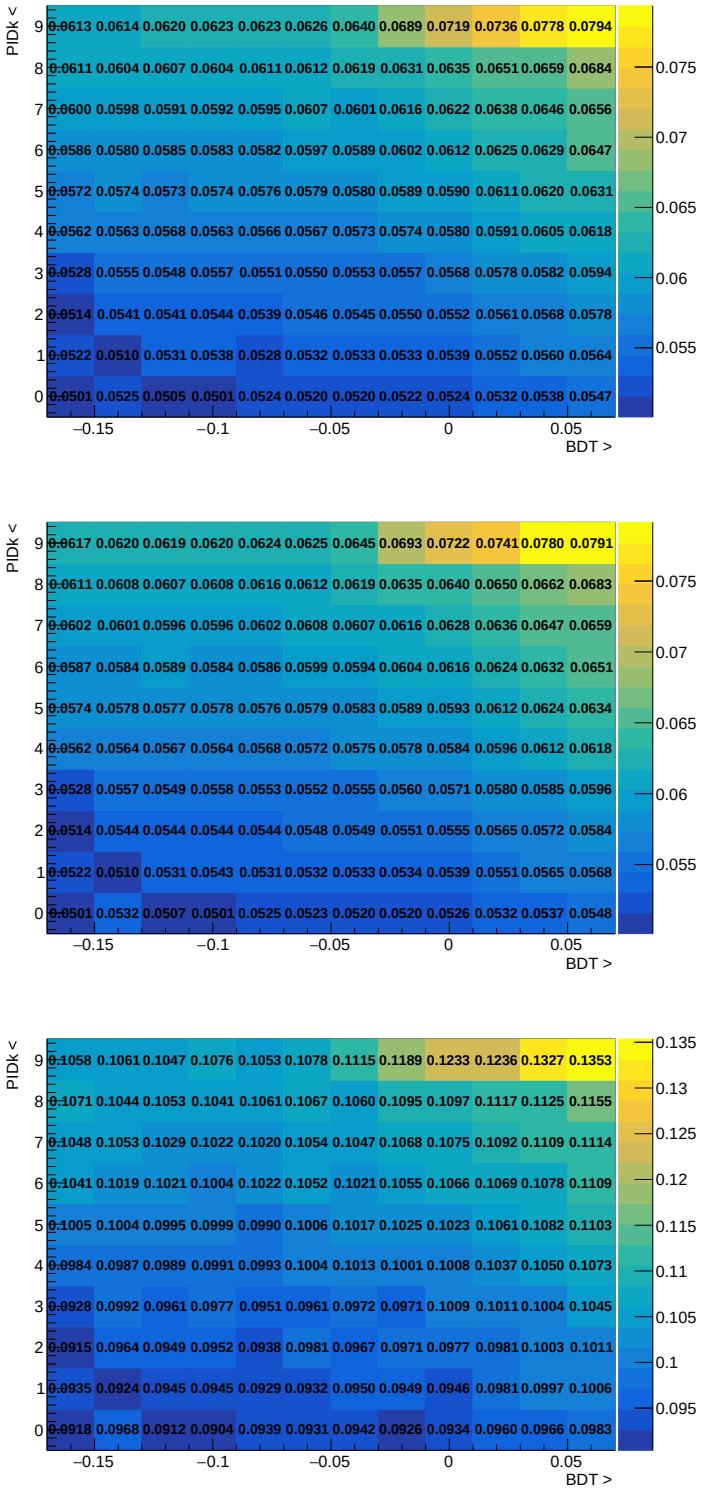

Figure 6.11: Distribution of the statistical uncertainty related to the $C_{K^+K^-}$, $S_{K^+K^-}$ and $A^{\Delta\Gamma}_{K^+K^-}$ parameters in the scanned range of $DLL_{K\pi}$ and $BDT_{K^+K^-}$. The value in each bin corresponds to the average of the statistical uncertainty on the *CP* parameters obtained performing the *CP* fit to the 10 pseudoexperiments generated for each configuration.

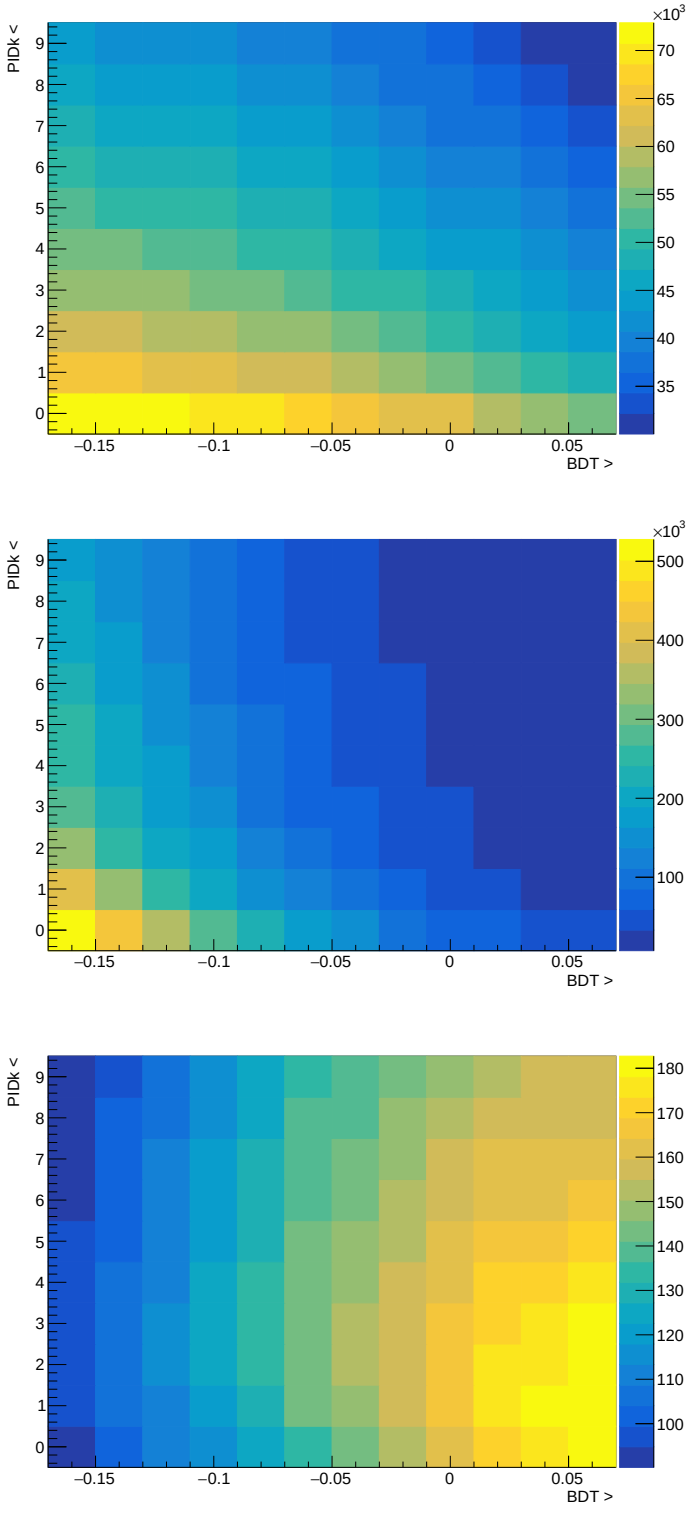

Figure 6.12: Distribution of the yields related to the $B_s^0 \to K^+K^-$ decay (top) and the combinatorial background (middle) obtained by means of a fit to the invariant mass spectrum for each configuration of $DLL_{K\pi}$ and $BDT_{K^+K^-}$ requirements. A similar distribution for the figure of merit $S/\sqrt{S+B}$ is also shown (bottom). Only the combinatorial background events lying under the signal mass peak are taken into account.

different combinations of $DLL_{K\pi}$ and BDT requirements.

In order to choose the best configuration two points should be considered:

- the pseudoexperiments generated in this study are not able to describe completely the complexity of the real data;
- the systematic uncertainties are not taken into account in this optimisation.

In particular the systematic uncertainties related to the cross-feed contamination, linked to the PID requirements, could assume very large values in case of very loose $DLL_{K\pi}$ selection.

For these reasons, in order to take under control any possible systematic source, a more conservative final event selection is preferred. The final $DLL_{K\pi}$ and BDT requirements for the two final state hypotheses ($\pi^+\pi^-$ and K^+K^-) are reported in Table 6.4. The application of these requirement configurations leads to a sensitivity on the *CP* asymmetries (σ) which is not very distant from the minimal one (σ_{best}) found in the scanned ranges, as reported in Table 6.5. Since no specific BDT has been trained for the $K^\pm\pi^\mp$ final state, the selection of such mass hypothesis rely only on a set of PID requirements. A dedicated study on the optimisation of the $DLL_{K\pi}$ requirements, used to identify the $K^+\pi^-$ final state, has been already performed in the Run 1 analysis, providing a level of the cross-feed contamination lower than 10% of the corresponding signal. this level of cross-feed contamination allows to keep under control the systematic uncertainties related to the modelling of the cross-feed backgrounds. Since this level of contamination is sufficiently low allowing to keep under control the cross-feed background systematic uncertainties the final $DLL_{K\pi}$ requirements used to identify the $K^+\pi^-$ final state have been set to the same one optimised in Run 1 analysis, which are summarised in Table 6.4.

Table 6.4: Final offline event selections, involving PID and BDT requirements, chosen with the aim to identified the three final states according to the $B^0 \to \pi^+\pi^-$ and $B_s^0 \to K^+K^-$ optimisations.

	$\pi^+\pi^-$ optimisation		K^+K^- optimisation	
BDT	> 0.04		> -0.04	
	$\pi^+\pi^-$ spectrum	$K^\pm\pi^\mp$ spectrum		K^+K^- spectrum
$DLL_{K\pi}$	$(\pi^\pm) < -2$	$(K^\pm) > 5$	$(\pi^\mp) < -5$	$(K^\pm) > 2$
$DLL_{p\pi}$	$(\pi^\pm) < 3$	-	$(\pi^\mp) < 3$	-
DLL_{Kp}	-	$(K^\pm) > -2$	-	$(K^\pm) > -2$

Table 6.5: Comparison of the sensitivity achieved using the chosen requirement configuration (σ) with respect to the one corresponding to the optimal configuration (σ_{best}), as found in the optimisation study. Both the comparison for the $B^0 \to \pi^+\pi^-$ and $B_s^0 \to K^+K^-$ optimisations are reported.

	$\pi^+\pi^-$ optimisation		K^+K^- optimisation	
	σ	σ_{best}	σ	σ_{best}
S	0.041	0.039	0.055	0.050
C	0.046	0.044	0.055	0.050

6.1.3 Background subtracted and fully-simulated samples

Analogously to the Run 1 analysis, both simulated samples corresponding to the various $H_b \to h^+h'^-$ decay modes and a background subtracted data sample are required in order to extract the values of some parameters, determine the shape of the cross-feed backgrounds as well as built the decay-time error and tagging mistag rate templates which will be fundamental ingredients in the final fit. In order to have events as much similar to the real data, the simulated samples have been reproduced using the same data taking conditions, trigger, reconstruction, stripping and Flavour Tagging used for the processing of the real data. The number of generated events for the different $H_b \to h^+h'^-$ decays is reported in Table 6.6. The complete list of the parameters is reported in Table 6.7. The invariant mass distributions for the various $H_b \to h^+h'^-$ decays are shown in Figure 6.13. The result of the best fit of the model is superimposed.

Table 6.6: Number of events available in fully-simulated samples for the various $H_b \to h^+h'^-$ decay modes generated with Run 2 data taking conditions (2015+2016).

Decays	Number of events
$B^0 \to K^+\pi^-$	977 550
$B^0 \to \pi^+\pi^-$	977 550
$B_s^0 \to \pi^+K^-$	132 308
$B_s^0 \to K^+K^-$	993 486
$B_s^0 \to \pi^+\pi^-$	139 650
$B^0 \to K^+K^-$	139 650

The background subtracted $H_b \to h^+h'^-$ sample, determined by means of the *sPlot* technique as describe in Section 5.1.6, is used to extract reliable templates for the decay-time error. In the fit to the invariant mass distribution, the relative fractions among the various $H_b \to h^+h'^-$ modes are fixed to the values measured by LHCb in Reference [58], except for the Λ_b^0 decays where the branching ratios

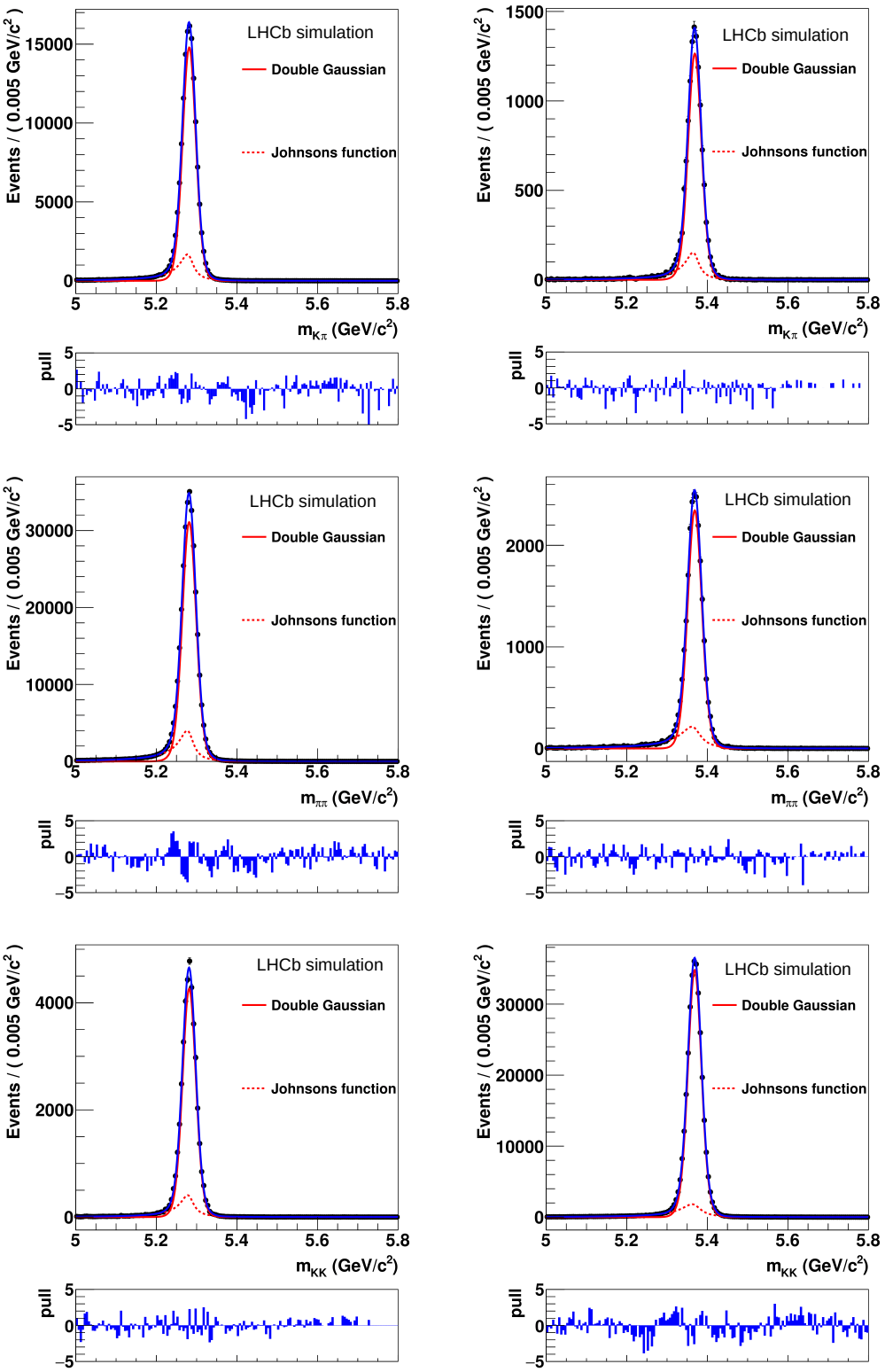

Figure 6.13: Invariant mass distributions for $B^0 \to K^+\pi^-$, $B_s^0 \to \pi^+K^-$, $B^0 \to \pi^+\pi^-$, $B_s^0 \to \pi^+\pi^-$, $B^0 \to K^+K^-$ and $B_s^0 \to K^+K^-$ simulated 2016 samples. (from top left to bottom right). The result of the best fit of the model described in Equation (5.11) are also superimposed.

Table 6.7: Parameters governing the signal mass shape of the p.d.f. reported in Equation (5.11), obtained from unbinned maximum likelihood fits to simulated $H_b \to h^+h'^-$ decays, which will be fixed in the fit to data.

Decay	f_{tail}	α_1	α_2
$B^0 \to K^+\pi^-$	0.143 ± 0.004	0.65 ± 0.01	0.64 ± 0.01
$B_s^0 \to \pi^+K^-$	0.136 ± 0.009	0.67 ± 0.03	0.65 ± 0.02
$B^0 \to \pi^+\pi^-$	0.163 ± 0.004	0.70 ± 0.01	0.65 ± 0.01
$B_s^0 \to \pi^+\pi^-$	0.200 ± 0.009	0.66 ± 0.02	0.57 ± 0.01
$B_s^0 \to K^+K^-$	0.109 ± 0.002	0.61 ± 0.01	0.62 ± 0.01
$B^0 \to K^+K^-$	0.119 ± 0.009	0.55 ± 0.03	0.67 ± 0.02

evaluated by HFLAV [71] are used instead. The invariant mass ($m_{\pi\pi}$) distribution and the result of the fit are shown in Figure 6.14.

6.2 PID calibration

The PID calibration is treated in the same was as in Run 1 analysis. The PID efficiency maps are built in bins of momentum p and pseudorapidity η, using the same binning as in Run 1, and $nSPD$, i.e. the multiplicity in the SPD, which describing the detector occupancy instead of the $nTracks$ variable. The $nSPD$ binning scheme used for the calibration is:

- $nSPD$: 3 bins in the interval [0, 450], 3 bins in the interval [450, 1000].

Also in this case the dependence on the event multiplicity can be integrated out, due to the fact that it is uncorrelated to the kinematic of the final state. The integration is performed in similar way to what shown in Section 5.2. The result of such a procedure are the maps of PID efficiencies in bin of p and η for the final-state particles of the $H_b \to h^+h'^-$ decays.

The $p - \eta$ plane, related to the protons, is again splitted in two parts, namely the "fiducial" and "non-fiducial" regions. The PID efficiency for pions, kaons and protons are evaluated as described in Run 1 analysis.

6.3 Fit model

The *CP*-violating parameters are obtained by means of a simultaneous fit on the all the three final state hypotheses. The fit model mainly consists of a part related to the invariant mass distribution and another part describing the decay-time distribution of the H_b candidates. There are four

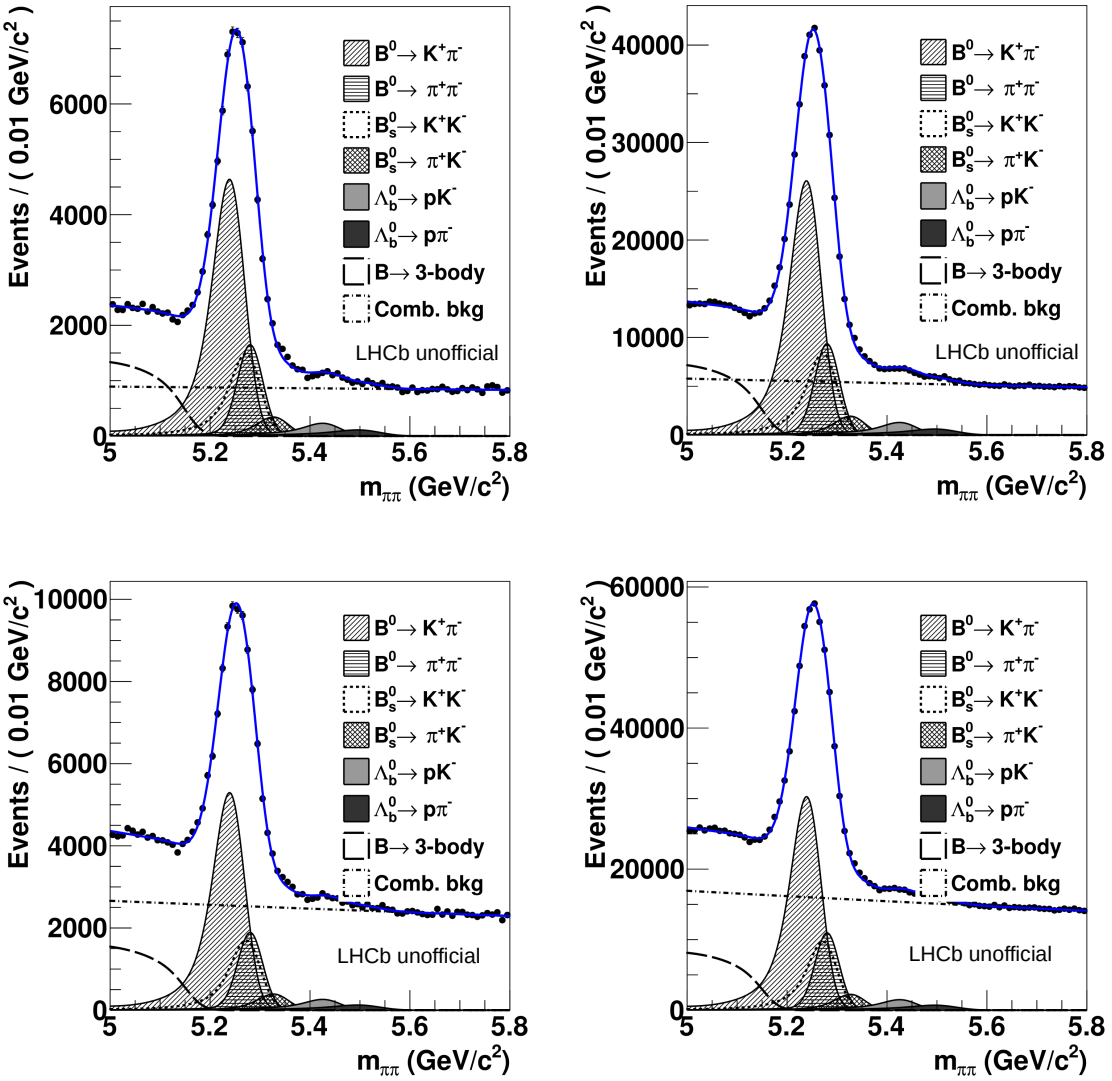

Figure 6.14: Distribution of invariant mass under the $\pi^+\pi^-$ final state hypothesis for the events surviving the full event selection for both the 2015 (left) and 2016 (right) data samples obtained applying the $\pi^+\pi^-$ (top) and K^+K^- (bottom) optimisation. The result of the fit used to extract the $H_b \to h^+h'^-$ weights, exploiting the *sPlot* technique, is also shown.

different components contributing to the $H_b \to h^+h'^-$ spectra that have to be parametrised: the signal decays and the corresponding the cross-feed backgrounds, the combinatorial and the partially reconstructed 3-body backgrounds. While the invariant mass model has remained completely untouched with respect to the Run 1 model, the decay-time model has been changed, revisiting the strategy used to determine the calibration of the decay-time resolution, as described in Section 6.3.1. The decay-time acceptance and the other ingredients entering in the decay-time model have been re-determined following the same strategy used in Run 1 analysis.

6.3.1 Decay-time resolution

The sensitivity on the *CP*-violating parameters in the B_s^0 sector is affected by the exact knowledge of the decay-time resolution. The calibration of the decay-time resolution $\tau_{err} = t - t_{true}$, as a function of the decay-time error δ_t, is performed using a data sample of $J/\psi \to \mu^+\mu^-$ candidates collected with the same data taking condition of the $H_b \to h^+h'^-$ sample. The J/ψ is a resonance with null lifetime, thus the reconstructed decay-time corresponds directly to the variable τ_{err}. To verify that the dependence of the decay-time resolution on the decay-time error is the same in the J/ψ and H_b modes, the calibration procedure is repeated on fully-simulated events of $J/\psi \to \mu^+\mu^-$ and $B_s^0 \to K^+K^-$ decays.

Calibration of the decay-time resolution

The functional dependence of the decay-time resolution (σ) is determined on the $J/\psi \to \mu^+\mu^-$ data sample by means of a simultaneous bi-dimensional unbinned fit on the δ_t and τ_{err} variables, where both of them have been determined by means of the DTF. The τ_{err} distribution is fitted, in the range $[-0.6, 0.6]$, through a Gaussian function with mean μ and width σ defined as a second order polynomial of δ_t:

$$\sigma(\delta_t) = p_0 + p_1(\delta_t - \hat{\delta}_t) + p_2(\delta_t - \hat{\delta}_t)^2 \tag{6.2}$$

where $\hat{\delta}_t$ in order to allow an easier comparison, has been fixed to 0.04, that corresponds to approximately the average of the δ_t distribution in the $B_s^0 \to K^+K^-$ sample. The result of the bi-dimensional fit is reported in Table 6.8 and the calibration curve, along with the δ_t distribution, is shown in Figure 6.15. Then the $J/\psi \to \mu^+\mu^-$ data sample has been splitted into 40 samples of the same size and increasing decay-time error. The fit result has been superimposed in each bin in order to check that the variation of τ_{err} matches the decay-time resolution assumed by the model. The distribution of the τ_{err} variable in each bins is reported in Appendix E with the results of the fit superimposed.

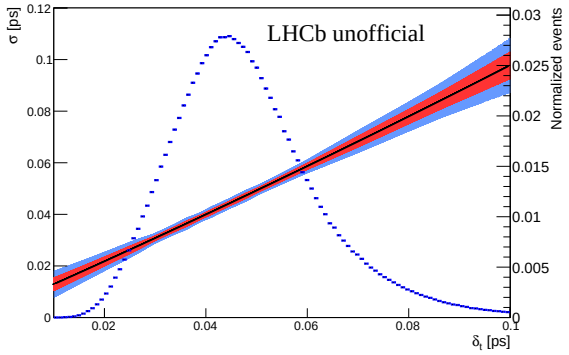

Figure 6.15: Functional dependence of the decay-time resolution on the decay-time error determined on a Run 2 data sample of $J/\psi \to \mu^+\mu^-$ decays. The distribution of the decay-time error is also shown.

Table 6.8: Parameters governing the calibration of the decay time resolution as function of the decay-time error, determined on Run 2 data sample of $J/\psi \to \mu^+\mu^-$ and fully simulated sample of $J/\psi \to \mu^+\mu^-$ and $\Upsilon(1S) \to \mu^+\mu^-$ decays.

Parameter	$J/\psi \to \mu^+\mu^-$ MC	$J/\psi \to \mu^+\mu^-$ data
μ [fs]	-0.57 ± 0.07	-3.49 ± 0.07
p_0 [fs]	37.1 ± 0.1	39.9 ± 0.1
p_1	0.907 ± 0.004	0.922 ± 0.004
p_2 [fs $^{-1}$]	$(-1.5 \pm 0.2) \times 10^{-3}$	$(7.0 \pm 0.2) \times 10^{-3}$

Cross-check on the calibration validity

The possibility to apply the decay-time resolution calibration, obtained on $J/\psi \to \mu^+\mu^-$ real candidates on the $H_b \to h^+h'^-$ sample, is verified using fully-simulated events. The calibration is repeated following the same procedure used in the previous subsection on a $B_s^0 \to K^+K^-$ and $J/\psi \to \mu^+\mu^-$ simulated samples. For the $B_s^0 \to K^+K^-$ decays, the τ_{err} distribution is not well described by a single Gaussian function, thus the sum of three Gaussian functions is used instead. All the three Gaussians share the same mean μ, while the widths are different: for the first Gaussian the width, σ_1 is defined as in Equation 6.2, while the second and third widths, σ_2 and σ_3, are defined as the product of σ_1 for a constant (q_1 and q_2). The value of $\hat{\delta}_t$ has been fixed to 0.04 for both the samples. In The $B_s^0 \to K^+K^-$ decays, the overall dilution effect $\mathcal{D}_t$ is defined as:

$$\mathcal{D}_t = \sum_{j=1}^{3} f_j \exp(-\Delta m_s^2 \sigma_j^2/2), \tag{6.3}$$

where f_j are the relative fraction of the three Gaussian functions. The equivalent effective single Gaussian resolution σ_{eff} is computed as:

$$\sigma_{eff} = \frac{\sqrt{-2\log \mathcal{D}_t}}{\Delta m_s}. \tag{6.4}$$

As done for the $J/\psi \to \mu^+\mu^-$ data, the correct description of the decay-time resolution model has been validated splitting the samples in categories of the decay-time error. In Appendix E, the τ_{err} distributions in categories of the decay-time error, with the fit result superimposed, are shown. The results of the fits are reported in Tables 6.8, 6.9 while in Figure 6.16 their functional dependence and δ_t distribution are shown, along with the δ_t distribution.The calibration parameters show similar value between the two decay modes, validating the calibration on the $J/\psi \to \mu^+\mu^-$ data sample. A comparison between the calibration function obtained on the fully simulated samples of $B_s^0 \to K^+K^-$ and $J/\psi \to \mu^+\mu^-$ is shown in Figure 6.17. Significant differences are observed only at high decay-time error however, as proved by the decay-time error distribution, the number of $B_s^0 \to K^+K^-$ events in this region is very low. Nevertheless the difference between the parameters will be taken into account as the systematic uncertainty.

As final cross-check we compared also the calibration obtained on data and fully-simulated samples of $J/\psi \to \mu^+\mu^-$ decays. The trend of the two calibration functions, shown in Figure 6.18, is approximately the same however there calibration performed on data is slightly vertically shifted.

Cross-check using the $\Upsilon(1S) \to \mu^+\mu^-$

A further cross-check is performed using data and simulated sample of $\Upsilon(1S) \to \mu^+\mu^-$ decays. The aim of such study is to verify if there is any discrepancy between the calibration obtained on the

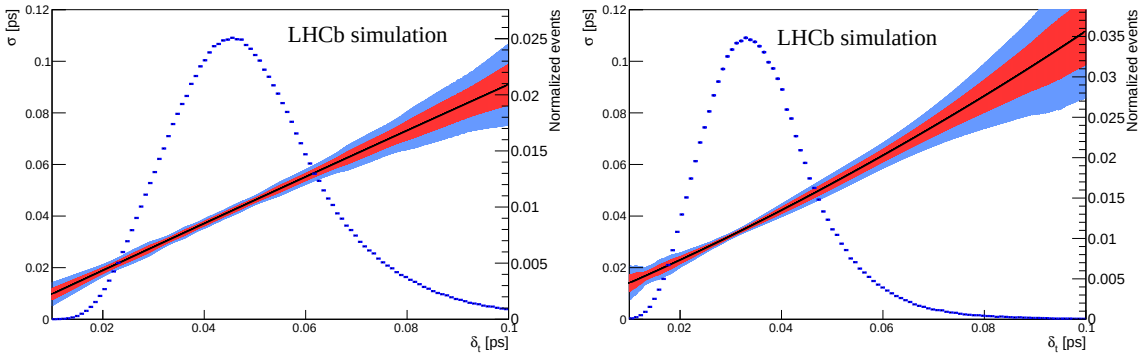

Figure 6.16: Functional dependence of the decay-time resolution on the decay-time error determined on a Run 2 fully-simulated samples of $J/\psi \to \mu^+\mu^-$ and $B_s^0 \to K^+K^-$ decays. The distribution of the decay-time error is also shown.

Table 6.9: Parameters governing the calibration of the decay time resolution as function of the decay-time error, determined on Run 2 fully simulated sample of $B_s^0 \to K^+K^-$ decays.

$B_s^0 \to K^+K^-$ MC			
Parameter	Value	Parameter	Value
μ [fs]	0.368 ± 0.039	q_0	1.69 ± 0.02
p_0 [fs]	38.5 ± 0.1	q_1	5.17 ± 0.11
p_1	0.968 ± 0.004	f_0	0.880 ± 0.006
p_2 [fs $^{-1}$]	$(3.2 \pm 0.2) \times 10^{-3}$	f_1	$(4.4 \pm 0.3) \times 10^{-3}$

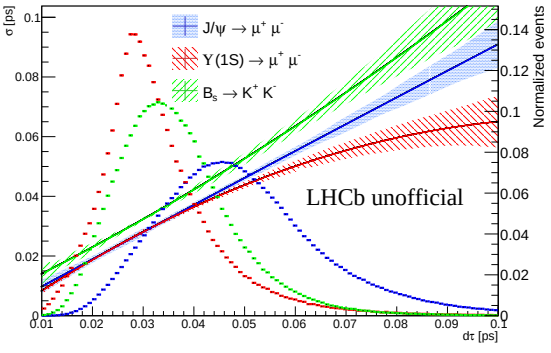

Figure 6.17: Comparison between the functional dependencies of the decay-time resolution on the δ_t determined on Run 2 fully simulated samples of $J/\psi \to \mu^+\mu^-$, $B_s^0 \to K^+K^-$ and $\Upsilon(1S) \to \mu^+\mu^-$ decays.

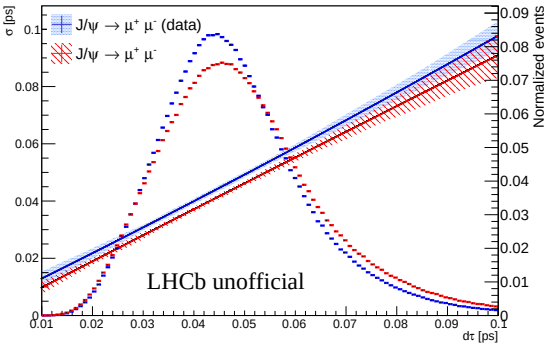

Figure 6.18: Comparison between the functional dependencies of the decay-time resolution on the δ_t determined on Run 2 data and fully simulated samples of $J/\psi \to \mu^+\mu^-$ decays.

J/ψ and on higher mass particle. The calibration of the decay-time resolution is performed following the same strategies described in the previous section. The functional dependence of the decay-time resolution on the decay-time error is shown in Figure 6.19. In the same figure also δ_t distribution is depicted. In Appendix E, the τ_{err} distributions in categories of the decay-time error are shown. The results of the simultaneous fit are reported in Table 6.10. The calibration function obtained on the fully-simulated sample results to be compatible with the ones obtained on both $J/\psi \to \mu^+\mu^-$ and $B_s^0 \to K^+K^-$ samples with significant differences observed only at high decay-time error, as shown in Figure 6.17.

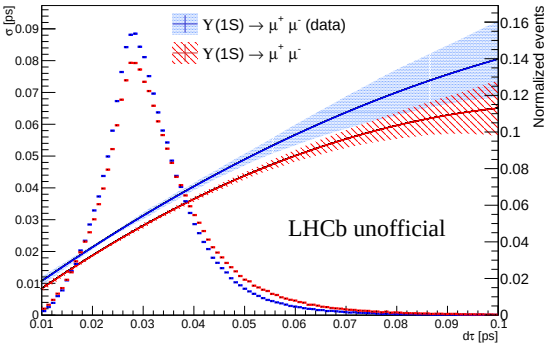

Figure 6.19: Comparison between the functional dependencies of the decay-time resolution on the δ_t determined on Run 2 data and fully simulated samples of $\Upsilon(1S) \to \mu^+\mu^-$ decays.

Statistical power of the decay-time resolution

Differently to the strategy followed in Run 1 analysis, in the final *CP* fit the decay-time resolution is not used on a per-event basis but an integrated value on the whole sample is used instead. The reason of this change lies in the strong correlation that has been found in Run 2. The introduction of this correlation in the decay-time resolution model and in the *CP* fit is very complicate. Thus using

Table 6.10: Parameters governing the calibration of the decay time resolution as function of the decay-time error, determined on Run 2 data and fully simulated sample of $\Upsilon(1S) \to \mu^+\mu^-$ decays.

Parameter	$\Upsilon(1S) \to \mu^+\mu^-$ MC	$\Upsilon(1S) \to \mu^+\mu^-$ data
μ [fs]	-0.308 ± 0.040	-4.16 ± 0.07
p_0 [fs]	36.42 ± 0.05	40.4 ± 0.1
p_1	0.785 ± 0.004	0.884 ± 0.007
p_2 [fs $^{-1}$]	$(-5.1 \pm 0.2) \times 10^{-3}$	$(-3.6 \pm 0.3) \times 10^{-3}$

an unique integrated value for the decay-time resolution would simplify considerably the *CP* fit. However, has mentioned in Section 5.4.1, the observed *CP* asymmetries are diluted by a factor D_{σ_t} depending on the decay-time resolution itself, therefore the impact of this new strategy on the final results has been verified using a fully-simulated sample of $B_s^0 \to K^+K^-$ candidates.

Defining $\mathcal{P}$ the statistical power of a resolution model, the uncertainty on the *CP* observables in the B_s^0 system is inversely proportional to the square root of $\mathcal{P}$ [135]:

$$\sigma_{CP}(B_s^0) \propto \frac{1}{\sqrt{\mathcal{P}}}. \tag{6.5}$$

Considering a model without using a per-event decay-time error and a Gaussian decay-time resolution with width σ_t, the dilution factor can be computed using the formula in Equation 5.18. The corresponding power of the model is evaluated as:

$$\mathcal{P} = D_{\sigma_t}^2 \tag{6.6}$$

In case of a resolution function consisting of multiple Gaussians each with a relative fraction f_j and width $\sigma_{t,j}$ the dilution is calculated as the average of the contribution of each Gaussian function:

$$D_{\sigma_t} = \sum_j f_j \exp\left(\frac{-\Delta m_s^2 \sigma_{t,j}^2}{2}\right), \tag{6.7}$$

and the power of the model is still the square of the average dilution.

Extending the definition of statistical power to Gaussian sum models exploiting a per-event decay-time errors, the per-event dilution $D_{\sigma_t,e}$ and the power $\mathcal{P}_e$, related to the event e, can be obtained from the Equations 6.7, 6.6 replacing the width $\sigma_{t,j}$ with $\sigma_{t,e}s_j$, where $\sigma_{t,e}$ is the estimated decay-time error of the event e and s_j represents a scale parameter related to the j-th Gaussian. Finally the average dilution and power can be computed as:

$$\langle D \rangle = \frac{\sum_e D_{\sigma_t,e}}{N}, \qquad \langle \mathcal{P} \rangle = \frac{\sum_e \mathcal{P}_e}{N}, \tag{6.8}$$

where N represents the total number of events used in the calculation.

As described in Reference [135], three different statement can be made:

- all resolution model, describing the data to the same extent, have the same value of dilution, regardless they use per-event decay-time errors or not;
- all resolution models, describing the data to the same extent, without using per-event decay-time errors have the same statistical power;
- resolution models based on a per-event decay-time error have no smaller statistical power than models without per-event decay-time errors.

The latest point is a direct consequence of the fact that the mean square value of a variable is larger than or equal to the square of the mean value by definition. In particular the equality occurs only when the variable has zero variance.

In order to evaluate the effect of using an integrated value in place of a per-event decay-time resolution the statistical power related to the two models has been compared. Firstly the per-event statistical power $\mathcal{P}_e$ has been calculated on a fully-simulated sample of $B_s^0 \to K^+K^-$ candidates, where the per-event decay-time error has been calibrated using the result of the fit reported in Section 6.3.1. Then the sample has been split according to different binning schemes of the decay-time error and for each scheme the corresponding average dilution and statistical power have been evaluated using Equation 6.8, where the sum is performed on the bins instead of the events. Also in this case the decay-time error information has been calibrated using the fit result reported in Section 6.3.1. The binning schemes taken into account consist of 2, 4, 10, 20 and 40 bins of the same size, in addition also the case with a unique bin, comprising all the events available in the sample, has been considered. The corresponding statistical powers are shown in Figure 6.20. The power related to the model using a per-event decay-time resolution is 0.621 while the power of the model with a unique bin, corresponding to using an integrated decay-time resolution value, is 0.608. The difference on the uncertainty of the *CP* observable $\sigma_{CP}(B_s^0)$ is about a relative 1%.

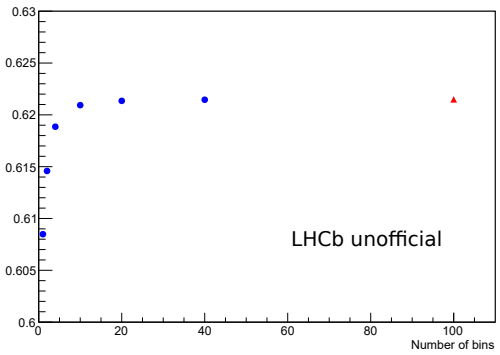

Figure 6.20: Distribution of the statistical power corresponding to the different binning schemes described in the text (blue points) and with a per-event decay-time error resolution (red point).

Table 6.11: Final values of the decay-time resolution for the $B_s^0 \to K^+K^-$ decay modes. The values have been determined using the calibration functions obtained in the J/ψ and $Upsilon(1S)$ decay mode as described in the text.

	Calibration modes	
	$J/\psi \to \mu^+\mu^-$ [fs]	$\Upsilon(1S) \to \mu^+\mu^-$ [fs]
$\sigma_{B_s^0 \to K^+K^-}$(data)	42.9 ± 0.1	44.1 ± 0.1

Final decay-time resolution values

As proved in the previous section, moving from a per-event decay time resolution to a unique average value valid for the whole sample, does not modify the power of the model significantly. The average decay-time resolution for the B_s^0 decays is determined using the calibration function obtained from the data sample of $J/\psi \to \mu^+\mu^-$ candidates. However, in order to take into account the difference between this decay mode and the $B_s^0 \to K^+K^-$, a scale factor equal to the ratio between the calibrations of fully simulated $B_s^0 \to K^+K^-$ and $J/\psi \to \mu^+\mu^-$ samples, is applied. Thus the final value of the decay-time resolution is evaluated in two steps: firstly the per-event dilution factor is computed for each $B_s^0 \to K^+K^-$ simulated event, as explained in the previous subsection, where the corresponding $\sigma_{t,e}$ is calculated as:

$$\sigma_{t,e} = \sigma_{J/\psi \to \mu^+\mu^-}(\text{data}) \cdot \frac{\sigma_{B_s^0 \to K^+K^-}(\text{MC})}{\sigma_{J/\psi \to \mu^+\mu^-}(\text{MC})} \tag{6.9}$$

where the σ values are obtained using the calibration parameters reported in Tables 6.8, 6.9 and evaluating the three functions to the decay-time error of the event of interest. In the second step the average dilution is evaluated and the final value of the decay-time resolution is computed by means of Equation 6.4. The final value obtained for the decay-time resolution of the $B_s^0 \to K^+K^-$ data sample is reported in Table 6.11. As a cross-check, the $B_s^0 \to K^+K^-$ decay time resolution has been evaluated also using the calibration functions obtained for both the $\Upsilon(1S) \to \mu^+\mu^-$ data and fully-simulated sample. The result, reported in Table 6.11, is similar to the one obtained using the J/ψ mode and the difference will be taken into account as systematic uncertainties.

6.4 Fit results

The final unbinned maximum fit to the data sample is performed joining all the ingredients described in the previous sections. The parameters fixed in the fit are the same as in Run 1 analysis:

- the parameters governing the tails of the signal invariant mass models which values are reported in Table 6.7;

- the endpoints of the ARGUS functions describing the invariant mass distributions of the partially reconstructed 3-body background components are fixed to the difference between the B meson and pion masses: 5.1446 GeV/c^2 for the B^0 and 5.2318 GeV/c^2 for the B_s^0 meson.
- the PID efficiencies related to the yields of the correctly identified and misidentified $H_b \to h^+h'^-$ decays contributing to the different invariant mass hypotheses;
- the integrated decay-time resolution is fixed to the value obtained by means if the $J/\psi \to \mu^+\mu^-$ data and fully-simulated samples, which is reported in Table 6.11;
- the shapes of the signal decay-time acceptances are fixed using the templates taken from the histograms, as described in Section 5.4.2;
- the calibration parameters of the various OS taggers, combined in a global OS algorithm, are fixed to the values reported in Table 4.11.
- the values of the mixing oscillation frequencies, the differences of the decay widths for B^0 and B_s^0 mesons and the decay width of the B_s^0 mesons are fixed to the HFLAV averages [71] summarized in Table 5.12.

The decay width of the B^0 meson is left free to vary in the fit, since it provides a validity cross-check of strategy used to determine the signal decay-time acceptances. The *CP*-violating parameters have been extracted using the optimised selection of $\pi^+\pi^-$ and the K^+K^- final states, described in Section 6.1.2. The fit has been performed using only the new OS taggers optimized on the Run 2. The SS*comb* and SS*K* taggers have not been included yet in the fit because of significant correlations, found between the mistag probability and the decay-time, which require a more deep and specific study in order to properly take them under control. The values of the OS calibration parameters have been determined separately for 2015 and 2016 data sample and are reported in Table 6.12. The *CP*-violating parameters related to the time-dependent asymmetries are in common for the 2015 and 2016 data sample while the time-integrated raw asymmetries have been calculated separately for 2015 and 2016 in order to take into account the possible differences in the final state and PID asymmetries, needed to extract the true *CP* asymmetries, between the two data taking periods. The values of the *CP* parameters are:

$$\begin{aligned} C_{\pi^+\pi^-} &= -0.38 \pm 0.06 \\ S_{\pi^+\pi^-} &= -0.68 \pm 0.05 \\ C_{K^+K^-} &= 0.12 \pm 0.05 \\ S_{K^+K^-} &= 0.19 \pm 0.05 \\ A^{\Delta\Gamma}_{K^+K^-} &= -0.79 \pm 0.07 \end{aligned} \tag{6.10}$$

Table 6.12: Calibration parameters of the flavour tagging obtained from the fit, using the $\pi^+\pi^-$ optimisation, for the 2015 and 2016 sample separately. The value of $\hat{\eta}_{OS}$ is fixed to 0.37 in both the cases.

Parameter	2015	2016
$\hat{\varepsilon}^{sig}_{OS}$	0.364 ± 0.004	0.369 ± 0.002
$\Delta\varepsilon^{sig}_{OS}$	-0.027 ± 0.015	-0.011 ± 0.006
$\hat{p}^{OS}_0$	0.397 ± 0.009	0.392 ± 0.004
Δp^{OS}_0	0.007 ± 0.013	0.009 ± 0.006
$\hat{p}^{OS}_1$	0.961 ± 0.083	0.918 ± 0.036
Δp^{OS}_1	0.138 ± 0.051	0.013 ± 0.022
$\hat{\eta}_{OS}$	0.37	0.37

and the values of the raw asymmetries are:

$$\begin{aligned} A_{raw}(B^0 \to K^+\pi^-)(2015) &= (-9.0 \pm 0.9)\% \\ A_{raw}(B^0 \to K^+\pi^-)(2016) &= (-9.2 \pm 0.4)\% \\ A_{raw}(B^0_s \to \pi^+K^-)(2015) &= (28.2 \pm 3.6)\% \\ A_{raw}(B^0_s \to \pi^+K^-)(2016) &= (24.6 \pm 1.6)\% \end{aligned} \tag{6.11}$$

where the parameters related to the $\pi^+\pi^-$ and $K^+\pi^-$ final states have been obtained from the fit performed using the $\pi^+\pi^-$ optimisation, while the *CP*-violating parameters corresponding to the $B^0_s \to K^+K^-$ decays have been determined from the fit performed using the K^+K^- optimisation. In Table 6.13 the statistical correlations among the various *CP* violating parameters, obtained using the $\pi^+\pi^-$ optimisation, are reported.

Table 6.13: Statistical correlations among the *CP* violation parameters are determined from the fit, performed using the $\pi^+\pi^-$ optimisation. Correlation factors lower than 10^{-4} are considered as negligible.

	$A_{raw}(B^0 \to K^+\pi^-)(2015)$	$A_{raw}(B^0 \to K^+\pi^-)(2016)$	$A_{raw}(B^0_s \to \pi^+K^-)(2015)$	$A_{raw}(B^0_s \to \pi^+K^-)(2016)$	$C_{\pi^+\pi^-}$	$S_{\pi^+\pi^-}$	$C_{K^+K^-}$	$S_{K^+K^-}$	$A^{\Delta\Gamma}_{K^+K^-}$
$A_{raw}(B^0 \to K^+\pi^-)(2015)$	1	0.0002	0.0289	-0.0001	-0.0028	0.0047	0.0026	-0.0035	0.0005
$A_{raw}(B^0 \to K^+\pi^-)(2016)$		1	negligible	0.0397	-0.0060	0.0209	0.0016	-0.0054	0.0013
$A_{raw}(B^0_s \to \pi^+K^-)(2015)$			1	0.0003	0.0001	negligible	0.0008	-0.0008	0.0003
$A_{raw}(B^0_s \to \pi^+K^-)(2016)$				1	0.0018	0.0013	0.0009	negligible	0.0003
$C_{\pi^+\pi^-}$					1	0.3860	-0.0060	-0.0151	-0.0005
$S_{\pi^+\pi^-}$						1	-0.0290	-0.0017	-0.0015
$C_{K^+K^-}$							1	-0.0255	0.0195
$S_{K^+K^-}$								1	0.0020
$A^{\Delta\Gamma}_{K^+K^-}$									1

The raw time dependent asymmetries of the $K^\pm\pi^\mp$ spectrum related to the B candidates lying under the signal region, defined requiring an invariant mass ($m_{K^\pm\pi^\mp}$) in range $[5.20, 5.32]\,\text{GeV}/c^2$, are shown in Figure 6.21. The raw time dependent asymmetries for the $\pi^+\pi^-$ and K^+K^- final states, observed in signal invariant mass regions corresponding to $5.20\,\text{GeV}/c^2 < m_{\pi^+\pi^-} < 5.35\,\text{GeV}/c^2$ and $5.30\,\text{GeV}/c^2 < m_{K^+K^-} < 5.44\,\text{GeV}/c^2$ respectively, are shown in Figure 6.22. The distributions

of all the observables used in the fit for all the three final states are reported in Figures 6.23, 6.24 and 6.25. The color scheme is reported in the legend in Figure 6.26. The production asymmetries are also estimated during the fit in order to reduce the systematic uncertainties on the *CP* asymmetries in the $K^+\pi^-$ mass hypothesis. Their values for the B^0 and B_s^0 mesons in the 2015 and 2016 data separately are found to be $A_P(B^0)(2015) = (-0.8 \pm 1.3)\%$, $A_P(B^0)(2016) = 0.04 \pm 0.55)\%$, $A_P(B_s^0)(2015) = (2.0 \pm 4.7)\%$ and $A_P(B_s^0)(2016) = 0.7 \pm 2.1)\%$, respectively.

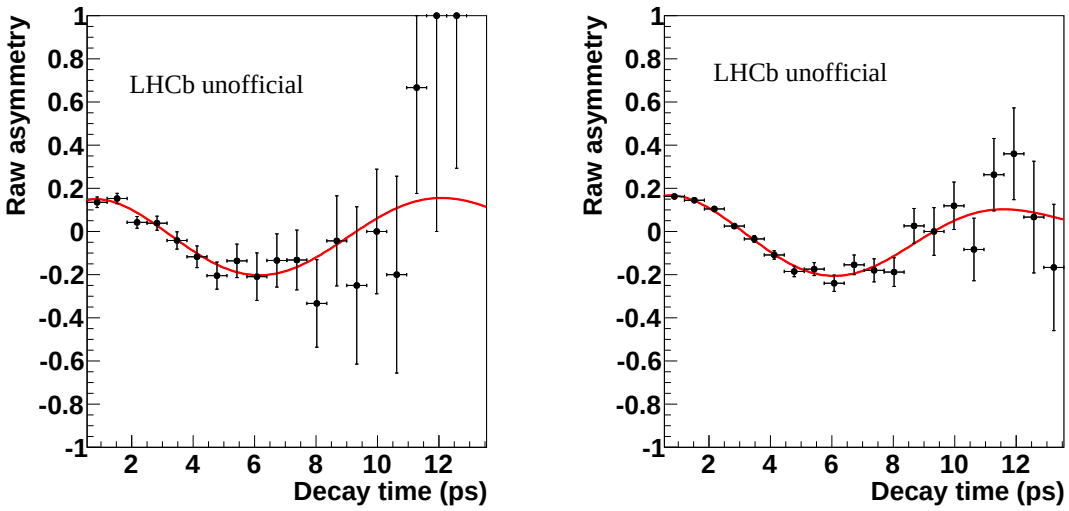

Figure 6.21: Raw time-dependent asymmetry for the $K^\pm\pi^\mp$ final state from the invariant mass region corresponding to $5.20\,\text{GeV}/c^2 < m < 5.32\,\text{GeV}/c^2$ dominated by the $B^0 \to K^+\pi^-$ decay. The asymmetry has been observed in the 2015 (left) and 2016 (right) data sample separately using only the OS tagger.

In order to verify the correct description of all the fit observable for every signal and background component the fit results have been projected in three different invariant mass region: a "3-body background" region in range [5.0, 5.2] GeV, a signal region between 5.2 GeV and 5.45 GeV, and a "combinatorial background" region in range [5.45, 5.8] GeV. The plots corresponding to these three regions for each final state are reported in Figures 6.27- 6.35. For the $K^\pm\pi^\mp$ final state the fit result have been project in the invariant mass spectrum distinguishing the $K^+\pi^-$ and π^+K^- final hypothesis, the corresponding plots are reported in Figure 6.36. The different height of the signal mass peak in the two mass hypothesis is a proportional to the *CP* violation in the $B^0 \to K^+\pi^-$ and $B_s^0 \to \pi^+K^-$ decays.

6.4.1 Corrections to $A_{CP}(B^0 \to K^+\pi^-)$ and $A_{CP}(B_s^0 \to \pi^+K^-)$

As mentioned in Section 5.4.3, in order to determine the *CP* asymmetries, $A_{CP}(B^0 \to K^+\pi^-)$ and $A_{CP}(B_s^0 \to \pi^+K^-)$, the raw asymmetries measured in the $B^0 \to K^+\pi^-$ and $B_s^0 \to \pi^+K^-$ channels

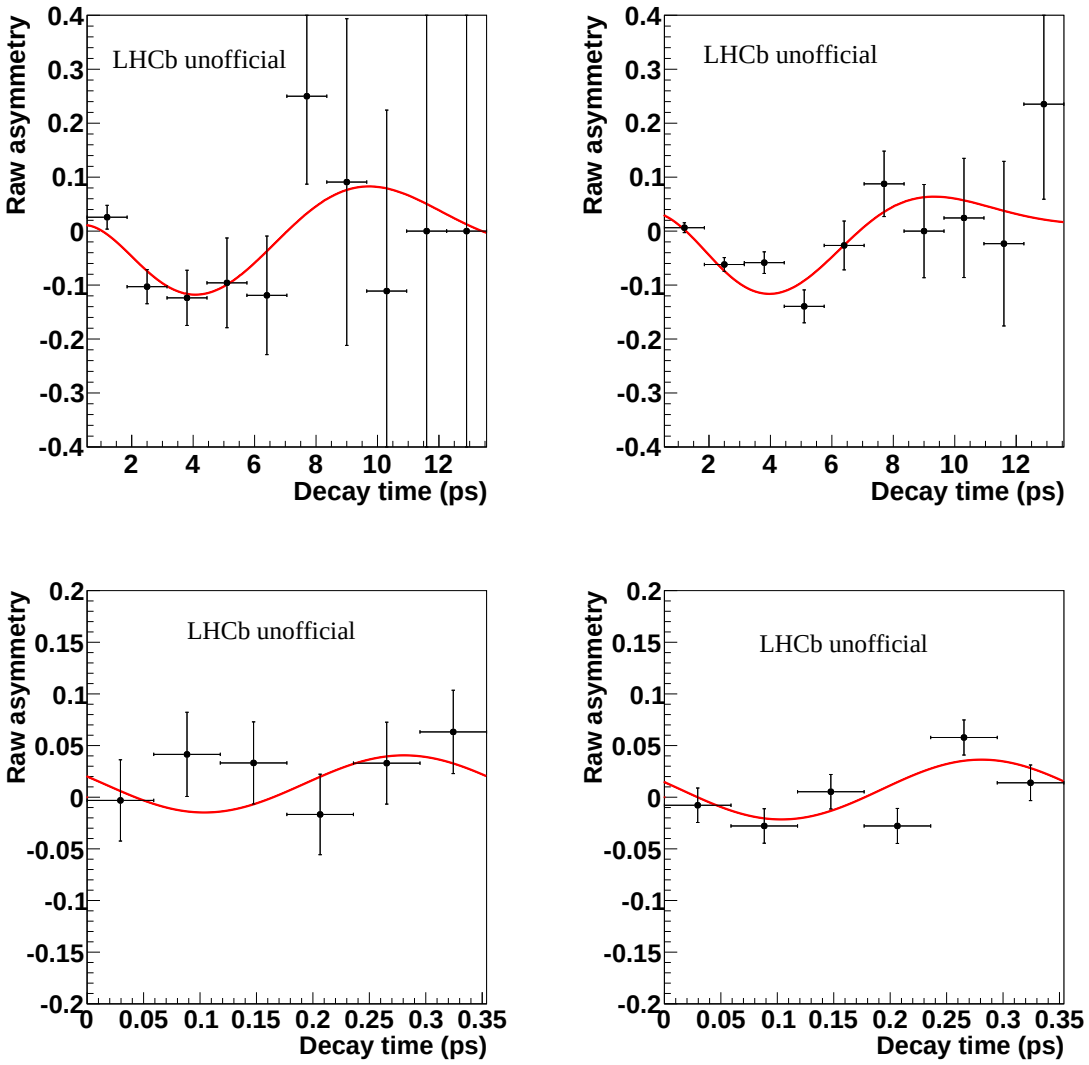

Figure 6.22: Raw time-dependent asymmetry, obtained using only the OS tagging information, for the $\pi^+\pi^-$ (top) and K^+K^- (bottom) final states from the invariant mass regions corresponding to $5.20\,\text{GeV}/c^2 < m < 5.35\,\text{GeV}/c^2$ and $5.30\,\text{GeV}/c^2 < m < 5.44\,\text{GeV}/c^2$, respectively. Both the projection of the asymmetries on the 2015 data (left) and on the 2016 data (right) are depicted.

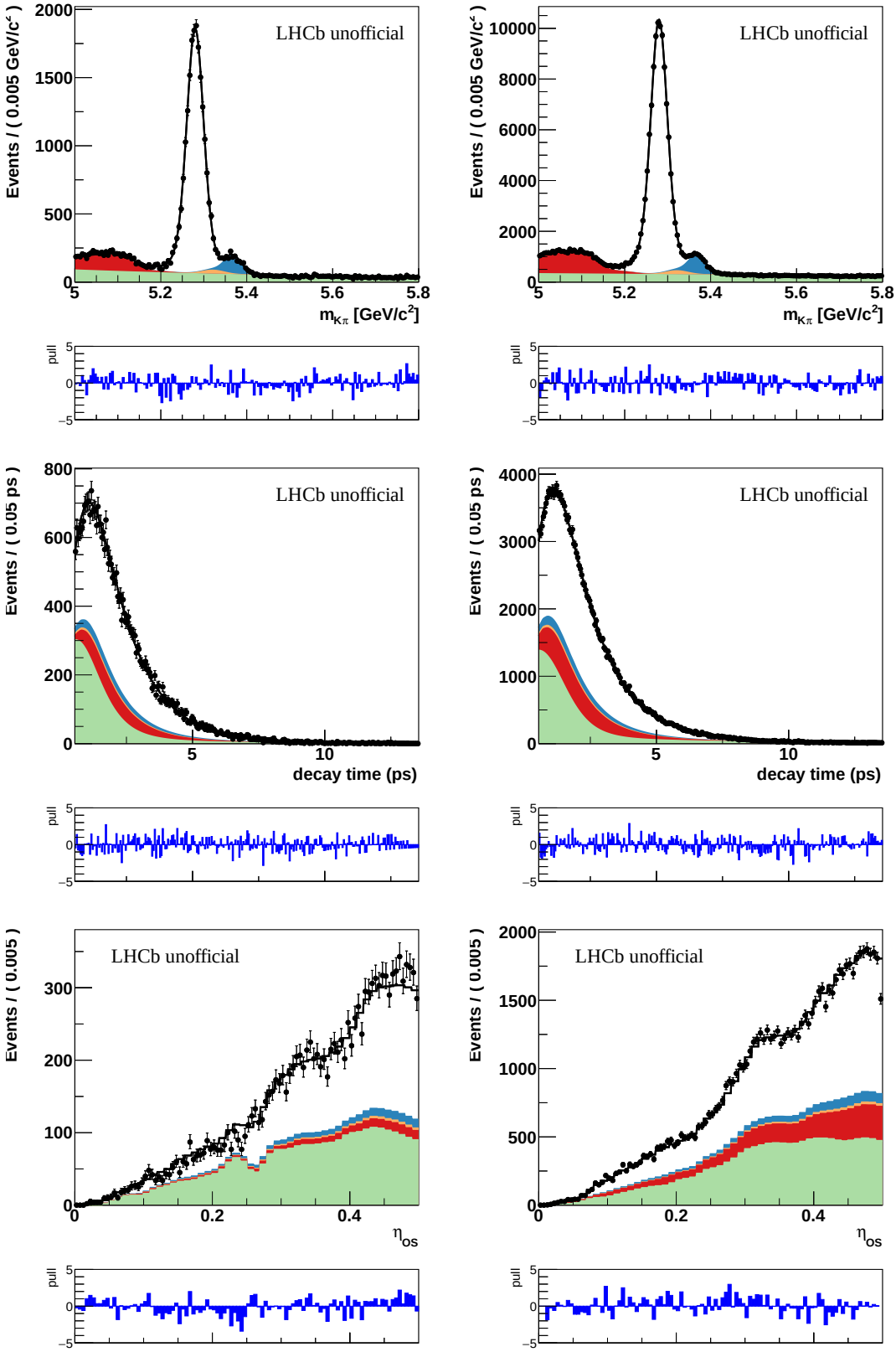

Figure 6.23: Distributions of the fit observables (invariant mass, decay-time and OS mistag) in the $K^{\pm}\pi^{\mp}$ final state for both 2015 (left) and 2016 (right) data sample. The result of the simultaneous fit is superimposed to data points.

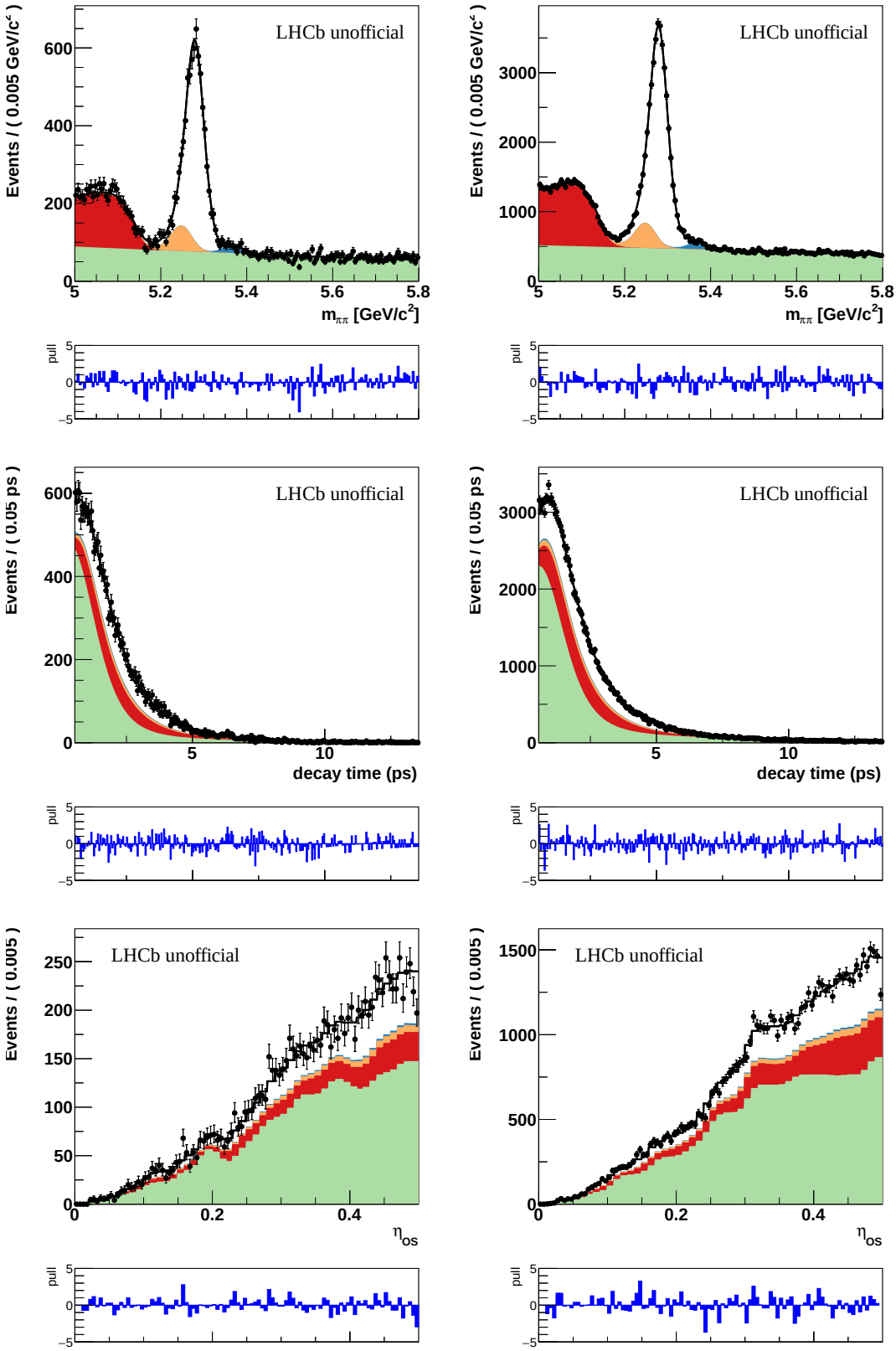

Figure 6.24: Distributions of the fit observables (invariant mass, decay-time and OS mistag) in the $\pi^+\pi^-$ final state for both 2015 (left) and 2016 (right) data samples. The result of the simultaneous fit is superimposed to data points.

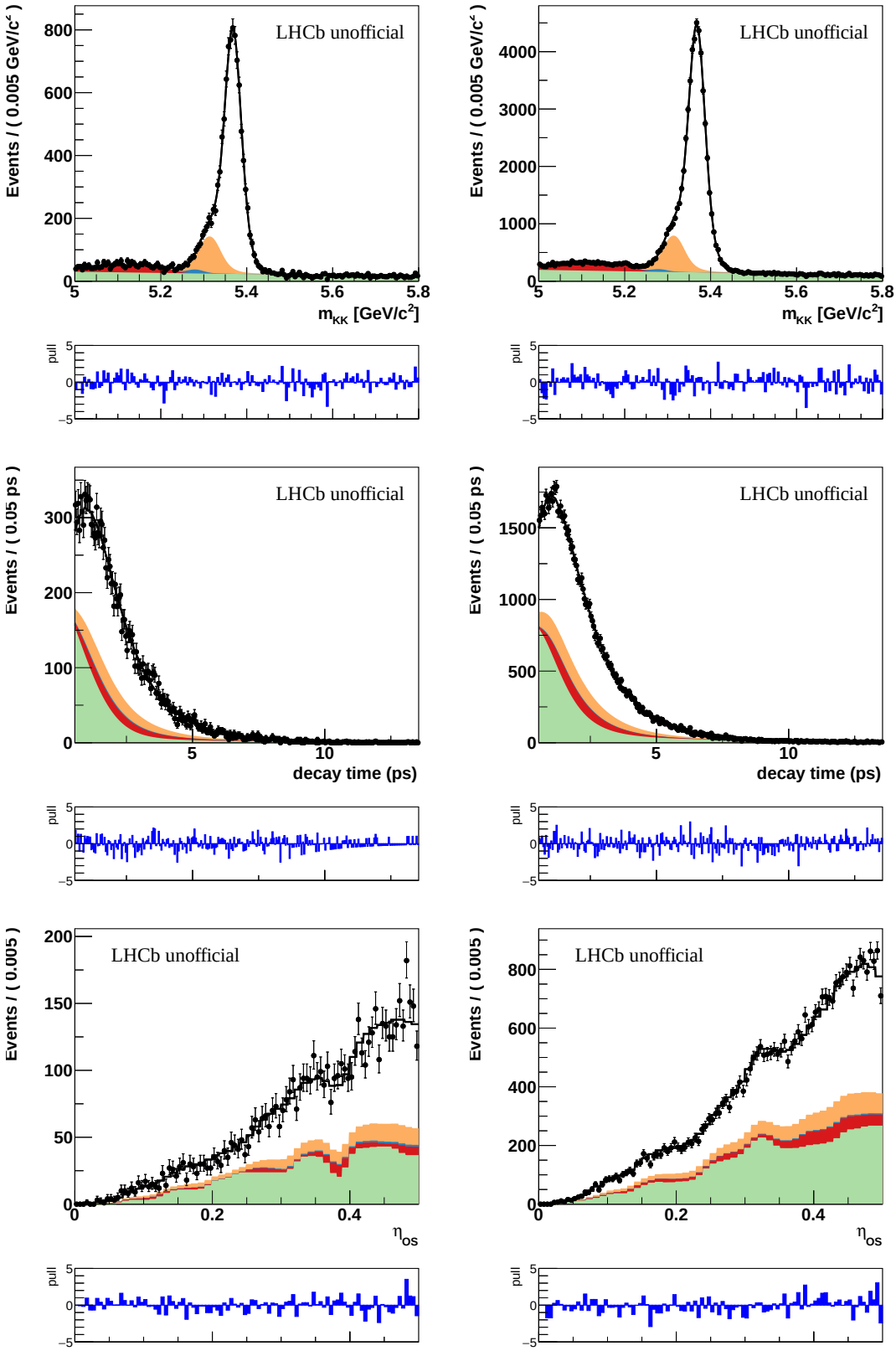

Figure 6.25: Distributions of the fit observables (invariant mass, decay-time and OS mistag) in the K^+K^- final state for both 2015 (left) and 2016 (right) data samples. The result of the simultaneous fit is superimposed to data points.

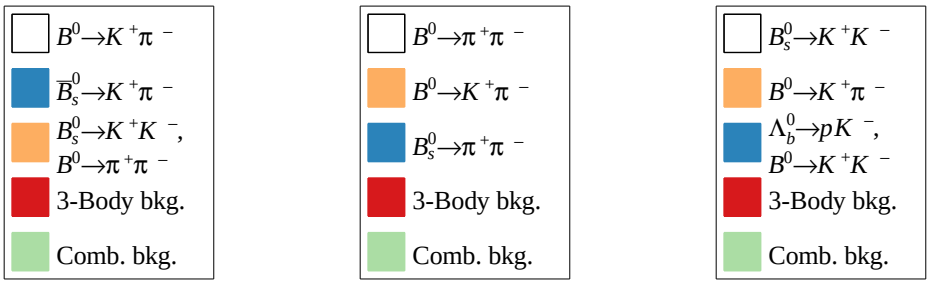

Figure 6.26: Colour legends related to to the distribution of the fit observables for all the three final state: $K^\pm\pi^\mp$, $\pi^+\pi^-$ and K^+K^-.

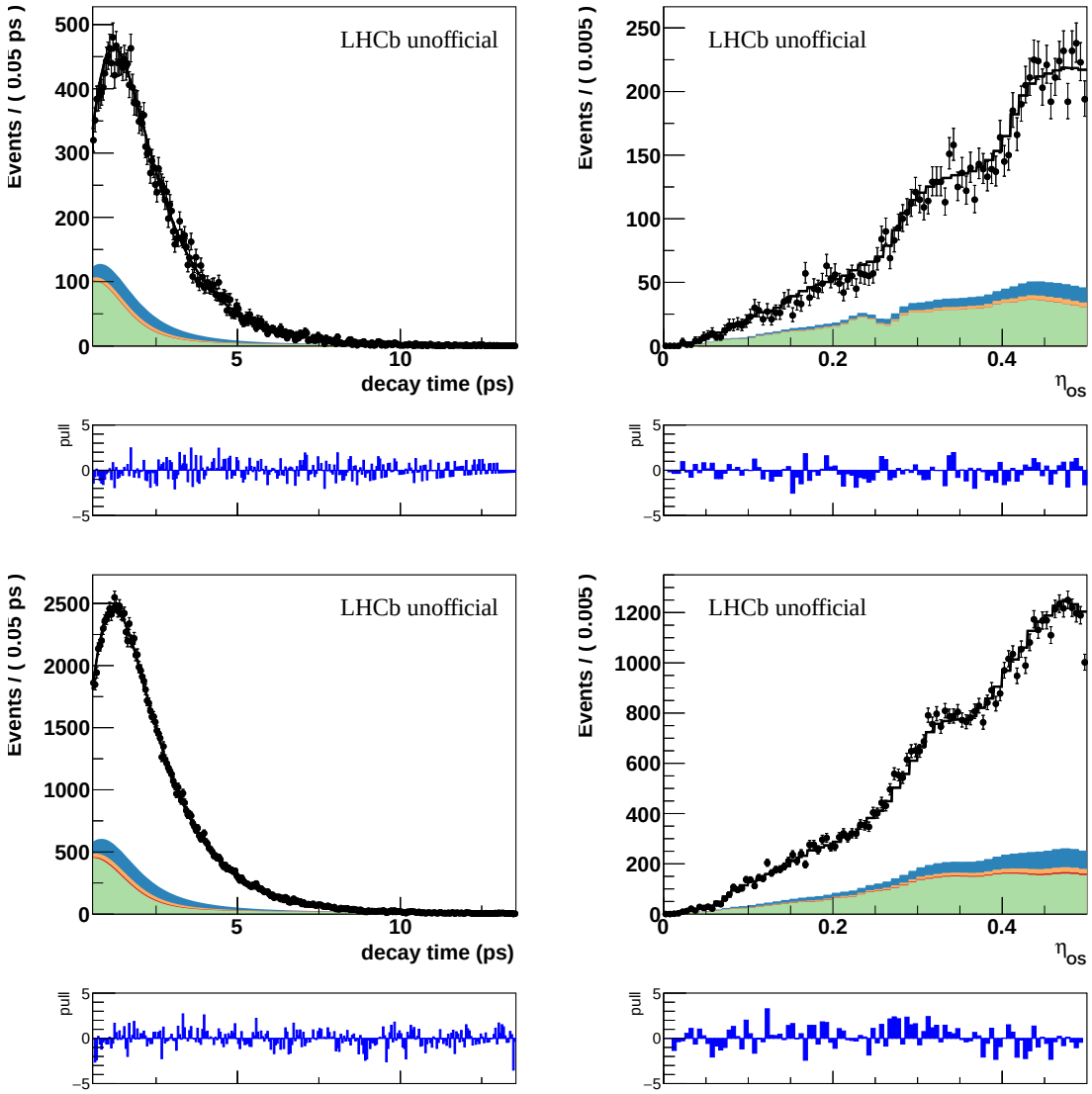

Figure 6.27: Distributions of the fit observables (invariant mass, decay-time and OS mistag) in the $K^\pm\pi^\mp$ final state corresponding to the signal region, [5.2, 5.45] GeV/c^2, for 2015 (top) and 2016 (bottom). The result of the simultaneous fit is superimposed to data points.

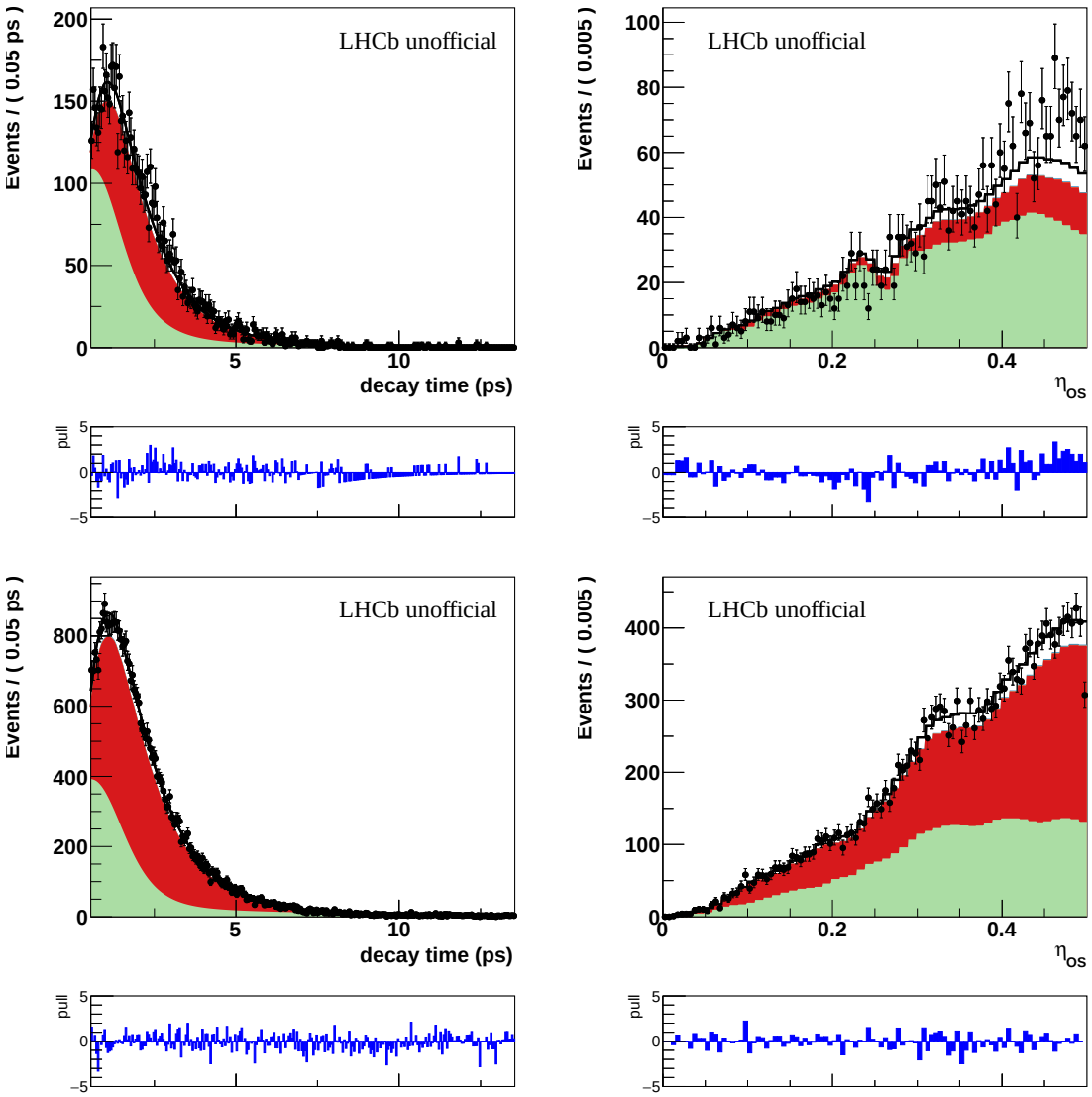

Figure 6.28: Distributions of the fit observables (invariant mass, decay-time and OS mistag) in the $K^{\pm}\pi^{\mp}$ final state corresponding to the "3-body background" region, [5.0, 5.2] GeV/c^2, for 2015 (top) and 2016 (bottom). The result of the simultaneous fit is superimposed to data points.

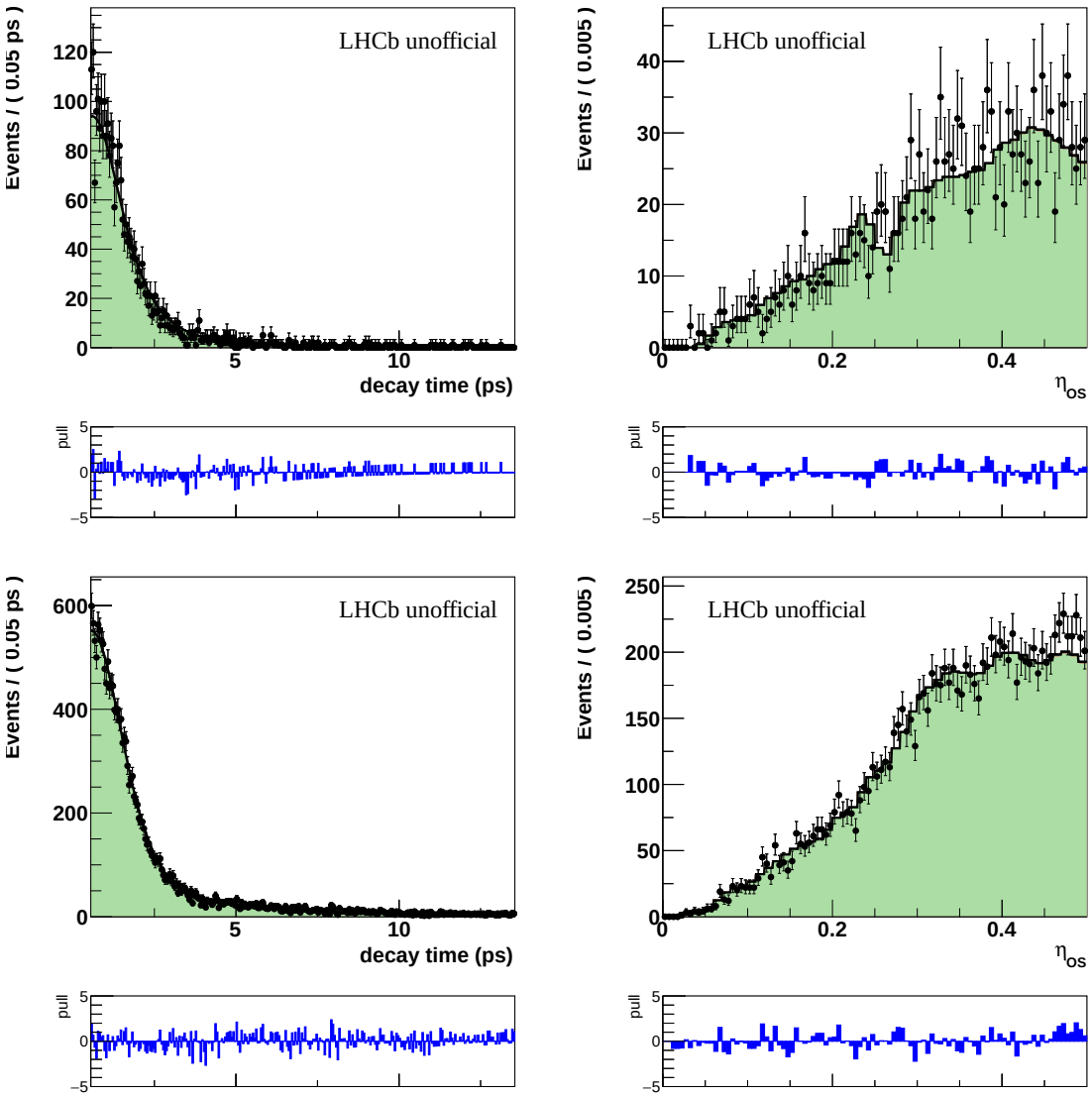

Figure 6.29: Distributions of the fit observables (invariant mass, decay-time and OS mistag) in the $K^{\pm}\pi^{\mp}$ final state corresponding to the "combinatorial background" region, [5.45, 5.8] GeV/c^2, for 2015 (top) and 2016 (bottom). The result of the simultaneous fit is superimposed to data points.

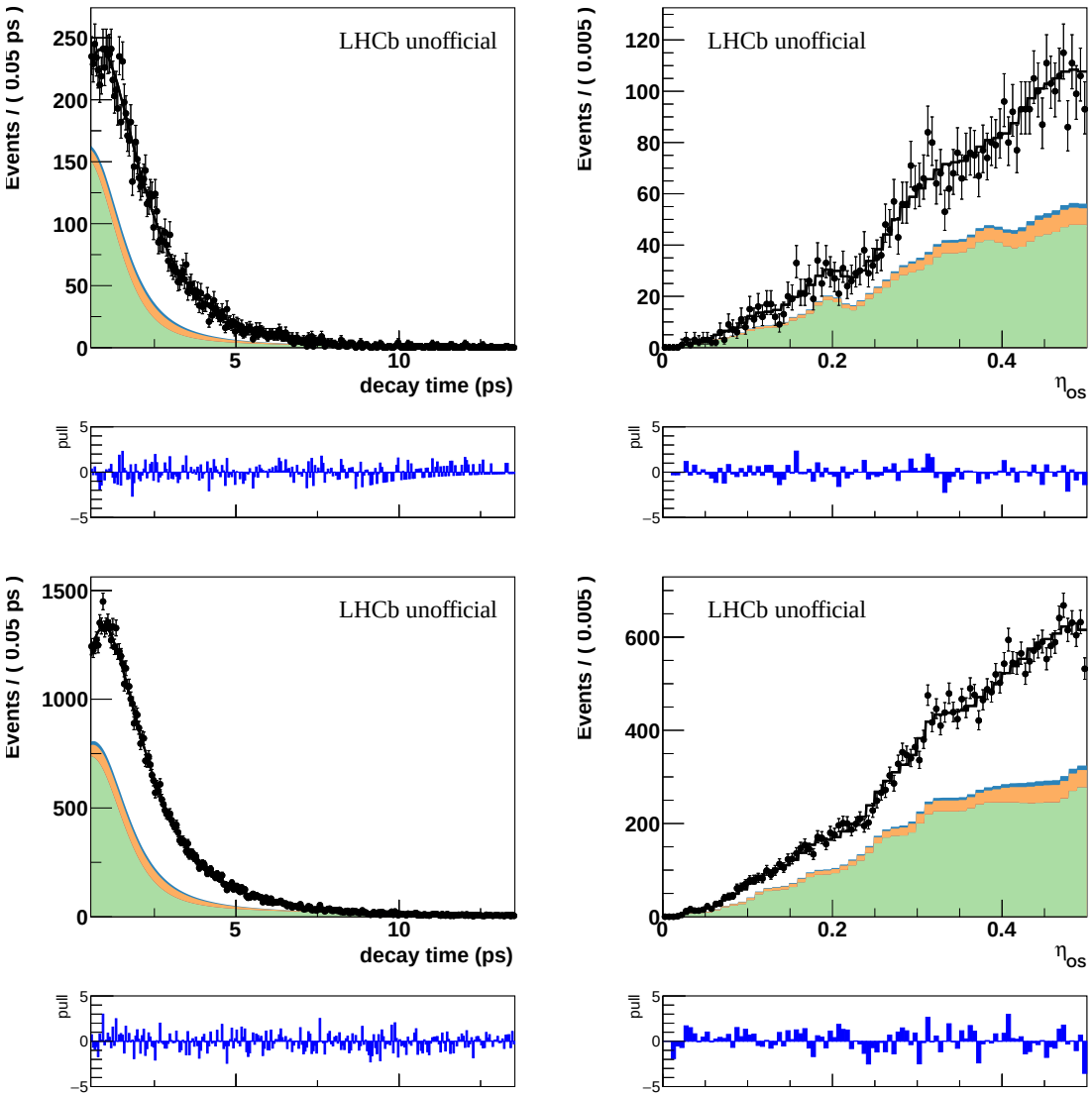

Figure 6.30: Distributions of the fit observables (invariant mass, decay-time and OS mistag) in the $\pi^\pm\pi^\mp$ final state corresponding to the signal region, [5.2, 5.45] GeV/c^2, for 2015 (top) and 2016 (bottom). The result of the simultaneous fit is superimposed to data points.

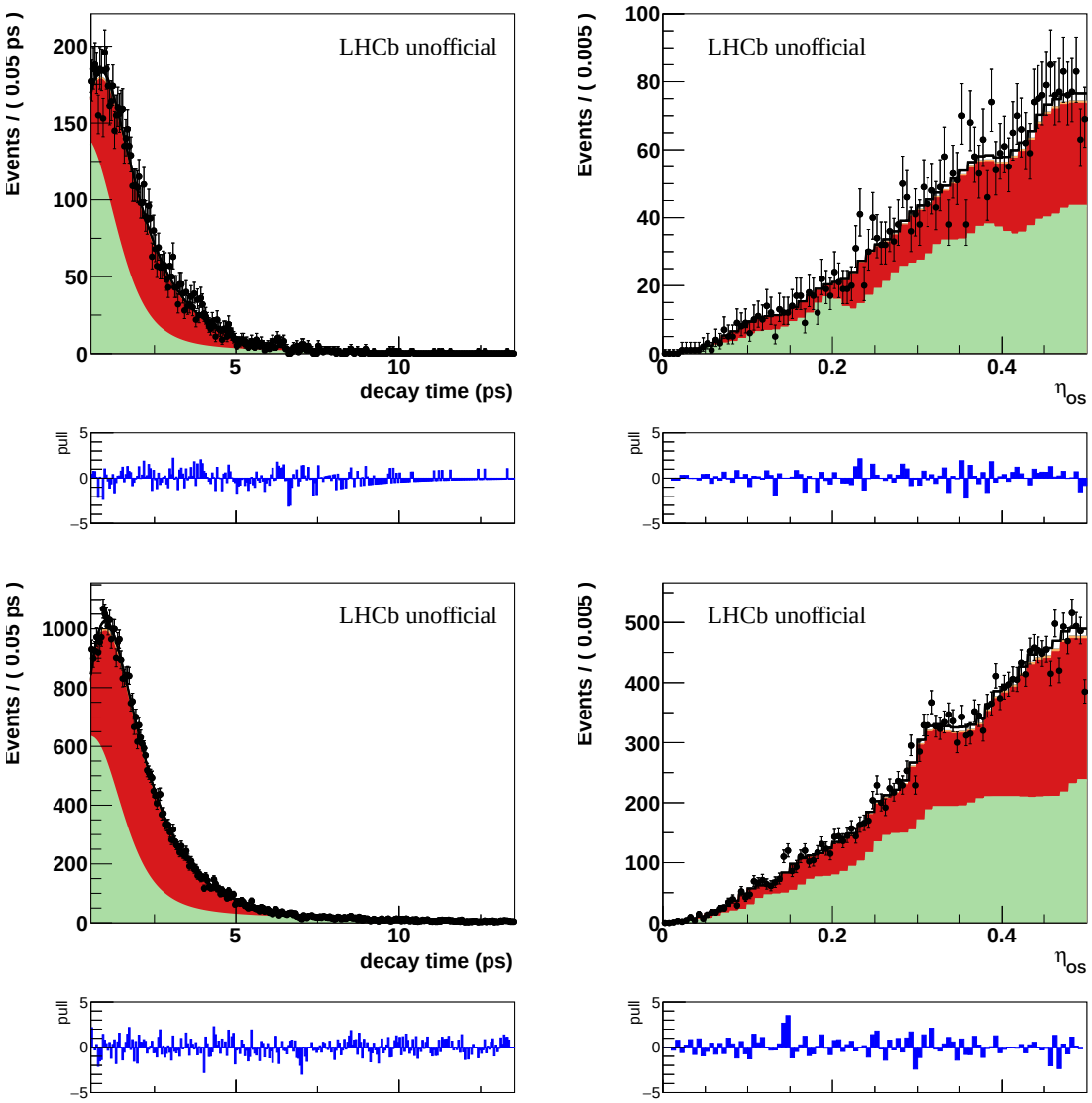

Figure 6.31: Distributions of the fit observables (invariant mass, decay-time and OS mistag) in the $\pi^{\pm}\pi^{\mp}$ final state corresponding to the "3-body background" region, [5.0, 5.2] GeV/c^2, for 2015 (top) and 2016 (bottom). The result of the simultaneous fit is superimposed to data points.

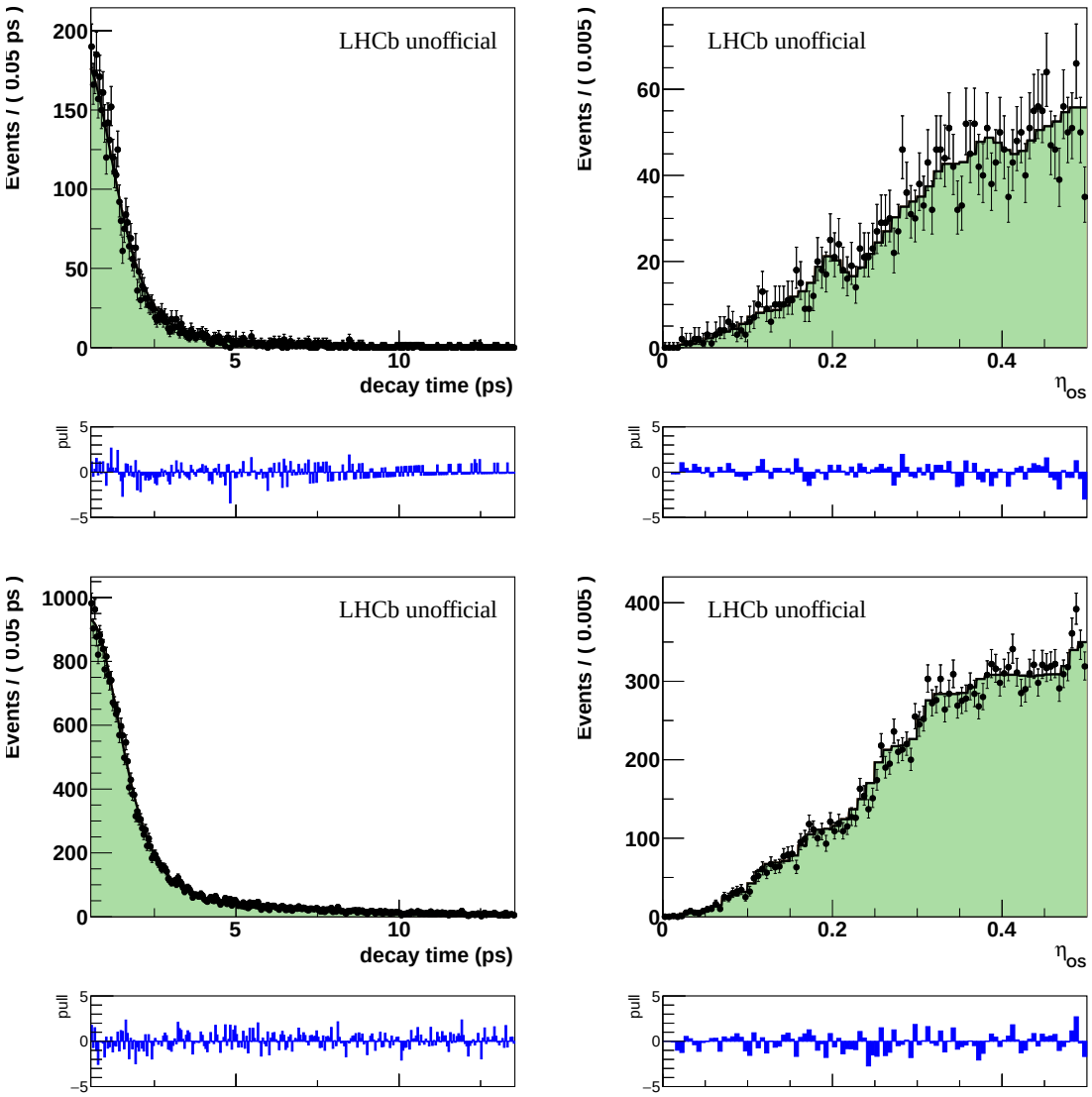

Figure 6.32: Distributions of the fit observables (invariant mass, decay-time and OS mistag) in the $\pi^{\pm}\pi^{\mp}$ final state corresponding to the "combinatorial background" region, [5.45, 5.8] GeV/c^2, for 2015 (top) and 2016 (bottom). The result of the simultaneous fit is superimposed to data points.

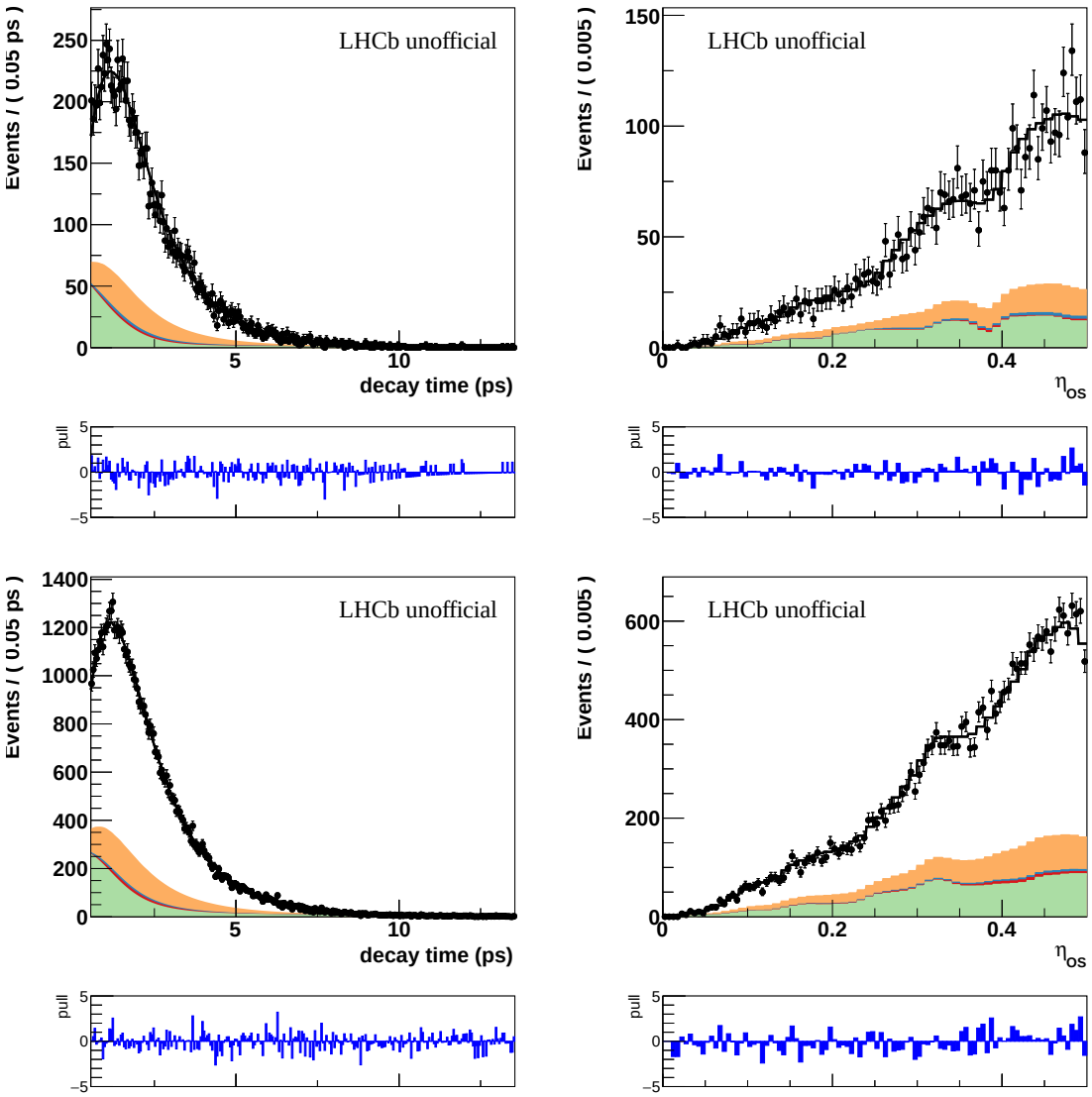

Figure 6.33: Distributions of the fit observables (invariant mass, decay-time and OS mistag) in the $K^{\pm}K^{\mp}$ final state corresponding to the signal region, [5.2, 5.45] GeV/c^2, for 2015 (top) and 2016 (bottom). The result of the simultaneous fit is superimposed to data points.

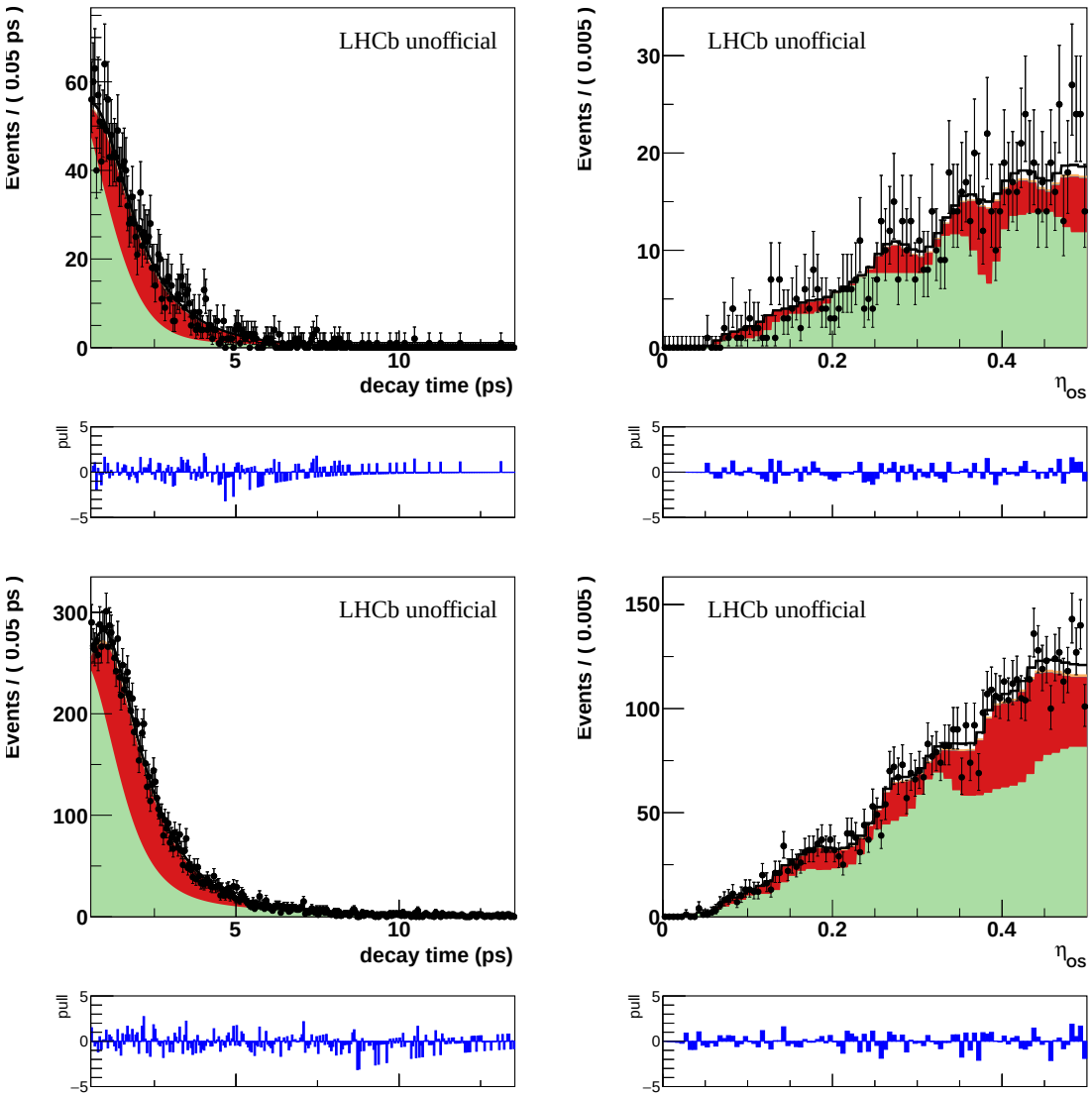

Figure 6.34: Distributions of the fit observables (invariant mass, decay-time and OS mistag) in the $K^{\pm}K^{\mp}$ final state corresponding to the "3-body background" region, [5.0, 5.2] GeV/c^2, for 2015 (top) and 2016 (bottom). The result of the simultaneous fit is superimposed to data points.

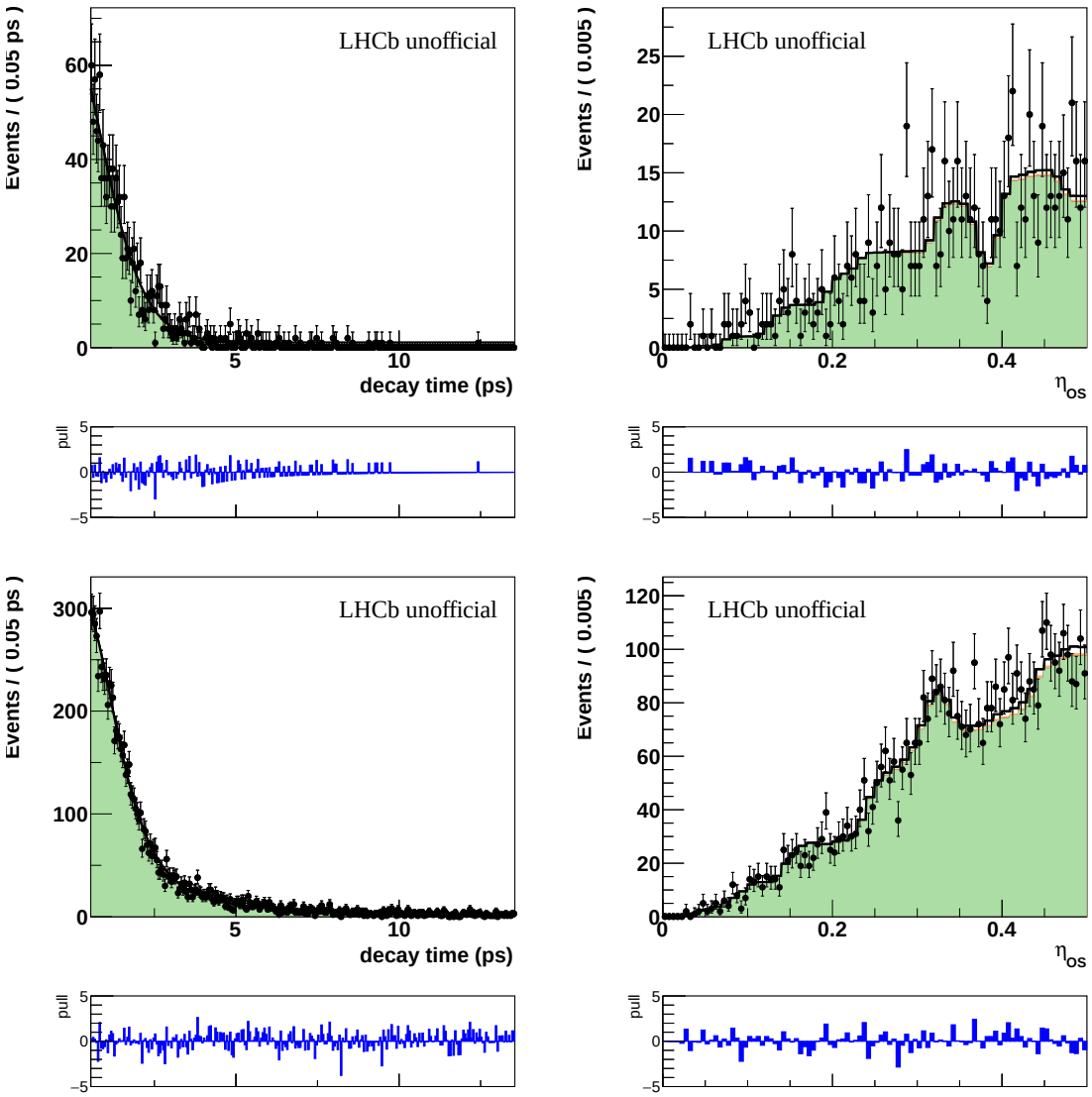

Figure 6.35: Distributions of the fit observables (invariant mass, decay-time and OS mistag) in the $K^{\pm}K^{\mp}$ final state corresponding to the "combinatorial background" region, [5.45, 5.8] GeV/c^2, for 2015 (top) and 2016 (bottom). The result of the simultaneous fit is superimposed to data points.

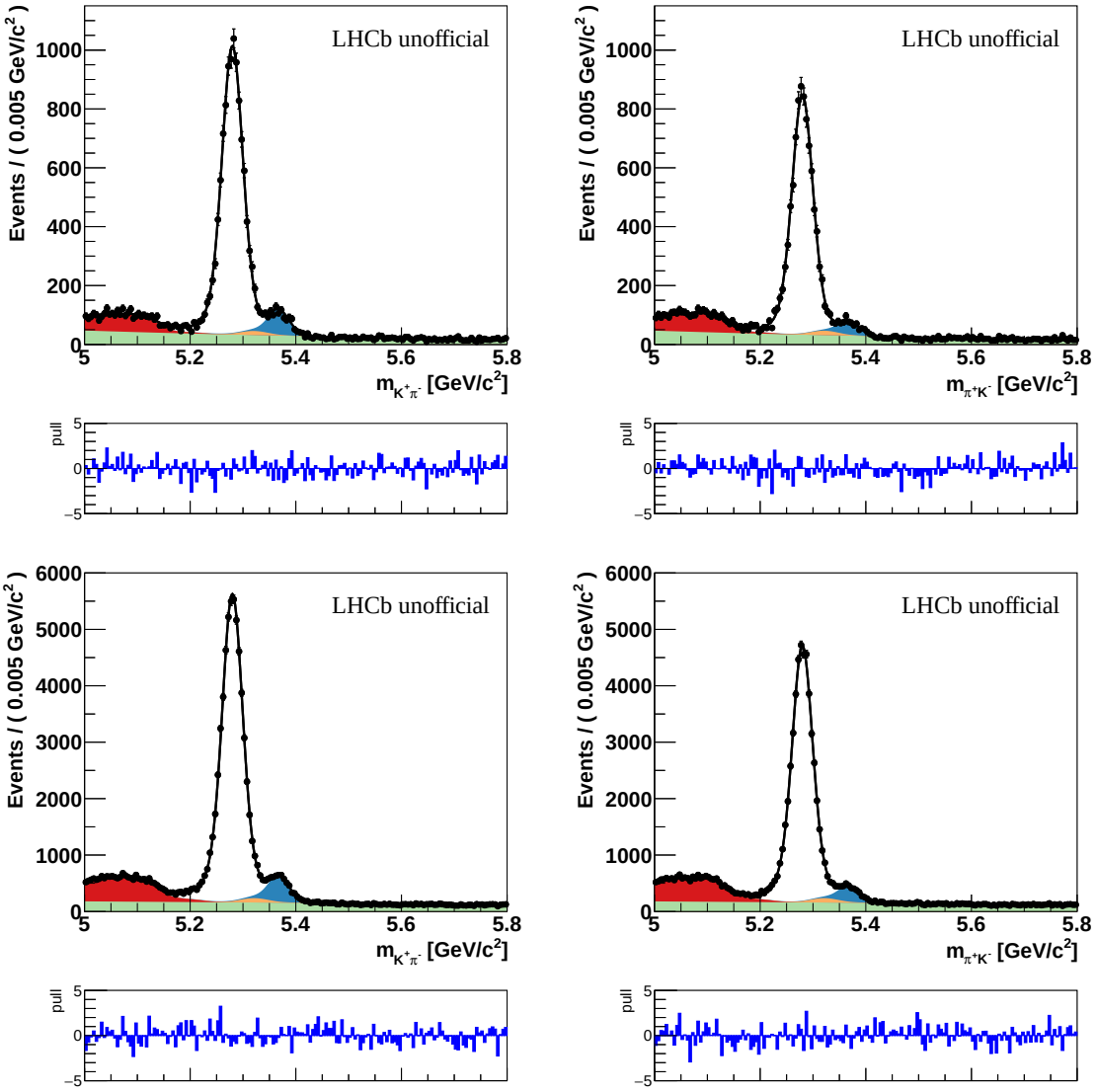

Figure 6.36: Distributions of the invariant mass related to the $K^{\pm}\pi^{\mp}$ final state split according to the $K^+\pi^-$ (left) and π^+K^- (right) mass hypothesis for 2015 (top) and 2016 (bottom). The different height of the two signal peak is directly proportional to the *CP* violation observed in the $B^0 \to K^+\pi^-$ and $B_s^0 \to \pi^+K^-$ decays. The result of the simultaneous fit is superimposed to data points.

have to be corrected for the final state detection and PID asymmetries, as it was done in the Run 1 analysis.

Asymmetries of the reconstruction and PID requirements efficiencies

The final state detection asymmetry, as well as the PID asymmetry, have been determined following the strategy described in Section 6.4. The values of $A_D^{K\pi}$ as function of the final state particle kinematic have been taken from an LHCb internal note [143] (unpublished) and are reported in Figure 6.37. The final values of the final state detection asymmetries, convolved with the $B \to h^+h'^-$ phase space, are:

$$\begin{aligned} A_D^{K\pi}(B^0 \to K^+\pi^-)(2015) &= (-1.0 \pm 0.3)\%, \\ A_D^{K\pi}(B^0 \to K^+\pi^-)(2016) &= (-1.1 \pm 0.1)\%, \\ A_D^{K\pi}(B_s^0 \to \pi^+K^-)(2015) &= (-1.0 \pm 0.3)\%, \\ A_D^{K\pi}(B_s^0 \to \pi^+K^-)(2016) &= (-1.1 \pm 0.1)\%, \end{aligned} \tag{6.12}$$

and turn out to be very compatible to each others. As done for the PID calibration, the *nTracks* variables is replaced by the *nSPD* variable in order to determine the PID asymmetry. The final value of the PID asymmetry, for both the $B^0 \to K^+\pi^-$ and $B_s^0 \to \pi^+K^-$ decays, is:

$$\begin{aligned} A_{\text{PID}}^{K\pi}(2015) &= (-1.2 \pm 0.7)\% \\ A_{\text{PID}}^{K\pi}(2016) &= (0.5 \pm 0.3)\% \end{aligned} \tag{6.13}$$

Extraction of the time-integrated *CP* asymmetries

Finally the extraction of the real *CP* asymmetries for the $B^0 \to K^+\pi^-$ and $B_s^0 \to \pi^+K^-$ decays can be performed. The values reported in Equation 6.11 are corrected by $A_D^{K\pi}$ in Equation 6.12 and $A_{\text{PID}}^{K\pi}$ in Equation 6.13. The final values of $A_{CP}(B^0 \to K^+\pi^-)$ and $A_{CP}(B_s^0 \to \pi^+K^-)$ are:

$$\begin{aligned} A_{CP}(B^0 \to K^+\pi^-)(2015) &= (-6.8 \pm 0.9 \pm 0.3 \pm 0.7)\% \\ A_{CP}(B^0 \to K^+\pi^-)(2016) &= (-8.6 \pm 0.4 \pm 0.1 \pm 0.3)\% \\ A_{CP}(B_s^0 \to \pi^+K^-)(2015) &= (26.1 \pm 3.6 \pm 0.3 \pm 0.7)\% \\ A_{CP}(B_s^0 \to \pi^+K^-)(2016) &= (24.0 \pm 1.6 \pm 0.1 \pm 0.3)\% \end{aligned} \tag{6.14}$$

where the first error is the statistical uncertainty, the second error comes from the $K^\pm\pi^\mp$ final state detection asymmetry and the third one comes from the uncertainty on the $A_{\text{PID}}^{K\pi}$ asymmetry. The final value of the time-integrated *CP* asymmetries are

$$\begin{aligned} A_{CP}(B^0 \to K^+\pi^-) &= (-8.3 \pm 0.3 \pm 0.3)\% \\ A_{CP}(B_s^0 \to \pi^+K^-) &= (24.4 \pm 1.4 \pm 0.3)\% \end{aligned} \tag{6.15}$$

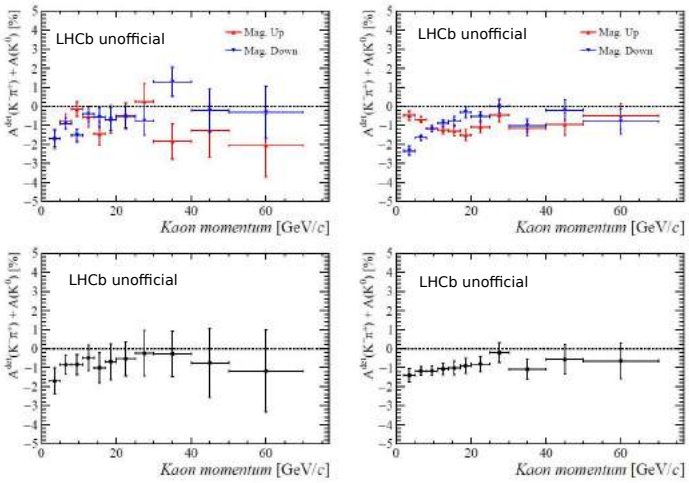

Figure 6.37: Values of $A_D^{K\pi}$ as function of the kaon momentum measured for 2015 (left) and 2016 data samples (right), and for up (red squares) and down magnet polarities (blue triangles). The two bottom figures show the arithmetic average between the two magnet polarities for 2015 (bottom left) and 2016 data sample (bottom right) [143].

where the values have been computed by means of a weighted average between the results obtained in 2015 and 2016 data sample. Results are perfectly in agreement with the values obtained in Run 1 analysis. Performing the test of the validity of the SM, suggested in Reference [140], the discriminant turns out to be $\Delta = -0.049 \pm 0.030 \pm 0.032$, where the first uncertainty is related to the measurements of the *CP* asymmetries and the second comes from the input values of the remaining parameters. In the calculation the average world values for the B^0 and B_s^0 mean lifetimes, for the quantity $f_s/f_d \times \mathcal{B}(B_s^0 \to \pi^+K^-)/\mathcal{B}(B^0 \to K^+\pi^-)$ and for the ratio of the production cross-sections f_s/f_d have been used. No evidence for a deviation from the expectation is observed with the present experimental precision.

6.4.2 Systematics uncertainties

The study of the various systematic uncertainties related to the *CP* parameters in Run 2 has not been finalised completely. For this reason this section contains only a brief discussion on the type of systematic sources that will be taken into account. The main systematic uncertainties for the time-integrated *CP* asymmetries are the ones related to the corrections applied to the raw asymmetries, due to the differences in the reconstruction and particle identification efficiencies between the charged-conjugate final states, as described in Section 6.4.1. Their corresponding systematic uncertainty is about 0.3%. All the other systematics sources have a completely negligible effect on such observables, as proved by the studies performed in Run 1 analysis.The only exception is represented

by the mass model systematic which, already in Run 1 analysis, provided a significant contribution to the systematic uncertainty of the $A_{CP}(B_s^0 \to \pi^+K^-)$ observable.

Regarding the time-dependent *CP* asymmetries, since the fit strategy is mostly unchanged with respect the Run 1 analysis, the main systematics sources involved are the same as the ones taken into account in the previous analysis. The calculation of such systematics uncertainties will be performed following the same two strategies described in Section 5.6. Therefore, the main contributions to *CP* parameters in the $\pi^+\pi^-$ final state are expected to come from the decay-time model of the cross-feed backgrounds and from the 3-body partially reconstructed background contamination. Analogously the main systematic uncertainties for the *CP* asymmetries in the K^+K^- final state, will be related to the calibration of the decay-time resolution, the contamination of 3-body background, the input parameters fixed in the *CP* fit. For the $A^{\Delta\Gamma}_{K^+K^-}$ parameter also the determination of the decay-time acceptance is expected to give significant contribution as systematic.

On the other hand, the changes introduced in the various analysis steps could introduce new systematic effects. The new nominal fit does not exploit a decay-time resolution on a per-event based, thus a new systematic effect, due to the neglected dependence of the decay-time error on the decay-time, has to be taken into account. A set of pseudoexperiments will be generated using a per-event decay-time resolution and then fitted by means of the nominal model, and the systematic uncertainties on the *CP* parameters will be computed taking the RMS of the corresponding distributions.

Most of the dominant systematic effects found in Run 1 analysis depend on the statistical power of the data sample used in the analysis. Thus they are expected to slightly decrease in Run 2 analysis, and in particular in case of a future combination between the Run 1 and Run 2 results. The only systematics not depending on the sample's statistics is the one related to the fixed parameters in the fit. In any case, the final precision on the *CP*-violating parameters in Run 2 analysis will be still dominated by the statistic uncertainty.

7

Conclusions

In this thesis the measurement of the time-dependent and time-integrated *CP* asymmetries performed using the events collected by LHCb during the Run 1 and the first part of the Run 2 data taking, are presented. They represent the status of art of the LHCb measurements in the charged charmless two body H_b decays. The Run 1 analysis is performed on a data sample corresponding to an integrated luminosity of 3 fb^{-1}; the obtained values for the various *CP* parameters are:

$$\begin{aligned} C_{\pi^+\pi^-} &= -0.34 \pm 0.06 \pm 0.01 \\ S_{\pi^+\pi^-} &= -0.63 \pm 0.05 \pm 0.01 \\ C_{K^+K^-} &= 0.20 \pm 0.06 \pm 0.02 \\ S_{K^+K^-} &= 0.18 \pm 0.06 \pm 0.02 \\ A^{\Delta\Gamma}_{K^+K^-} &= -0.79 \pm 0.07 \pm 0.10 \\ A_{CP}(B^0 \to K^+\pi^-) &= -0.084 \pm 0.004 \pm 0.003 \\ A_{CP}(B^0_s \to \pi^+K^-) &= 0.213 \pm 0.015 \pm 0.007 \end{aligned} \tag{7.1}$$

where the first uncertainties are statistical and the second and third are systematic. The results are in good agreement with the previous measurements performed by *B*-factories, CDF and LHCb itself on a subsample of Run 1 data, corresponding to an integrated luminosity of 1 fb $^{-1}$. The values of $C_{\pi^+\pi^-}$, $S_{\pi^+\pi^-}$, $A_{CP}(B^0 \to K^+\pi^-)$ and $A_{CP}(B^0_s \to \pi^+K^-)$ are the most precise measurement achieved by a single experiment and the values of the direct time-integrated *CP* symmetries dominate the world average. The statistical and the systematic uncertainties on $C_{K^+K^-}$ and $S_{K^+K^-}$ have been halved with respect the previous LHCb measurements while the parameter $A^{\Delta\Gamma}_{K^+K^-}$ has been measured for the very first time. Performing a χ^2 test statistic, the significance for the $C_{K^+K^-}$, $S_{K^+K^-}$ and $A^{\Delta\Gamma}_{K^+K^-}$ to differ from (0, 0, -1) is determined to be 4.0 standard deviations. This results represents the strongest evidence for the time-dependent *CP* violation in the B^0_s meson sector to date. Performing the validity test of the SM, described in Reference [140], using the measurements of

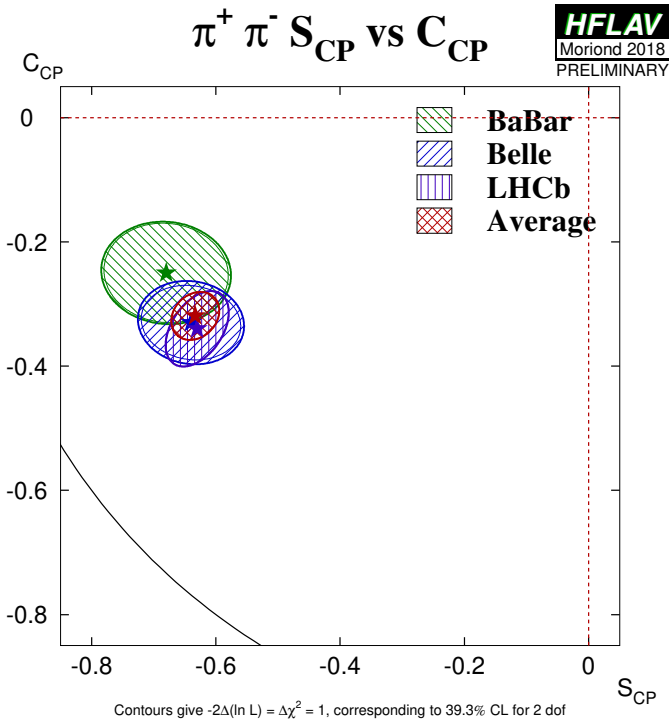

Figure 7.1: Representation of the direct and mixed-induced *CP* parameters for the $B \to \pi^+\pi^-$ decay [71] including the Run 1 measurements presented in this thesis.

$A_{CP}(B^0 \to K^+\pi^-)$ and $A_{CP}(B_s^0 \to \pi^+K^-)$ obtained in this analysis no evidence for a deviation from the expectation is observed. These new measurements will improve the constraints on the CKM *CP*-violating phases, using processes whose amplitudes receive significant contributions from penguin diagrams both in mixing and decay of B^0 and B_s^0 mesons. In addition, a comparison with the measurements of the same phases performed on B decay dominated by tree-level diagrams will provide tests of the SM and constrain possible New Physics effects. The results of this analysis are published in Reference [1]. An updated representation of all available time-dependent CP asymmetries for the $B^0 \to \pi^+\pi^-$ decay, including the results on the Run 1 analysis presented in this thesis, is shown in Figure 7.1 while in Figure 7.2 the new HFLAV averages of $C_{\pi^+\pi^-}$ and $S_{\pi^+\pi^-}$ are depicted.

In the second part of the thesis an update of the analysis is presented, using the data sample collected during the first years of the Run 2 data taking, corresponding to an integrated luminosity of 2 fb^{-1}, an update of the analysis is performed. The analysis is still ongoing, the preliminary

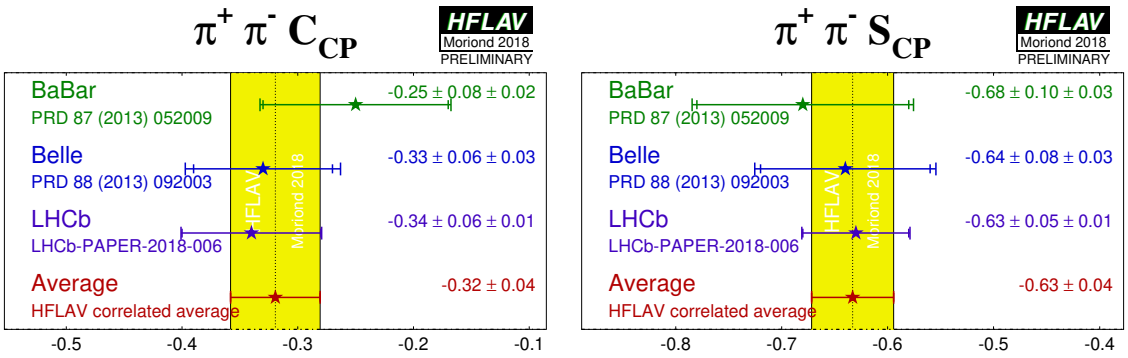

Figure 7.2: HFLAV average of the *CP* violation parameters in $B \to \pi^+\pi^-$ decay [71] including the Run 1 measurements presented in this thesis.

results obtained using the combination of the OS tagging algorithms are:

$$
\begin{aligned}
C_{\pi^+\pi^-} &= -0.38 \pm 0.06 \\
S_{\pi^+\pi^-} &= -0.68 \pm 0.05 \\
C_{K^+K^-} &= 0.12 \pm 0.05 \\
S_{K^+K^-} &= 0.19 \pm 0.05 \\
A^{\Delta\Gamma}_{K^+K^-} &= -0.79 \pm 0.07 \\
A_{CP}(B^0 \to K^+\pi^-) &= -0.083 \pm 0.003 \pm 0.003 \\
A_{CP}(B^0_s \to \pi^+K^-) &= \quad 0.244 \pm 0.014 \pm 0.003
\end{aligned}
\tag{7.2}
$$

where the uncertainties on the *CP* parameters are statistical while for the time-integrated integrated *CP* asymmetries the two uncertainties are statistical and systematic, respectively. The results are in very good agreement with the Run 1 values with comparable statistical precision. The statistical precision on the TD *CP* asymmetries is expected to be reduced by a relative 30% when adding the SS tagging algorithms. The study of the systematic uncertainties has to be finalized and the overall size of these uncertainties is expected to be slightly lower than what found in Run 1 analysis. Performing the validity test of the SM, described in Reference [140], using the measurements of $A_{CP}(B^0 \to K^+\pi^-)$ and $A_{CP}(B^0_s \to \pi^+K^-)$ obtained in this analysis no evidence for a deviation from the expectation is observed.

Since the Run 2 analysis is not be completed yet no combination of the results obtained in the two analyses is presented in this thesis. However the Run 1+Run 2 combined analysis is expected to significantly improve the precision of the results obtained so far by the LHCb collaboration and in particular the *CP* violation in the $B^0_s \to K^+K^-$ decays is expected to be confirmed at more than 5 standard deviations.

A

Development of a novel SSΛ tagging algorithm

As discussed in Section 4, the initial flavour at production of a B_s^0 meson candidate can be identified by means of SS tagging algorithms exploiting the charge of the particle coming from the remnants of the signal b fragmentation. In the most of the times this particle is a K however in some cases it could be a Λ baryon. No instance of such a tagger has been ever developed in the LHCb collaboration to date. This appendix briefly describes the study performed to develop a novel SSΛ algorithm in order to further improve the global tagging power available in the $B \to h^+h'^-$ Run 2 analysis. The full description of this study is reported in Reference [120] (unpublished).

Two different possibilities have been investigated developing the SSΛ algorithm: the first one based on completely data-driven method using a sample of $B_s^{**} \to B^+K^-$, the latter exploiting a sample of fully-simulated events of $B_s^0 \to D_s^-\pi^+$ decays. In both the cases the expected charge correlation between the Λ particle and the B_s^0 candidate is given by the following relation:

$$\begin{aligned} \text{Righttag}: & B_s^0\overline{\Lambda} \quad \text{or} \quad \overline{B}_s^0\Lambda \\ \text{Wrongtag}: & B_s^0\Lambda \quad \text{or} \quad \overline{B}_s^0\overline{\Lambda} \end{aligned} \tag{A.1}$$

The Λ particles used to develop the algorithm have been reconstructed from the combination of two opposite charged tracks, a pion and a proton respectively, identified as downstream (DD) or long (LL) tracks.

A.1 Development of the data-driven method

In this first approach the SSΛ tagger is trained directly on a data sample of $B_s^{**} \to B^+K^-$ decays. The reason of this choice lies in the fact that the B_s^{**} mesons decay due to the strong interaction so quickly that they can not oscillate. This means that the flavour at production is exactly the same as the one

at the decay, which can be reconstructed using the charge of the decay products. In order to get rid of the background contribution the sPlot technique [122] is exploited using the ΔQ distribution as discriminant variable. The ΔQ variable is defined as:

$$\Delta Q = m(B+K) - m(B) - m(K) \tag{A.2}$$

where $m(X)$ represents the invariant mass of the X system. The ΔQ distribution shows three narrow peaks at 11, 22 and 67 MeV/c^2, representing the $B_{s2}^{*0}(5840) \to B^+K^-$, $B_{s2}^{*0}(5840) \to B^{*+}(\to B^+\gamma)K^-$ and $B_{s1}^{*0}(5830) \to B^{*+}(\to B^+\gamma)K^-$ decays. The latest two peak distributions are shifted down by $m(B^{*+}) - m(B^+) = 45.0 \pm 0.4\ MeV/c^2$ from their nominal ΔQ values due to the emitted photons not reconstructed in the B^{*+} decays. The B^+ candidates are reconstructed in four final states: $B^+ \to J/\psi(\to \mu\mu)K^+$, $B^+ \to D^0(\to K\pi)\pi^+$, $B^+ \to D^0(\to K\pi\pi\pi)\pi^+$ and $B^+ \to D^0(\to K\pi)\pi^+\pi^-\pi^+$. The ΔQ distribution of the whole sample is shown in Figure A.1 and the maximum likelihood fit, used to extract the sWeights, is superimposed.

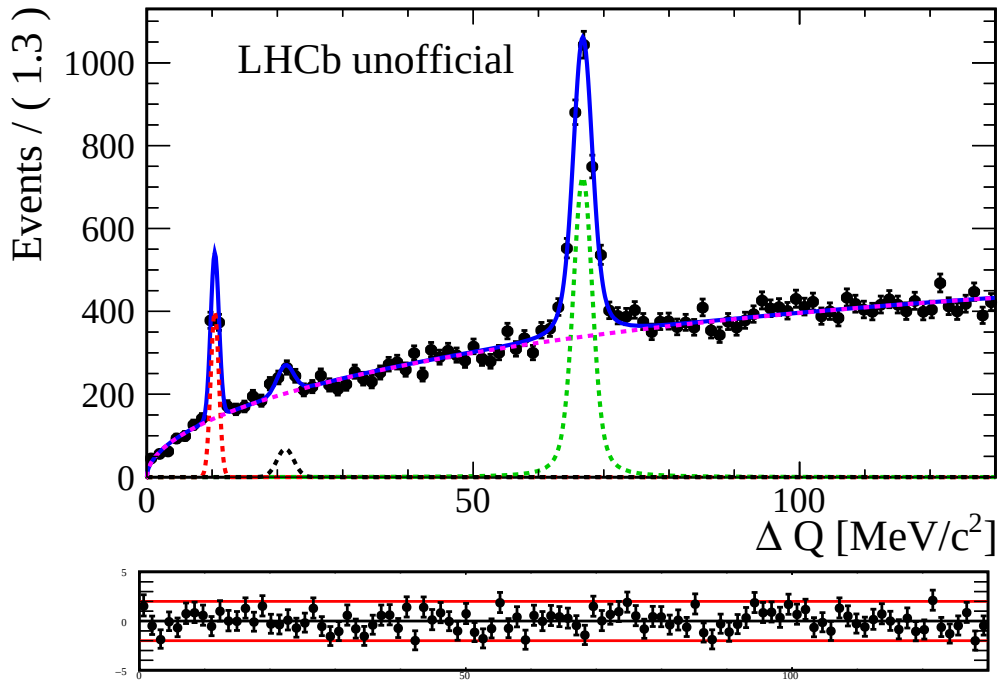

(a)

Figure A.1: Distribution of the mass difference ΔQ of the B^+K^- sample, including all the B^+ decay mode. The black points and the blue solid line represent the data and function fitted to these data. From left to right three peaks are identified: $B_{s1}^{*0}(5830) \to B^{*+}(\to B^+\gamma)K^-$ (red), $B_{s2}^{*0}(5840) \to B^{*+}(\to B^+\gamma)K^-$ (black), $B_{s2}^{*0}(5840) \to B^+K^-$ (green). The background is represented with a pink dashed line.

A huge amount of Λ comes from a random combination of two tracks, as shown in plot A.2, and thus a strong selection is required to get rid of this background. A Boost Decision Tree (BDT)

classifier is used to identify the true Λ, taking as input variables kinematic and geometric properties both of the mother and the daughters. The BDT is trained on a simulated sample of $B^+ \to J/\psi K^+$ since the Λ reconstruction is supposed to be independent on the B decay mode used. The signal and background are defined by means of the MC truth on the Λ ID information. The list of input variables is reported in Table A.1.

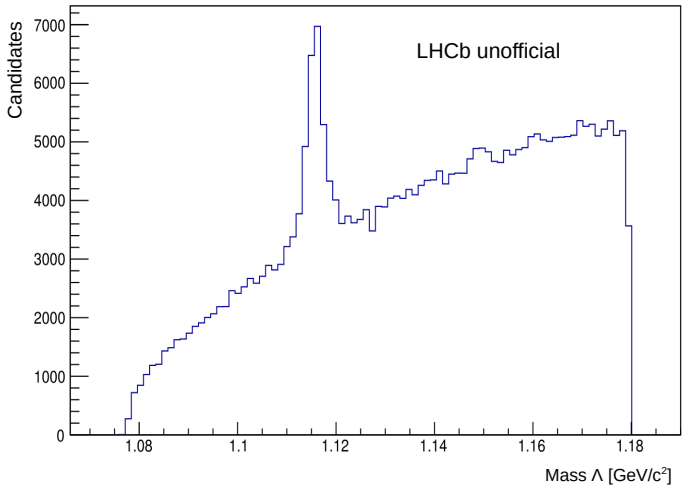

(a)

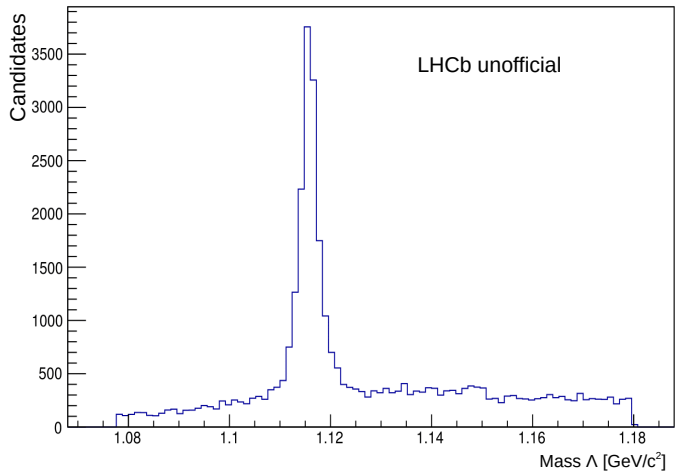

(b)

Figure A.2: Comparison between the Λ mass distribution before and after the requirement on the BDT output.

The BDT is used to select Λ candidates in the $B^{*0}_{s2} \to B^+K^-$ data sample. An optimisation is performed on the BDT requirements to the sample of $B^{*0}_{s2} \to B^+K^-$ such that the number of background Λ is reduced from 12 227 to only 373 candidate with a selection efficiency of 90% as shown

Table A.1: List of the input parameters used to train the BDT selecting the true Λ particles.

Variable	Description
$\log(p^{\Lambda})$	Logarithm of the Λ momentum
$\log(p_T^{\Lambda})$	Logarithm of the Λ transverse momentum
FD	Flight distance of the Λ particle
IP^{Λ}	Impact parameter of the Λ particle
$\log(IPCHI2)$	Logarithm of the χ^2 of IP^{Λ}
$DOCA$	Distance of closest approach
$\log(DOCACHI2)$	Logarithm of the χ^2 of $DOCA$
$DIRA$	Cosine of the angle between the Λ momentum and direction vectors
IP^{p}	Impact parameter of the proton daughter
IP^{π}	Impact parameter of the pion daughter

in Figure A.2

Unfortunately the amount of remaining Λ candidate is not sufficient to train a BDT classifier without introducing a significant overtraining. Thus, since the most of the events contain only one Λ candidate, all the Λ available are considered as possible tagging candidates. The tagging power provided by the algorithm on the $B_s^{**} \to B^+K^-$ data sample is found to be $\varepsilon_{eff} = (0.064 \pm 0.018)\%$ with a tagging efficiency $\varepsilon_{tag} = (2.528 \pm 0.039)\%$.

A.2 Development using fully-simulated events

The second approach studied consists in developing the SSΛ tagger by means of a sample of fully-simulated sample of $B_s^0 \to D_s^- \pi^+$ decays generated with Run 2 data taking conditions. The $B_s^0 \to D_s^- \pi^+$ sample is splitted in three subsamples of the same size that will be used for the BDT training, the BDT calibration and the mistag probability calibration, following the same strategy exploited in the development of the SSπ and SSp algorithms [117]. In this case the true Λ candidate can be identified through the MC truth related to particle ID information. In the simulated sample, new variables can be used to select Λ candidate more efficiently, as the fragmentation information. This feature allows to train the BDT using only the Λ coming from the b fragmentation as signal allowing to consider all the remaining Λ as background. The variables used as input in the BDT training are reported in Table A.2.A Also in this case the BDT response, shown in Figure A.4, results to be affected by an overtraining effect due to the relative small number of Λ candidates available in the sample.

Then the dependency of the mistag rate, ω, on the BDT response is studied. The second sub-

sample of $B_s^0 \to D_s^- \pi^+$ has been splitted in bins of the BDT response and in each bin the mistag rate is evaluated using Equation 4.1. The relation between ω and the BDT response is fitted by means of a third order polynomial and it is used to estimate the mistag η predicted by the algorithm. The mistag average of the events decreases significantly with high BDT value, as shown in Figure A.3.

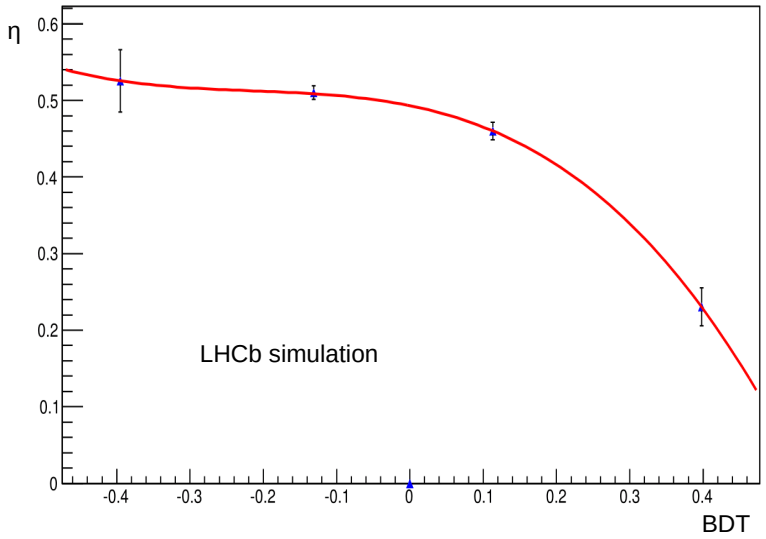

(a)

Figure A.3: Polynomial curve on the test subsample. The magenta area shows the confidence range within $\pm 1\sigma$.

Finally, the third subsample is splitted in bins of η and in each bins the mistag rate is determined as done in the previous subsample. The dependence of ω as function of η is fitted with the linear function reported in Equation 4.10.

The last step consists in applying the BDT on a set of real data, using the sample of $B_s^{**} \to B^+ K^-$ decays. The Λ candidates have been selected as explained in the previous section and a cut on the BDT response is applied in order to remove the most of the background contamination. The mistag probability predicted by the algorithm is calibrated using the linear relation determined on the simulated events, since the number of Λ available in the data sample is not sufficient to provide a reliable calibration. The tagging power provided by the algorithm on the $B_s^{**} \to B^+ K^-$ data sample is found to be $\varepsilon_{eff} = (0.055 \pm 0.011)\%$ with a tagging efficiency $\varepsilon_{tag} = (2.21 \pm 0.012)\%$.

A.3 Final considerations

Using both the strategies the achieved tagging power for the SSΛ tagger is found to be lower than 0.1%: $(0.064 \pm 0.018)\%$ with the data-driven method and $(0.055 \pm 0.011)\%$ using fully-simulated

Table A.2: List of the input parameters used to train the BDT selecting the true Λ particles coming from the b-quark fragmentation.

Variable	Description
$\log p^{\Lambda}$	Logarithm of the Λ momentum
$\log p_T^{\Lambda}$	Logarithm of the Λ transverse momentum
$\log IPCHI2$	Logarithm of the χ^2 of IP^{Λ}
$\Delta\eta$	Difference between B_s and Λ pseudorapidity
$\Delta\phi$	Difference between B_s and Λ azimuthal angle
ΔR	$\sqrt{\Delta\phi^2 + \Delta\eta^2}$
ΔQ	$m(B_s + \Lambda) - m(B_s) - m(\Lambda)$
$\log p^{B_s}$	Logarithm of the B_s momentum
$\log p_T^{B_s}$	Logarithm of the B_s transverse momentum

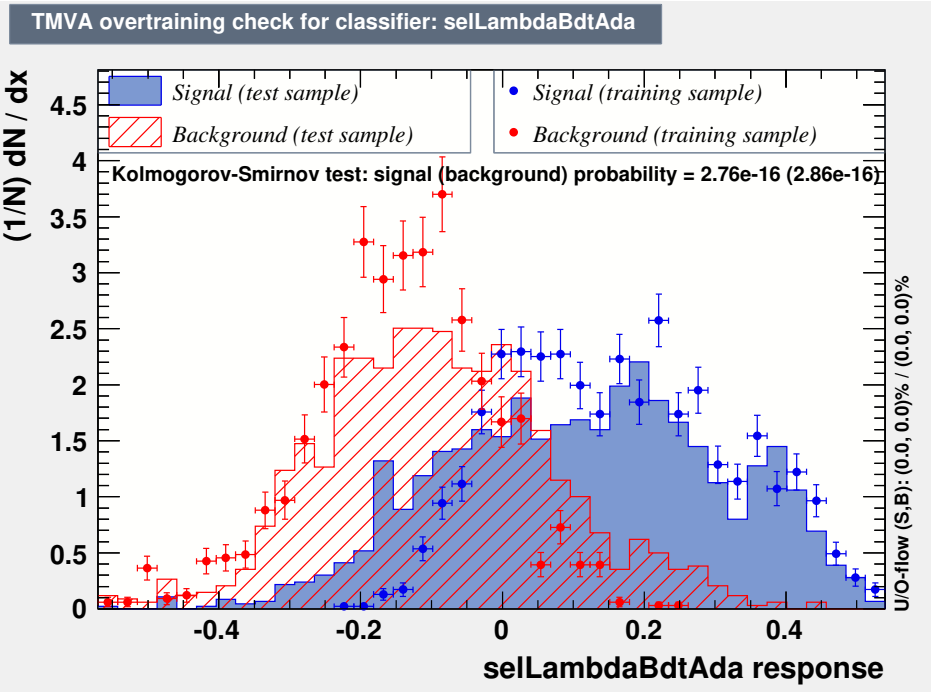

(a)

Figure A.4: Distribution of the final response of the BDT used to select the best Λ tagging candidate. The blue distribution represents the right charge correlated Λ coming from the b-quark fragmentation (signal) while the red distribution corresponds to the all the other Λ (background). Both distributions are normalized to the number of entries.

events. The reason behind a so low performance lies mostly in the very low tagging efficiency: only 2-3% of the signal events can be associated to a Λ candidate. In addition the low Λ multiplicity, about 1.25, don't allow to apply any selecting to the Λ particles since removing a candidate entails directly a loss in the tagging efficiency which is not compensated by the enhancement in the mistag probability. Given the humble results obtained, the SSΛ algorithm has not been used in the $B \to h^+h'^-$ Run 2 analysis.

B

Studies on the $SSkNN$ tagger

As discussed in Section 4.4.3 the S$SkNN$ algorithm is used to identify the flavour at production of the B_s^0 mesons. A dedicated study concerning the dependence of the S$SkNN$ calibration parameters on the event kinematic has been performed exploiting a simulated sample of $B_s^0 \to \pi^+ K^-$ decays. The aim of such a study lies in checking whether the code used is able to retrieve the correct value of the mistag rate ω. In a first step the true decay time is used in order to avoid any nuisance effect on the determination of ω due to the decay time resolution. A requirement on the B transverse momentum, i.e. $p_T^B > (<) 9\,\text{GeV}/c$, is used to split and study the $B_s^0 \to \pi^+ K^-$ sample in two different kinematic regions. Similarly to what done in Section 4.4.3 the calibration fit is performed both using a per-event mistag, in order to obtain precise results, and splitting the sample in categories of the predicted mistag probability η, checking the linearity of the functional relation of ω as function of η. For the sake of simplicity in the comparison of the results evaluated with the two methods, the η average is fixed to 0.44. The results of the per-event fit, both for the two kinematic subsamples and the whole sample, are reported in Table B.1. The linearity of the relations between ω and η are also shown in Figure B.1, where both ω value estimated from the category fit and the one evaluated using the MC truth are shown. The difference between the calibration functions in the two kinematic regions is reported in Figure B.2. In each subsample the ω values obtained from the fit seems to be in very good agreement with the MC truth, nevertheless a small trend is observed in p_1 increasing between the two kinematic bins, as reported in Table B.1.

The second step of this study is performed introducing the reconstructed decay time, in place of the true decay time used previously, and including the decay time resolution in the fit. Following the same procedure of the first step, the fit is repeated using both a per-event mistag rate and splitting the sample in η categories. The decay-time resolution is considered on a per-event basis and the average value of η is fixed to 0.44. The fit results are reported in Table B.2 while the functional relation of $\omega(\eta)$ and the difference between the calibrations, obtained in the two p_T^B bins, are shown

Table B.1: *SSkNN* calibration parameters obtained in different kinematic regions, using the true decay-time in the fit.

p_T^B	Category			Event		
	p_0	p_1	$\rho_{p0,p1}$	p_0	p_1	$\rho_{p0,p1}$
–	0.4410 ± 0.0014	0.952 ± 0.015	0.270	0.4409 ± 0.0014	0.953 ± 0.015	0.246
< 9	0.4423 ± 0.0017	0.906 ± 0.023	0.130	0.4423 ± 0.0017	0.917 ± 0.023	0.123
> 9	0.4389 ± 0.0025	0.970 ± 0.019	0.434	0.4389 ± 0.0025	0.975 ± 0.021	0.403

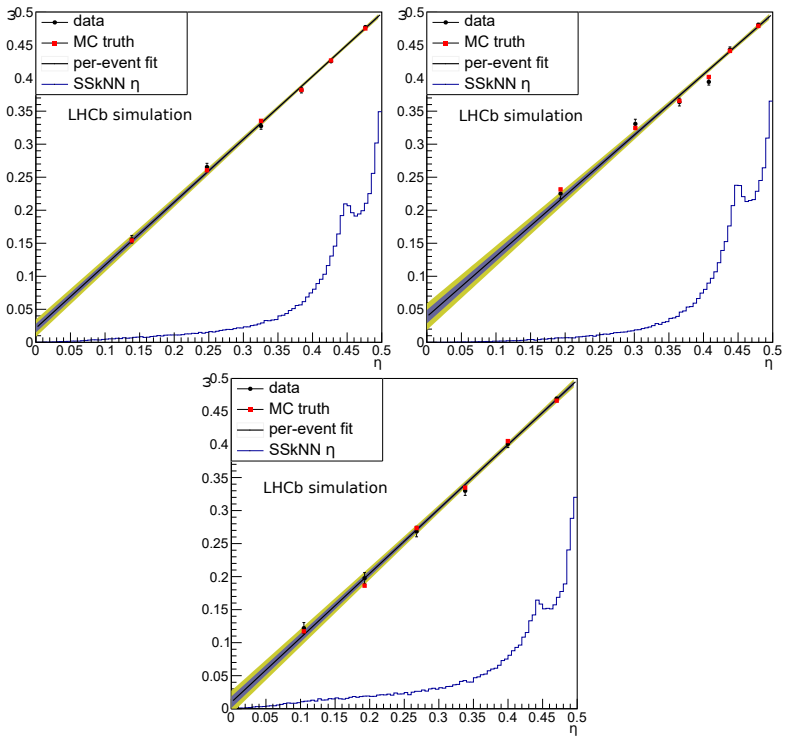

Figure B.1: *SSkNN* calibration plots corresponding to different kinematic regions: whole sample (left), sub-sample with $p_T^B < 9\,\text{GeV}/c$ (center) and sub-sample with $p_T^B > 9\,\text{GeV}/c$ (right). The ω values estimated from the category fit using the true decay-time are reported in black, while the true mistag obtained from the MC truth is drawn in red. The two bands in blue and in yellow represent the 66% and 95% of confidence level. In addition the *SSkNN* η distribution, corresponding to each sample, is superimposed.

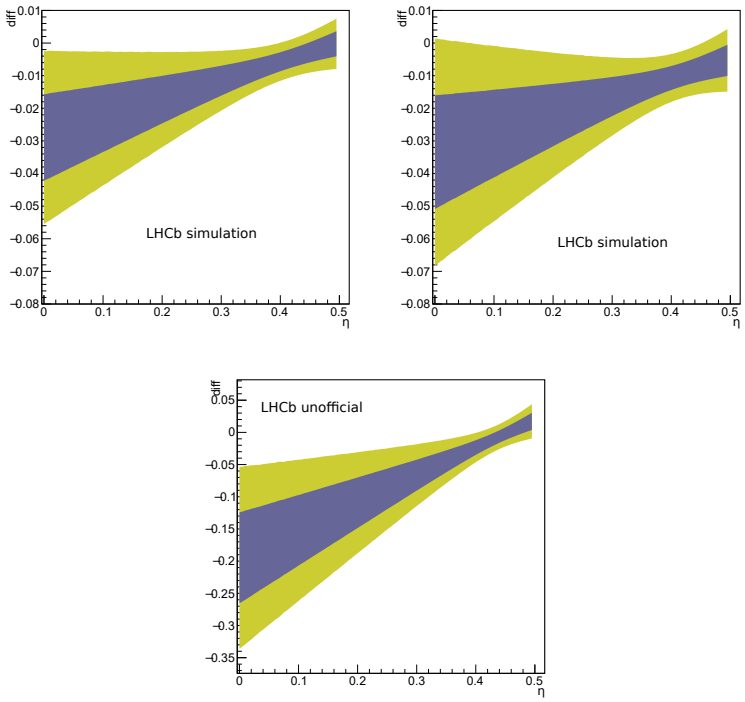

Figure B.2: Differences between the calibration functions in the two kinematic regions, $p_T^B < 9\,\text{GeV}/c$ and $p_T^B > 9\,\text{GeV}/c$, using the true decay-time on fully simulated $B_s^0 \to \pi^+ K^-$ sample (left), the reconstructed decay-time on fully simulated $B_s^0 \to \pi^+ K^-$ sample (center) and a data sample of $B_s^0 \to D_s^- \pi^+$ decays (right).

in Figure B.3 and B.2, respectively. In agreement with the results of the previous test, the response of the S*SkNN* tagger turns out to be compatible with the expected MC value, the same dependence of the calibration parameters on the B transverse momentum and a similar trend of the difference between the two calibrations are observed.

Table B.2: S*SkNN* calibration parameters obtained in different kinematic regions, using the reconstructed decay-time in the fit and including a per-event decay-time resolution.

p_T^B	Category			Event		
	p_0	p_1	$\rho_{p0,p1}$	p_0	p_1	$\rho_{p0,p1}$
–	0.4427 ± 0.0018	0.969 ± 0.019	0.266	0.4427 ± 0.0019	0.964 ± 0.020	0.242
< 9	0.4460 ± 0.0022	0.914 ± 0.031	0.119	0.4460 ± 0.0022	0.921 ± 0.031	0.112
> 9	0.4376 ± 0.0030	0.976 ± 0.024	0.416	0.4376 ± 0.0030	0.978 ± 0.027	0.385

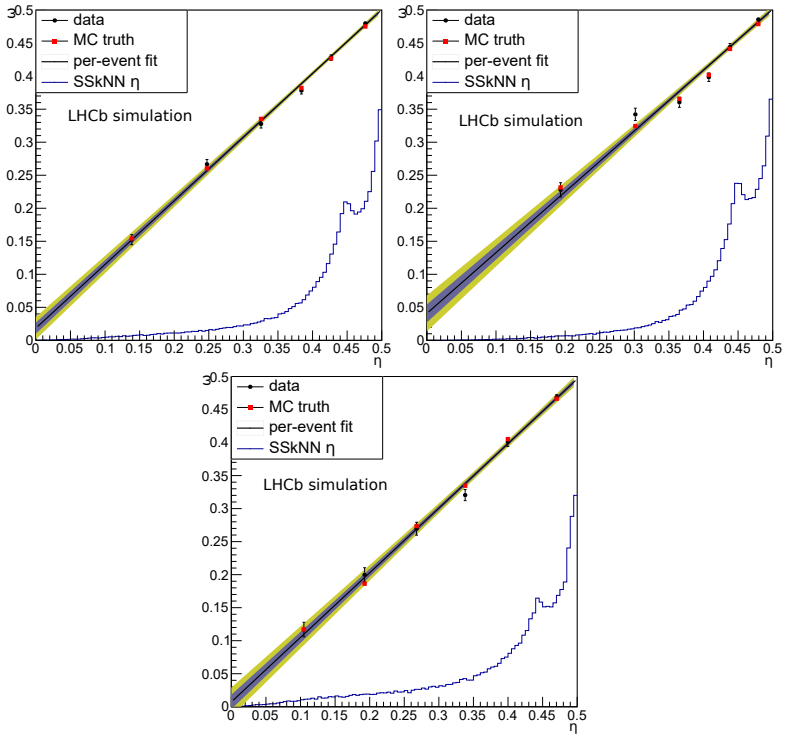

Figure B.3: S*SkNN* calibration plots corresponding to different kinematic regions: whole sample (left), sub-sample with $p_T^B < 9\,\text{GeV}/c$ (center) and sub-sample with $p_T^B > 9\,\text{GeV}/c$ (right). The ω values estimated from the category fit using the reconstructed decay-time are reported in black, while the true mistag obtained from the MC truth is drawn in red. The two bands in blue and in yellow represent the 66% and 95% of confidence level. In addition the S*SkNN* η distribution, corresponding to each sample, is superimposed.

A final check is performed in order to verify the correct match of the results obtained using simulated sample with the ones obtainable on real data. Since the yield of $B_s^0 \to \pi^+ K^-$ on data, after

having applied the selection described in Section 5.1, is not sufficient to provide a reliable S*SkNN* calibration, the $B_s^0 \to D_s^- \pi^+$ decay mode is used instead. The sample is splitted according to the same p_T requirements used in the previous steps. In Table B.3 the results of the category and per-event fits are reported, while the corresponding calibration plots are shown in Figure B.4. Finally in Figure B.2 the difference between the calibrations obtained in the two kinematic regions is shown. The S*SkNN* calibration parameters show a trend similar to what observed in fully simulated events, however in this case the dependence on the B transverse momentum results to be much larger.

Table B.3: S*SkNN* calibration parameters obtained in different kinematic regions using a data sample of $B_s^0 \to D_s^- \pi^+$ decays.

p_T^B	Category			Event		
	p_0	p_1	$\rho_{p0,p1}$	p_0	p_1	$\rho_{p0,p1}$
–	0.4401 ± 0.0047	1.028 ± 0.071	0.087	0.4402 ± 0.0047	1.028 ± 0.069	0.112
< 9	0.4451 ± 0.0075	0.664 ± 0.144	-0.087	0.4450 ± 0.0075	0.713 ± 0.138	-0.048
> 9	0.4384 ± 0.0061	1.154 ± 0.082	0.170	0.4386 ± 0.0061	1.141 ± 0.080	0.218

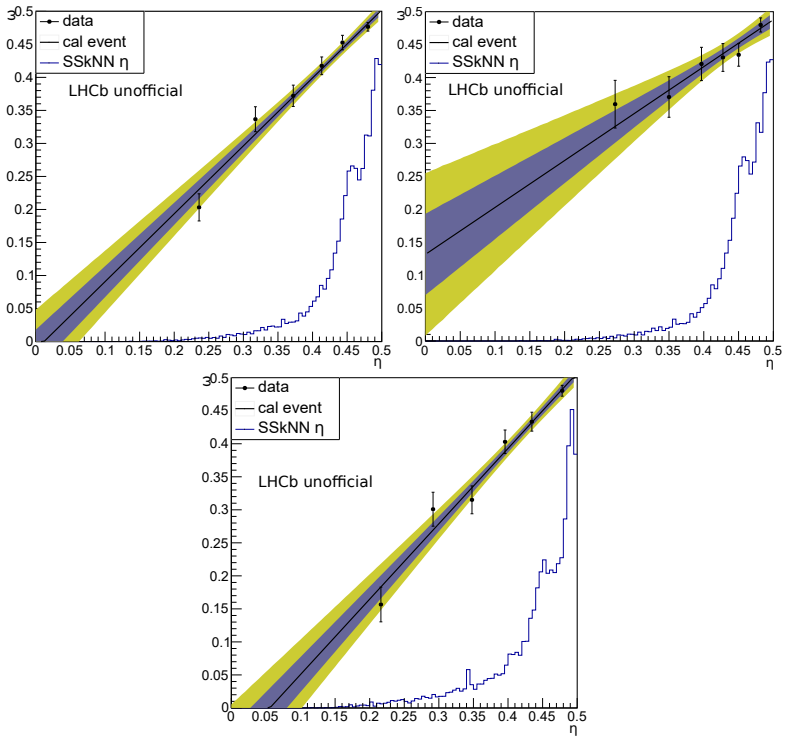

Figure B.4: S*SkNN* calibration plots obtained using a $B_s^0 \to D_s^- \pi^+$ data sample. Different kinematic regions are shown: whole sample (left), sub-sample with $p_T^B < 9\,\text{GeV}/c$ (center) and sub-sample with $p_T^B > 9\,\text{GeV}/c$ (right). The two bands in blue and in yellow represent the 66% and 95% of confidence level. In addition the S*SkNN* η distribution, corresponding to each sample, is superimposed.

C

BDT used in the Stripping preseletion for the $H_b \to h^+h'^-$ analysis

A BDT classifier is used in the stripping preselection of the $H_b \to h^+h'^-$ Run 1 analysis, discussed in Section 5.1.3. The BDT takes both kinematic and geometrical variables as input, which are reported in Table C.1. They comprise the largest and the smallest transverse momentum (p_T) and impact parameter of the two tracks (d_{IP}^{track}), the quality of the common vertex fit of the two tracks (χ^2_{vtx}), the d_{CA} between the two tracks, the $p_T^{H_b}$, the flight distance (FD) with respect to the associated PV[1] and the impact parameter of the H_b signal candidate ($d_{IP}^{H_b}$). The combinatorial background is described using the high-mass sideband, requiring the invariant mass, evaluated assuming the pion mass hypothesis for both the tracks in the final state ($m_{\pi^+\pi^-}$), to be greater than 5.6 GeV/c^2. The signal events are parametrised using a cocktail of $B^0 \to K^+\pi^-$, $B_s^0 \to \pi^+K^-$, $B^0 \to \pi^+\pi^-$ and $B_s^0 \to K^+K^-$ decays, where the fraction of each decay corresponds to the ratio of branching fractions [58]. Both the signal and the background samples were splitted in two equivalent parts: one used for the training of the BDT classifier, labelled as "training", and the second used to check the presence of possible overtraining effects, labelled "test". The distribution of the BDT response is reported in Figure C.2, while the correlation between the input variables for both the signal and background are shown in Figure C.1. The optimal value of the cut requested in the preselection to the BDT output has been set in order to reduce as much as possible the retention rate without affecting the signal selection efficiency.

[1] The primary vertex associated to the signal candidate is the one with the smallest χ^2 of the impact parameter

Table C.1: Input variables used to train the BDT classifier used in the stripping line.

Input variables			
$min(p_T^{\text{track}^+}, p_T^{\text{track}^-})$		$min(d_{IP}^{\text{track}^+}, d_{IP}^{\text{track}^-})$	
$max(p_T^{\text{track}^+}, p_T^{\text{track}^-})$		$max(d_{IP}^{\text{track}^+}, d_{IP}^{\text{track}^-})$	
FD		d_{CA}	χ^2_{vtx}
		$p_T^{H_b}$	$d_{IP}^{H_b}$

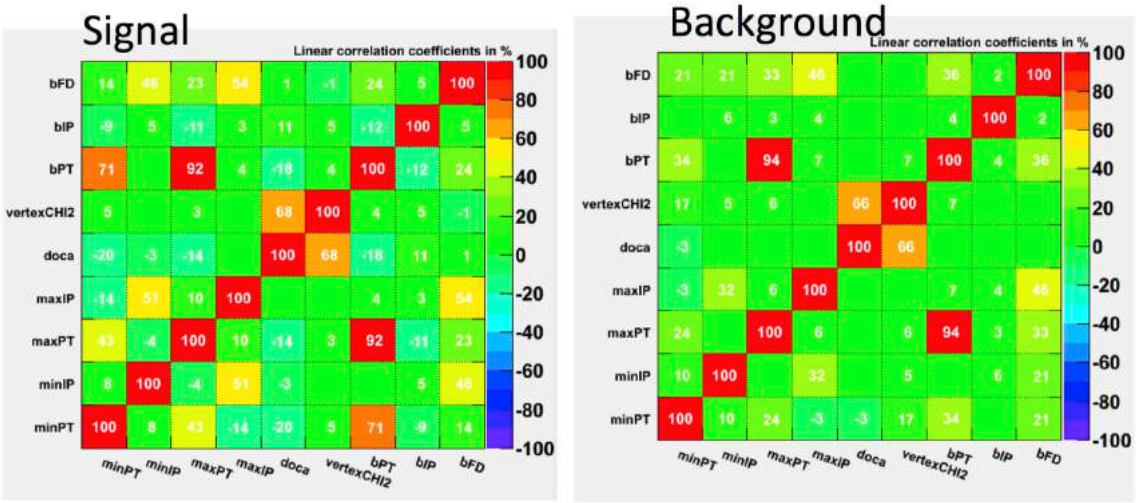

Figure C.1: Correlation among the input variables used to train the stripping BDT for both the signal, on the left, and background, on the right.

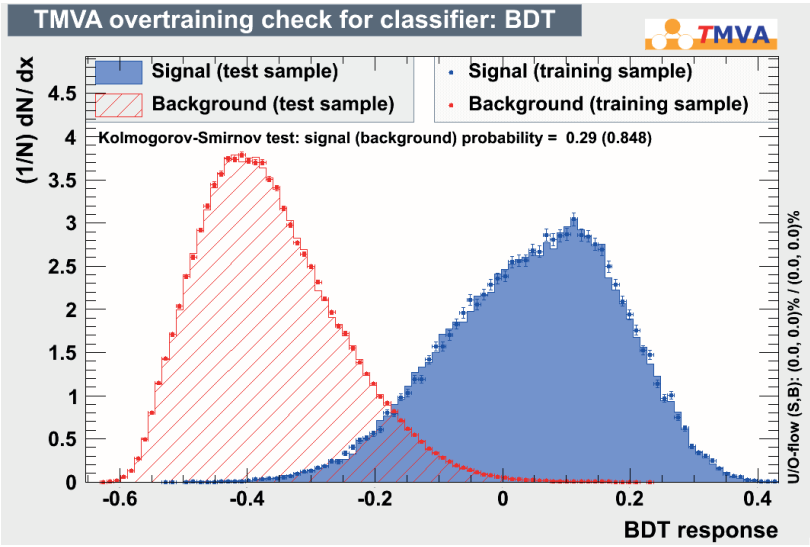

Figure C.2: Distribution of the response of the BDT used in the stripping, when applied both to the "training" and "test" sub-samples.

D

Decay time resolution calibration using time-dependent fits

As described in Section 5.4.1 the calibration of the decay-time resolution in H_b 2hh Run 1 analysis is determined using a data sample of $B_s^0 \to D_s^- \pi^+$ decays. The validity of the procedure used to determine the parameters governing the calibration of the decay time resolution, has been verified using fully simulated samples of $B_s^0 \to \pi^+ K^-$ and $B_s^0 \to D_s^- \pi^+$ decays. The tagged decay time distributions have been described with the same model used for the data. Exploiting the MC truth information to tag the B candidate it has been possible fixing the tagging efficiencies to 1 and the mistag probabilities to 0. The numerical values found for the q_0 and q_1 parameters are reported in Table D.1 while the decay time distributions and the corresponding time-dependent asymmetries are shown in Figure D.1. A slightly difference in the values of q_0 and q_1, with respect to the values reported in Table 5.11, of about 1 fs and 0.01-0.06 respectively is observed. These discrepancies are treated as source of systematic uncertainty, as well as the differences between the calibration parameters for the $B_s^0 \to \pi^+ K^-$ and $B_s^0 \to D_s^- \pi^+$ decays, as discussed in Section 5.6.

Table D.1: Parameters governing the calibration of the decay time resolution for fully simulated $B_s^0 \to \pi^+ K^-$ and $B_s^0 \to D_s^- \pi^+$ decays. The results are obtained from tagged time-dependent unbinned maximum likelihood fits to the distributions of simulated samples.

Decay	q_0	q_1	$\rho(q_0, q_1)$
$B_s^0 \to \pi^+ K^-$	34.71 ± 0.27 fs	1.041 ± 0.028	-0.44
$B_s^0 \to D_s^- \pi^+$	35.84 ± 0.21 fs	1.143 ± 0.018	-0.33

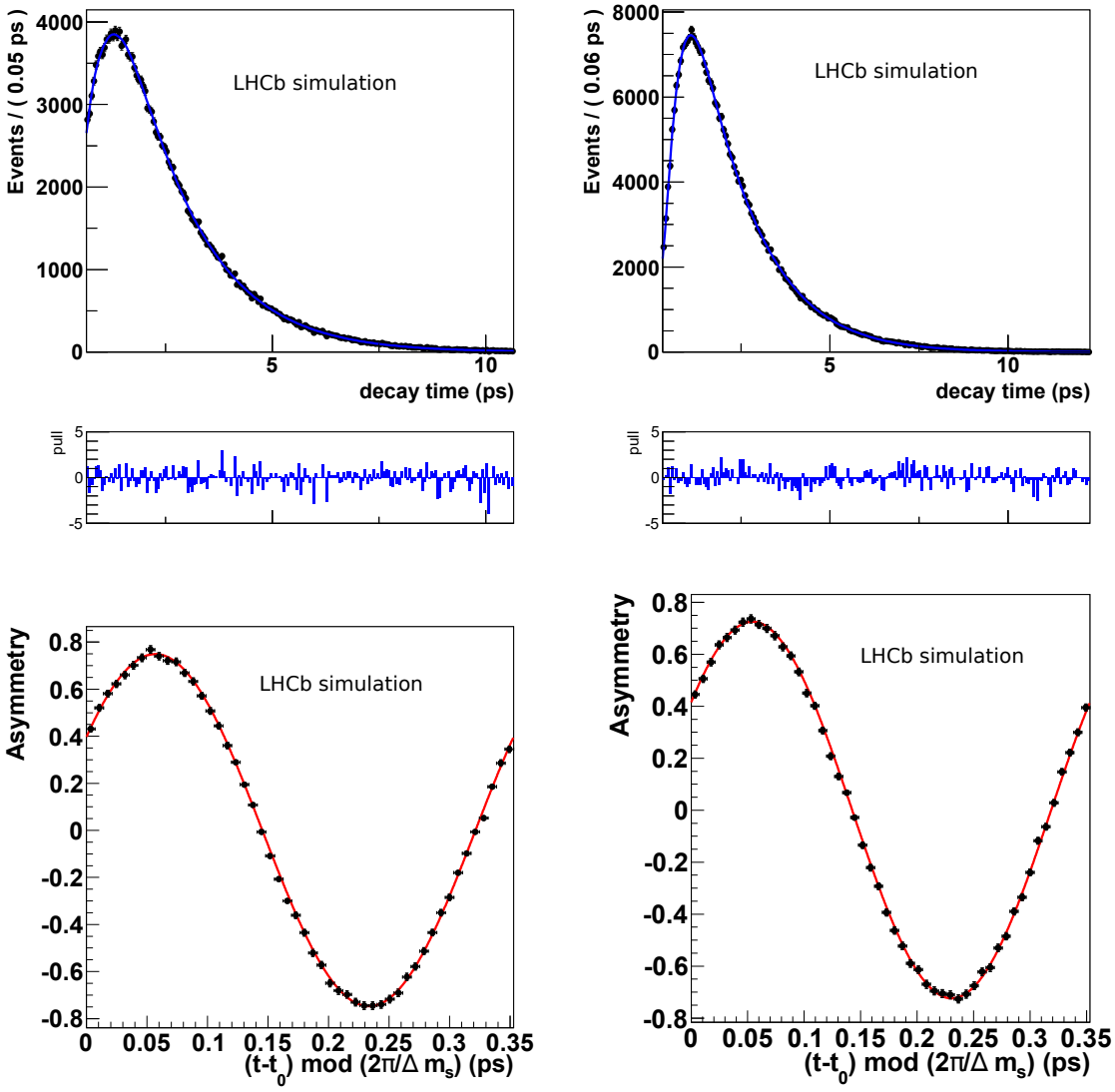

Figure D.1: Distribution of the decay time (top) and time-dependent asymmetry (bottom) for fully simulated $B_s^0 \to \pi^+ K^-$ (left) and $B_s^0 \to D_s^- \pi^+$ (right) decays. The result of the best fit are superimposed on data points.

E

Additional plots from the fit performed for the $\sigma(\delta_t)$ calibration

The calibration of the decay-time resolution in Run 2 analysis, described in Section 6.3.1, is determined by means of a bi-dimensional fit performed on the $J\psi \to \mu^+\mu^-$ and $\Upsilon \to \mu^+\mu^-$ data and fully-simulated sample and the $B_s^0 \to K^+K^-$ fully-simulated sample. In this appendix the projection of the fits in bins of the decay-time error are reported.

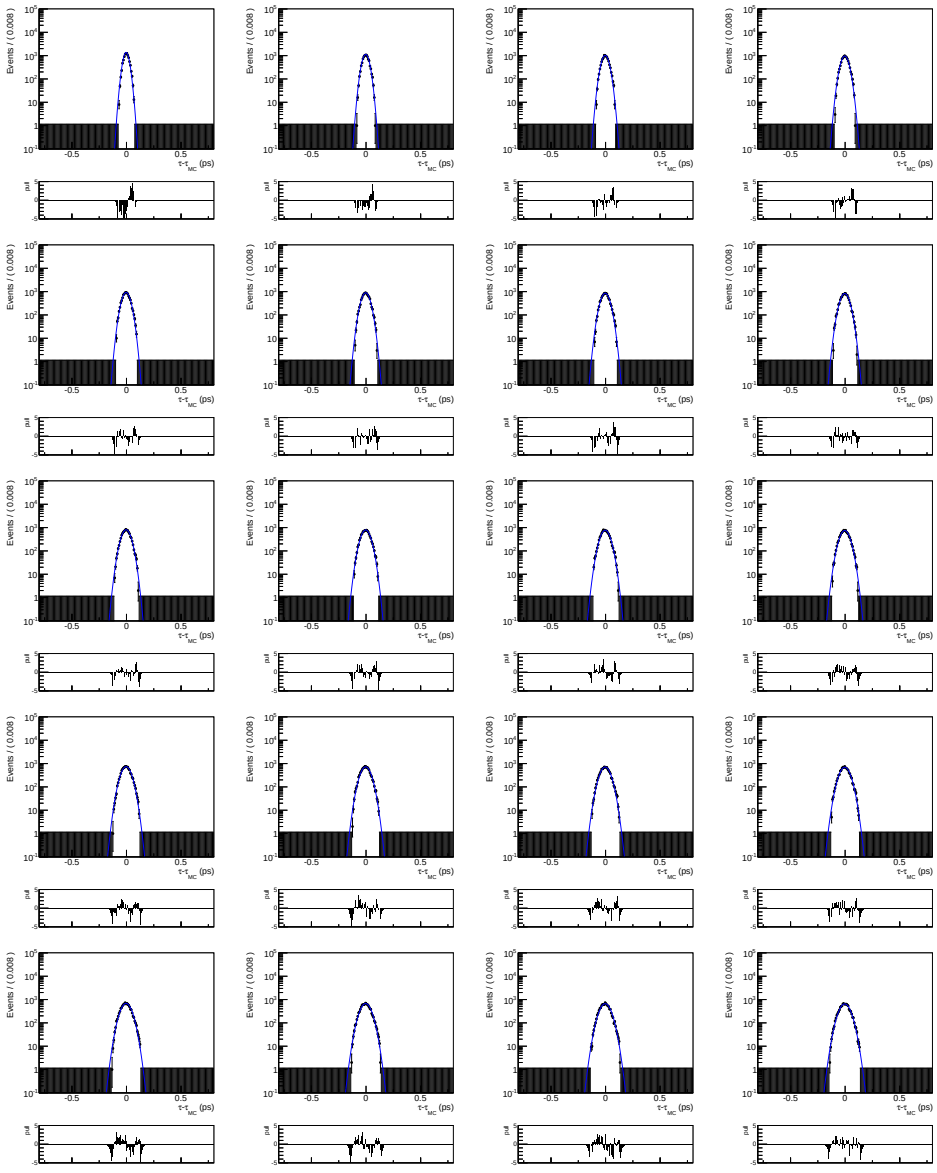

Figure E.1: Projection of the bi-dimensional fit in bins of the decay-time error for the $J/\psi \to \mu^+\mu^-$ data Run 2 sample.

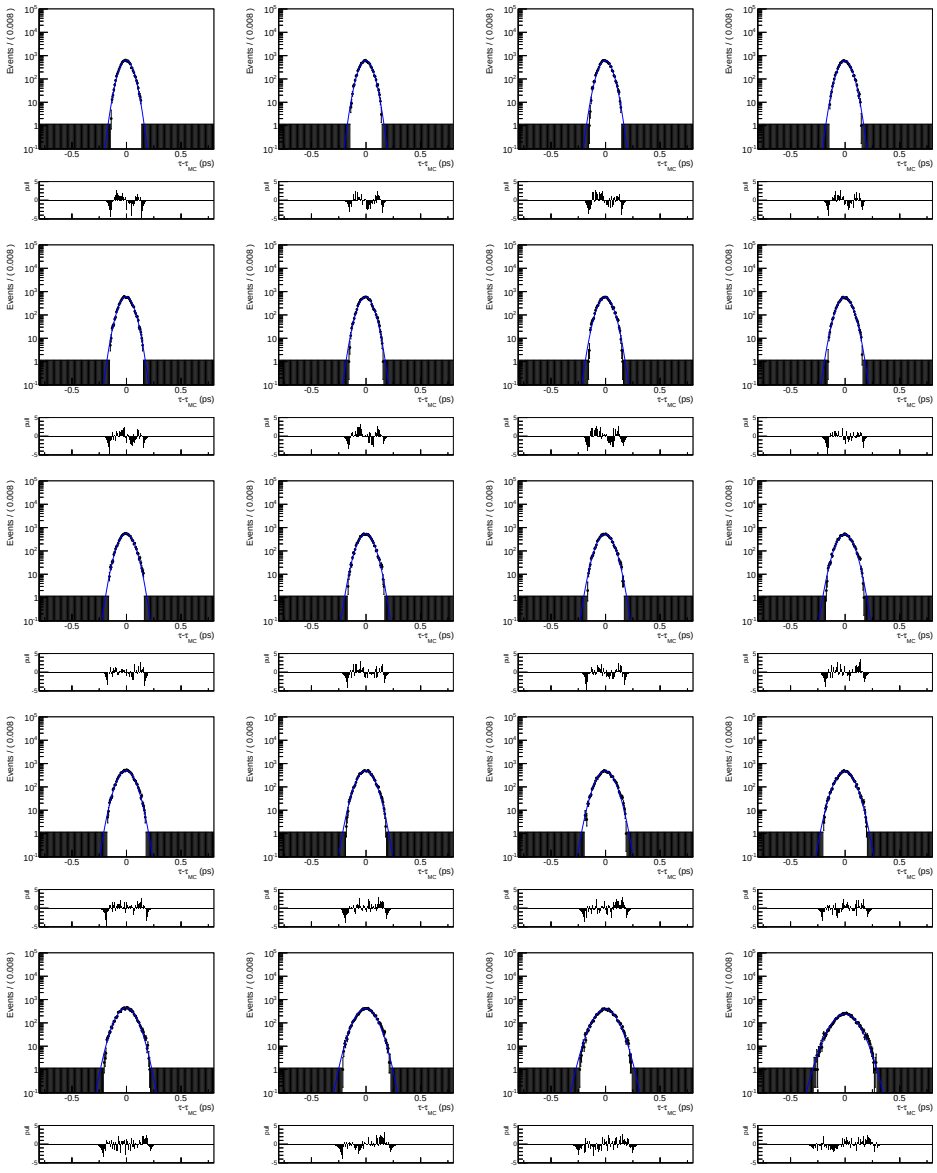

Figure E.2: Projection of the bi-dimensional fit in bins of the decay-time error for the $J/\psi \to \mu^+\mu^-$ data Run 2 sample.

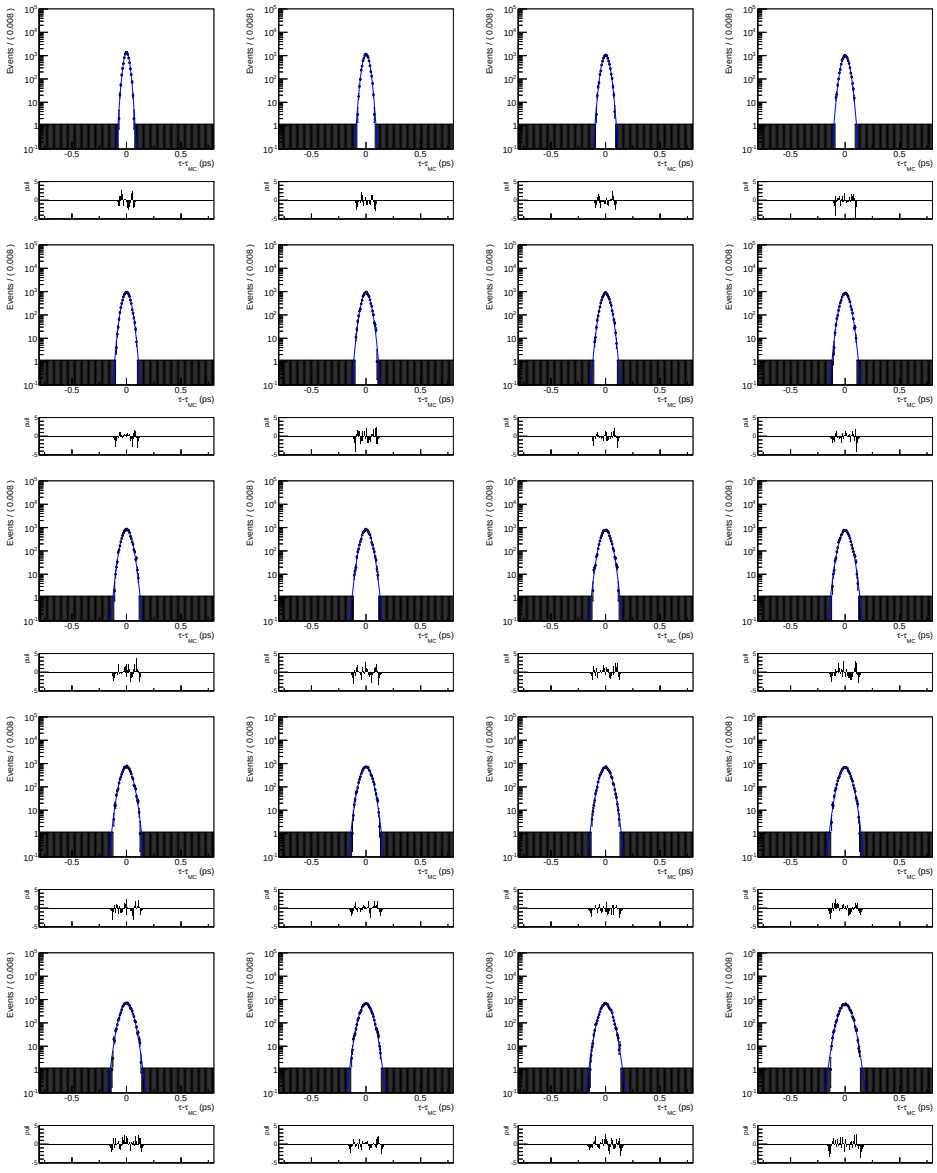

Figure E.3: Projection of the bi-dimensional fit in bins of the decay-time error for the $\Upsilon(1S) \to \mu^+\mu^-$ fully-simulated Run 2 sample.

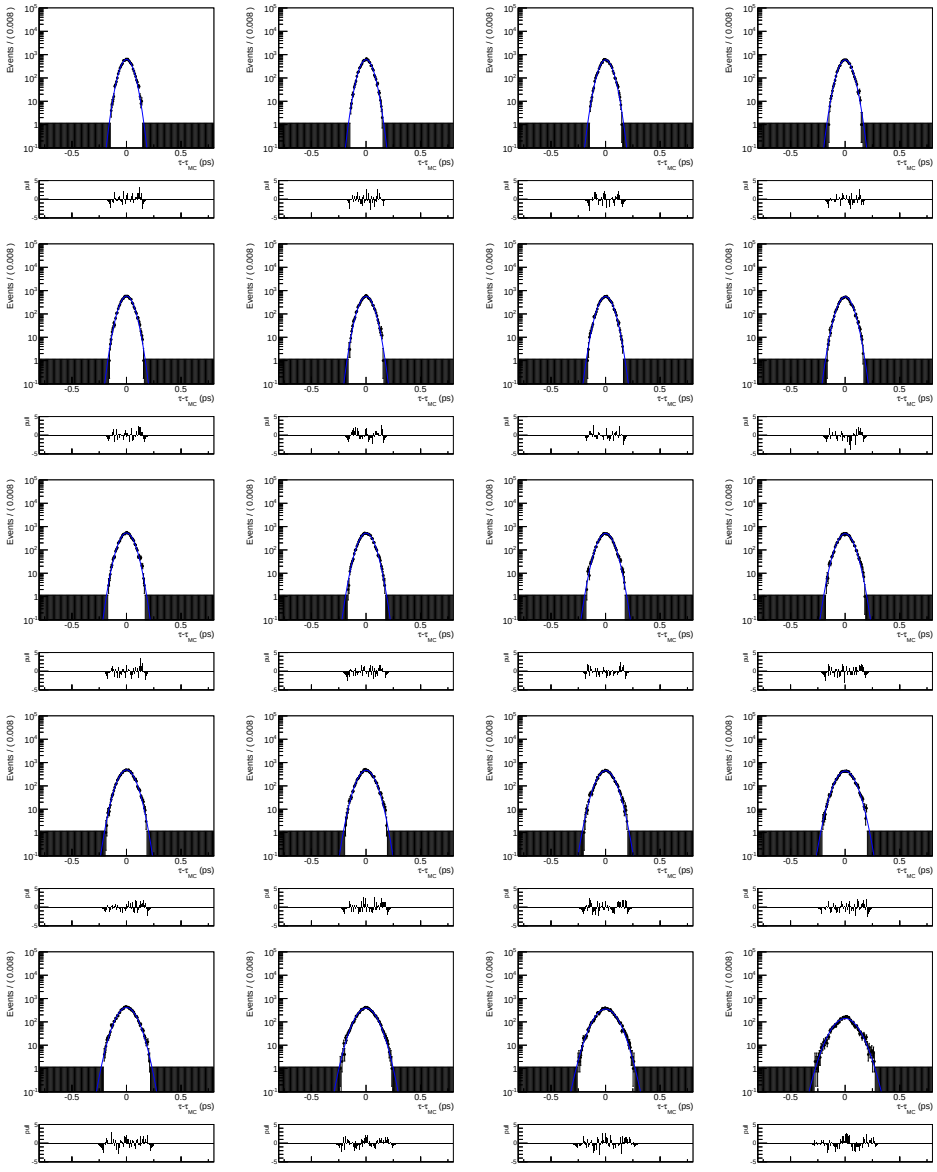

Figure E.4: Projection of the bi-dimensional fit in bins of the decay-time error for the $J/\psi \to \mu^+\mu^-$ fully-simulated Run 2 sample.

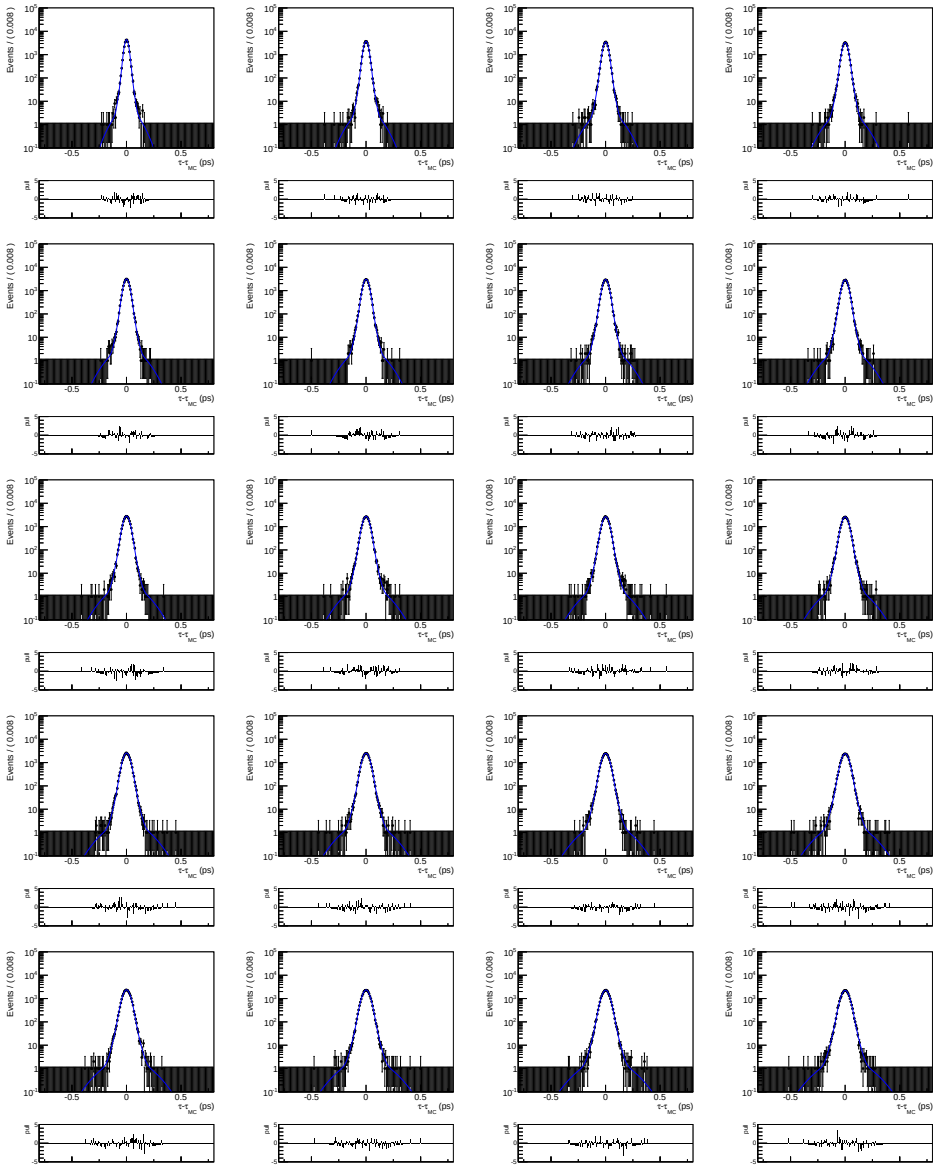

Figure E.5: Projection of the bi-dimensional fit in bins of the decay-time error for the $B_s^0 \to K^+K^-$ fully-simulated Run 2 sample.

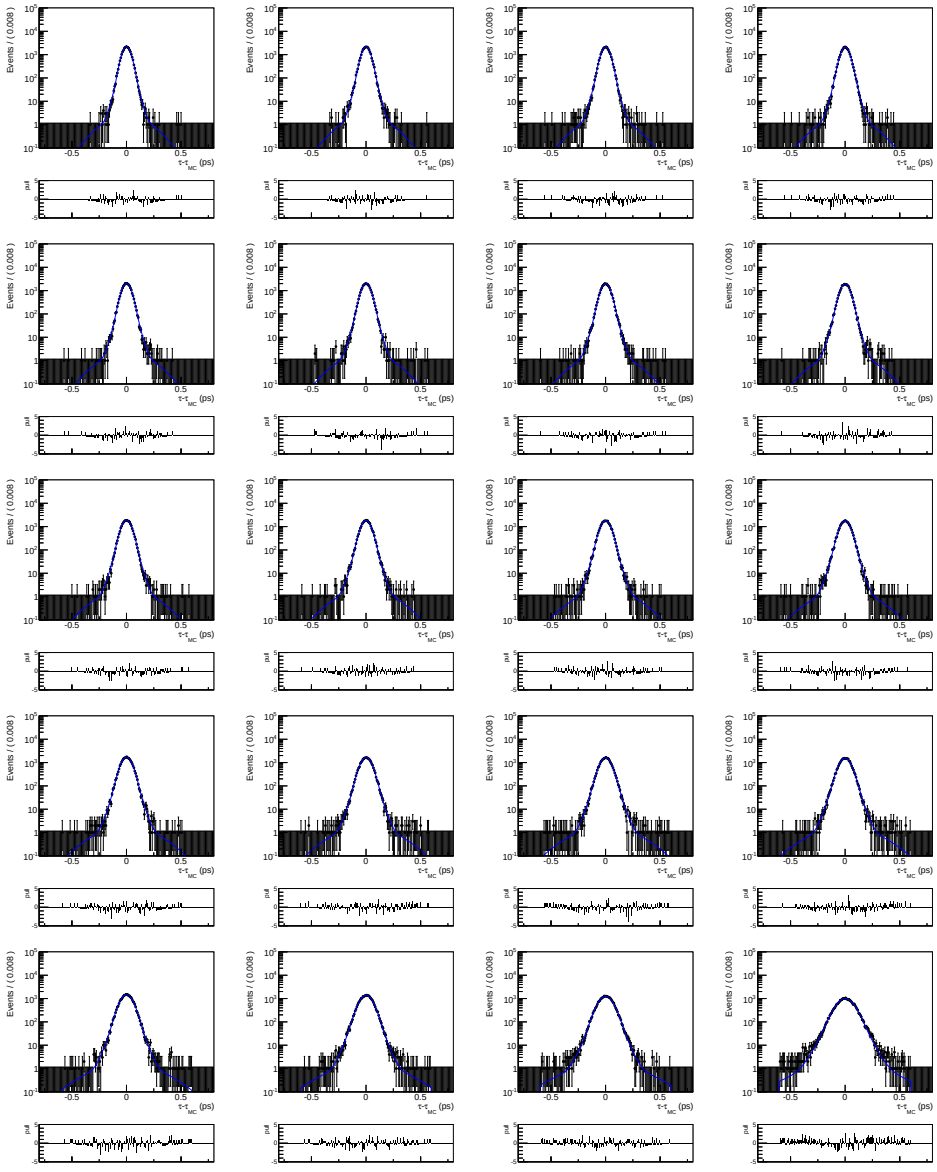

Figure E.6: Projection of the bi-dimensional fit in bins of the decay-time error for the $B_s^0 \to K^+K^-$ fully-simulated Run 2 sample.

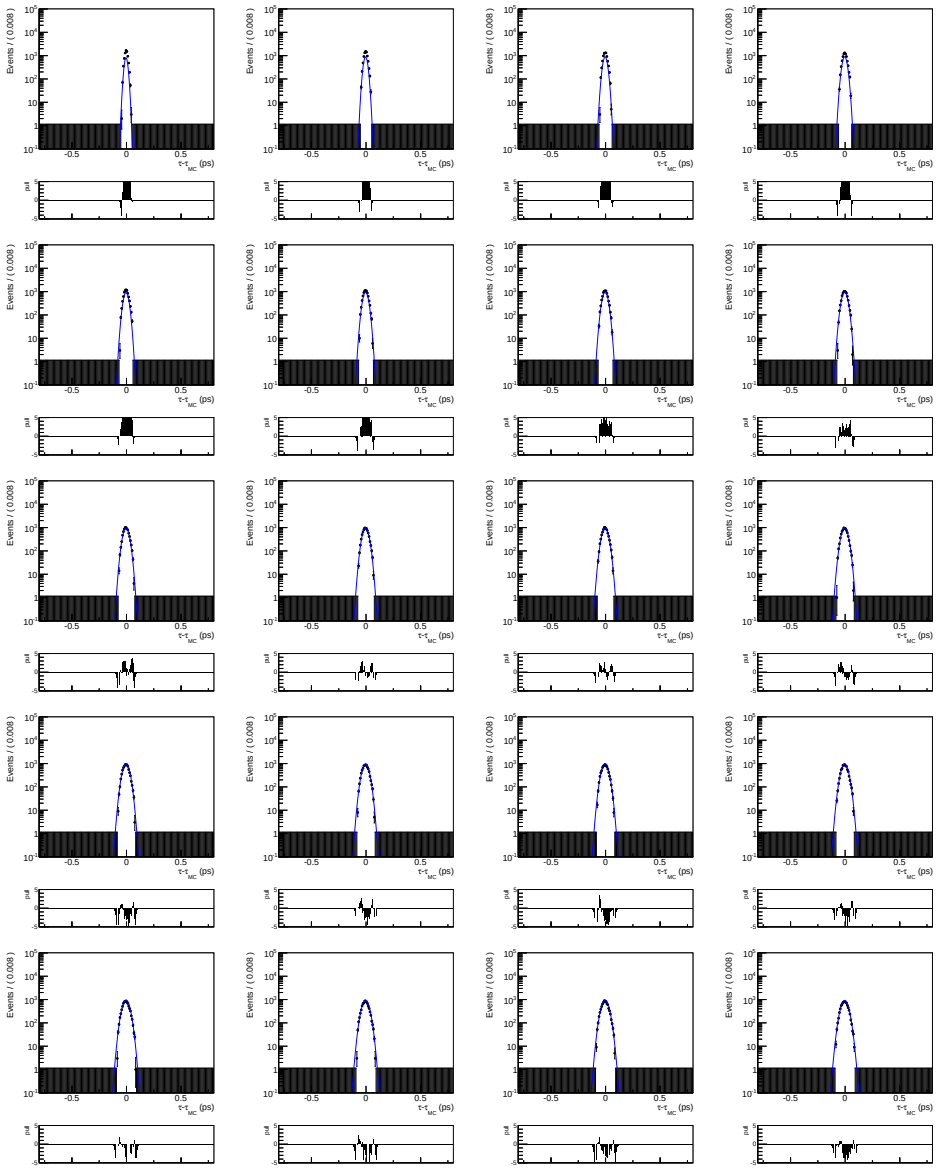

Figure E.7: Projection of the bi-dimensional fit in bins of the decay-time error for the $\Upsilon(1S) \to \mu^+\mu^-$ data Run 2 sample.

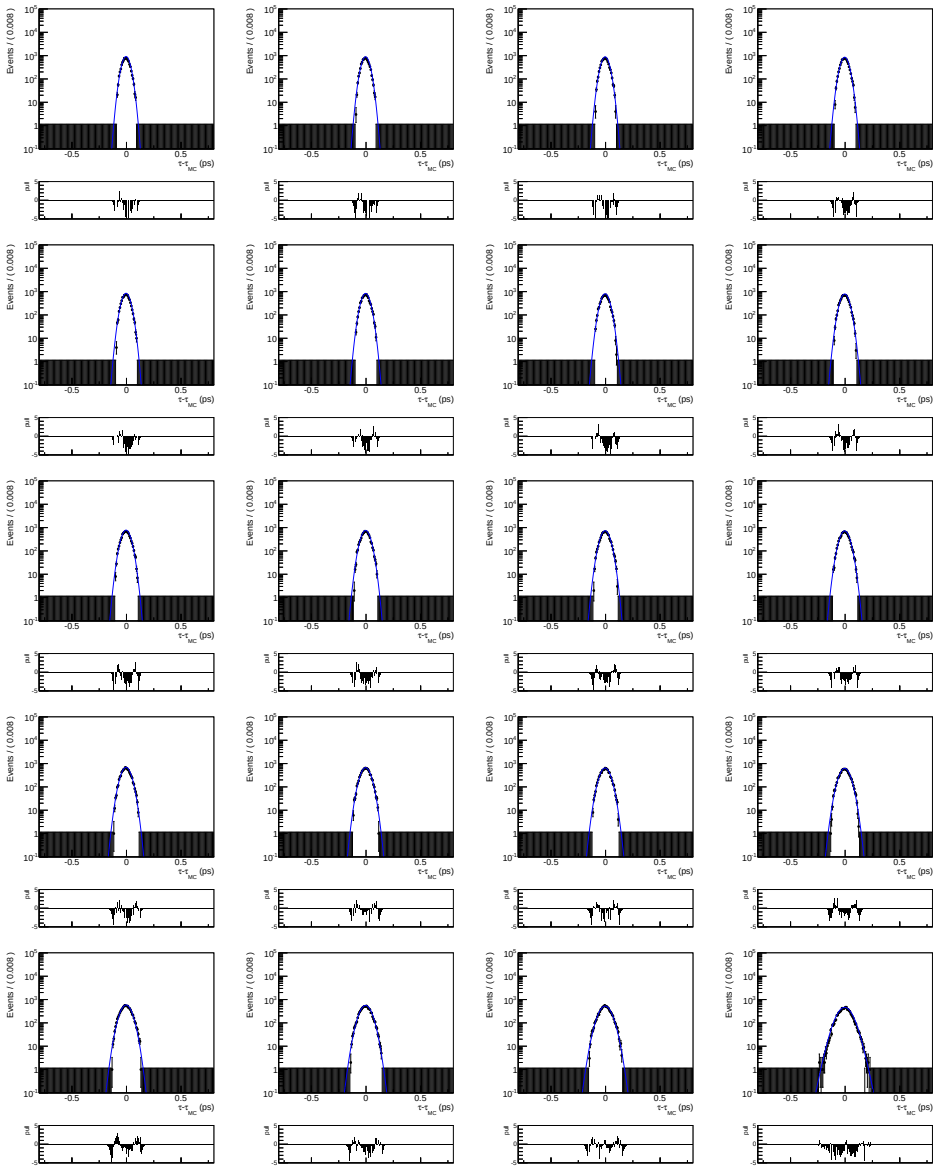

Figure E.8: Projection of the bi-dimensional fit in bins of the decay-time error for the $\Upsilon(1S) \to \mu^+\mu^-$ data Run 2 sample.

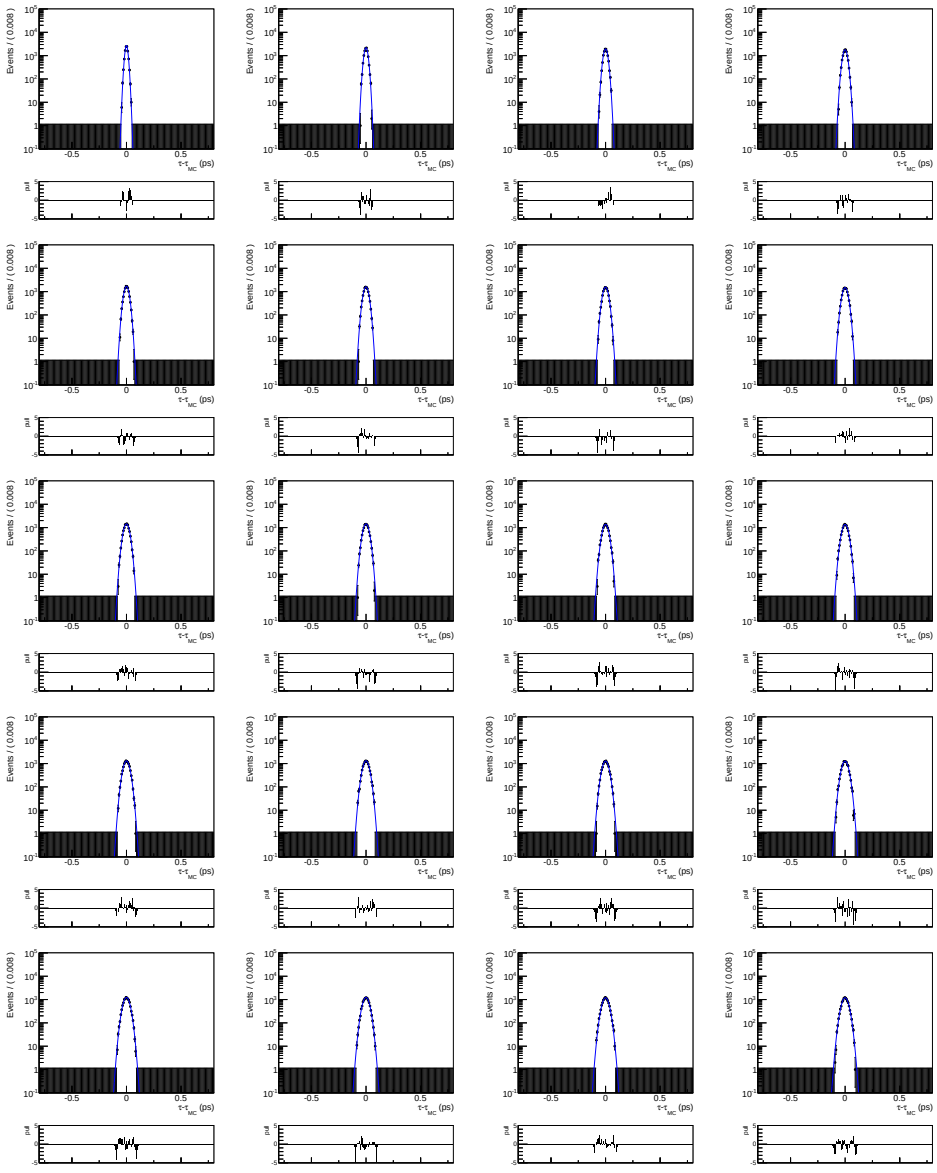

Figure E.9: Projection of the bi-dimensional fit in bins of the decay-time error for the $\Upsilon(1S) \to \mu^+\mu^-$ fully-simulated Run 2 sample.

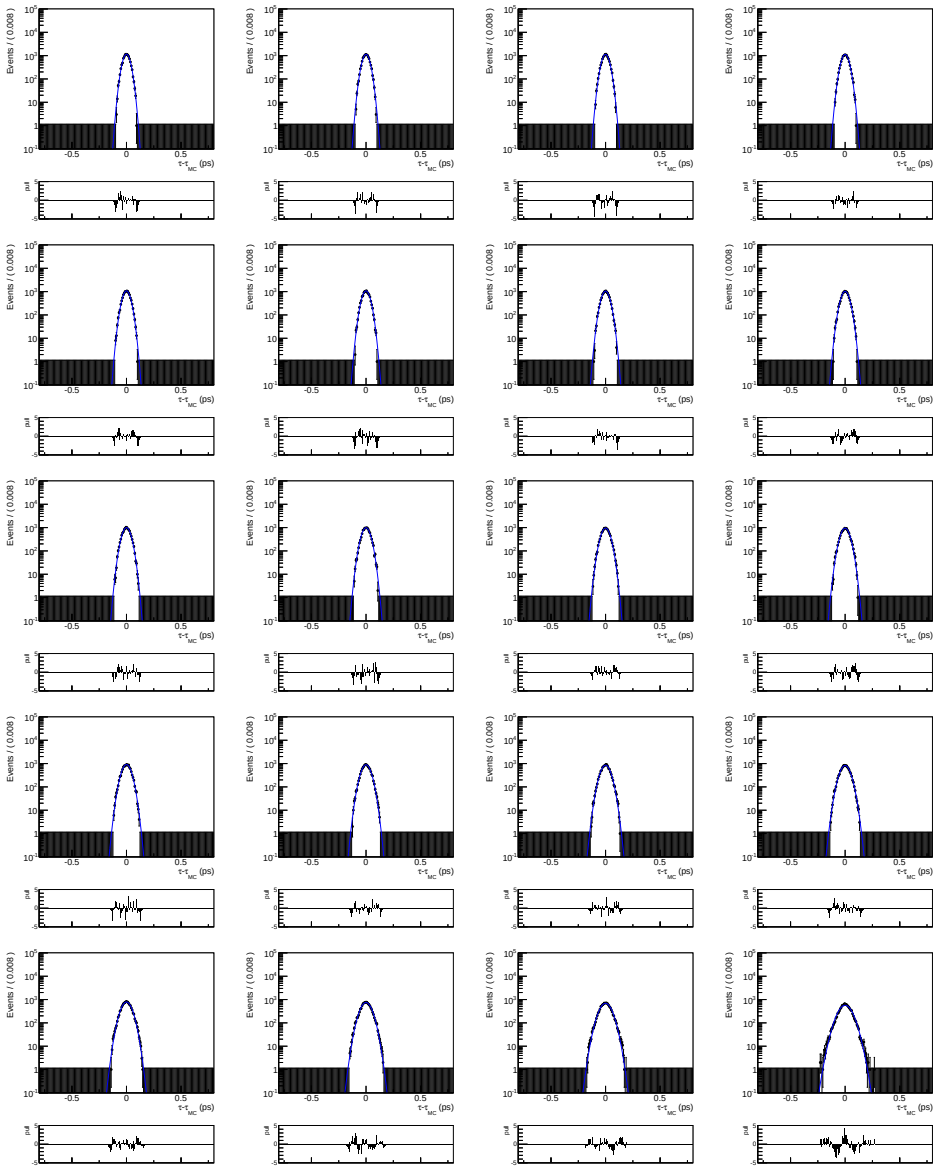

Figure E.10: Projection of the bi-dimensional fit in bins of the decay-time error for the $\Upsilon(1S) \to \mu^+\mu^-$ fully-simulated Run 2 sample.

Bibliography

[1] LHCb collaboration, R. Aaij et al., *Measurement of CP asymmetries in two-body $B^0_{(s)}$-meson decays to charged pions and kaons*, *Phys. Rev.* **D98** (2018) 032004 [1805.06759].

[2] J. H. Christenson, J. W. Cronin, V. L. Fitch and R. Turlay, *Evidence for the 2π decay of the K^0_2 meson*, *Phys. Rev. Lett.* **13** (1964) 138.

[3] LHCb collaboration, R. Aaij et al., *Evidence for CP violation in time-integrated $D^0 \to h^-h^+$ decay rates*, *Phys. Rev. Lett.* **108** (2012) 111602.

[4] LHCb collaboration, R. Aaij et al., *Search for CP violation in the phase space of $D^0 \to \pi^+\pi^-\pi^+\pi^-$ decays*, *Physics Letters B* **769** (2017) 345 .

[5] M. B. Gavela, P. Hernández, J. Orloff and O. Péne, *Standard model CP-violation and baryon asymmetry*, *Modern Physics Letters A* **09** (1994) 795 [hep-ph/9312215].

[6] S. L. Glashow, *Partial-symmetries of weak interactions*, *Nuclear Physics* **22** (1961) 579 .

[7] S. Weinberg, *A model of leptons*, *Phys. Rev. Lett.* **19** (1967) 1264.

[8] A. Salam, *Weak and electromagnetic interactions*, *Conf. Proc.* **C680519** (1968) 367.

[9] LHCb collaboration, R. Aaij et al., *Evidence for exotic hadron contributions to $\Lambda^0_b \to J/\psi p\pi^-$ decays*, *Phys. Rev. Lett.* **117** (2016) 082003.

[10] LHCb collaboration, R. Aaij et al., *Observation of $J/\psi p$ resonances consistent with pentaquark states in $\Lambda^0_b \to J/\psi K^- p$ decays*, *Phys. Rev. Lett.* **115** (2015) 072001.

[11] LHCb collaboration, R. Aaij et al., *Observation of $J/\psi\phi$ structures consistent with exotic states from amplitude analysis of $B^+ \to J/\psi\phi K^+$ decays*, *Phys. Rev. Lett.* **118** (2017) 022003.

[12] LHCb collaboration, R. Aaij et al., *Amplitude analysis of $B^+ \to J/\psi\phi K^+$ decays*, *Phys. Rev. D* **95** (2017) 012002.

[13] E. Noether, *Invariant variation problems*, *Transport Theory and Statistical Physics* **1** (1971) 186 [https://doi.org/10.1080/00411457108231446].

[14] P. W. Higgs, *Broken Symmetries and the Masses of Gauge Bosons*, *Phys. Rev. Lett.* **13** (1964) 508.

[15] M. Tanabashi et al., *PDG, (Particle Data Group)*, *Phys. Rev. D* **98** (2018) .

[16] N. Cabibbo, *Unitary symmetry and leptonic decays*, *Phys. Rev. Lett.* **10** (1963) 531.

[17] M. Kobayashi and T. Maskawa, *CP violation in the renormalizable theory of weak interaction*, *Prog. Theor. Phys.* **49** (1973) 652.

[18] C. Jarlskog, *Commutator of the quark mass matrices in the standard electroweak model and a measure of maximal CP non-conservation*, *Phys. Rev. Lett.* **55** (1985) 1039.

[19] UTfit collaboration, "UTfit collaboration web page." http://www.utfit.org/UTfit/.

[20] CKMfitter collaboration, "Ckmfitter collaboration web page." http://ckmfitter.in2p3.fr/.

[21] U. Nierste, *Three lectures on meson mixing and CKM phenomenology*, in *Heavy quark physics. Proceedings, Helmholtz International School, HQP08, Dubna, Russia, August 11-21, 2008*, pp. 1–38, 2009, 0904.1869.

[22] K. Anikeev et al., *B physics at the Tevatron: Run II and beyond*, in *Workshop on B Physics at the Tevatron: Run II and Beyond Batavia, Illinois, September 23-25, 1999*, 2001, hep-ph/0201071.

[23] BaBar collaboration, D. Boutigny et al., *The BABAR physics book: Physics at an asymmetric B factory*, in *Workshop on Physics at an Asymmetric B Factory (BaBar Collaboration Meeting) Pasadena, California, September 22-24, 1997*, 1998, http://www-public.slac.stanford.edu/sciDoc/docMeta.aspx?slacPubNumber=SLAC-R-504.

[24] UA1 collaboration, C. Albajar et al., *Search for $B^0 - \overline{B}^0$ oscillations at the CERN proton-antiproton collider*, *Physics Letters B* **186** (1987) 247 .

[25] ARGUS collaboration, H. Albrecht et al., *Observation of $B^0 - \overline{B}^0$ mixing*, *Phys. Lett.* **B192** (1987) 245.

[26] CDF collaboration, A. Abulencia et al., *Observation of $B_s^0 - \overline{B}_s^0$ oscillations*, *Phys. Rev. Lett.* **97** (2006) 242003 [hep-ex/0609040].

[27] S. L. Glashow, J. Iliopoulos and L. Maiani, *Weak interactions with lepton-hadron symmetry*, *Phys. Rev.* **D2** (1970) 1285.

[28] V. Weisskopf and E. Wigner, *Berechnung der natürlichen linienbreite auf grund der diracschen lichttheorie*, *Zeitschrift für Physik* **63** (1930) 54.

[29] V. Weisskopf and E. Wigner, *Über die natürliche linienbreite in der strahlung des harmonischen oszillators*, *Zeitschrift für Physik* **65** (1930) 18.

[30] C. S. Wu, E. Ambler, R. W. Hayward, D. D. Hoppes and R. P. Hudson, *Experimental test of parity conservation in β decay*, *Phys. Rev.* **105** (1957) 1413.

[31] Christenson, J. H. and Cronin, J. W. and Fitch, V. L. and Turlay, R., *Evidence for the 2π decay of the K_2^0 meson*, *Phys. Rev. Lett.* **13** (1964) 138.

[32] R. Fleischer, *B physics and CP violation*, *Lect. Notes Phys.* **647** (2004) 42 [hep-ph/0210323].

[33] G. Buchalla, A. J. Buras and M. E. Lautenbacher, *Weak decays beyond leading logarithms*, *Rev. Mod. Phys.* **68** (1996) 1125 [hep-ph/9512380].

[34] A. J. Buras, R. Fleischer and T. Mannel, *Penguin topologies, rescattering effects and penguin hunting with $B_{u,d} \to K\overline{K}$ and $B^{\pm} \to \pi^{\pm}K$*, *Nucl. Phys.* **B533** (1998) 3 [hep-ph/9711262].

[35] A. J. Buras, M. Jamin, M. E. Lautenbacher and P. H. Weisz, *Effective Hamiltonians for $\Delta S = 1$ and $\Delta B = 1$ nonleptonic decays beyond the leading logarithmic approximation*, *Nucl. Phys.* **B370** (1992) 69.

[36] A. J. Buras and R. Fleischer, *Quark mixing, CP violation and rare decays after the top quark discovery*, *Adv. Ser. Direct. High Energy Phys.* **15** (1998) 65 [hep-ph/9704376].

[37] R. Fleischer, *CP violation in the B system and relations to $K \to \pi\nu\bar{\nu}$ decays*, *Physics Reports* **370** (2002) 537 .

[38] N. G. Deshpande and X.-G. He, *Isospin structure of penguin diagrams and their consequences in B meson physics*, *Phys. Rev. Lett.* **74** (1995) 26.

[39] M. Gronau, O. F. Hernandez, D. London and J. L. Rosner, *Broken SU(3) symmetry in two-body B decays*, *Phys. Rev.* **D52** (1995) 6356 [hep-ph/9504326].

[40] A. J. Buras and R. Fleischer, *Limitations in measuring the angle β by using SU(3) relations for B meson decay amplitudes*, *Phys. Lett.* **B341** (1995) 379 [hep-ph/9409244].

[41] M. Ciuchini, E. Franco, G. Martinelli, M. Pierini and L. Silvestrini, *Charming penguins strike back*, *Phys. Lett.* **B515** (2001) 33 [hep-ph/0104126].

[42] R. Fleischer, *New strategies to extract β and γ from $B_d \to \pi^+\pi^-$ and $B_s \to K^+K^-$*, *Physics Letters B* **459** (1999) 306 .

[43] CDF collaboration, T. Aaltonen et al., *Observation of new charmless decays of bottom hadrons*, *Phys. Rev. Lett.* **103** (2009) 031801.

[44] CDF collaboration, T. Aaltonen et al., *Evidence for the charmless annihilation decay mode $B_s^0 \to \pi^+\pi^-$*, *Phys. Rev. Lett.* **108** (2012) 211803 [1111.0485].

[45] CDF collaboration, A. Abulencia et al., *Observation of $B_s^0 \to K^+K^-$ and measurements of branching fractions of charmless two-body decays of B^0 and B_s^0 mesons in $\overline{p}p$ collisions at $\sqrt{s} = 1.96$ TeV*, *Phys. Rev. Lett.* **97** (2006) 211802.

[46] CDF collaboration, T. Aaltonen et al., *Measurements of direct CP violating asymmetries in charmless decays of strange bottom mesons and bottom baryons*, *Phys. Rev. Lett.* **106** (2011) 181802.

[47] BABAR collaboration, B. Aubert et al., *Measurement of CP asymmetries and branching fractions in $B^0 \to \pi^+\pi^-$, $B^0 \to K^+\pi^-$, $B^0 \to \pi^0\pi^0$, $B^0 \to K^0\pi^0$ and isospin analysis of $B \to \pi\pi$ decays*, in *Proceedings, 34th International Conference on High Energy Physics (ICHEP 2008): Philadelphia, Pennsylvania, July 30-August 5, 2008*, 2008, 0807.4226, https://arxiv.org/abs/0807.4226.

[48] BELLE collaboration, S.-W. Lin et al., *Measurements of branching fractions for $B \to K\pi$ and $B \to \pi\pi$ decays*, *Phys. Rev. Lett.* **99** (2007) 121601.

[49] BELLE collaboration, H. Ishino et al., *Observation of direct CP violation in $B^0 \to \pi^+\pi^-$ decays and model-independent constraints on the quark-mixing angle ϕ_2*, *Phys. Rev. Lett.* **98** (2007) 211801.

[50] BABAR collaboration, B. Aubert et al., *Search for the decay $B^0 \to p\overline{p}$*, *Phys. Rev.* **D69** (2004) 091503 [hep-ex/0403003].

[51] BELLE collaboration, Y.-T. Tsai et al., *Search for $B^0 \to p\overline{p}$, $\Lambda\overline{\Lambda}$ and $B^+ \to p\overline{\Lambda}$ at Belle*, *Phys. Rev. D* **75** (2007) 111101.

[52] BELLE collaboration, Y.-T. Tsai et al., *Difference in direct charge-parity violation between charged and neutral B meson decays*, *Nature* **452** (2008) 332.

[53] LHCB collaboration, R. Aaij et al., *First measurement of time-dependent CP violation in $B_s^0 \to K^+K^-$ decays*, *JHEP* **10** (2013) 183 [1308.1428].

[54] LHCB collaboration, R. Aaij et al., *First observation of CP violation in the decays of B_s^0 mesons*, *Phys. Rev. Lett.* **110** (2013) 221601.

[55] R. Fleischer, *$B_{s,d} \to \pi\pi$,πK,KK: status and prospects*, *The European Physical Journal C* **52** (2007) 267.

[56] LHCb collaboration, B. Adeva et al., *Roadmap for selected key measurements of LHCb*, 0912.4179.

[57] C. Patrignani and P. D. Group, *Review of particle physics*, *Chinese Physics C* **40** (2016) 100001.

[58] LHCb collaboration, R. Aaij et al., *Measurement of b-hadron branching fractions for two-body decays into charmless charged hadrons*, *JHEP* **10** (2012) 037 [1206.2794].

[59] R. Mohanta, *Effects of R-parity violation on CP asymmetries in $\Lambda_b \to p\pi$ decay*, *Phys. Rev.* **D63** (2001) 056006 [hep-ph/0005240].

[60] LHCb collaboration, R. Aaij et al., *Search for CP violation in $\Lambda_b^0 \to pK^-$ and $\Lambda_b^0 \to p\pi^-$ decays*, 1807.06544.

[61] N. B. Mistry, *Prospects for CP-violation and B physics at e^+e^- collider B factories*, *Nuclear Physics B - Proceedings Supplements* **27** (1992) 316 .

[62] BaBar collaboration, J. P. Lees et al., *Measurement of CP asymmetries and branching fractions in charmless two-body B-meson decays to pions and kaons*, *Phys. Rev.* **D87** (2013) 052009 [1206.3525].

[63] Belle collaboration, I. Adachi et al., *Measurement of the CP violation parameters in $B^0 \to \pi^+\pi^-$ decays*, *Phys. Rev.* **D88** (2013) 092003 [1302.0551].

[64] Belle collaboration, Y.-T. Duh et al., *Measurements of branching fractions and direct CP asymmetries for $B \to K\pi$, $B \to \pi\pi$ and $B \to KK$ decays*, *Phys. Rev. D* **87** (2013) 031103.

[65] B. Lampe and T. Sack, *Precise determination of the top mass*, *Physics Letters B* **272** (1991) 339 .

[66] F. Abe and others., *Measurement of the B-meson and b-quark cross sections at $\sqrt{s}$ =1.8 TeV using the exclusive decay $B^{\pm} \to J/\psi\, K^{\pm}$*, *Phys. Rev. Lett.* **68** (1992) 3403.

[67] CDF, D0 collaboration, M. Paulini, *B physics at the Tevatron*, *Czech. J. Phys.* **54** (2004) A321 [hep-ex/0402020].

[68] M. Pepe Altarelli and F. Teubert, *B Physics at LHCb*, *Int. J. Mod. Phys.* **A23** (2008) 5117 [0802.1901].

[69] CDF collaboration, T. Aaltonen and S. others, *Measurements of direct CP-violating asymmetries in charmless decays of bottom baryons*, *Phys. Rev. Lett.* **113** (2014) 242001.

[70] LHCb collaboration, R. Aaij et al., *Measurement of time-dependent CP-violating asymmetries in $B^0 \to \pi^+\pi^-$ and $B_s^0 \to K^+K^-$ decays at LHCb, LHCB-CONF-2016-018*, .

[71] Heavy Flavor Averaging Group collaboration, Y. Amhis et al., *Averages of b-hadron, c-hadron, and τ-lepton properties as of summer 2016*, *Eur. Phys. J.* **C77** (2017) 895 [1612.07233].

[72] LHCb collaboration, R. Aaij et al., *Measurement of the time-dependent CP asymmetry in $B^0 \to J/\psi K_S^0$ decays*, *Phys. Lett.* **B721** (2013) 24 [1211.6093].

[73] LHCb collaboration, R. Aaij et al., *Determination of γ and $-2\beta_s$ from charmless two-body decays of beauty mesons*, *Physics Letters B* **741** (2015) 1 .

[74] L. Evans and P. Bryant, *LHC Machine*, *Journal of Instrumentation* **3** (2008) S08001.

[75] ALICE collaboration, K. Aamodt et al., *The ALICE experiment at the CERN LHC*, *Journal of Instrumentation* **3** (2008) S08002.

[76] ATLAS collaboration, G. Aad et al., *The ATLAS experiment at the CERN Large Hadron Collider*, *Journal of Instrumentation* **3** (2008) S08003.

[77] CMS collaboration, S. Chatrchyan et al., *The CMS experiment at the CERN LHC*, *Journal of Instrumentation* **3** (2008) S08004.

[78] LHCb collaboration, A. A. Alves, Jr. et al., *The LHCb Detector at the LHC*, *JINST* **3** (2008) S08005.

[79] LHCf collaboration, O. Adriani et al., *The LHCf detector at the CERN Large Hadron Collider*, *Journal of Instrumentation* **3** (2008) S08006.

[80] MoEDAL collaboration, B. Acharya et al., *The physics programme of the MoEDAL experiment at the LHC*, *Int. J. Mod. Phys.* **A29** (2014) 1430050 [1405.7662].

[81] TOTEM collaboration, G. Anelli et al., *The TOTEM experiment at the CERN Large Hadron Collider*, *Journal of Instrumentation* **3** (2008) S08007.

[82] LHCb collaboration, R. Aaij et al., *LHCb Detector Performance*, *Int. J. Mod. Phys.* **A30** (2015) 1530022 [1412.6352].

[83] LHCb collaboration, "LHCb Operations Plots Webpage." https://lbgroups.cern.ch/online/OperationsPlots/index.htm.

[84] W. Herr, *Effects of PACMAN bunches in the LHC, CERN-LHC-PROJECT-REPORT-039*, 1996.

[85] E. Norrbin and T. Sjöstrand, *Production and hadronization of heavy quarks*, *Eur. Phys. J.* **C17** (2000) 137 [hep-ph/0005110].

[86] R. Placakyte, *Parton Distribution Functions*, in *Proceedings, 31st International Conference on Physics in collisions (PIC 2011): Vancouver, Canada, August 28-September 1, 2011*, 2011, 1111.5452, https://inspirehep.net/record/954990/files/arXiv:1111.5452.pdf.

[87] LHCb collaboration, "The LHCb Collaboration webpage." http://lhcb.web.cern.ch/lhcb/.

[88] B. Andersson, G. Gustafson, G. Ingelman and T. Sjöstrand, *Parton fragmentation and string dynamics*, *Physics Reports* **97** (1983) 31 .

[89] E. Norrbin, *Heavy quark production asymmetries*, in *Proceedings, International Europhysics Conference on High energy physics (EPS-HEP 1999): Tampere, Finland, July 15-21, 1999*, pp. 408–410, 1999, hep-ph/9909437.

[90] T. Sjöstrand, S. Mrenna and P. Z. Skands, *PYTHIA 6.4 Physics and Manual*, *JHEP* **05** (2006) 026 [hep-ph/0603175].

[91] DELPHI collaboration, *The DELPHI detector at LEP*, *Nuclear Instruments and Methods in Physics Research Section A: Accelerators, Spectrometers, Detectors and Associated Equipment* **303** (1991) 233 .

[92] LHCb collaboration, *LHCb VELO TDR: Vertex locator. Technical design report, CERN-LHCC-2001-011*, 2001.

[93] LHCb collaboration, "LHCb Silicon Tracker." http://lhcb.physik.uzh.ch/SiliconTracker/.

[94] LHCb collaboration, *LHCb: Inner Tracker technical design report, CERN-LHCC-2002-029*, 2002.

[95] LHCb collaboration, *LHCb: Outer Tracker technical design report, CERN-LHCC-2001-024*, 2001.

[96] LHCb collaboration, *Performance of the LHCb Outer Tracker*, *Journal of Instrumentation* **9** (2014) P01002 [1311.3893].

[97] LHCb collaboration, *LHCb magnet: technical design report, CERN-LHCC-2000-007*, 2000.

[98] LHCb collaboration, *LHCb: RICH technical design report, CERN-LHCC-2000-037*, 2000.

[99] LHCb collaboration, *LHCb calorimeters: technical design report, CERN-LHCC-2000-036*, 2000.

[100] J. R. Harrison, *Radiation damage studies in the LHCb VELO detector and searches for lepton flavour and baryon number violating tau decays, CERN-THESIS-2014-068*, Ph.D. thesis, Manchester U., 2014.

[101] LHCb collaboration, *LHCb: Addendum to the muon system technical design report, CERN-LHCC-2003-002*, 2003.

[102] A. A. Alves, Jr. et al., *Performance of the LHCb muon system*, *JINST* **8** (2013) P02022 [1211.1346].

[103] R. Aaij et al., *The LHCb trigger and its performance in 2011*, *JINST* **8** (2013) P04022 [1211.3055].

[104] W. D. Hulsbergen, *The global covariance matrix of tracks fitted with a Kalman filter and an application in detector alignment*, *Nuclear Instruments and Methods in Physics Research A* **600** (2009) 471 [0810.2241].

[105] M. Clemencic, G. Corti, S. Easo, C. R. Jones, S. Miglioranzi, M. Pappagallo et al., *The LHCb simulation application, Gauss: design, evolution and experience*, *Journal of Physics: Conference Series* **331** (2011) 032023.

[106] T. Sjöstrand, S. Ask, J. R. Christiansen, R. Corke, N. Desai, P. Ilten et al., *An Introduction to PYTHIA 8.2*, *Comput. Phys. Commun.* **191** (2015) 159 [1410.3012].

[107] D. J. Lange, *The EvtGen particle decay simulation package*, *Nuclear Instruments and Methods in Physics Research Section A: Accelerators, Spectrometers, Detectors and Associated Equipment* **462** (2001) 152 .

[108] P. Golonka and Z. Was, *PHOTOS Monte Carlo: a precision tool for QED corrections in Z and W decays*, *The European Physical Journal C - Particles and Fields* **45** (2006) 97.

[109] S. Agostinelli, J. Allison et al., *Geant4-a simulation toolkit*, *Nuclear Instruments and Methods in Physics Research Section A: Accelerators, Spectrometers, Detectors and Associated Equipment* **506** (2003) 250 .

[110] J. Allison et al., *Geant4 developments and applications*, *IEEE Transactions on Nuclear Science* **53** (2006) 270.

[111] LHCb collaboration, "Boole webpage." http://lhcbdoc.web.cern.ch/lhcbdoc/boole/.

[112] LHCb collaboration, "Moore webpage." http://lhcbdoc.web.cern.ch/lhcbdoc/moore/.

[113] LHCb collaboration, "Brunel webpage." http://lhcbdoc.web.cern.ch/lhcbdoc/brunel/.

[114] LHCb collaboration, "Davinci webpage." http://lhcbdoc.web.cern.ch/lhcbdoc/davinci/.

[115] LHCb collaboration, R. Aaij et al., *Opposite-side flavour tagging of B mesons at the LHCb experiment*, *Eur. Phys. J.* **C72** (2012) 2022 [1202.4979].

[116] LHCb collaboration, R. Aaij et al., *B flavour tagging using charm decays at the LHCb experiment*, *JINST* **10** (2015) P10005 [1507.07892].

[117] LHCb collaboration, R. Aaij et al., *New algorithms for identifying the flavour of* B^0 *mesons using pions and protons*, *Eur. Phys. J. C* **77** (2016) 238. 23 p [1610.06019].

[118] D. Fazzini, M. Calvi and B. Khanji, *Development of "same side" flavour tagging algorithms for measurements of flavour oscillations and CP violation in the* B^0 *mesons system*, *CERN-THESIS-2015-040*, Ph.D. thesis, Mar, 2015.

[119] R. Aaij et al., *A new algorithm for identifying the flavour of* B_s^0 *mesons at LHCb*, *Journal of Instrumentation* **11** (2016) P05010 [1602.07252].

[120] M. Calvi, D. Fazzini and M. Rotondo, *Studies on the SS*Λ *tagger*, Tech. Rep. LHCb-INT-2018-031. CERN-LHCb-INT-2018-031, CERN, Geneva, Oct, 2018.

[121] LHCb collaboration, R. Aaij et al., *Optimization and calibration of the LHCb flavour tagging performance using 2010 data, LHCb-CONF-2011-003*, .

[122] M. Pivk and F. R. Le Diberder, *SPlot: a statistical tool to unfold data distributions*, *Nucl. Instrum. Meth.* **A555** (2005) 356 [physics/0402083].

[123] J. Wimberley et al., "Espresso performance monitor." https://gitlab.cern.ch/lhcb-ft/EspressoPerformanceMonitor, 2017.

[124] W. Verkerke and others, "RooFit." http://roofit.sourceforge.net/.

[125] W. D. Hulsbergen, *Decay chain fitting with a kalman filter*, *Nuclear Instruments and Methods in Physics Research Section A: Accelerators, Spectrometers, Detectors and Associated Equipment* **552** (2005) 566 .

[126] A. Carbone, D. Derkach, D. Galli, U. Marconi, S. Perazzini, V. Vagnoni et al., *Measurement of time-dependent CP-violating asymmetries in* $B^0 \to \pi^+\pi^-$ *and* $B_s^0 \to K^+K^-$ *decays at LHCb, LHCb-ANA-2013-040*, .

[127] A. Carbone, D. Derkach, D. Galli, U. Marconi, S. Perazzini, V. Vagnoni et al., *Measurement of time-dependent CP violation in charmless charged two-body B decays, LHCb-CONF-2012-007*, .

[128] B. P. Roe, H.-J. Yang, J. Zhu, Y. Liu, I. Stancu and G. McGregor, *Boosted decision trees, an alternative to artificial neural networks*, *Nucl. Instrum. Meth.* **A543** (2005) 577 [physics/0408124].

[129] K. Cranmer, *Kernel estimation in high-energy physics*, *Computer Physics Communications* **136** (2001) 198 .

[130] LHCb collaboration, R. Aaij et al., *Measurement of b-hadron production fractions in 7 TeV pp collisions*, *Phys. Rev.* **D85** (2012) 032008 [1111.2357].

[131] Belle collaboration, A. Zupanc et al., *Measurement of the branching fraction $\mathcal{B}(\Lambda_c^+ \to pK^-\pi^+)$*, *Phys. Rev. Lett.* **113** (2014) 042002 [1312.7826].

[132] H. Albrecht et al., *Measurement of the polarization in the decay $B \to J/\psi K^*$*, *Physics Letters B* **340** (1994) 217 .

[133] LHCb RICH Group collaboration, M. Adinolfi et al., *Performance of the LHCb RICH detector at the LHC*, *Eur. Phys. J.* **C73** (2013) 2431 [1211.6759].

[134] A. Carbone, F. Ferrari, S. Perazzini and V. Vagnoni, *Search for the $B^0 \to K^+K^-$ decay with $\int \mathcal{L}\, dt = 3\, fb^{-1}$, LHCb-ANA-2016-016*, .

[135] R. Aaij, Y. Amhis, G. Cowan, D. van Eijk, W. Hulsbergen, B. Khanji et al., *Selections and lifetime measurements for exclusive $b \to J/\psi X$ decays with $J/\psi \to \mu^+\mu^-$ with 2010 data, LHCb-CONF-2011-001*, .

[136] S. Perazzini, V. Vagnoni, F. Ferrari, F. Betti and A. Carbone, *Measurement of time-dependent CP-violating asymmetries in $B^0 \to \pi^+\pi^-$ and $B_s^0 \to K^+K^-$ decays at LHCb, LHCb-ANA-2016-070*, .

[137] T. M. Karbach, G. Raven and M. Schiller, *Decay time integrals in neutral meson mixing and their efficient evaluation*, 1407.0748.

[138] A. Carbone, F. Ferrari, S. Perazzini and V. Vagnoni, *Measurement of B^0, B_s^0, B^+ and Λ_b^0 production asymmetries in 7 TeV and 8 TeV pp collisions, LHCb-ANA-2016-037*, .

[139] LHCb collaboration, R. Aaij et al., *Measurement of CP asymmetry in $D^0 \to K^-K^+$ and $D^0 \to \pi^-\pi^+$ decays*, *JHEP* **07** (2014) 041 [1405.2797].

[140] H. J. Lipkin, *Is observed direct CP violation in $B_d \to K^+\pi^-$ due to new physics? Check standard model prediction of equal violation in $B_s \to K^-\pi^+$*, *Phys. Lett.* **B621** (2005) 126 [hep-ph/0503022].

[141] LHCb Collaboration collaboration, *Updated average f_s/f_d b-hadron production fraction ratio for 7 TeV pp collisions, LHCb-CONF-2013-011*, .

[142] S. Perazzini, D. Fazzini, V. Vagnoni, F. Ferrari, F. Betti and A. Carbone, *Measurement of time-dependent CP-violating asymmetries in $B^0 \to \pi^+\pi^-$ and $B_s^0 \to K^+K^-$ decays at LHCb, LHCb-ANA-2017-003*, .

[143] A. Davis, L. Dufour, F. Ferrari, S. Stahl, M. A. Vesterinen and J. Van Tilburg, *Measurement of the $K^-\pi^+$ two-track detection asymmetry in Run 2 using the Turbo stream*, Tech. Rep. LHCb-INT-2017-023. CERN-LHCb-INT-2017-023, CERN, Geneva, Sep, 2017.